

2014

Simulation of Electrohydraulic Forming Using Anisotropic, Rate-dependent Plasticity Models

Amir Hassannejadasl
University of Windsor

Follow this and additional works at: <http://scholar.uwindsor.ca/etd>

Recommended Citation

Hassannejadasl, Amir, "Simulation of Electrohydraulic Forming Using Anisotropic, Rate-dependent Plasticity Models" (2014).
Electronic Theses and Dissertations. Paper 5205.

This online database contains the full-text of PhD dissertations and Masters' theses of University of Windsor students from 1954 forward. These documents are made available for personal study and research purposes only, in accordance with the Canadian Copyright Act and the Creative Commons license—CC BY-NC-ND (Attribution, Non-Commercial, No Derivative Works). Under this license, works must always be attributed to the copyright holder (original author), cannot be used for any commercial purposes, and may not be altered. Any other use would require the permission of the copyright holder. Students may inquire about withdrawing their dissertation and/or thesis from this database. For additional inquiries, please contact the repository administrator via email (scholarship@uwindsor.ca) or by telephone at 519-253-3000ext. 3208.

Simulation of Electrohydraulic Forming Using Anisotropic, Rate-dependent Plasticity Models

by

Amir Hassannejadasl

A Dissertation
Submitted to the Faculty of Graduate Studies
through the Department of Mechanical, Automotive & Materials Engineering
in Partial Fulfillment of the Requirements for
the Degree of Doctor of Philosophy
at the University of Windsor

Windsor, Ontario, Canada

2014

© 2014 Amir Hassannejadasl

Simulation of Electrohydraulic Forming Using Anisotropic, Rate-dependent Plasticity Models

by
Amir Hassannejadasl

APPROVED BY:

Dr. P.D. Wu, External Examiner
McMaster University

Dr. S.F. Golovashchenko, Industrial Advisor
Ford Research & Advanced Engineering, Dearborn, MI

Dr. S. Cheng
Department of Civil and Environmental Engineering

Dr. N. Zamani
Department of Mechanical, Automotive & Materials Engineering

Dr. W. Altenhof
Department of Mechanical, Automotive & Materials Engineering

Dr. D.E. Green, Advisor
Department of Mechanical, Automotive & Materials Engineering

September 11, 2014

Declaration of Previous Publication

This dissertation includes one original paper that will be published in the proceedings of the ICTP2014 conference (Nagoya, Japan). Two journal papers were written and are ready to be submitted for publication. However, due to co-authorship limitation and requirements, these papers are on hold at the present time and they will be submitted as soon as the other partner of this project (University of Waterloo) receives their final publication approval.

Thesis Chapter	Publication title/full citation	Publication status
<i>Chapter 4</i>	<i>Prediction of DP600 flow surfaces at various strain-rates using Yld2004-18p yield function</i>	<i>“accepted for Publication”</i>

I certify that I have obtained a written permission (Appendix-A3) from the copyright owner(s) to include the above published material in my dissertation. I certify that the above material describes work completed during my registration as graduate student at the University of Windsor.

I declare that, to the best of my knowledge, my dissertation does not infringe upon anyone’s copyright nor violate any proprietary rights and that any ideas, techniques, quotations, or any other material from the work of other people included in my dissertation, published or otherwise, are fully acknowledged in accordance with the standard referencing practices. Furthermore, to the extent that I have included copyrighted material that surpasses the bounds of fair dealing within the meaning of the Canada Copyright Act, I certify that I have obtained a written permission from the copyright owner(s) to include such material(s) in my dissertation.

I declare that this is a true copy of my dissertation, including any final revisions, as approved by my dissertation committee and the Graduate Studies office, and that this dissertation has not been submitted for a higher degree to any other University or Institution.

Abstract

Electrohydraulic forming (EHF) is a pulsed forming process in which two or more electrodes are positioned in a chamber filled with a liquid and a high-voltage discharge between the electrodes generates a high-pressure to form the sheet. Deformation history of a sheet material in EHF process shows substantial changes in the strain rate of the material during the forming process. In this research, the mechanical properties of DP600, TRIP780, and AA5182-O were obtained at different strain rates. Uniaxial tensile tests showed significant strain-rate sensitivity in all three material orientations (RD, DD, and TD) for DP600 and TRIP780. In contrast, AA5182-O exhibits almost near-zero strain-rate sensitivity. Several anisotropic yield functions were calibrated at various strain rates to evaluate the effect of strain rate on the flow surface shape. By comparing the quasistatic and updated flow surfaces of DP600 and TRIP780 predicted by Yld2000-2d, results show a relatively considerable effect of updating anisotropy coefficients for higher strain rates (1000 s^{-1}).

Several rate-dependent anisotropic material models (plane stress and general) were developed, by combining updated anisotropic yield functions and a rate-dependent hardening model (KHL). The developed models were implemented as user-defined material subroutines (VUMATs) based on implicit stress integration algorithm for ABAQUS/Explicit code to simulate electrohydraulic free-forming (EHFF) and die-forming (EHDF) processes. EHF simulations were completed, using Eulerian elements and ignition-and-growth model. The EHFF process was simulated for four different geometries (representing four different strain paths). Also, the EHDF process was simulated using a conical die. The EHFF simulation results for the DP600 biaxial specimen showed that von Mises predicts a maximum effective plastic strain around 11% greater than Yld2000-2d for the same amount of applied energy.

The EHDF simulation result for DP600 showed that with the same applied energy magnitude, von Mises overpredicts major, minor and through-thickness shear strains and consequently effective plastic strain (14% higher) compared to Yld2004-18p. Results showed that 82% of the effective plastic strain occurs under a proportional biaxial strain path before contacting the die. Also, results showed that von Mises overpredicts maximum absolute compressive through-thickness stress and shear strain compared to the values predicted by Yld2004-18p.

Acknowledgements

I would like to acknowledge my dear advisor, Dr. Daniel Green who substantially helped and guided me to complete this work. Dr. Green; I would like to say it was a great opportunity for me to work with you and I really appreciate all your great support throughout the duration of this work.

I would also like to express my gratitude to my best friend/colleague, Chris Maris for his kind and unbelievable support and assistance. Chris; I was very lucky to have such a nice and mature friend as at the desk next to mine.

I would like to express my appreciation to Dr. Sergey Golovashchenko who technically guided me during this project. His expertise and knowledge was really amazing and I learnt a lot from him.

I would also like to thank my favorite professor, Dr. William Altenhof, who always generously contributed his exceptional knowledge and expertise to me and our team.

And finally, I would like to express my warm gratitude to my beloved wife, MONA, for her patience and understanding throughout the duration of this work.

Table of Contents

Declaration of Previous Publication	iii
Abstract	iv
Acknowledgements	v
List of Tables	x
List of Figures	xii
1 Introduction	1
2 Literature Review	7
2.1 Introduction	7
2.2 High speed metal forming	8
2.2.1 High strain rate metal forming processes.....	8
2.2.2 Electrohydraulic forming (EHF).....	11
2.3 Constitutive model.....	15
2.3.1 Anisotropic yield functions.....	16
2.3.2 Flow rule	24
2.3.3 Rate-dependent hardening models	26
2.4 Experiments; high strain rate tests.....	31
3 Rate-dependent Constitutive Model	35
3.1 Anisotropic yield functions	35
3.1.1 Hill 1948 (Hill48)	35
3.1.2 Hill 1990 (Hill90)	37
3.1.3 Barlat 1989 (Barlat89)	39
3.1.4 Barlat 1996 (Yld96)	40
3.1.5 Barlat 2003 (Yld2000-2d).....	42
3.1.6 Barlat 2005 (Yld2004-18p).....	44
3.2 Experimental work	47
3.2.1 Sheet materials	47
3.2.2 Quasi-static, intermediate and high strain rate tests.....	48
3.2.3 Experimental results.....	49

3.3	Anisotropy coefficients.....	61
3.3.1	Evolution of flow stresses.....	61
3.3.2	Calculation of biaxial flow stress at higher strain rates.....	67
3.3.3	Determination of anisotropy coefficients for different yield functions.....	72
3.3.4	Updating Yld2000-2d anisotropy coefficients w.r.t. strain rate.....	85
3.4	Rate-dependent hardening models.....	88
3.4.1	Johnson-Cook (JC).....	88
3.4.2	Khan-Huang-Liang (KHL).....	89
3.4.3	Surajit Kumar Paul (SKP).....	90
3.5	Determination of constants for different hardening models.....	91
4	Effect of Updating Anisotropy Coefficients on the Flow Surface.....	97
4.1	Planar Distribution of Anisotropic Data (uniaxial flow stress and r-value)...	97
4.1.1	Uniaxial Anisotropic Data Formulation.....	100
4.1.2	Predicted Anisotropic Data (flow stress and r-value).....	106
4.2	Effect of Updating Anisotropy Coefficients on the Flow Surface.....	119
4.2.1	Comparison between the Updated and Quasistatic Yld2000-2d.....	120
4.2.2	Comparison between the Updated and Quasistatic Hill48-r.value.....	121
4.2.3	Comparison between the Updated Hill`s family and Updated Barlat`s family	121
4.2.4	Comparison between the Updated Yld2000-2d and von Mises.....	123
4.2.5	Comparison between the Updated and Quasistatic Yld2000-2d at different levels of normalized shear stress.....	124
5	Rate-dependent Implicit Stress Integration Scheme	144
5.1	Introduction.....	144
5.2	Stress Integration.....	146
5.2.1	Derivatives of Hardening Functions.....	153
5.2.2	Derivatives of Yield Functions.....	156
5.3	Transverse Shear Stiffness.....	160
5.4	Verification of the User Material Subroutine (VUMAT).....	161
5.4.1	Uniaxial tension at various strain rates.....	162
5.4.2	Biaxial loading at various strain rates.....	164
5.4.3	Bending of a cantilever beam.....	167

5.4.4	Combined tension-shear.....	168
6	Finite Element Simulation of Electrohydraulic Forming.....	171
6.1	Introduction	171
6.2	Experimental work	172
6.2.1	EHF Tooling	173
6.2.2	Sheet material, geometry and preparation.....	175
6.2.3	Deformed EHF Specimens.....	177
6.2.4	Strain measurements	178
6.3	Finite element modelling.....	179
6.3.1	Single element model.....	179
6.3.2	EHF model	179
6.4	Results and Discussion	189
6.4.1	Single element results	189
6.4.2	EHFF Results and discussion.....	196
6.4.3	EHDF Results	222
6.4.4	Experimental and numerical energy	230
6.4.5	Computation time.....	232
7	Overall Summary and Conclusions.....	234
7.1	Summary.....	234
7.2	Conclusions	235
7.2.1	Material characterization tests	235
7.2.2	Yield function and hardening model calibration.....	236
7.2.3	Effect of Updating anisotropy coefficients on the flow surface	236
7.2.4	Finite element simulation.....	237
7.3	Recommendations for selecting an appropriate constitutive model for DP600, TRIP780 and AA5182-O	240
7.4	Future work.....	242
	Bibliography	244

Appendices	253
A1. Anisotropy coefficients identification of Yld2004-18p	253
A2. Implicit integration algorithm for implementation of rate-dependent hardening model (VUMAT)	255
A3. ICTP written permission	256
VITA AUCTORIS	257

List of Tables

Table 2.1 Mathematical formulation of phenomenological rate-dependent hardening models.....	29
Table 3.1. Chemical composition of DP600, TRIP780, and AA5182-O	47
Table 3.2. DP600 input data at various strain rates; for calibration of different yield functions.....	74
Table 3.3. Hill48 coefficients for DP600 at various strain rates.....	74
Table 3.4. Hill90 coefficients for DP600 at various strain rates.....	75
Table 3.5. Barlat89 coefficients for DP600 at various strain rates (exponent $a = 6$).....	75
Table 3.6. Yld96 coefficients for DP600 at various strain rates (exponent $a = 6$).....	76
Table 3.7. Yld2000-2d coefficients for DP600 at various strain rates (exponent $a = 6$) ..	76
Table 3.8. Yld2004-18P coefficients for DP600 at various strain rates (exponent $a = 6$)	77
Table 3.9. TRIP780 input data at various strain rates; for calibration of different yield functions.....	78
Table 3.10. Hill48 coefficients for TRIP780 at various strain rates	78
Table 3.11. Hill90 coefficients for TRIP780 at various strain rates	79
Table 3.12. Barlat89 coefficients for TRIP780 at various strain rates (exponent $a = 6$) ..	79
Table 3.13. Yld96 coefficients for TRIP780 at various strain rates (exponent $a = 6$).....	80
Table 3.14. Yld2000-2d coefficients for TRIP780 at various strain rates (exponent $a = 6$)	80
Table 3.15. Yld2004-18P coefficients for TRIP780 at various strain rates (exponent $a = 6$)	81
Table 3.16. AA5182 input data at various strain rates; for calibration of different yield functions.....	82
Table 3.17. Hill48 coefficients for AA5182-O at various strain rates.....	82
Table 3.18. Hill90 coefficients for AA5182-O at various strain rates.....	83
Table 3.19. Barlat89 coefficients for AA5182-O at various strain rates (exponent $a = 8$)	83

Table 3.20. Yld96 coefficients for AA5182-O at various strain rates (exponent a = 8)...	84
Table 3.21. Yld2000-2d coefficients for AA5182-O at various strain rates (exponent a = 8)	84
Table 3.22. Yld2004-18P coefficients for AA5182-O at various strain rates (exponent a = 8)	85
Table 3.23. 4th-order equations fitted to Yld2000-2d coefficients for DP600	87
Table 3.24. 4th-order equations fitted to Yld2000-2d coefficients for TRIP780	87
Table 3.25. 4th-order equations fitted to Yld2000-2d coefficients for AA5182-O	87
Table 3.26. Constants in the JC hardening model for DP600, TRIP780, and AA5182-O	91
Table 3.27. Constants in the KHL hardening model for DP600, TRIP780, and AA5182-O	92
Table 3.28. Constants in the SKP hardening model for DP600, TRIP780, and AA5182-O	92
Table 6.1. Ignition-and-growth parameters for Comp-B	184
<i>Table 6.2. DP600 experimental and numerical input energy</i>	<i>232</i>
<i>Table 6.3. AA5182-O experimental and numerical input energy</i>	<i>232</i>

List of Figures

Figure 1-1 Role of constitutive material model in nonlinear FE analysis	2
Figure 2-1 Schematic of EHF process and related tools.....	12
Figure 2-2. Schematic of flow curves at quasi-static and high strain rate regimes	28
Figure 3-1 a) ASTM-E8 and b) miniature dog-bone specimen geometries (mm), (Rahmaan et al., 2014)	48
Figure 3-2 DP600 engineering stress-strain curves at various strain rates in; a) RD b) DD c) TD	50
Figure 3-3 TRIP780 engineering stress-strain curves at various strain rates in; a) RD b) DD c) TD	51
Figure 3-4 AA5182-O engineering stress-strain curves at various strain rates in; a) RD b) DD c) TD	52
Figure 3-5 DP600 true stress versus effective plastic strain curves obtained at various strain rates in RD, DD, and TD.....	53
Figure 3-6. TRIP780 true stress versus effective plastic strain curves obtained at various strain rates in RD, DD, and TD.....	54
Figure 3-7. AA5182-O true stress versus effective plastic strain curves obtained at various strain rates in RD, DD, and TD.....	55
Figure 3-8. Biaxial and uniaxial true stress versus effective plastic strain curves at 0.001 s ⁻¹ for a) DP600 b) TRIP780 c) AA5182-O.....	56
Figure 3-9. DP600 width versus longitudinal true strain curves obtained from uniaxial tension in RD, DD and TD at various strain rates	58
Figure 3-10. TRIP780 width versus longitudinal true strain curves obtained from uniaxial tension in RD, DD and TD at various strain rates	59
Figure 3-11. AA5182-O width versus longitudinal true strain curves obtained from uniaxial tension in RD, DD and TD at various strain rates	60
Figure 3-12. Evolution of DP600 uniaxial and biaxial flow stresses normalized to the uniaxial flow stress in the RD at various strain rates.....	64
Figure 3-13. Evolution of TRIP780 uniaxial and biaxial flow stresses normalized to the uniaxial flow stress in the RD at various strain rates.....	65

Figure 3-14. Evolution of AA5182-O uniaxial and biaxial flow stresses normalized to the uniaxial flow stress in the RD at various strain rates.....	66
Figure 3-15. Calculation of DP600 biaxial flow curves at strain rates of 0.1, 1, 10, 100 and 1000 s-1	69
Figure 3-16. Calculation of TRIP780 biaxial flow curves at strain rates of 0.1, 1, 10, 100 and 1000 s-1	70
Figure 3-17. Calculation of AA5182-O biaxial flow curves at strain rates of 0.1, 1, 10, 100 and 1000 s-1	71
Figure 3-18. Anisotropy variation w.r.t. strain rate for DP600; a) normalized flow stress b) r-value.....	72
Figure 3-19. Anisotropy variation w.r.t. strain rate for TRIP780; a) normalized flow stress b) r-value.....	72
Figure 3-20. Anisotropy variation w.r.t. strain rate for AA5182-O; a) normalized flow stress b) r-value.....	73
Figure 3.21. Variation of Yld2000-2d anisotropy coefficients w.r.t. strain rate for DP600	86
Figure 3.22. Variation of Yld2000-2d anisotropy coefficients w.r.t. strain rate for TRIP780.....	86
Figure 3.23. Variation of Yld2000-2d anisotropy coefficients w.r.t. strain rate for AA5182-O.....	86
Figure 3-24. Flow curves predicted by JC, KHL, and SKP models for DP600	94
Figure 3-25. Flow curves predicted by JC, KHL, and SKP models for TRIP780.....	95
Figure 3-26. Flow curves predicted by JC, KHL, and SKP models for AA5182-O	96
Figure 4-1. Orthotropy axes of the rolled sheet metals.....	97
Figure 4-2. a) Uniaxial flow stress corresponding to a direction in the plane of the sheet metal, b) Tensile specimen extracted at the angle θ ; measured from the rolling direction	98
Figure 4-3. Measured and predicted anisotropy of the flow stress and the r-value; for DP600 at 0.001 s-1	109
Figure 4-4. Measured and predicted anisotropy of the flow stress and the r-value; for DP600 at 0.1 s-1	109

Figure 4-5. Measured and predicted anisotropy of the flow stress and the r-value; for DP600 at 1 s-1	110
Figure 4-6 Measured and predicted anisotropy of the flow stress and the r-value; for DP600 at 10 s-1	110
Figure 4-7 Measured and predicted anisotropy of the flow stress and the r-value; for DP600 at 100 s-1	111
Figure 4-8 Measured and predicted anisotropy of the flow stress and the r-value; for DP600 at 1000 s-1	111
Figure 4-9 Measured and predicted anisotropy of the flow stress and the r-value; for TRIP780 at 0.001 s-1	112
Figure 4-10 Measured and predicted anisotropy of the flow stress and the r-value; for TRIP780 at 0.1 s-1	112
Figure 4-11 Measured and predicted anisotropy of the flow stress and the r-value; for TRIP780 at 1 s-1	113
Figure 4-12 Measured and predicted anisotropy of the flow stress and the r-value; for TRIP780 at 10 s-1	113
Figure 4-13 Measured and predicted anisotropy of the flow stress and the r-value; for TRIP780 at 100 s-1	114
Figure 4-14 Measured and predicted anisotropy of the flow stress and the r-value; for TRIP780 at 1000 s-1	114
Figure 4-15 Measured and predicted anisotropy of the flow stress and the r-value; for AA5182-O at 0.001 s-1	115
Figure 4-16 Measured and predicted anisotropy of the flow stress and the r-value; for AA5182-O at 0.1 s-1	115
Figure 4-17 Measured and predicted anisotropy of the flow stress and the r-value; for AA5182-O at 1 s-1	116
Figure 4-18 Measured and predicted anisotropy of the flow stress and the r-value; for AA5182-O at 10 s-1	116
Figure 4-19 Measured and predicted anisotropy of the flow stress and the r-value; for AA5182-O at 100 s-1	117

Figure 4-20 Measured and predicted anisotropy of the flow stress and the r-value; for AA5182-O at 1000 s ⁻¹	117
Figure 4-21 Anisotropy variation for DP600 as predicted by Yld2000-2d at various strain rates; a) normalized flow stress b) r-value	118
Figure 4-22 Anisotropy variation for TRIP780 as predicted by Yld2000-2d at various strain rates; a) normalized flow stress b) r-value	119
Figure 4-23 Anisotropy variation for AA5182-O as predicted by Yld2000-2d at various strain rates; a) normalized flow stress b) r-value	119
Figure 4-24 Flow surface for DP600 predicted by Yld2000-2d at various strain rates; using initial and updated anisotropy coefficients.....	126
Figure 4-25 Flow surface for TRIP780 predicted by Yld2000-2d at various strain rates; using initial and updated anisotropy coefficients.....	127
Figure 4-26 Flow surface for AA5182-O predicted by Yld2000-2d at various strain rates; using initial and updated anisotropy coefficients.....	128
Figure 4-27 Flow surface for DP600 predicted by Hill48.r-value at various strain rates; using initial and updated anisotropy coefficients.....	129
Figure 4-28 Flow surface for TRIP780 predicted by Hill48.r-value at various strain rates; using initial and updated anisotropy coefficients.....	130
Figure 4-29 Flow surface for AA5182-O predicted by Hill48.r-value at various strain rates; using initial and updated anisotropy coefficients	131
Figure 4-30 Comparison between the flow surfaces for DP600 predicted by Hill`s and Barlat`s families at various strain rates; using updated anisotropy coefficients	133
Figure 4-31 Comparison between the flow surfaces for TRIP780 predicted by Hill`s and Barlat`s families at various strain rates; using updated anisotropy coefficients	135
Figure 4-32 Comparison between the flow surfaces for AA5182-O predicted by Hill`s and Barlat`s families at various strain rates; using updated anisotropy coefficients	137
Figure 4-33 Comparison between the flow surfaces for DP600 predicted by Yld2000-2d and von Mises at various strain rates; using updated anisotropy coefficients for Yld2000- 2d.....	138
Figure 4-34 Comparison between the flow surfaces for TRIP780 predicted by Yld2000- 2d and von Mises at various strain rates; using updated anisotropy coefficients for Yld2000-2d	139

Figure 4-35 Comparison between the flow surfaces for AA5182-O predicted by Yld2000-2d and von Mises at various strain rates; using updated anisotropy coefficients for Yld2000-2d	140
Figure 4-36 Flow surfaces for DP600 predicted by Yld2000-2d with contours of normalized shear stress in 0.1 increments from 0 to 0.5 at various strain rates; using initial and updated anisotropy coefficients	141
Figure 4-37 Flow surfaces for TRIP780 predicted by Yld2000-2d with contours of normalized shear stress in 0.1 increments from 0 to 0.5 at various strain rates; using initial and updated anisotropy coefficients	142
Figure 4-38 Flow surfaces for AA5182-O predicted by Yld2000-2d with contours of normalized shear stress in 0.1 increments from 0 to 0.5 at various strain rates; using initial and updated anisotropy coefficients	143
Figure 5-1 Schematic of a multi-steps return mapping procedure for AFR in the 2D stress space.....	151
Figure 5-2. Schematic of the single element model for the uniaxial tension in a) RD b) TD	163
Figure 5-3. Comparison between experimental and predicted DP600 uniaxial flow curves; at various strain rates, a) RD b) TD.....	164
Figure 5-4. Schematic of the single element model for biaxial tension.....	165
Figure 5-5 Comparison between experimental and predicted DP600 biaxial flow curves; at various strain rates	165
Figure 5-6. Comparison between experimental and predicted uniaxial and biaxial DP600 flow curves; a)10 s-1 b) 100 s-1 c) 1000 s-1.....	166
Figure 5-7. Schematic of the cantilever beam model	167
Figure 5-8. Effective stress variation along the top surface of a DP600 beam.....	168
Figure 5-9. Effective stress contours in the deformed DP600 beam; a) VUMAT, b)ABAQUS built-in material model.....	168
Figure 5-10. Schematic of the combined tension-shear model.....	169
Figure 5-11. Comparison between the predicted flow stresses obtained by the VUMAT and the ABAQUS built-in material model; at two different sets of velocities	169
Figure 6-1. Schematic of a typical EHDF setup (Maris, 2014)	173

Figure 6-2. Different geometries of specimens used in EHFF; a) uniaxial b) intermediate draw c) plane strain d) biaxial.....	177
Figure 6-3. Safe EHFF specimens for DP600 (top) and AA5182-O (bottom); a) uniaxial b) intermediate draw c) plane strain d) biaxial	178
Figure 6-4. Safe EHDF DP600 specimen	178
Figure 6-5. Mechanism of shockwave generation by; a) underwater electrical discharge b) UNDEX	181
Figure 6-6. Section-view of the EHF finite element model; a) EHFF b) EHDF	182
Figure 6-7. Predicted effective plastic strain for DP600 using Yld2000-2d and von Mises yield functions; a) biaxial, b) plane strain, and c) relative error	190
Figure 6-8. Predicted effective plastic strain for DP600 using Yld2000-2d and Hill48 yield functions; a) biaxial, b) plane strain and c) relative error	191
Figure 6-9 Predicted effective plastic strain for TRIP780 using Yld2000-2d and von Mises yield functions; a) biaxial, b) plane strain and c) relative error	192
Figure 6-10. Predicted effective plastic strain for TRIP780 using Yld2000-2d and Hill48 yield functions; a) biaxial, b) plane strain and c) relative error	193
Figure 6-11. Predicted effective plastic strain for AA5182-O using Yld2000-2d and von Mises yield functions; a) biaxial, b) plane strain and c) relative error	194
Figure 6-12. Predicted effective plastic strain for AA5182-O using Yld2000-2d and Hill48 yield functions; a) biaxial, b) plane strain and c) relative error	195
Figure 6-13. Measured and predicted data for DP600 uniaxial EHFF specimen; a) major strain, b) minor strain, c) thickness and d) height	198
Figure 6-14 Measured strain distribution and predicted strain path for an element at the centre of the gauge section for DP600 uniaxial EHFF specimen	199
Figure 6-15. Effective plastic strain and effective strain rate histories for an element at the centre of the DP600 uniaxial EHFF specimen.....	199
Figure 6-16. Measured and predicted data for AA5182-O uniaxial EHFF specimen; a) major strain, b) minor strain, c) thickness and d) height	201
Figure 6-17. Measured strain distribution and predicted strain path for an element at the centre of the gauge section for AA5182-O uniaxial EHFF specimen	202
Figure 6-18. Effective plastic strain and effective strain rate histories for an element at the centre of the AA5182-O uniaxial EHFF specimen.....	202

Figure 6-19. Measured and predicted data for DP600 intermediate draw EHFF specimen; a) major strain, b) minor strain, c) thickness and d) height	204
Figure 6-20. Measured strain distribution and predicted strain path for an element at the centre of the gauge section for DP600 intermediate draw EHFF specimen	205
Figure 6-21. Effective plastic strain and effective strain rate histories for an element at the centre of the DP600 intermediate draw EHFF specimen.....	205
Figure 6-22. Measured and predicted data for AA5182-O intermediate draw EHFF specimen; a) major strain, b) minor strain, c) thickness and d) height	207
Figure 6-23. Measured strain distribution and predicted strain path for an element at the centre of the gauge section for AA5182-O intermediate draw EHFF specimen	208
Figure 6-24. Effective plastic strain and effective strain rate histories for an element at the centre of the AA5182-O intermediate draw EHFF specimen.....	208
Figure 6-25. Measured and predicted data for DP600 plane strain EHFF specimen; a) major strain, b) minor strain, c) thickness and d) height	210
Figure 6-26. Measured strain distribution and predicted strain path for an element at the centre of the gauge section for DP600 plane strain EHFF specimen	211
Figure 6-27. Effective plastic strain and effective strain rate histories for an element at the centre of the DP600 plane strain EHFF specimen	211
Figure 6-28. Measured and predicted data for AA5182-O plane strain EHFF specimen; a) major strain, b) minor strain, c) thickness and d) height	214
Figure 6-29. Measured strain distribution and predicted strain path for an element at the centre of the gauge section for AA5182-O plane strain EHFF specimen.....	215
Figure 6-30. Effective plastic strain and effective strain rate histories for an element at the centre of the AA5182-O plane strain EHFF specimen	215
Figure 6-31. Measured and predicted data for DP600 biaxial EHFF specimen; a) major strain, b) minor strain, c) thickness and d) height	217
Figure 6-32. Measured strain distribution and predicted strain path for an element at the centre of the DP600 biaxial EHFF specimen.....	218
Figure 6-33. Effective plastic strain and effective strain rate histories for an element at the centre of the DP600 biaxial EHFF specimen.....	218
Figure 6-34. Measured and predicted data for AA5182-O biaxial EHFF specimen; a) major strain, b) minor strain, c) thickness and d) height	220

Figure 6-35. Measured strain distribution and predicted strain path for an element at the centre of the AA5182-O biaxial EHFF specimen.....	221
Figure 6-36. Effective plastic strain and effective strain rate histories for an element at the centre of the AA5182-O biaxial EHFF specimen.....	221
Figure 6-37. Effective plastic strain contours predicted by Yld2000-2d for DP600; a) uniaxial, b) intermediate draw, c) plane strain and d) biaxial.....	222
Figure 6-38. Measured and predicted data for DP600 in EHDF; a) major strain, b) minor strain and c) height.....	224
Figure 6-39. Measured strain distribution and predicted strain path for an element at 5mm distance from the centre of DP600 specimen in EHDF.....	226
Figure 6-40. Effective plastic strain and effective strain rate histories for an element at 5mm distance from the centre of DP600 specimen in EHDF.....	227
Figure 6-41. Shear strain and minimum principal stress histories for an element at 5mm distance from the centre of DP600 specimen in EHDF.....	229
Figure 6-42. Pressure distribution history through the water during EHDF (pressure unit in GPa)	231
Figure 6-43. Computation times for EHFF simulations	233

1 Introduction

Finite element (FE) simulations can be used to investigate sheet metal forming processes for many reasons such as analysing stress, strain and temperature distributions, predicting material flow and deformation history, and predicting potential locations of strain localization and failure. FE simulations can significantly reduce the time and cost to design and optimize manufacturing processes. The development of modern computational techniques, especially the advancement of commercial finite element codes have made modelling and simulation indispensable components of product design and optimization in an integrated manufacturing environment. In FE simulations of sheet metal forming processes, the accuracy of the predicted results can be influenced by many parameters such as the constitutive material model which represents the elasto-plastic behaviour of the material, tribological and contact conditions, and numerical factors such as element type and formulation. The computation time and geometrical representations should also be considered for reliable and cost effective FE simulation. In the first few decades of FE simulation development, attention was focused on improving the formulations, methodology, algorithm, and computational efficiency. As these issues were gradually resolved and the FE approach was used for a broader range of applications, substantial efforts were put into developing and modifying different constitutive material models. Many material models were developed to represent the behaviour of a variety of materials.

Generally, sheet metal forming processes involve large deformations and rotations which lead to substantial material and geometrical nonlinearity, respectively. In the analytical and numerical analysis of these processes, the logarithmic strain and conjugate Cauchy stress tensors are widely used to generate the constitutive material equations. A co-rotational coordinate system in which the reference system rotates with the material is

generally used to express all stress, strain, and internal state variables. The constitutive material model plays a critical role in many sheet metal forming areas such as formability analysis, defect analysis (such as wrinkling and earing), localization and failure analysis, and prediction of springback. The material model affects many aspects of a sheet forming analysis because it is used to update the stress and all internal state variables based on the deformation rate tensor. Due to the path-dependency (nonlinearity and irreversibility) nature of plastic deformation, the incremental formulation scheme is the most convenient approach for writing all elasto-plastic constitutive material equations. Therefore, for any constitutive material equation implemented into a FE code, the relation between the strain increment (or deformation rate) and stress increment must be derived (so-called incremental plasticity). The overall response is determined incrementally by integrating the rate-type constitutive and field equations along a given path of loading or deformation. Figure 1-1 shows the role of a general constitutive model in predicting the material deformation in nonlinear FE analysis.

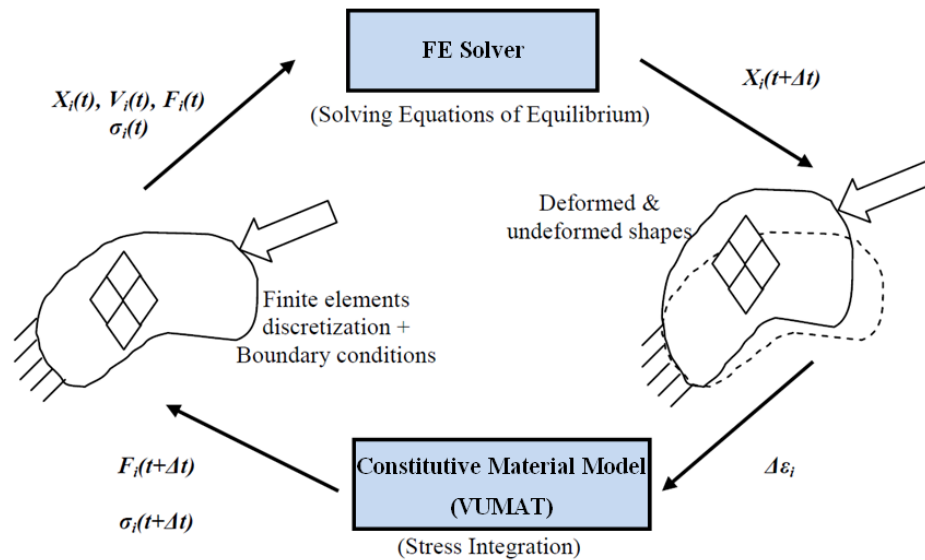


Figure 1-1 Role of constitutive material model in nonlinear FE analysis

In the FE simulation of sheet metal forming, an acceptable constitutive material model should be able to capture many different phenomena that occur during plastic deformation, including the anisotropic material behaviour for different material

orientations, and the strain rate and/or temperature dependent hardening (flow stress) behaviour. Many factors should be considered when selecting a constitutive material model for a FE sheet metal forming analysis. First, the nature of the actual forming process must be carefully analyzed to recognize the parameters which are effective in the elasto-plastic mechanical responses (deformation history) of the material during the plastic deformation. For instance, it is now well known that the mechanical response of many materials including the initial yield stress, flow stress, and ductility, can change significantly with strain rate and temperature. Accordingly, the sensitivity of the mechanical response to strain rate should be considered in the simulations of rate-dependent (dynamic) forming processes, such as electrohydraulic forming (EHF). At the same time, the constitutive material equation should not be so complicated that it requires an excessive number of coefficients, because the experimental tests to calibrate the model, the numerical implementation, and the computational procedures will be expensive. The robustness of a constitutive material model can be assessed with a thorough comparison to experimental findings. An appropriate material model should provide the best possible fit to the actual material properties at a reasonable cost.

Generally, constitutive material models can be categorized into either micro-structural or phenomenological models. Micro-structural models are based on some description of the crystal structure and crystallographic texture. These types of models often produce accurate results, but usually require numerous complex experimental tests and the computing time needed to carry out these computations is prohibitive in the design stage of a forming process. Phenomenological constitutive models generally include an anisotropic yield function, a flow rule, and a hardening model. These models are assumed to be well described with a flow surface that evolves during plastic deformation. In spite of the limitations of a single flow surface associated with isotropic hardening, this approach is appealing at the forming process design stage, because they require less and simpler experimental tests and also shorter computation times compared to micro-structural models.

The change of the material properties, specifically material anisotropy, has seldom been considered in sheet metal forming analysis, since it is difficult to quantify

experimentally. Recently, it was demonstrated that in addition to flow stresses, the mechanical properties associated with the material anisotropy behaviour changed with strain rate (Lee et al., 2010). Among material parameters, the flow stresses and r-values under different loading conditions influence the initial anisotropic state of the sheet material. The initial anisotropy of a material is represented by the flow surface shape which determines residual stress and strain distributions in the sheet when the forming process is completed. Therefore, an accurate description of the anisotropy behaviour of sheet materials can be one of the most effective parameters in the simulation of sheet metal forming processes.

For decades, many researchers have reported changes in the hardening behaviour of a variety of materials as a function of strain rate. The changes in hardening behaviour have a significant effect on the flow surface evolution of the material. But, to the best of the author's knowledge, researchers do not take strain-rate sensitivity into consideration when calibrating anisotropic yield functions. Despite the importance of accurately capturing the evolution of the flow surface by correlating the anisotropic yield functions to strain rate, a comprehensive study to evaluate simultaneously the influence of the strain rate in both material anisotropy and hardening behaviour has not been completed to date. The variation in the material anisotropy coefficients with strain rate can potentially alter the flow surface shape, which consequently changes the residual stress and strain in the as-formed part in a rate-dependent forming analysis. Therefore, the author proposes to investigate the effect of both anisotropy and hardening changes of material as a function of strain rate in the simulation of sheet metal forming processes.

In this work, the mechanical properties (including flow stresses and r-values) of three sheet materials (DP600, TRIP780, and AA5182-O) were obtained at different strain rates (0.001, 0.1, 1, 10, 100, and 1000 s^{-1}) under uniaxial tension (in the rolling, diagonal, and transverse directions) and biaxial tension conditions. Several anisotropic yield functions were calibrated at each level of strain rate. Using the mechanical properties, a comprehensive study was then completed to evaluate the effect of strain rate on the flow surface shape for each yield function. Also, in order to capture the hardening behaviour

of the materials, three different rate-dependent hardening models (Johnson-Cook, JC; Khan-Huang-Liang, KHL; and Surajit Kumar Paul, SKP) were calibrated.

After a thorough review of different constitutive models, several associative rate-dependent material models (based on associated flow rule, AFR) were developed. The new material models, which are a combination of updated anisotropic yield functions, (the anisotropy coefficients are updated depending on the strain rate) and rate-dependent hardening model, were developed to predict both anisotropic and rate-dependent hardening characteristics as accurately as possible. It should be mentioned that the “updated” expression implies that the anisotropy coefficients were updated to the corresponding values for the current strain rate, by applying 4th-order strain rate dependent polynomial functions instead of the initial constant anisotropy coefficients. In developing the rate-dependent material models, an effort was made to maintain the numerical implementation as efficient as possible.

Among all the anisotropic yield functions and hardening models, Yld2000-2d (for plane stress conditions) and Yld2004-18p (for general stress state conditions) as yield functions were selected to combine with KHL as hardening model to develop rate-dependent anisotropic user-defined material subroutines (VUMATs). Finally, an implicit stress integration algorithm, using the multi-step return mapping method, was used to develop rate-dependent anisotropic constitutive material models. The developed implicit integration method has a general form that can be implemented with any quadratic or non-quadratic yield function paired with any rate-dependent hardening model. The developed models were implemented as VUMATs for ABAQUS/Explicit code to simulate electrohydraulic forming of both DP600 and AA5182-O sheet materials under different process conditions, using Eulerian elements and the ignition-and-growth model to simulate the pulsed pressure wave in EHF. The simulation results under different EHF conditions using the developed material models were then compared with experimental measurements in order to validate the model.

This dissertation is subdivided into the following sections:

- **Chapter 1.** Introduction
- **Chapter 2.** Literature review
- **Chapter 3.** Rate-dependent constitutive model
- **Chapter 4.** Effect of updating anisotropy coefficients on the flow surface
- **Chapter 5.** Rate-dependent implicit stress integration scheme
- **Chapter 6.** Finite element simulation of electrohydraulic forming
- **Chapter 7.** Overall summary and conclusions

2 Literature Review

2.1 Introduction

The automotive and aerospace industries have been requesting material suppliers to develop lighter and stronger materials at reasonable production costs for decades. However, many of the developed low-cost and light-weight materials, such as aluminum alloys and advanced high strength steels (AHSS) have limited formability in conventional forming processes. Researchers have shown that, to overcome this barrier, non-traditional forming operations can be designed for these types of materials instead of merely substituting these alloys. High speed metal forming processes are recognized as a potential replacement for conventional forming processes to increase material formability.

One of the main barriers to the industrial implementation of high speed metal forming processes is the lack of experience to predict sheet material behaviour under large plastic deformation. Numerical simulations of sheet metal forming processes are routinely used to achieve substantial time and cost reductions in the design process. When a sheet is accelerated in a forming process, the strain rate effect becomes important. Therefore, it is vital to consider the strain rate effect to accurately predict the deformation history and final shape in simulations of high speed metal forming processes.

Among all the parameters in the simulation of a forming process, the constitutive model has a very significant effect on the accuracy of numerical results. Three major concepts are involved in a constitutive model: the yield function, the flow rule, and the hardening model, which determine a general stress-strain relationship for plastic deformation. In this chapter a brief literature review is presented on the incremental

constitutive equations of high strain rate plasticity. Incremental constitutive equations are obtained based on the minimum plastic-work theory and have been widely used in advanced computational plasticity for decades (Hill, 1986; Chung and Richmond, 1993; Yoon et al., 1999a and 1999b). This chapter also contains a review of the experimental and numerical work on high speed metal forming processes, and intermediate and high speed material characterization tests.

2.2 High speed metal forming

2.2.1 High strain rate metal forming processes

According to work done by many researchers (Wood, 1967; Daehn, 2006; Ferreira et al., 2004; Golovashchenko et al., 2003), high strain rate forming can improve formability, suppress wrinkling, decrease springback and lead to more uniform strain distributions in sheet metal parts. For decades, one of the main desires of the automotive industry has been to improve the fuel economy of the vehicles. One of the most effective ways of reducing fuel consumption is to reduce the weight of the vehicle body, by replacing mild steels with advanced high strength steels (AHSS) or light-weight alloys such as aluminum (Cheah and Heywood, 2011). The main concern with the implementation of AHSS and aluminum alloys is their lower formability compared to typical steels. To overcome this barrier, the automotive industry has been investigating various forming techniques which can enhance material formability.

According to many investigations on metallic alloys (Balanethiram and Daehn, 1994; Mynors and Zhang, 2002; Golovashchenko et al., 2003; Imbert et al., 2005, Psyk et al., 2011), it was observed that sheet formability can exceed the conventional limits in high velocity forming processes. Pulsed forming processes such as explosive forming (EF), electromagnetic forming (EMF), and electro-hydraulic forming (EHF) are the most common high speed or high strain rate metal forming technologies (Benedict, 1987; Amstead et al., 1987; Groover, 2007). From a manufacturing point of view, the use of one sided tools in the pulsed forming rather than mating two-sided tools in conventional forming, leads to significant cost savings. The advantage of one sided tooling is

highlighted when very large dies are needed for low volume productions, particularly in the aerospace industry. Moreover, the elimination of the hard tooling from one side of the sheet reduces the friction and strain gradients and thus delays strain localization in the corner areas of complex dies (Golovashchenko et al., 2003). Furthermore, pulsed forming processes typically require less lubrication than conventional stamping (Mynors and Zhang, 2002).

What distinguishes EF, EMF, and EHF processes from each other is the source of the forming energy and the method of energy transformation into the sheet. In explosive forming, an explosive charge, which is generally submerged in water, provides the energy to form the sheet material. In both EMF and EHF, the required energy is stored in high voltage capacitors. In EMF, the energy is released through a multi-turn coil positioned close to the sheet that is to be formed. The rapid increase of current in the coil induces an eddy current which generates significant repulsive forces and consequently accelerates the sheet. Instead of using coils, EHF uses (at least one pair) electrodes submerged in water to transfer the energy from the capacitors to the sheet. The discharge of energy across the electrodes creates a plasma channel that generates a high pressure wave in the water, which in turn accelerates the sheet.

EHF is superior to EF due to its shorter cycle duration and much safer process. However, in view of the significant amount of energy in chemical explosives, the EF process is more practical to form larger parts, particularly in aerospace and military applications. Compared to EMF, EHF is more suitable for industrial applications, since it is applicable to almost all metallic materials. EMF cannot be used with materials that have poor electrical conductivity and in contrast with EHF, EMF requires expensive and complex coils that need to be replaced after only a few cycles.

Needleman (1991) showed that in high velocity metal forming processes necking was postponed due to inertial effects (referred to as inertial stabilization), by reducing the stress-triaxiality factor in the necked region. During the 1990's Balanethiram and Daehn (1992, 1994), and Balanethiram et al. (1994) showed that for AA6061 aluminum alloy, interstitial free (IF) iron, and HCOF copper, formability also improved due to substantial

through-thickness compressive and shear stresses (so-called “inertial ironing” effect) that were created as a results of the dynamic sheet/die interaction under pulsed die-forming conditions. Vohnout and Daehn (2002) reported formability enhancement in 6111-T4 and 5754-O aluminum sheets in the EMF process after applying a certain quasi-static pre-strain in uniaxial tension.

Golovashchenko et al. (2003) also observed formability improvement in high velocity forming due to dynamic sheet-die interaction. In a pulsed forming process before the sheet contacts the die, the sheet is accelerated into an open space of the die cavity and the strain-rate sensitivity as well as inertial effects contribute toward material formability improvement. The advantages of a pulsed forming process become evident when the sheet approaches its final shape and impacts the die surface. More recently, Seth et al. (2005) reported a remarkable formability improvement in low carbon steel sheets that were accelerated by an EMF coil toward missile-shaped and wedge-shaped punches. Due to the low electrical conductivity of dual phase steels, the efficiency of the EMF technique is limited for these material types unless a driver with high electrical conductivity is used as an interface.

Imbert et al. (2005) reported a formability enhancement of AA5754 and AA5182 aluminum sheet alloys in EMF in the die-forming condition, while the formability improvement was negligible in free-forming. Similar to Balanethiram and Daehn (1992, 1994), Imbert showed that the significant formability improvement was due to the bending-unbending effect as a consequence of the sheet/die interaction; however their simulation of the experiments used a rate-independent constitutive material model. An abrupt change of stress state was observed, from plane stress to a three-dimensional stress state, incorporating through-thickness shear and compressive stresses due to sheet-die interaction. The through-thickness stresses were shown to suppress the nucleation and coalescence of voids within the sheet metal, and consequently postpone the onset of necking and failure.

Olivera et al. (2005) reported a moderate formability improvement in AA5754 and AA5182 subject to EMF. But larger maximum strain values were measured in safe grids

far from the fractured zone. Golovashchenko et al. (2007) reported almost 250% elongation increase in AA6111-T4 and AA5754 sheets in EMF compared to conventional forming, when formed into conical and v-shape dies. Dariani et al. (2009) reported significant formability improvement in the high strain rate regime compared to low and intermediate strain rates for AA6061-T6 and 1045 steel. Golovashchenko et al. (2011a) showed that in addition to the formability improvement in pulsed forming, a more uniform strain distribution though a much broader area of the sheet can be achieved. The uniform strain distribution can be beneficial to form very complex geometries, where the material in pulsed forming can flow easier into difficult to form regions compared to conventional forming by introducing a two-step forming process. This easier flow of material allows the usage of less ductile materials to be formed into complex shapes. Liu et al. (2011) showed formability enhancement of sheets that were prestrained quasi-statically and then subject to EMF compared to the forming limits obtained in a conventional hydraulic bulge test.

2.2.2 Electrohydraulic forming (EHF)

In EHF, two or more electrodes are positioned in a chamber filled with a liquid (generally water), a high-voltage discharge between the electrodes generates a high-pressure and high-temperature plasma channel. The plasma channel expands and creates a shockwave that propagates through the water and accelerates the sheet toward the die cavity (Figure 2-1). Generally, an EHF process is completed in less than a millisecond depending on the sheet material type, the position of the electrodes, the input energy magnitude and duration, and the chamber geometry.

The main constraint in EHF relates to the availability of a bank of capacitors to store sufficient energy. The amount of energy required for a discharge strongly depends on the size of the part and the material grade of the sheet metal blank. Realistically, EHF is ideally suited for small to medium-sized sheet and tubes with relatively small thicknesses (Mynors and Zhang, 2002). Lane (1767) and Priestly (1769) were first reported the ability of an electrical discharge into a liquid to generate strong mechanical forces to form parts. Later on, Yutkin (1955), Bruno (1968), Davies and Austin (1970) and

Chachin (1978) conducted several lab-scaled and preliminary industrial applications of the EHF. In a combined conventional-pulsed forming study, Sandford (1970) developed a technology where the sheet was first preformed in a quasi-static hydroforming process before being completely filled into the die cavity with EHF. Daehn (2006) provided an overview of the experimental and development work that has been done more recently in high speed forming.

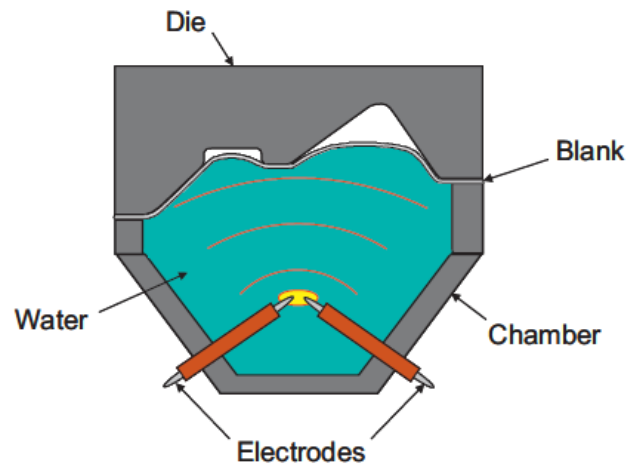


Figure 2-1 Schematic of EHF process and related tools

The automotive industry has recently shown increased interest in the EHF process. Golovashchenko et al. (2003, 2005, 2007, 2011a, 2013) made substantial efforts to apply EHF to higher volume applications. These efforts include development of a durable electrode and sealing system, an efficient water-air system, and a finite element (FE) modeling technique. The superiority of EHF to EMF was demonstrated for applications where several successive discharges are needed to completely form the sheet into the die cavity and calibrate springback without opening the EHF chamber. Several EHF pulses can be conducted without opening the tool but, several coils and clamping presses are needed to complete a multistage EMF process (Golovashchenko et al., 2013). Golovashchenko and Mamutov (2005) studied the evolution of the plasma channel shape during the EHF process. The pressure distribution history within the chamber in EHF simulation showed the reflected dynamic forces from the walls of the chamber and from

the sheet are converted into ellipses, which divide into smaller volumes and finally close towards the end of the process.

Golovashchenko (2007) observed a circular split failure mode in the apex region of the die formed samples in EHF. Strains measured in some circle grids far from the fractured zone moderately exceeded the quasi-static forming limit, which was attributed to inertia in the plastic flow instability, as described by Drucker (1959). More recently, Rohatgi et al. (2011a; 2011b) experimentally quantified the deformation behaviour of AA5182-O and DP590 during EHF using high-speed cameras and the digital image correlation (DIC) strain analysis technique. The measurements (sheet velocity and strain rate) of the in-process parameters helped to understand the roles of strain rate and sheet-die interaction in sheet formability enhancement at intermediate and high strain rates. They recorded a maximum velocity and strain rate of 100 m/s and 664 s^{-1} , respectively, during electrohydraulic die-forming (EHDF). Unfortunately the conical die angle they used was so high, that they were not able to capture an effective dynamic sheet/die interaction during EHDF. Melander et al. (2011) developed a finite element model to simulate EHFF and EHDF of sheet steels which used an isotropic yield function (von Mises) and they calibrated the parameters in the JC model according to experimental uniaxial tensile tests for a range of strain rates up to 1000 s^{-1} . They used acoustic elements to simulate the liquid medium within the EHF chamber.

Substantial efforts have been dedicated to the analysis of pulsed forming processes, and EHF in particular. However, a detailed understanding of the reasons leading to the increased formability of sheet materials in high rate forming into a die cavity has not yet been accomplished due to the complexity of the effects taking place. In order to capture the mechanics of the sheet's deformation into the die cavity, the development of the pressure pulse applied to the sheet needs to be taken into account; in EHF a pressure pulse propagates from the discharge channel to the surface of the sheet through the water-filled chamber with multiple reflections from the walls of the chamber. This effect was described in detail by Golovashchenko et al. (2013) and also by Gillard et al. (2013) who developed a numerical technique to model the complex loading mechanism using LS-DYNA. However, the numerical analysis of this phenomenon takes most of the

computation time required for the analysis of the EHF process. A very fine mesh in a small discharge channel and in the area around it requires a very small time step in an explicit integration procedure, and most of the computation time is consumed before any pressure has been applied to the sheet. This approach provides full details on the pressure propagation mechanism, but practically, it required the researchers (Golovashchenko et al., 2011a; 2011b; 2013) to employ a shell model of the deformed sheet (Theory of Shells, LS-DYNA manual, 2006). The use of shell elements to model the sheet limits the analysis to a plane-stress formulation that omits the through-thickness stresses from the analysis and excludes the dynamic sheet-die interaction. The plane stress formulation makes it impossible to analyse the mechanics of the coining effect or to predict the correct strain rate variation when the sheet hits the die, which is recognized as the main phenomenon that helps to improve material formability. Also, in these simulations an isotropic yield function (von Mises) was paired with the Johnson-Cook hardening model. Hence, in addition to the formability enhancement mechanisms, the effect of anisotropy at high strain rates was ignored in numerical simulations. The simulation and experimental results showed that, the sheet/die interaction creates very high strain rates in EHF. Numerical results showed a peak strain rate of approximately $20,000 \text{ s}^{-1}$, in EHF, when the sheet was able to completely fill the die cavity, but less than $7,000 \text{ s}^{-1}$ when the die was not completely filled.

Also, Golovashchenko et al. (2013) reported the formability limits of different dual phase steels (DP500, DP590, DP780, and DP980) in EHF compared to the conventional quasi-static limiting dome height (LDH) test. Substantial formability improvement was observed by comparing the maximum strains resulting from EHF into conical and v-shaped dies to the maximum strains obtained in LDH tests. The relative improvement in plane strain formability in EHF conditions was between 63% and 190%, depending on the grade of dual phase steel.

In a hybrid conventional-pulsed forming study, Gillard et al. (2013) reported substantial formability improvement in the DP780 and DP980 sheets that were preformed in a quasi-static hydraulic bulge forming step first, then formed electrohydraulically into conical and v-shaped dies. The formability of the DP steels formed in the hybrid process

was less than what was observed in a single pulsed forming process, but still greater than the quasi-static conventional forming limits. Also, Gillard et al. (2013) distinguished between two different failure modes in EHF experiments using a conical die: a quasi-static failure mode, where the crack propagates through the pole of the dome-shaped specimen, occurred when the sheet was not able to completely fill the die cavity, and a dynamic fracture mode, in which the crack propagates circumferentially in the area away from the pole of the cone-shaped specimen, occurred when the energy level was high enough for the sheet to completely fill the die cavity.

Most recently, Maris (2014) designed and optimized several specimen geometries to obtain the experimental FLC under electrohydraulic free-forming conditions. A series of EHF tests for DP600 and AA5182-O, covering the entire range of deformation modes (uniaxial, intermediate draw, plane strain, and biaxial) were conducted under proportional loading paths. The strains were measured throughout necked specimens (no edge cracking or splitting was observed in the deformed specimens). Comparison of the measured strains of the electrohydraulic free-formed specimens with the quasi-static FLC, showed that the formability improvement depends on the material grade. For instance, some formability improvement was reported for AA5182-O, whereas no formability improvement was observed for DP600.

Although very complex and comprehensive FE models were recently developed to simulate the EHF process (Golovashchenko et al, 2013), the effect of material anisotropy was not considered in the high strain rate regime in any of the above-mentioned work. An extensive review of the literature has shown that, in all of the up-to-date pulsed forming FE simulations, only an isotropic yield function (von Mises) combined with the JC rate-dependent hardening model has been used (Imbert et al., 2005; Melander et al., 2011; Golovashchenko et al., 2013).

2.3 Constitutive model

The finite element (FE) method has been widely used in the automotive industry over the years to simulate crashworthiness and metal forming operations (such as deep-

drawing, rolling, cold, warm and hot-forming, forging, and extrusion). Among all of the parameters that affect the quality of FE analysis, the constitutive material model is known to be the predominant factor. An appropriate set of constitutive equations should be able to replicate the deformation behaviour of the material under different loading conditions. Generally a phenomenological constitutive model consists of a yield function, a flow rule, and a hardening model. A constitutive model should be selected depending on the available experimental data associated with the material behaviour, the deformation history of the part during the actual forming process, and the knowledge of the user.

2.3.1 Anisotropic yield functions

A flat rolled sheet can be significantly anisotropic due to complex phenomena occurring during the thermo-mechanical processing of the sheet and especially during the cold-rolling. The anisotropy depends on the initial anisotropy of the as-rolled sheet and the complex plastic deformation during the actual forming operation. The initial anisotropy of the rolled sheet is typically an orthotropic symmetry but when the principal axes of deformation are not co-linear with the principal axes of orthotropy, the deformation-induced anisotropy becomes non-symmetrical. Accordingly, the implementation of material anisotropy into a FE code can be very complex. But, in order to reduce computation times and simplify the numerical analysis of industrial forming operations, the progressive change of material anisotropy during an industrial forming process is usually assumed to be negligible compared to the initial anisotropy induced by the cold-rolling process.

Two approaches have been widely used for consideration of anisotropy in a FE analysis. In the first approach the material is assumed to be a polycrystal. This approach is based on the physical phenomena of plastic deformation that occurs by the movement of dislocations on certain crystallographic planes and/or by twinning. The crystallographic texture is the main input to these models and each point in the continuous medium is assumed to be composed of a large number of grains where dislocation glide occurs on specific slip systems (Becker, 1993; Baudoin et al., 1994). Since the lattice rotation in each grain can be tracked in crystal plasticity models, the

material anisotropy is able to evolve throughout the deformation history, which makes this approach unique. However, in these models the material characterization is complex and computationally time-intensive, so they are rarely used for industrial-scale metal forming applications. There have been many attempts to simplify the polycrystal approach to overcome these drawbacks. A single grain behaviour has been used in FE simulations (Lequeu et al., 1987; Arminjon, 1991; Darrieulat and Piot, 1996; Maniatty and Yu, 1996; Gambin and Barlat, 1997). Also, a unified polycrystal behaviour was associated to the grain orientation distribution of the material by Toth et al. (1991), Arminjon and Imbault (1994), and Van Houtte (1994).

The second approach is phenomenological, where the plastic behaviour of the material is described by a flow surface that evolves during plastic deformation. In this approach, the yield function is not necessarily associated with the microstructure of the material, but is rather associated with the anisotropy of the flow stress and the anisotropy of the plastic flow (or plastic strain). The anisotropy of the flow stress can be determined by measuring the flow stress in different material orientations (rolling, RD, diagonal, DD, and transverse, TD directions). The anisotropy associated with the plastic flow is generally described by the Lankford coefficient (r -value), which is defined as the ratio of the width strain to the thickness strain during a tensile test. In addition to the anisotropy, the Bauschinger effect, hydrostatic stress, etc., are other parameters that affect the plastic yielding of sheet metals. Based on many experimental observations, Bishop and Hill (1951a and 1951b), and Hecker (1976) showed that the assumption of a yield surface as the potential for plastic strain is valid for polycrystals and single phase materials. For many years, the evolution of the flow surface was a topic of great interest in both theoretical and experimental research. For many metal forming simulations, the flow surface is assumed to expand isotropically during plastic deformation. This assumption is numerically very efficient and it is verified for many single phase materials subjected to relatively smooth and continuous loading paths. Compared to crystal plasticity models, phenomenological models are easier to implement into FE codes, computationally more efficient, and require much simpler material characterization tests.

Hill (1948, 1950) introduced the first phenomenological anisotropic yield function, as an expansion of the von Mises (1928) quadratic yield function. Hill's function has been widely used in FE analysis of forming simulations since it is applicable to three-dimensional stress states and represents linear relationships between stresses and strain increments. Acceptable results are obtained for steel sheets using this function, but observations showed that Hill's theory does not correlate with the behaviour of aluminum alloys (Mellor and Parmar, 1978; Mellor, 1981). Hill's yield function was not able to describe the plastic flow of materials that display so-called "anomalous behaviour". Therefore, several researchers such as Gotoh (1977), Hill (1979, 1990, 1993), Barlat and Lian (1989), Weixan (1990), Montheillet et al. (1991), Lin and Ding (1996), Barlat et al. (1991, 1997, 2003, 2005) have developed different non-quadratic yield functions to improve the plastic behaviour for aluminum alloys. Phenomenological yield functions have been reviewed in more detail by Zyczkowski (2001), Banabic (2001), Yu (2002) and Barlat et al. (2004).

The linear transformation of the stress tensor has received much attention as a particular case of transformation theory. Sobodka (1969) and Boehler and Sawczuck (1970) were among the first to apply linear transformations to the stress tensor. Later on, Barlat and Lian (1989) combined the principal values of these transformed stress tensors with an isotropic yield function to describe the anisotropic behaviour of materials for the plane stress conditions. Barlat et al. (1991) and Karafillis and Boyce (1993) extended this approach to three-dimensional stress states by proposing a general yield function. Cazacu and Barlat (2004) showed that this theory is general and is compatible with a wide range group of materials, such as HCP metals. Since, many of the above-mentioned yield functions were not able to accurately capture the anisotropic behaviour of aluminum sheets, Barlat et al. (2003) introduced a plane stress yield function that is expressed by two linear transformations of the stress tensor (Yld2000-2d). Also, Bron and Besson (2004) extended Karafillis and Boyce's (1993) function to two linear transformations. Barlat et al. (2005) proposed a new yield function (Yld2004-18P) that is able to describe the anisotropy of materials subject to a three-dimensional stress state.

In most non-quadratic yield functions (Logan and Hosford, 1980; Hosford, 1992; Hosford, 1996; Barlat et al., 1991, 1994, 1996, 2003, 2005), the exponent of the function is associated with the material crystal structure, and is equal to 6 and 8 for BCC and FCC materials, respectively. Recent progress in developing advanced anisotropic yield functions shows that the order of anisotropic yield functions becomes higher to more accurately describe the plastic behaviour of metal sheets. Higher order yield functions have more variables which require calibration from different types of experiments.

Many of the above yield functions were implemented in different metal forming FE simulations for a wide variety of metals by applying the isotropic hardening assumption (Chung and Shah, 1992; Yoon et al., 1999a and 1999b; Tugcu and Neale, 1999; Andersson et al., 1999; Inal et al., 2000; Worswick and Finn, 2000; Yoon et al., 2000). The effect of anisotropic yield functions has been limited to the FE simulation of conventional metal forming processes. To the best of the author's knowledge, no anisotropic yield function has ever been calibrated and applied to simulate a high speed metal forming process such as EHF. An extensive literature review failed to identify any research that considered the changes of the material anisotropy according to the strain rate. Several of the most frequently-used phenomenological anisotropic yield functions for sheet metals have been reviewed in this section. More details about the formulation and calibration procedure of some of them are presented here.

2.3.1.1 Hill 1948 (Hill48)

Hill's (1948) quadratic yield function (Hill48) is no doubt the most widely used anisotropic yield functions. The plane stress form of this function can be written as

$$(G + H)\sigma_{11}^2 - 2H\sigma_{11}\sigma_{22} + (H + F)\sigma_{22}^2 + 2N\sigma_{12}^2 - 1 = 0 \quad (2-1)$$

where F , G , H , and N are anisotropy coefficients which can be defined as functions of either flow stresses or r-values. The equations related to these coefficients are described in detail in chapter 3.

2.3.1.2 Hosford 1979

Hosford (1979) introduced an anisotropic yield function based on Hershey's (1954) idea, which uses principal stresses to describe isotropic polycrystalline metals. This function is an extended form of Hosford's (1972) non-quadratic yield function which is applicable to three-dimensional stress states.

$$F|\sigma_1 - \sigma_2|^m + G|\sigma_2 - \sigma_3|^m + F|\sigma_3 - \sigma_1|^m - 1 = 0 \quad (2-2)$$

where σ_1 , σ_2 , and σ_3 are principal stresses and m is generally equal to 6 and 8 for BCC or FCC metals, respectively.

2.3.1.3 Hill 1979 (Hill79)

Hill (1979) proposed a general non-quadratic yield function for aluminum alloys, based on Hosford's (1979) idea.

$$F|\sigma_2 - \sigma_3|^m + G|\sigma_3 - \sigma_1|^m + H|\sigma_1 - \sigma_2|^m + L|2\sigma_1 - \sigma_2 - \sigma_3|^m \\ + M|2\sigma_2 - \sigma_3 - \sigma_1|^m + N|2\sigma_3 - \sigma_1 - \sigma_2|^m - 1 = 0 \quad (2-3)$$

where, similar to Hill48, F , G , H , L , M , and N are anisotropy coefficients. m is determined based on the experimental uniaxial and biaxial data.

2.3.1.4 Barlat and Lian 1989 (Barlat89)

Barlat and Lian (1989) introduced a non-quadratic yield function (Barlat89) applicable to anisotropic polycrystals, but is limited to the plane stress condition.

$$a|K_1 + K_2|^m + a|K_1 - K_2|^m + (2 - a)|2K_2|^m - 2\bar{\sigma}^m = 0 \quad (2-4)$$

where K_1 and K_2 are written as

$$K_1 = \frac{\sigma_{11} + h\sigma_{22}}{2}, \quad K_2 = \sqrt{\left(\frac{\sigma_{11} - h\sigma_{22}}{2}\right)^2 + p^2\sigma_{12}^2} \quad (2-5)$$

where a , c , h and p are the material anisotropy coefficients, which can be obtained either from measured flow stresses or r-values. The equations related to these coefficients are presented in Chapter 3.

2.3.1.5 Hill 1990 (Hill90)

Hill (1990) proposed another non-quadratic yield function (Hill90) to improve upon the drawbacks of Hill's 1979 function, which is only applicable to the plane stress condition.

$$|\sigma_1 + \sigma_2|^m + \left(\frac{\sigma_b}{\tau}\right)^m |\sigma_1 - \sigma_2|^m + |\sigma_1^2 + \sigma_2^2|^{(m/2)-1}. \quad (2-6)$$

$$\{-2a(\sigma_1^2 - \sigma_2^2) + b(\sigma_1 - \sigma_2)^2 \cos 2\alpha\} \cdot \cos 2\alpha - (2\sigma_b)^m = 0$$

where σ_b is the equibiaxial flow stress, τ is the shear flow stress, α is the angle between the first principal stress and the axis of orthotropy, and a and b are the anisotropy coefficients.

2.3.1.6 Barlat 1991 (Yld91)

Barlat et al. (1991) proposed a non-quadratic yield function (Yld91) for orthotropic materials, which is applicable to three-dimensional stress states.

$$|S_1 - S_2|^a + |S_2 - S_3|^a + |S_3 - S_1|^a - 2\bar{\sigma}^a = 0 \quad (2-7)$$

where S_i are known as the principal values of an isotropic plasticity equivalent (IPE). A linear transformation of the stress tensor is defined as

$$\mathbf{S} = \mathbf{L} \cdot \boldsymbol{\sigma} \quad (2-8)$$

where \mathbf{L} is a symmetric fourth-order tensor associated with the material anisotropy, and $\boldsymbol{\sigma}$ is the Cauchy stress tensor (interested readers are referred to Barlat et al. (1991) for more details).

2.3.1.7 Hill 1993 (Hill93)

Hill (1993) introduced a non-quadratic non-homogenous yield function to accurately capture the material flow behaviour of highly anisotropic materials, but it is only applicable to the plane stress condition.

$$\sigma_1^2 - \left(2 - \frac{\sigma_u^2}{\sigma_b^2}\right)\sigma_1\sigma_2 + \sigma_2^2 + \left[(p+q) - \frac{p\sigma_1 + q\sigma_2}{\sigma_b}\right]\sigma_1\sigma_2 - \sigma_u^2 = 0 \quad (2-9)$$

where σ_b is the equibiaxial flow stress, and p and q are anisotropic parameters. Also, σ_u can be identified as the flow stress in either the rolling or transverse direction.

2.3.1.8 Karafillis and Boyce 1993

Karafillis and Boyce (1993) proposed a non-quadratic anisotropic yield function (KB) based on the combination of two isotropic yield functions, and it is applicable to three-dimensional stress states.

$$(1-c)(|S_1 - S_2|^m + |S_2 - S_3|^m + |S_3 - S_1|^m) + c \frac{3^m}{2^{m-1} + 1} (|S_1|^m + |S_2|^m + |S_3|^m) - 2\bar{\sigma}^m = 0 \quad (2-10)$$

where S_i are the principal values of the IPE, c is a material parameter ($0 \leq c \leq 1$), and L is associated with different types of material anisotropy (triclinic, monoclinic, orthotropic, etc.). If $c = 0$ and the L tensors are isotropic, KB represents the Tresca yield function when $m \rightarrow \infty$, and the von Mises yield function when m is equal to 2.

2.3.1.9 Barlat 1994 and 1997 (Yld94 and Yld96)

Barlat et al. (1997a) proposed a non-quadratic yield function (Yld94) based on KB's model to capture more accurate experimental as well as polycrystalline flow surfaces of alloys with highly anisotropic variations w.r.t. material orientations.

$$\alpha_1|S_2 - S_3|^a + \alpha_2|S_3 - S_1|^a + \alpha_3|S_1 - S_2|^a - 2\bar{\sigma}^a = 0 \quad (2-11)$$

where S_i and \mathbf{L} are defined the same way as in the KB yield function. α_k are additional parameters to describe material anisotropy which are defined as

$$\alpha_k = \alpha_x p_{1k}^2 + \alpha_y p_{2k}^2 + \alpha_z p_{3k}^2 \quad (2-12)$$

where α_x , α_y and α_z are material coefficients, and p_{ij} are the components of the transformation matrix \mathbf{p} between the principal axes of anisotropy and the principal axes of \mathbf{S} . Since Yld94 is limited to plane stress states, Barlat et al. (1997) developed an improved format of the Yld94 function, known as Yld96, to capture material behaviour in 3D stress states. More details on the formulation and calibration procedure for Yld96 are presented in Chapter 3.

2.3.1.10 Barlat 2003 (Yld2000-2d)

Barlat et al. (2003) developed one of the most advanced anisotropic yield functions (Yld2000-2d), to describe material anisotropy behaviour more accurately, in the plane stress condition. Compared to Yld96, Yld2000-2d guarantees the convexity and is more user-friendly to implement in a FE code.

$$|X'_1 - X'_2|^a + |2X''_2 + X''_1|^a + |2X''_1 + X''_2|^a - 2\bar{\sigma}^a = 0 \quad (2-13)$$

where X'_i and X''_i are the principal components of the two linear transformation tensors (\mathbf{X}' and \mathbf{X}''), which are defined as

$$\mathbf{X}' = \mathbf{L}' \boldsymbol{\sigma}, \quad \mathbf{X}'' = \mathbf{L}'' \boldsymbol{\sigma} \quad (2-14)$$

where \mathbf{L}' and \mathbf{L}'' are high-ranked tensors, describing material anisotropy coefficients as functions of eight coefficients, α_1 to α_8 . More details on the formulation and calibration procedure of Yld2000-2d are presented in Chapter 3.

2.3.1.11 Barlat 2005 (Yld2004-18P)

Barlat et al. (2005) introduced another advanced yield function (Yld2004-18p) by building on the foundation of Yld2000-2d which is applicable to three-dimensional stress

states. Due to flexibility of the calibration procedure of Yld2004-18p, it is applicable to a wide variety of materials with substantial anisotropy variation in different material orientations (Barlat et al., 2005).

$$|\tilde{S}'_1 - \tilde{S}''_2|^a + |\tilde{S}'_2 - \tilde{S}''_3|^a + |\tilde{S}'_3 - \tilde{S}''_1|^a - \left\{ |\tilde{S}'_1|^a + |\tilde{S}'_2|^a + |\tilde{S}'_3|^a \right\} + |\tilde{S}''_1|^a + |\tilde{S}''_2|^a + |\tilde{S}''_3|^a - 4\bar{\sigma}^a = 0 \quad (2-15)$$

where S'_i and S''_i are the principal values of two linear transformations of the \mathbf{S}' and \mathbf{S}'' deviatoric stress tensors. More details on the formulation and calibration procedure of Yld2004-18p are presented in Chapter 3.

2.3.2 Flow rule

In the phenomenological approach, the plastic strain increment is specified by the flow rule once the material has yielded. Based on experimental observations, the Levy-Mises and the Prandtl-Reuss relations were developed in such a way that the incremental plastic strain is coaxial with the deviatoric part of the total stress. These equations are widely used as specific forms of the flow rule in classical theory of plasticity (Hill, 1950). Drucker (1951) proposed a general approach to establish plastic stress-strain relations based on his stability rule, which applies to any anisotropic yield function. Based on Drucker's stability postulate, a material is stable if the following inequality is satisfied

$$W = \int_{C_\sigma} \Delta\boldsymbol{\sigma} : d\boldsymbol{\varepsilon} = \int_{C_\sigma} (\boldsymbol{\sigma} - \boldsymbol{\sigma}^0) : d\boldsymbol{\varepsilon} \geq 0 \quad (2-16)$$

where C_σ is a closed stress cycle. Ilyushin (1961) also showed that for a broad range of materials, the net work in an arbitrary closed strain cycle is non-negative, which is a weaker restriction on the material behaviour compared to Drucker's rule. The requirements of both Drucker's and Ilyushin's postulates can only be satisfied in materials with a positive hardening rate.

Bishop and Hill (1951a and 1951b) showed that according to some microstructural considerations, certain properties of a continuum yield function can be obtained. They showed that, based on the Schmid law for a single crystal, dislocation glide occurs on a slip system when the shear stress reaches a critical value. The resulting flow surface was shown to be convex and the associated plastic strain is normal to the slip plane. Their observations also showed that these phenomena can be extended to polycrystals by averaging the behaviour of a number of grains without making any extra assumptions about the interaction between grains or the deformation gradient uniformity. Observations by Hecker (1976) who conducted many multiaxial experiments to assess the flow surface shape showed that the normality and convexity assumptions are valid for a wide range of metals.

Based on the postulates of both Drucker and Ilyushin, the yield function f serves as a plastic potential and the current plastic strain increment must be co-directional with the normal vector to the corresponding yield surface, and the plastic strain increment is defined by

$$d\varepsilon_i^p = d\lambda \frac{\partial f}{\partial \sigma_i} \quad (2-17)$$

where $d\lambda$ is called the plastic multiplier which is a non-negative parameter representing the size of the strain increment, and f is the yield function. Eq. (2.17) shows that the plastic strain increment is proportional to the gradient of the flow surface ($\partial f / \partial \sigma$). This equation is referred to as the normality condition and a flow rule derived from this equation is known as the associated flow rule (AFR). Also, a flow rule in which the plastic strain increment is not normal to the yield surface is known as a non-associated flow rule (NAFR). The AFR can be generalized to describe the behaviour of both isotropic and anisotropic materials. Spitzig et al. (1976, 1984) conducted several experiments under different hydrostatic stresses and found small volume changes for several metal alloys, which were negligible compared to those calculated by AFR assumption. They concluded that the yielding in metals does not depend on a superimposed hydrostatic pressure and the AFR assumption is valid for a wide range of

metallic alloys. However, their observations showed that the AFR is not valid for highly porous materials, polymers, or for materials subjected to very high pressure (known as pressure sensitive materials).

2.3.3 Rate-dependent hardening models

Generally, the flow stress represents a material's resistance to plastic flow under different loading conditions. The hardening equation is a mathematical equation that represents the relationship between the flow behaviour of a material and parameters such as plastic strain, strain rate, temperature, and so on. Depending on the actual forming conditions, the hardening equation can also contain more variables related to the previous loading condition (pre-straining), thermo-mechanical history or microstructural material information (such as grain size, different phases, dislocation density, etc.). Among the well-known parameters, strain rate and temperature are the most influential parameters in the accurate description of material hardening behaviour in conventional and high-speed metal forming, high-velocity impact, high-speed machining, and other dynamic applications. Taylor (1942), and von Karman and Duwez (1950) were among the first researchers to make a substantial contribution to the development of several hardening models based on experimental observations.

Over the years, several hardening models were developed for use in computational mechanics to predict the flow behaviour of different materials over a wide range of strain rates and temperatures. Hardening models are generally classified into two main groups; physics-based models and phenomenological models. Each class of hardening model has its own drawbacks and advantages, which can be highlighted or ignored based on many factors, such as; required accuracy, computational time, user-friendliness of implementing a model into a FE code, the availability of different experimental data sets, and more.

In physics-based models, the material flow stress is the superposition of thermal, athermal and viscous drag components (Mecking and Kocks, 1981; Nemat-Nasser et al., 2001). The dislocation accumulation is the main motivation in generating plastic deformation of metal under the rate-controlled deformation mechanism. In an active

thermal deformation, plastic flow is considered by short-range and long-range obstacles which are controlled by the motion of dislocations. Generally, the short-range obstacles include forest dislocations (in FCC materials), Peierls stress (in BCC materials), impurities, deposits, and so on, which can be overcome by thermal activation. The long-range obstacles may include grain boundaries and the stress field of dislocation forests which are independent of temperature (athermal). Nemat-Nasser et al. (2001) showed that the viscous-drag component is active in high strain rate and high-temperature deformations. Armstrong et al. (1988) showed that the activation volume in BCC metals is much smaller than in FCC metals, which results in a much greater strain rate and temperature sensitivity. Many experimental studies have been conducted for a variety of materials to explore the micro-mechanisms underlying the material deformation in different loading conditions (Christian, 1983; Gray and Rollett, 1992; and Gourdin and Lassila, 1995). The consideration of microstructural details in physics-based models allows these models to more accurately describe the deformation behaviour of materials over a wide range of strain rates and temperatures. However, these models are not generally preferred for industrial applications because the determination of material constants requires numerous and more complex characterization tests.

Compared to physics-based models, phenomenological hardening models are more widely used and applied into FE codes for numerical simulations of many industrial applications. Johnson and Cook (1983), JC, and Zerilli and Armstrong (1987), ZA, were amongst the first phenomenological models implemented to predict the deformation behaviour of various materials under dynamic loading conditions. Experimental results for different BCC, FCC, and HCP metals showed that the rate of strain hardening (or work hardening) behaviour could be changed by the strain rate as well as the plastic strain. Liang and Khan (1999) showed that the increase of strain rate can change the strain hardening rate in some FCC metals. Figure 2-2 illustrates a schematic of a decrease in strain hardening rate of a material with increasing strain rate. Liang and Khan modified the original JC model to include the strain-rate sensitivity of the material in the strain hardening term. This modification led to a much better correlation than the original JC model, particularly for mild steels (Khan and Liang, 2000; Khan and Zhang, 2000; Khan

et al. 2004, 2007a, 2007b) over a wide range of strain rates ($10^{-6} - 10^3 \text{ s}^{-1}$) and temperatures ($298\text{K} - 589\text{K}$).

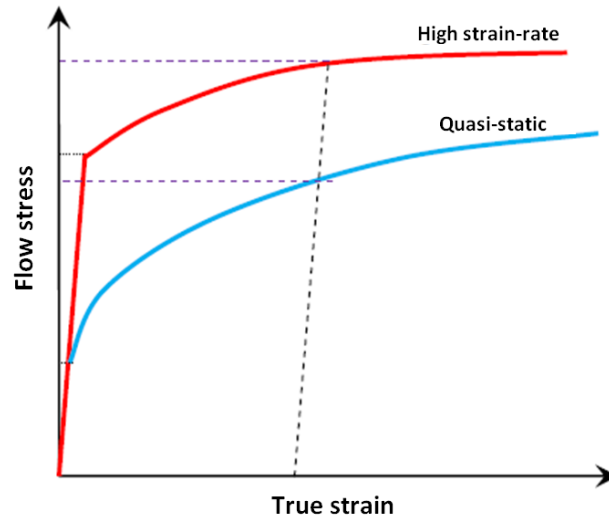


Figure 2-2. Schematic of flow curves at quasi-static and high strain rate regimes

The most recent modified Khan–Huang–Liang (KHL) model (Liu and Khan, 2011) showed the strength of the model to more accurately describe the behaviour of alloys under multiaxial loading conditions, including dynamic torsion and non-proportional biaxial compression. Most recently, Paul (2012) proposed a phenomenological model (SKP) that was shown to be able to capture the flow behaviour for a variety of materials (DP600, TRIP780, and mild steel) with adequate accuracy and reliability over a wide range of strain rates and temperatures. In another aspect, depending upon their mathematical formulation, rate-dependent phenomenological hardening models can be classified into four groups. Different rate-dependent mathematical formulations are shown in Table 2.1, where σ_0 is the yield stress, α is the back stress, ε^p is the plastic strain, and $\dot{\varepsilon}$ is the strain rate.

Table 2.1 Mathematical formulation of phenomenological rate-dependent hardening models

Category	Mathematical formulation	
1	$\sigma = \sigma_0 f(\dot{\epsilon}) + \alpha(\epsilon^p)$ Zerilli and Armstrong (1987) for BCC metals, El-Magd et al. (2001)	(2-18)
2	$\sigma = \sigma_0 + \alpha(\epsilon^p) f(\dot{\epsilon})$ Zerilli and Armstrong (1987) for FCC metals	(2-19)
3	$\sigma = [\sigma_0 + \alpha(\epsilon^p)] f(\dot{\epsilon})$ Johnson and Cook (1983), Cowper and Symonds (1958), Lin and Wagoner (1987)	(2-20)
4	$\sigma = \sigma_0 f(\dot{\epsilon}) + \alpha(\epsilon^p) g(\dot{\epsilon})$ Zhao (1997), Khan and Liang (1999), Kaps et al. (1999), Rusinek et al. (2007), Paul (2012)	(2-21)

As can be seen from the mathematical formulation, the models belonging to the fourth category are more flexible to describe the flow behaviour of more materials (BCC, FCC, and HCP metals), due to dependency of both yield stress and back stress on strain rate, considering two different functions, $f(\dot{\epsilon})$ and $g(\dot{\epsilon})$. Paul (2012) showed that Kaps et al. (1999) model is able to account for strain rate but not temperature dependency, while both the Zhao (1997) and Paul (2012) models are able to show a good correlation with the experiments over a wide range of strain rates and temperatures for various metallic alloys. Here, four hardening models, JC, ZA, KHL and SKP are briefly discussed. The JC, KHL, and SKP formulations and material parameters are discussed in more detail in Chapter 3.

2.3.3.1 Johnson-Cook (JC)

The JC model (Johnson and Cook, 1983) is implemented into most commercial FE codes (ABAQUS and LS-DYNA) and it is widely used in the simulation of problems under dynamic loading. The JC equation is a multiplication of three terms; strain

hardening, strain rate hardening, and thermal softening. The decoupling of the three terms leads to a constant strain hardening (or work hardening) rate over different strain rates and temperatures. The JC model can be written as

$$\sigma = [A + B\varepsilon_p^n][1 + C\ln\dot{\varepsilon}^*] \left[1 - \left(\frac{T - T_r}{T_m - T_r} \right)^m \right] \quad (2-22)$$

where ε_p is the plastic strain, $\dot{\varepsilon}^*$ is a dimensionless strain rate ($\dot{\varepsilon}^* = \dot{\varepsilon}/\dot{\varepsilon}_0$, where $\dot{\varepsilon}_0$ is the reference strain rate), and T , T_r , T_m are the current, room and melting temperatures. Also, A , B , n , C , and m are material constants which are generally calibrated based on the least-squares method.

2.3.3.2 Zerilli-Armstrong (ZA)

The ZA (Zerilli and Armstrong, 1987) model is a dislocation-based hardening model which considers the strain hardening, strain rate hardening, and thermal softening based on the thermal activation theory. Zerilli and Armstrong introduced different equations according to the crystallographic texture of each particular material (BCC, FCC, and HCP). The following equation shows the hardening relation for BCC materials

$$\sigma = C_0 + B_0 e^{-(\beta_0 - \beta_1 \ln \dot{\varepsilon})T} + K\varepsilon_p^n \quad (2-23)$$

where ε_p is the plastic strain, $\dot{\varepsilon}$ is the strain rate, and T is the current temperature. Also, C_0 , B_0 , β_0 , β_1 , K , and n are the material constants. Similar to the JC, the ZA model also predicts a constant strain hardening (or work hardening) rate over a wide range of strain rates and temperatures, which is not able to model the behaviour of BCC materials accurately.

2.3.3.3 Khan-Huang-Liang (KHL)

The KHL (Khan and Liang, 1999) is a phenomenological hardening model, that incorporates strain hardening, strain rate hardening as well as thermal softening effects. In contrast with JC and ZA, the strain hardening rate is not constant in the KHL model and can be significantly changed over a large strain rate range ($10^{-5} - 10^4 \text{ s}^{-1}$).

$$\sigma = \left[A + B \varepsilon_p^{n_0} \left(1 - \frac{\ln \dot{\varepsilon}^*}{\ln D_0^p} \right)^{n_1} \right] [\dot{\varepsilon}^*]^C \left[\frac{T_m - T}{T_m - T_r} \right]^m \quad (2-24)$$

where ε_p is the plastic strain, $\dot{\varepsilon}^*$ is a dimensionless strain rate, T , T_r , T_m are the current, room and melting temperatures, D_0^p is equal to 10^6 s^{-1} and is used to non-dimensionalize the strain rate. Also, A , B , n_0 , n_1 , C , and m are material constants that are generally determined in a numerical optimization procedure.

2.3.3.4 SKP

The SKP (Paul, 2012) model was proposed to overcome the inability of some hardening models, such as KHL, to correlate well with the experiments particularly for mild steels and a few AHSS steels. Similar to the KHL, the SKP model is able to accurately predict the material flow over a wide range of strain rates and temperatures by automatically considering the local temperature rise (adiabatic thermal softening) effect. The general form of the SKP model can be expressed as

$$\sigma = \sigma_0 e^{A \ln(\dot{\varepsilon}^*) - K(T - T_a)} + [B \varepsilon_p^n + C(1 - e^{-\beta \varepsilon_p})] (1 - H \ln(\dot{\varepsilon}^*)) (1 - G(T - T_a)) \quad (2-25)$$

where ε_p is the plastic strain, $\dot{\varepsilon}^*$ is a dimensionless strain rate, and T and T_a are the current and absolute temperatures. Also, σ_0 , A , K , B , C , β , H and G are material constants that can be determined either in a systematic calibration procedure (Paul, 2012) or via a numerical optimization procedure.

2.4 Experiments; high strain rate tests

Many tests over a wide range of strain rates are required to determine the material constants in both yield functions and hardening models as material property input in FE analysis. The experimental procedure to characterize material flow behaviour can alter, depending upon the required strain rate. Mechanical or/and hydraulic tensile testing machines are generally used to acquire the flow behaviour of materials at low strain rate regimes, under so called isothermal quasi-static conditions (below 1 s^{-1}). Quasi-static

tests are widely standardized, while intermediate and high strain rate tests have been under development for decades. Generally, in strain rates greater than 10 s^{-1} , the inertia effect generates a dynamic stress which could significantly change the material behaviour, particularly in steels. The Kolsky's bar test or the split Hopkinson pressure bar (SHPB) test is a widely used technique to acquire the flow stress of materials at high strain rates (10^3 - 10^5 s^{-1}). The SHPB technique is not valid at intermediate strain rates (1 - 500 s^{-1}), since the one-dimensional stress wave theory is no longer valid due to activation of quasi-static and dynamic effects simultaneously at this strain-rate range (Huh et al., 2002). Lim (2007) showed that both low and intermediate strain rate material behaviour can be captured by an open loop servo-hydraulic dynamic tensile testing machine. In most conventional metal forming processes, the material generally is subjected to low to intermediate strain rates, while in pulsed forming technologies (such as EF, EMF, and EHF), high strain rate levels are expected. Therefore, there is a critical need for intermediate and high strain rate material characterization tests. Experimental observations showed that the majority of the plastic work is converted to heat during plastic deformation. The temperature increase can be calculated as follow s;

$$\Delta T = \frac{\eta}{\rho_M c_p} \int_0^{\varepsilon_p} \sigma d\varepsilon_p \quad (2-26)$$

where ρ_M is the density, c_p is the specific heat at constant pressure, σ is the stress, and ε_p is the plastic strain. In quasi-static conditions, almost all the heat generated during plastic deformation has significant time to dissipate into the surrounding material, so the process is considered isothermal. In high strain rate plastic deformation, the process is considered adiabatic, since the heat generated does not have time to conduct and/or convect away (Khan and Liang, 1999). In Eq. (2.26), the coefficient η is generally considered between 0.9 and 1.0 at high strain rates (Khan and Liang, 1999), and zero for quasi-static conditions. However, at intermediate strain rate regimes, quantifying the coefficient η is very challenging since the process is neither isothermal nor adiabatic but somewhere in between. Therefore, it is more convenient for a hardening model to predict the material flow behaviour without considering separate thermal effects at intermediate and at high strain rate ranges.

A large amount of experimental work has been conducted to characterize the material behaviour of metals at different strain rates. Dusek (1970) studied the high strain rate mechanical behaviour of Armco-iron and low-alloyed steels. He reported a substantial increase in the yield stress of these materials at high strain rates (10^2 - 10^4 s^{-1}), while a slow increase occurs at low and intermediate strain rates (10^{-3} – 10^2 s^{-1}). He also showed that Young's modulus is constant in all strain rate regimes. Vashchenko et al. (1989) conducted an experimental study on dynamic testing of several steels and showed an increase of elongation in the range of strain rates 10^3 – 5×10^4 s^{-1} , while under 10^3 s^{-1} no improvement and even a slight decrease in elongation was observed. Experimental observations by Regazzoni et al., (1987), and Hu and Daehn (1996) showed higher failure strains can be achieved by delaying the onset of necking at intermediate and high strain rate regimes.

Also, El-Magd (1997) reported a substantial delay in the onset of plastic instability under dynamic loading conditions for materials with greater strain-rate sensitivity. Many experimental tests were conducted by Nemat-Nasser et al. (1998) to investigate the mechanical behaviour of OFHC copper in both as-received and annealed conditions for the strain rate range of 10^{-3} to 8000 s^{-1} . Picu et al., (2005) and Hughes et al. (1998) performed a series of compression tests in the strain rate range of 10^{-3} to 1 s^{-1} . They reported a negative strain-rate sensitivity and a dynamic strain aging deformation mechanism at room temperature for AA5182-O. Bleck and Schael (2000) conducted high-speed tensile tests using flat sheet specimens of dual phase steels up to a maximum strain rate of 200 s^{-1} . They reported substantial strain-rate sensitivity even for the intermediate strain rate regime. Khan et al. (2000) conducted non-proportional multiaxial tests to investigate the mechanical behaviour of AerMet 100 steel and tantalum at different strain rates. Experimental observations by Borvik et al. (2001) for several aluminum and steel alloys showed that the fracture strain is less sensitive to strain rate than to the stress-triaxiality and Lode parameters. Huang et al. (2011) conducted tensile experiments which showed no improvement in elongation of mild and dual phase steels up to 10^3 s^{-1} . Priem et al. (2007) showed that the inertial effect generates additional stresses outside the

necking region which lead to further uniform deformation in the part before the onset of severe necking and fracture.

Oliver et al. (2007) reported microstructural changes in DP780 and TRIP780 in the strain rate range of 10^{-3} to 200 s^{-1} under tensile loading conditions. Observations showed lower ductility in DP800 by increasing the strain rate, while the opposite response was experienced in TRIP780. Van Slycken et al. (2007) showed that in TRIP steels, at high strain rate regimes, the austenite phase has a positive strain-rate sensitivity, while the ferrite and bainite phases are independent of strain rate. Khan and Farrokh (2006), and Khan et al. (2007a and 2007b) developed a non-proportional biaxial compression channel fixture to investigate the material behaviour of Al2024-T351 at high strain rate regimes. Tarigopula et al. (2008) studied the behaviour of DP steels in order to investigate the strain localization at intermediate strain rates using a servo-hydraulic testing machine ($10^{-3} - 200 \text{ s}^{-1}$), and at high strain rates using the SHPB test ($150 - 600 \text{ s}^{-1}$). Yu et al. (2009) conducted dynamic tensile tests at strain rates of 500 to 1600 s^{-1} to study the mechanical behaviour of DP590. Additionally, he used the Johnson-Cook rate-dependent constitutive model to simulate the material behaviour at different strain rates.

This literature review has highlighted the most significant research in high speed metal forming processes in the development of constitutive models that can describe the behaviour of anisotropic sheet metal at high strain rates and the experimental characterization tests required to determine material behaviour at high strain rates

3 Rate-dependent Constitutive Model

3.1 Anisotropic yield functions

The proper selection and calibration of a yield function is recognised as one of the most critical factors in classical plasticity. Calibrating a yield function is complicated because of complex functions and the number of experimental parameters required. An accurate description of the flow surface shape, which is crucial to the prediction of material plastic deformation, can only be obtained using an appropriate anisotropic yield function. For decades, many quadratic and non-quadratic yield functions were developed to describe the material anisotropy behaviour more accurately to improve the predictions of FE simulations. The formulation for several of the most frequently used and advanced phenomenological anisotropic yield functions (Hill 1948, Hill 1990, Barlat89, Yld96, Yld2000-2d and Yld2004-18p) and the corresponding calibration procedure for each, are presented in detail.

3.1.1 Hill 1948 (Hill48)

Hill (1948) proposed a quadratic yield function (Hill48) as a generalization of the Huber-Mises-Hencky criterion. The simplicity of the Hill48 yield function has led to its popularity as one of the most widely used anisotropic yield functions. The material is assumed to have anisotropy w.r.t. three orthogonal symmetry planes. The plane-stress ($\sigma_{33} = \sigma_{31} = \sigma_{32} = 0$) form of Hill48's function can be written as

$$2\phi = (G + H)\sigma_{xx}^2 - 2H\sigma_{xx}\sigma_{yy} + (H + F)\sigma_{yy}^2 + 2N\sigma_{xy}^2 - \bar{\sigma}^2 = 0 \quad (3-1)$$

where G , H , F and N are constants related to the anisotropy of the material. The effective flow stress ($\bar{\sigma}$) is assumed to be equal to the flow stress in the RD ($\bar{\sigma} = \sigma_{xx} = \sigma_0$) for all the yield functions in this work.

3.1.1.1 Calibration procedure

The determination of the Hill48 constants can be completed based on either experimental flow stresses or r-values (plastic flow or Lankford coefficients) in different material orientations. The selection of either experimental flow stresses or r-values is at the user's discretion and is often guided by the availability of experimental data. In this work, both procedures are considered so as to make a more comprehensive study of the effect of calibration procedure on the accuracy of plastic deformation behaviour. The Hill48 function that is calibrated based on experimental r-values will be denoted as "Hill48-r.value", but it will be called "Hill48-stress" when it is calibrated with experimental flow stresses. In this manuscript, the same nomenclature will be used for other yield functions, as applicable.

3.1.1.2 Hill48-stress

The Hill48 constants can be expressed in terms of stress

$$G = \frac{\bar{\sigma}^2}{2} \left[\frac{1}{\sigma_{xx}^2} + \frac{1}{\sigma_b^2} - \frac{1}{\sigma_{yy}^2} \right], \quad H = \frac{\bar{\sigma}^2}{2} \left[\frac{1}{\sigma_{xx}^2} + \frac{1}{\sigma_{yy}^2} - \frac{1}{\sigma_b^2} \right], \quad (3-2)$$

$$F = \frac{\bar{\sigma}^2}{2} \left[\frac{1}{\sigma_{yy}^2} + \frac{1}{\sigma_b^2} - \frac{1}{\sigma_{xx}^2} \right], \quad N = \frac{1}{\sigma_{xy}^2} = \frac{\bar{\sigma}^2}{4} \left[\frac{4}{\sigma_{45}^2} - \frac{1}{\sigma_b^2} \right]$$

where x , y , z are the principal anisotropic axes, which are assumed to be aligned with the principal plastic stretch directions. In sheet metals it is generally assumed that the x -axis is parallel to the rolling direction (RD), y is parallel to the transverse direction (TD), and z is oriented in the normal direction (through-thickness). Therefore, σ_{xx} (σ_0), σ_{45} and σ_{yy} (σ_{90}) are uniaxial flow stresses in the rolling, diagonal, and transverse directions, respectively. σ_{xy} is the shear flow stress, and σ_b is the equi-biaxial flow stress. It is worth

noting that constant N was determined based on the stress-transformation in two-dimensional (2D) stress space.

3.1.1.3 Hill48-r.value

The Hill48 constants can also be expressed in terms of r-values

$$G = \frac{1}{1 + r_0}, \quad H = \frac{r_0}{1 + r_0}, \quad F = \frac{r_0}{(1 + r_0)r_{90}}, \quad (3-3)$$

$$N = \left(\frac{1}{1 + r_0} \right) \left(\frac{1 + 2r_{45}}{2} \right) \left(\frac{r_0 + r_{90}}{r_{90}} \right)$$

where r_0 , r_{45} , and r_{90} are the experimental r-values in the rolling (RD), diagonal (DD) and transverse (TD) directions, respectively.

3.1.2 Hill 1990 (Hill90)

Hill (1990) introduced a non-quadratic yield function (Hill90) expressed in a general coordinate system for the plane-stress condition. This function was mainly developed to eliminate the severe limitations of Hill's 1979 function, which was only applicable when the directions of the principal stresses were coincident with the material orthotropic axes.

$$\begin{aligned} \phi = & \left| \sigma_{xx} + \sigma_{yy} \right|^m + (\sigma_b/\tau)^m \left| (\sigma_{xx} - \sigma_{yy})^2 + 4\sigma_{xy}^2 \right|^{m/2} \\ & + \left| \sigma_{xx}^2 + \sigma_{yy}^2 + 2\sigma_{xy}^2 \right|^{(m/2)-1} \cdot \{-2a(\sigma_{xx}^2 - \sigma_{yy}^2) + b(\sigma_{xx} - \sigma_{yy})^2\} \\ & - (2\sigma_b)^m = 0 \end{aligned} \quad (3-4)$$

where τ is the pure shear stress ($\sigma_1 = -\sigma_2$), and σ_b is the flow stress in equi-biaxial tension. a , b , and m are material constants.

3.1.2.1 Calibration procedure

Similar to Hill48, the Hill90 material constants can be determined on the basis of either experimental flow stresses or r-values. The exponent “ m ” is obtained from the following equation

$$m = \frac{\ln(2(r_{45} + 1))}{\ln(2\sigma_b/\sigma_{45})} \quad (3-5)$$

where σ_{45} and r_{45} are the flow stress and r-value in the diagonal direction (DD).

3.1.2.1.1 Hill90-stress

The ratio σ_b/τ can be expressed as a function of flow stresses

$$\left(\frac{\sigma_b}{\tau}\right)^m = \left(\frac{2\sigma_b}{\sigma_{45}}\right)^m - 1 \quad (3-6)$$

Constants a and b are obtained by the following equations

$$a = \frac{1}{4} \left[\left(\frac{2\sigma_b}{\sigma_{90}}\right)^m - \left(\frac{2\sigma_b}{\sigma_0}\right)^m \right], \quad b = \frac{1}{2} \left[\left(\frac{2\sigma_b}{\sigma_0}\right)^m + \left(\frac{2\sigma_b}{\sigma_{90}}\right)^m \right] - \left(\frac{2\sigma_b}{\sigma_{45}}\right)^m \quad (3-7)$$

where σ_0 and σ_{90} are the flow stresses in the rolling (RD) and transverse (TD) directions, respectively.

3.1.2.1.2 Hill90-r.value

The ratio σ_b/τ can be derived as a function of r_{45}

$$\left(\frac{\sigma_b}{\tau}\right)^m = 1 + 2r_{45} \quad (3-8)$$

Constants a and b are determined by the following equations

$$a = \frac{(r_0 - r_{90})[1 - ((m - 2)/2)r_{45}]}{(r_0 + r_{90}) - (m - 2)r_0r_{90}}, \quad b = \frac{m[2r_0r_{90} - r_{45}(r_0 + r_{90})]}{(r_0 + r_{90}) - (m - 2)r_0r_{90}} \quad (3-9)$$

where r_0 and r_{90} are the r-values in the rolling (RD) and transverse (TD) directions, respectively.

3.1.3 Barlat 1989 (Barlat89)

Barlat and Lian (1989) proposed a non-quadratic yield function (Barlat89) for polycrystals with planar anisotropy that is restricted to the plane-stress condition

$$\phi = a|K_1 + K_2|^M + a|K_1 - K_2|^M + c|2K_2|^M - 2\bar{\sigma}^M = 0 \quad (3-10)$$

where M is an integer exponent that is generally equal to 6 for BCC metals or 8 for FCC metals. Also, K_1 and K_2 are stress tensor invariants and are given by

$$K_1 = \frac{\sigma_{xx} + h\sigma_{yy}}{2}, \quad K_2 = \sqrt{\left(\frac{\sigma_{xx} - h\sigma_{yy}}{2}\right)^2 + p^2\sigma_{xy}^2} \quad (3-11)$$

where a , c , h and p are material constants.

3.1.3.1 Calibration procedure

Similar to the Hill family of yield functions, the Barlat89 material constants can be determined based on either the flow stress or the r-value, depending upon the availability of experimental data.

3.1.3.1.1 Barlat89-stress

The Barlat89 constants can be expressed in terms of stress

$$a = \frac{2\left(\frac{\bar{\sigma}}{\tau_{s2}}\right)^M - 2\left(1 + \frac{\bar{\sigma}}{\sigma_{90}}\right)^M}{1 + \left(\frac{\bar{\sigma}}{\sigma_{90}}\right)^M - \left(1 + \frac{\bar{\sigma}}{\sigma_{90}}\right)^M}, \quad c = 2 - a, \quad (3-12)$$

$$h = \frac{\bar{\sigma}}{\sigma_{90}}, \quad p = \frac{\bar{\sigma}}{\tau_{s1}} \left(\frac{2}{2a + 2^M c}\right)^{1/M}$$

where σ_{90} is the flow stress in the transverse direction (TD), and τ_{s1} and τ_{s2} are the flow stresses obtained from two different shear tests; $\tau_{s1} = \sigma_{xy}$ when $\sigma_{xx} = \sigma_{yy}$, and $\tau_{s2} = \sigma_{xx} = -\sigma_{yy}$ when $\sigma_{xy} = 0$. In this work, due to the unavailability of experimental shear stress data, p was calculated by a numerical procedure.

3.1.3.1.2 Barlat89-r.value

The Barlat89 constants can also be expressed in terms of r-value

$$a = 2 - 2 \sqrt{\frac{r_0}{1+r_0} \frac{r_{90}}{1+r_{90}}}, \quad c = 2 - a, \quad h = \sqrt{\frac{r_0}{1+r_0} \frac{1+r_{90}}{r_{90}}} \quad (3-13)$$

where r_0 and r_{90} are the r-values in the rolling (RD) and transverse (TD) directions, respectively.

3.1.4 Barlat 1996 (Yld96)

Barlat et al. (1997) proposed a non-quadratic yield function (Yld96) for three-dimensional stress states, to overcome some limitations in the FE implementation of Yld94 (Barlat et al., 1997) for metal forming simulations. This function is based on the KB model (Karafillis and Boyce, 1993) which was developed to capture the experimental and polycrystalline flow surfaces for sheet metal alloys that have undergone a large amount of cold reduction. Yld96 yield function is written as follows

$$\phi = \alpha_1 |S_2 - S_3|^a + \alpha_2 |S_3 - S_1|^a + \alpha_3 |S_1 - S_2|^a - 2\bar{\sigma}^a = 0 \quad (3-14)$$

where S_i are the principal deviatoric stresses, a is an integer exponent which in all Barlat's yield functions is set to 6 and 8 for BCC and FCC metals, respectively, and coefficients α_1 , α_2 and α_3 are calculated based on weight factors α_x , α_y and α_z , using the following transformation equation

$$\alpha_k = \alpha_x p_{1k}^2 + \alpha_y p_{2k}^2 + \alpha_z p_{3k}^2 \quad k = 1,2,3 \quad (3-15)$$

where p_{1k} , p_{2k} and p_{3k} are components of a rotation matrix, \mathbf{p} , correlating the anisotropy axes to the principal directions of the deviatoric stress tensor \mathbf{s} .

$$\mathbf{s} = \mathbf{L}\boldsymbol{\sigma}, \quad (3-16)$$

where \mathbf{L} is a linear transformation matrix. In the plane stress condition, \mathbf{L} can be written as

$$\mathbf{L} = \begin{bmatrix} \frac{c_2 + c_3}{3} & \frac{-c_3}{3} & \frac{-c_2}{3} & 0 & 0 & 0 \\ \frac{-c_3}{3} & \frac{c_3 + c_1}{3} & \frac{-c_1}{3} & 0 & 0 & 0 \\ \frac{-c_2}{3} & \frac{-c_1}{3} & \frac{c_1 + c_2}{3} & 0 & 0 & 0 \\ 0 & 0 & 0 & c_4 & 0 & 0 \\ 0 & 0 & 0 & 0 & c_5 & 0 \\ 0 & 0 & 0 & 0 & 0 & c_6 \end{bmatrix} \quad (3-17)$$

where c_1 , c_2 and c_3 are the constants describing the material anisotropy.

3.1.4.1 Calibration procedure

For the plane stress condition, seven material coefficients ($c_1, c_2, c_3, c_6, \alpha_1, \alpha_2$ and α_3) are determined from uniaxial tension tests in three different directions ($\sigma_0, \sigma_{45}, \sigma_{90}, r_0, r_{45}$ and r_{90}) in addition to the biaxial bulge (σ_b) test. The yield conditions for uniaxial tension in the rolling (F_0) and transverse (F_{90}) directions, and equi-biaxial tension (F_b), can be written as

$$\begin{cases} F_0 = \alpha_x |c_2 - c_3|^a + \alpha_y |2c_2 + c_3|^a + |c_2 + 2c_3|^a - 2(3\bar{\sigma}/\sigma_0)^a = 0 \\ F_{90} = \alpha_x |c_3 + 2c_1|^a + \alpha_y |c_3 - c_1|^a + |2c_3 + c_1|^a - 2(3\bar{\sigma}/\sigma_{90})^a = 0 \\ F_b = \alpha_x |2c_1 + c_2|^a + \alpha_y |c_1 + 2c_2|^a + |c_1 - c_2|^a - 2(3\bar{\sigma}/\sigma_b)^a = 0 \end{cases} \quad (3-18)$$

First, c_1, c_2 , and c_3 are determined using the Newton-Raphson method to solve the above non-linear system of equations, assuming $\alpha_x = \alpha_y = 1$ as initial values. Then, in a multistep iterative procedure, the α_x and α_y values are modified in such a way as to satisfy the RD and TD r-values (r_0 and r_{90}). In a similar iterative manner, c_6 and α_z are calculated in order to approach to the flow stress (σ_{45}) and r-value (r_{45}) for uniaxial tension in the diagonal direction.

3.1.4.2 Calculation of r_b from Yld96

The parameter r_b ($\dot{\epsilon}_{yy}/\dot{\epsilon}_{xx}$) is analogous to the r-value obtained in uniaxial tension, and it characterizes the slope of the yield surface in the balanced biaxial tension stress state ($\sigma_{11} = \sigma_{22}$). This parameter can be evaluated using three different approaches;

experimentally by performing compression tests on circular disks, or computationally from a crystal plasticity simulation, or theoretically using an advanced yield function such as Yld96 (Barlat et al., 2003). In this work, since it was not possible to perform compression tests or carry out crystal plasticity simulations for a wide of range of strain rates ($10^{-3} - 10^3 \text{ s}^{-1}$), Yld96 was used to calculate the r_b at various strain rates. A non-linear system of five equations of the five unknowns (α_x , α_y , c_1 , c_2 and c_3) is required to be solved, assuming the associated flow rule (Barlat et al., 2005). After solving this system of equations using the Newton-Raphson method, r_b can be defined by

$$\begin{aligned}
r_b = & \left[-\alpha_x(c_3 + 2c_1)(2c_1 + c_2)|2c_1 + c_2|^{a-2} + \alpha_y(c_3 - c_1)(c_1 + 2c_2)|c_1 + \right. \\
& 2c_2|^{a-2} - (2c_3 + c_1)(c_1 - c_2)|c_1 - c_2|^{a-2}] / \left[-\alpha_x(c_2 - c_3)(2c_1 + c_2)|2c_1 + \right. \\
& c_2|^{a-2} - \alpha_y(2c_2 + c_3)(c_1 + 2c_2)|c_1 + 2c_2|^{a-2} + (c_2 + 2c_3)(c_1 - c_2)|c_1 - \\
& \left. c_2|^{a-2} \right]
\end{aligned} \tag{3-19}$$

3.1.5 Barlat 2003 (Yld2000-2d)

Barlat et al. (2003) developed an incompressible plane stress yield function (Yld2000-2d), which very accurately describes the anisotropic behaviour of sheet metals, in particular, aluminum alloys and guarantees the convexity of the flow surface. Two linear transformations of the Cauchy stress tensor were introduced into the formulation of the yield function.

$$\phi = \phi' + \phi'' = |X'_1 - X'_2|^a + |2X''_2 + X''_1|^a + |2X''_1 + X''_2|^a - 2\bar{\sigma}^a = 0 \tag{3-20}$$

where X'_i and X''_i are the principal components of two linear transformations (\mathbf{X}' and \mathbf{X}'') of the Cauchy stress tensor, which are defined as follows

$$\mathbf{X}' = \mathbf{L}'\boldsymbol{\sigma}, \quad \mathbf{X}'' = \mathbf{L}''\boldsymbol{\sigma} \tag{3-21}$$

where \mathbf{L}' and \mathbf{L}'' are two linear high-ranked tensors expressing the anisotropy of the material as functions of independent coefficients α_1 to α_8 .

$$\begin{bmatrix} L'_{11} \\ L'_{12} \\ L'_{21} \\ L'_{22} \\ L'_{33} \end{bmatrix} = \begin{bmatrix} 2/3 & 0 & 0 \\ -1/3 & 0 & 0 \\ 0 & -1/3 & 0 \\ 0 & 2/3 & 0 \\ 0 & 0 & 1 \end{bmatrix} \begin{bmatrix} \alpha_1 \\ \alpha_2 \\ \alpha_7 \end{bmatrix}, \quad \begin{bmatrix} L''_{11} \\ L''_{12} \\ L''_{21} \\ L''_{22} \\ L''_{33} \end{bmatrix} = \frac{1}{9} \begin{bmatrix} -2 & 2 & 8 & -2 & 0 \\ 1 & -4 & -4 & 4 & 0 \\ 4 & -4 & -4 & 1 & 0 \\ -2 & 8 & 2 & -2 & 0 \\ 0 & 0 & 0 & 0 & 9 \end{bmatrix} \begin{bmatrix} \alpha_3 \\ \alpha_4 \\ \alpha_5 \\ \alpha_6 \\ \alpha_8 \end{bmatrix} \quad (3-22)$$

The principal values of \mathbf{X}' and \mathbf{X}'' tensors can be calculated as

$$X'_{1,2} = \frac{1}{2} \left(X'_{xx} + X'_{yy} \pm \sqrt{(X'_{xx} - X'_{yy})^2 + 4X'^2_{xy}} \right) \quad (3-23)$$

3.1.5.1 Calibration procedure

Due to the fact that eight constants (α_1 to α_8) are incorporated in the \mathbf{L}' and \mathbf{L}'' , eight input data are required to characterise the anisotropy of the material. Uniaxial tension tests in the RD, DD and TD ($\sigma_0, \sigma_{45}, \sigma_{90}, r_0, r_{45}, r_{90}$), in addition to the biaxial bulge test (σ_b) provide seven input parameters. The eighth parameter, r_b , can be calculated based on Yld96 function, as mentioned in the previous section. It should be noted that all the independent coefficients α_k reduce to one in the case of an isotropic material. A system of eight nonlinear equations must be solved using the Newton-Raphson method to determine the α_i parameters. This system consists of four yield equations for the flow stresses and their corresponding derivatives for the r-values in both uniaxial and biaxial conditions. The function ϕ can therefore be rewritten as

$$\phi = |\alpha_1 \gamma - \alpha_2 \delta|^a + |\alpha_3 \gamma + 2\alpha_4 \delta|^a + |2\alpha_5 \gamma + \alpha_6 \delta|^a - 2(\bar{\sigma}/\sigma)^a = 0 \quad (324)$$

The loading for uniaxial (RD and TD) and biaxial stress states can be characterized by the two deviatoric stress components, $s_x = \gamma\sigma$ and $s_y = \delta\sigma$.

$$\begin{cases} F_{0,90,b} = \phi - 2(\bar{\sigma}/\sigma_{0,90,b})^a = 0 \\ G_{0,90,b} = q_x \frac{\partial \phi}{\partial s_{xx}} - q_y \frac{\partial \phi}{\partial s_{yy}} = 0 \end{cases} \quad (3-25)$$

where s_{ij} denote the deviatoric stresses, and γ , δ , q_x and q_y are given in Table 3.1 based on the stress state.

Table 3.1. The definition of γ , δ , q_x , q_y parameters in uniaxial RD, TD and biaxial conditions

	γ	δ	q_x	q_y
RD (0°)	2/3	-1/3	$1 - r_0$	$2 + r_0$
TD (90°)	-1/3	2/3	$2 + r_{90}$	$1 - r_{90}$
Biaxial	-1/3	-1/3	$1 + 2r_b$	$2 + r_b$

Coefficients α_1 to α_6 can be determined by solving the system of equations (3-25), expressed in terms of the uniaxial (RD, TD) and biaxial stress states. The remaining coefficients, α_7 and α_8 are obtained from data points in the diagonal direction (σ_{45} , r_{45}).

$$\left\{ \begin{array}{l} F_{45} = \left| \frac{\sqrt{K_2'^2 + 4\alpha_7^2}}{2} \right|^a + \left| \frac{3K_1'' - \sqrt{K_2''^2 + 4\alpha_8^2}}{4} \right|^a + \left| \frac{3K_1'' + \sqrt{K_2''^2 + 4\alpha_8^2}}{4} \right|^a - 2 \left(\frac{\bar{\sigma}}{\sigma_{45}} \right)^a = 0 \\ G_{45} = \frac{\partial \phi}{\partial \sigma_{xx}} + \frac{\partial \phi}{\partial \sigma_{yy}} - \frac{2a}{(1 + r_{45})} (\bar{\sigma}/\sigma_{45})^a = 0 \end{array} \right. \quad (3-26)$$

where K_2' , K_1'' and K_2'' are defined as

$$K_2' = \frac{\alpha_1 - \alpha_2}{3}, \quad K_1'' = \frac{2\alpha_5 + \alpha_6 + \alpha_3 + 2\alpha_4}{9}, \quad K_2'' = \frac{2\alpha_5 + \alpha_6 - \alpha_3 - 2\alpha_4}{3} \quad (3-27)$$

The equation G_{45} is quite large when derived and expanded, so for the sake of brevity, the details are not presented here. Using the Newton-Raphson method, α_1 to α_8 can be determined by solving eight equations (3-25 and (3-26) simultaneously.

3.1.6 Barlat 2005 (Yld2004-18p)

Barlat et al. (2005) proposed another advanced yield function (Yld2004-18p) for a 3D stress state based on two linear transformations, by expanding on the core of Yld2000-2d. Due to the large amount of experimental data required for the calibration, this function is able to accurately capture the anisotropy behaviour of a variety of materials. The main

advantage of this model is its ability to describe the out-of-plane (through-thickness) anisotropy of sheet metals.

$$\begin{aligned} \phi = & |S'_1 - S''_1|^a + |S'_1 - S''_2|^a + |S'_1 - S''_3|^a + |S'_2 - S''_1|^a + |S'_2 - S''_2|^a + |S'_2 - S''_3|^a \\ & + |S'_3 - S''_1|^a + |S'_3 - S''_2|^a + |S'_3 - S''_3|^a - 4\bar{\sigma}^a = 0 \end{aligned} \quad (3-28)$$

where $S'i$ and $S''j$ are the principal stresses of two linear transformations (\mathbf{s}' and \mathbf{s}'') of the Cauchy stress tensor ($\boldsymbol{\sigma}$).

$$\begin{cases} \mathbf{s}' = \mathbf{C}'\mathbf{T}\boldsymbol{\sigma} = \mathbf{L}'\boldsymbol{\sigma} \\ \mathbf{s}'' = \mathbf{C}''\mathbf{T}\boldsymbol{\sigma} = \mathbf{L}''\boldsymbol{\sigma} \end{cases} \quad (3-29)$$

where \mathbf{C}' and \mathbf{C}'' are the two linear transformation matrices incorporating the anisotropy coefficients, and \mathbf{T} is the transformation matrix of the Cauchy stress to its deviatoric components.

$$\begin{aligned} \mathbf{C}' = & \begin{bmatrix} 0 & -c'_{12} & -c'_{13} & 0 & 0 & 0 \\ -c'_{21} & 0 & -c'_{23} & 0 & 0 & 0 \\ -c'_{31} & -c'_{32} & 0 & 0 & 0 & 0 \\ 0 & 0 & 0 & c'_{44} & 0 & 0 \\ 0 & 0 & 0 & 0 & c'_{55} & 0 \\ 0 & 0 & 0 & 0 & 0 & c'_{66} \end{bmatrix}, \\ \mathbf{C}'' = & \begin{bmatrix} 0 & -c''_{12} & -c''_{13} & 0 & 0 & 0 \\ -c''_{21} & 0 & -c''_{23} & 0 & 0 & 0 \\ -c''_{31} & -c''_{32} & 0 & 0 & 0 & 0 \\ 0 & 0 & 0 & c''_{44} & 0 & 0 \\ 0 & 0 & 0 & 0 & c''_{55} & 0 \\ 0 & 0 & 0 & 0 & 0 & c''_{66} \end{bmatrix}, \quad \mathbf{T} = \frac{1}{3} \begin{bmatrix} 2 & -1 & -1 & 0 & 0 & 0 \\ -1 & 2 & -1 & 0 & 0 & 0 \\ -1 & -1 & 2 & 0 & 0 & 0 \\ 0 & 0 & 0 & 3 & 0 & 0 \\ 0 & 0 & 0 & 0 & 3 & 0 \\ 0 & 0 & 0 & 0 & 0 & 3 \end{bmatrix} \end{aligned} \quad (3-30)$$

3.1.6.1 Calibration procedure

The two linear transformations provide a total of 18 coefficients to describe the material anisotropy. When all the coefficients are equal to one and the exponent a is equal to 2, Yld2004-18p reduces to the von Mises isotropic yield function. For determination of all the coefficients, seven uniaxial flow stresses and the corresponding r-

values are required in 15 degree increments relative to the rolling direction, the biaxial flow stress and the corresponding r-value, and four extra input data characterizing the out-of-plane material behaviour (two uniaxial and two simple-shear flow stresses) are required. Generally, crystal plasticity simulations are used to determine out-of-plane characteristics (Barlat et al., 2005). In order to determine the anisotropy coefficients, an error function is minimized.

$$E(C'_{ij}, C''_{ij}) = \sum_{p,q} \left[w_p \left(\frac{\sigma_p^{pr}}{\sigma_p^{ex}} - 1 \right)^2 + w_q \left(\frac{r_q^{pr}}{r_q^{ex}} - 1 \right)^2 \right] \quad (3-31)$$

where p correlates with the number of available experimental flow stresses, from uniaxial, biaxial and/or simple-shear tests, and q correlates with the corresponding r-values. Also, the superscript denotes whether the corresponding value is experimental (ex) or predicted (pr). w_i represents the weight factor for each term in the error function. Due to the higher influence of flow stress in the material anisotropy behaviour compared to the r-values, applying different weight factors can lead to more accurate anisotropy coefficient determination. In this work, as recommended by Barlat et al. (2005), weight factors 1.0, 0.1 and 0.01 were used for the in-plane flow stresses, in-plane r-values and out-of-plane flow stresses, respectively.

Here, due to the unavailability of the crystallographic texture of materials, the out-of-plane flow stresses were set to their isotropic values, where $\sigma/\bar{\sigma} = 1$ for uniaxial tension and $\tau/\bar{\sigma} = 1/(1 + 2^{a-1})^{1/a}$ for simple-shear. Also, due to a lack of experimental data for the uniaxial tension tests at 15° increments from the rolling direction, Yld2000-2d (Barlat et al., 2003) was used to generate flow stresses and corresponding r-values for the 15°, 30°, 60° and 75° directions. Similar to the Yld2000-2d calibration procedure, Yld96 function was used to determine the biaxial r-value, r_b . Analytical flow stress and r-value formulations for in-plane and out-of-plane conditions are presented in detail in Appendix-1.

3.2 Experimental work

3.2.1 Sheet materials

Three sheet materials that are widely used in the automotive industry, DP600 (dual phase steel), TRIP780 (transformation induced plasticity steel) and AA5182-O (aluminum alloy) each with a nominal thickness of 1.5 mm were selected for this study. The steel sheets (DP600 and TRIP780) were supplied by ArcelorMittal and AA5182-O sheets were supplied by Novelis. The chemical compositions of the three materials are given in Table 3.1.

Table 3.1. Chemical composition of DP600, TRIP780, and AA5182-O

	C (%)	Si (%)	S (%)	S_n (%)	P (%)	Mn (%)	Ni (%)	Cr (%)	Mo (%)
DP600	0.107	0.175	0.001	0.004	0.011	1.5	0.015	0.18	0.21
	C (%)	Si (%)	S (%)	S_n (%)	P (%)	Mn (%)	Ni (%)	Cr (%)	Mo (%)
TRIP780	0.21	0.05	0.002	<0.02	0.01	1.74	<0.02	0.2	<0.02
	Mg (%)	Mn (%)	Fe (%)	Si (%)	Cr (%)	Cu (%)	Ti (%)		
AA5182-O	4.5	0.35	0.3	0.11	0.045	0.09	0.04		

DP600 exhibits relatively high strength and good formability due to the presence of martensite and ferrite. Generally, the strength of DP steels is related to the amount of martensite, while the ductility is due to the presence of ferrite. In addition to the ferrite and martensite, TRIP780 contains bainite and retained austenite. During plastic deformation, the retained austenite gradually transforms to martensite, resulting in high work hardening. Van Slycken et al. (2007) showed that in the high strain rate regime, the bainite and ferrite phases can be considered strain rate independent compared to the austenite which shows a positive strain-rate sensitivity.

3.2.2 Quasi-static, intermediate and high strain rate tests

In order to quantify the effect of strain rate on the flow stress and determine the material constants in different yield functions w.r.t. strain rate, the mechanical responses of the three materials were obtained under uniaxial and biaxial tension conditions at different strain rates. The quasi-static biaxial flow stresses were obtained from the work of Al-Nasser (2009) for DP600 and TRIP780, and from the work of Etienne Combaz of Novelis Switzerland-SA for AA5182-O (interested readers are referred to Chapter-4 of Al-Nasser, 2009 for details on the biaxial testing procedure and analysis). The validity of the biaxial flow stresses from the aforementioned literatures was determined by examining the uniaxial flow stress results in the rolling direction. The uniaxial flow stress results showed very good agreement with the experimental results for the materials studied in this work, and were therefore deemed to also adequately represent the biaxial flow stress of these materials. Uniaxial flow stresses and the corresponding r -values were obtained from uniaxial tension tests in three different material orientations (RD, DD and TD) for a wide range of strain rates ($0.001, 0.1, 1.0, 10, 100$ and 1000 s^{-1}) at room temperature. The experimental uniaxial tension tests were performed by Professor Worswick's research team at the University of Waterloo. A specimen based on the standard ASTM-E8 specification was used for testing at strain rates below 1 s^{-1} , while a miniature "dog-bone" shaped specimen was used for testing above 1 s^{-1} (Figure 3-1). Experimental work by Smerd et al. (2005) for aluminum alloys and by Bardelcik et al. (2012) for high strength steels confirmed that the flow stress obtained from ASTM specimens is in good agreement with the flow stress from miniature dog-bone specimens. It should be noted that all the specimens were machined in three different material orientations (RD, DD and TD) and were tested in the as-received condition.

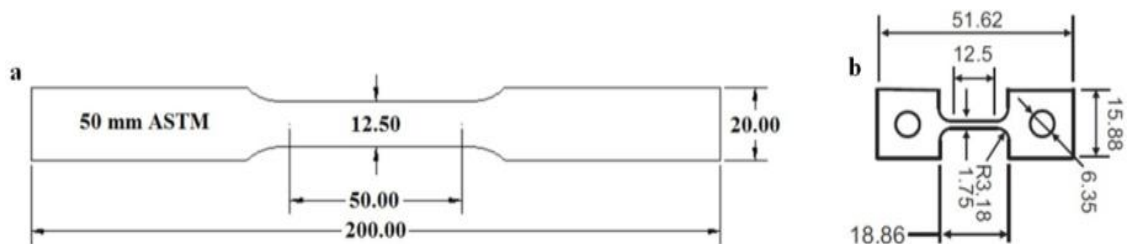


Figure 3-1 a) ASTM-E8 and b) miniature dog-bone specimen geometries (mm),
(Rahmaan et al., 2014)

A closed-loop Instron servo-hydraulic testing machine, a hydraulic intermediate strain rate (HISR) testing machine and a split Hopkinson pressure bar (SHPB) apparatus were used to perform uniaxial tests at strain rates of $0.001 - 1 \text{ s}^{-1}$, 10 and 100 s^{-1} and approximately 1000 s^{-1} , respectively. For strain rates below 1 s^{-1} a biaxial extensometer was used to measure the longitudinal and width strains in the gauge of the specimens, and the Digital Image Correlation (DIC) technique using high speed digital cameras was used for higher strain rates.

3.2.3 Experimental results

3.2.3.1 Flow stress

Figure 3-2-Figure 3-4 show the engineering stress-strain curves for DP600, TRIP780, and AA5182-O measured in the rolling (RD), diagonal (DD), and transverse (TD) directions at various strain rates. Three to five tests were repeated for each case and the average results are presented here. Also, Figure 3-5-Figure 3-7 show the true stress versus effective plastic strain (also known as flow stress) curves are calculated from the measured engineering stress-strain data, for DP600, TRIP780, and AA5182-O in RD, DD, and TD at various strain rates.

Results show a significant strain-rate sensitivity of DP600 and TRIP780 in all three orientations (RD, DD, and TD), which can be attributed to the large volume fraction of ferrite in these steels (Kim et al., 2013). In contrast, AA5182-O exhibits almost zero or even a small negative strain-rate sensitivity, which is attributed to the dynamic strain aging effect of aluminum alloys (Smerd et al., 2005). A general conclusion about the relationship between work hardening and strain rate is not possible due to the variance of this phenomenon amongst the materials and orientations.

Figure 3-8 shows the biaxial true stress versus effective plastic strain curves for DP600, TRIP780, and AA5182-O. The biaxial flow stress is remarkably different from the uniaxial flow stress in the RD for DP600 and TRIP780. The dissimilarity of the biaxial results demonstrates how important the biaxial flow stress is in order to accurately predict the flow surfaces of the steel sheets. Comparison of the biaxial and uniaxial flow

stresses of AA5182-O shows almost the same mechanical response of material in these two stress states, i.e., the biaxial flow stress can be assumed to be the same as the flow stress in uniaxial tension in RD for AA5182-O.

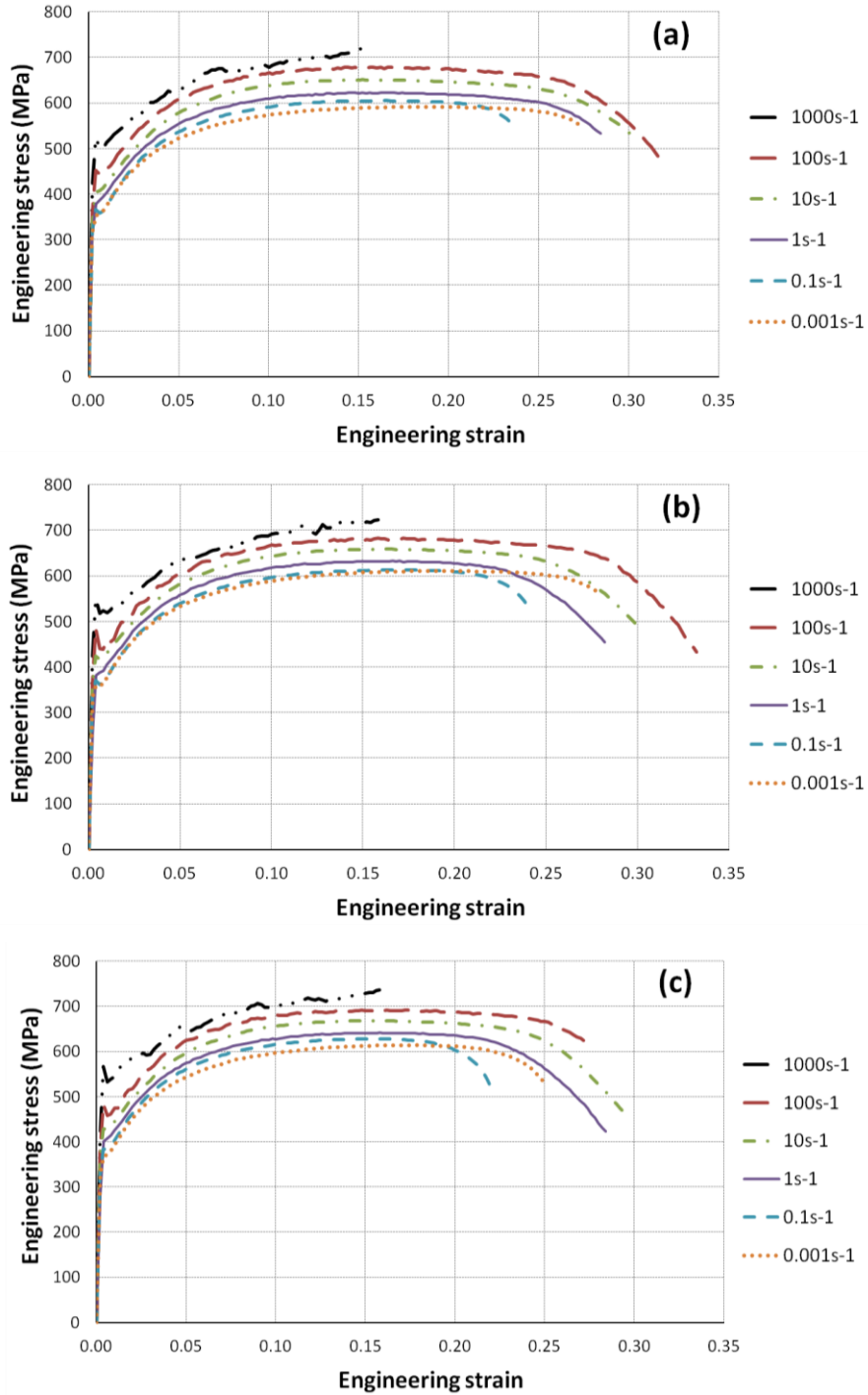


Figure 3-2 DP600 engineering stress-strain curves at various strain rates in; a) RD b) DD c) TD

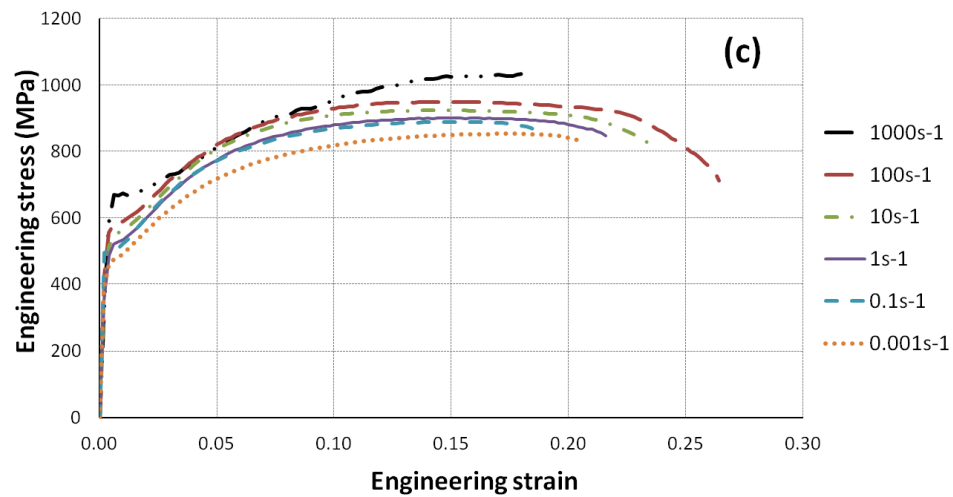
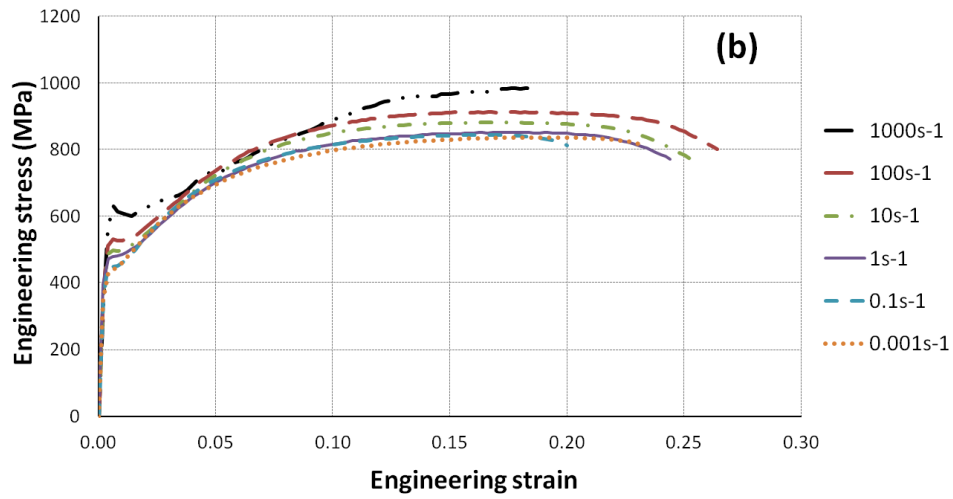
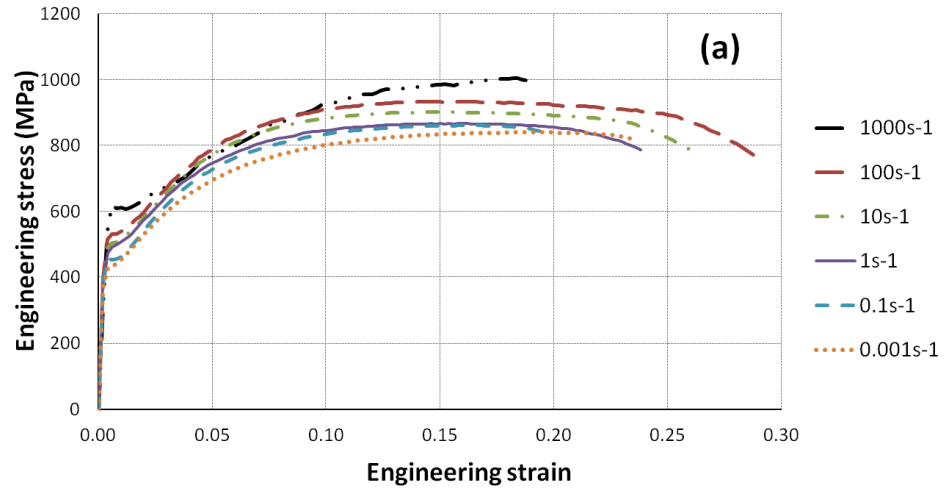


Figure 3-3 TRIP780 engineering stress-strain curves at various strain rates in; a) RD b) DD c) TD

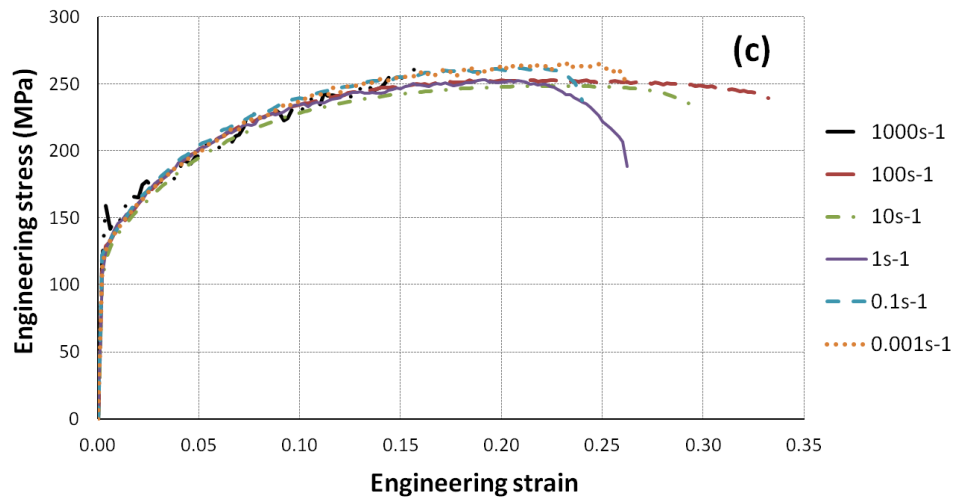
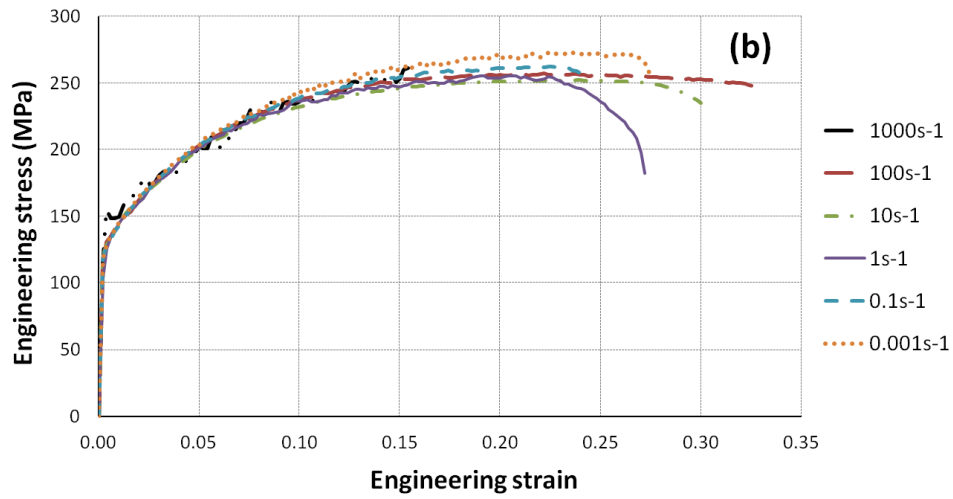
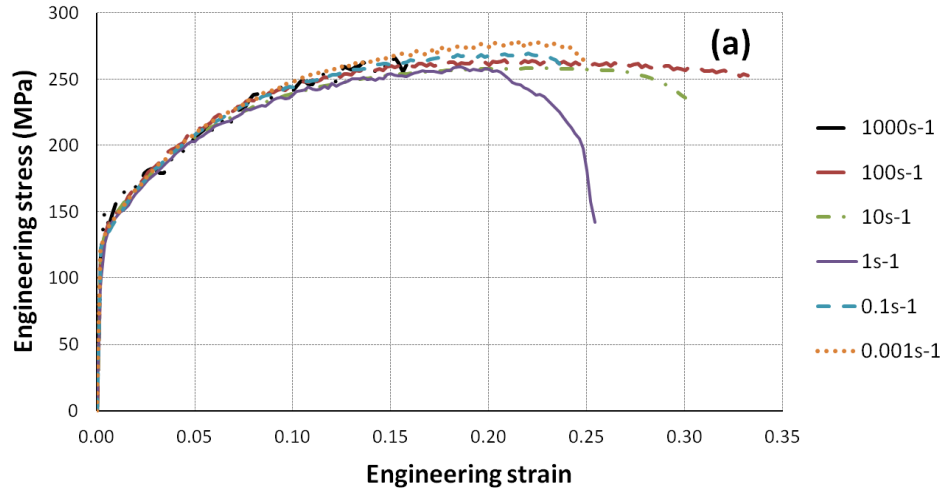


Figure 3-4 AA5182-O engineering stress-strain curves at various strain rates in; a) RD b) DD c) TD

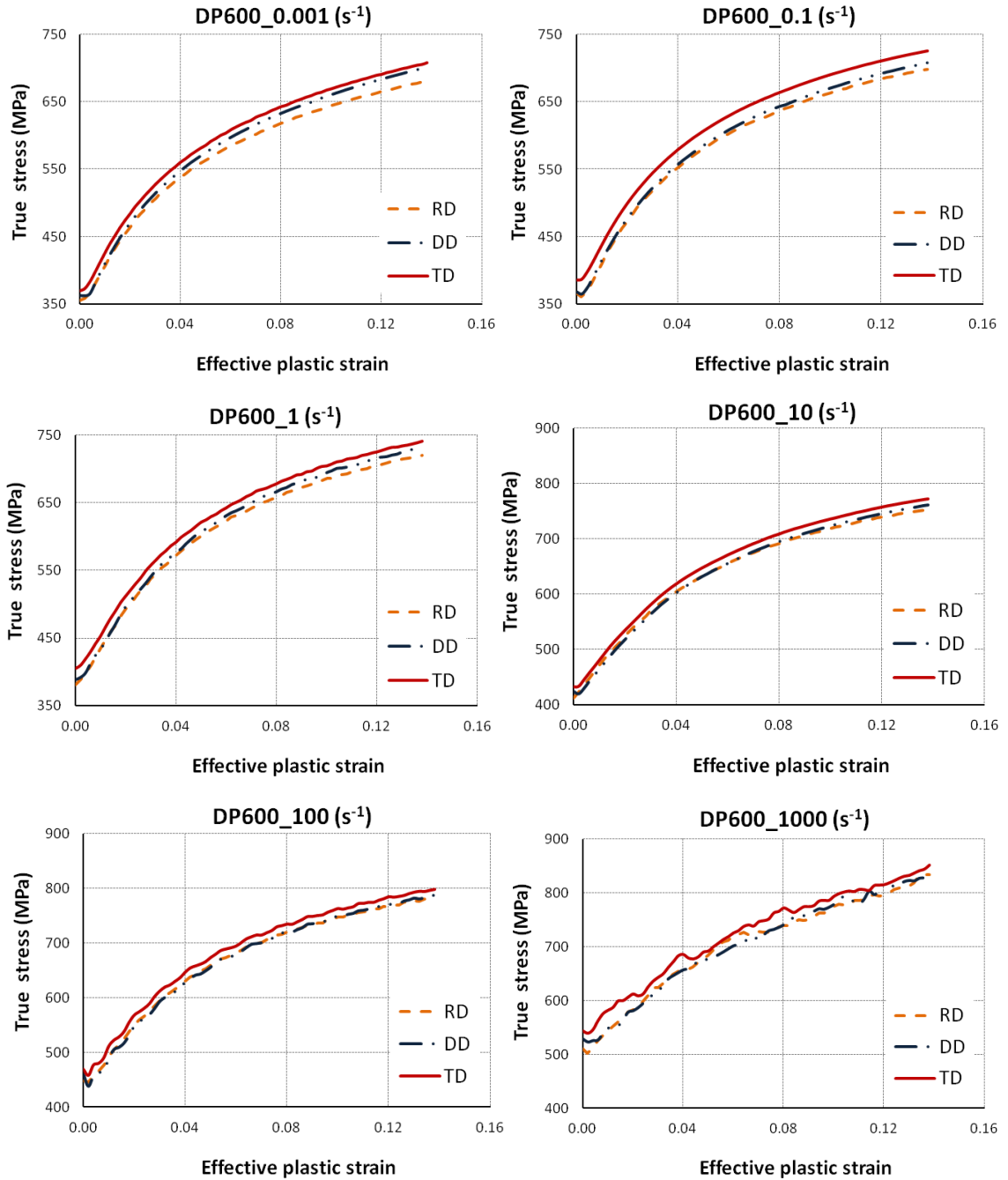


Figure 3-5 DP600 true stress versus effective plastic strain curves obtained at various strain rates in RD, DD, and TD

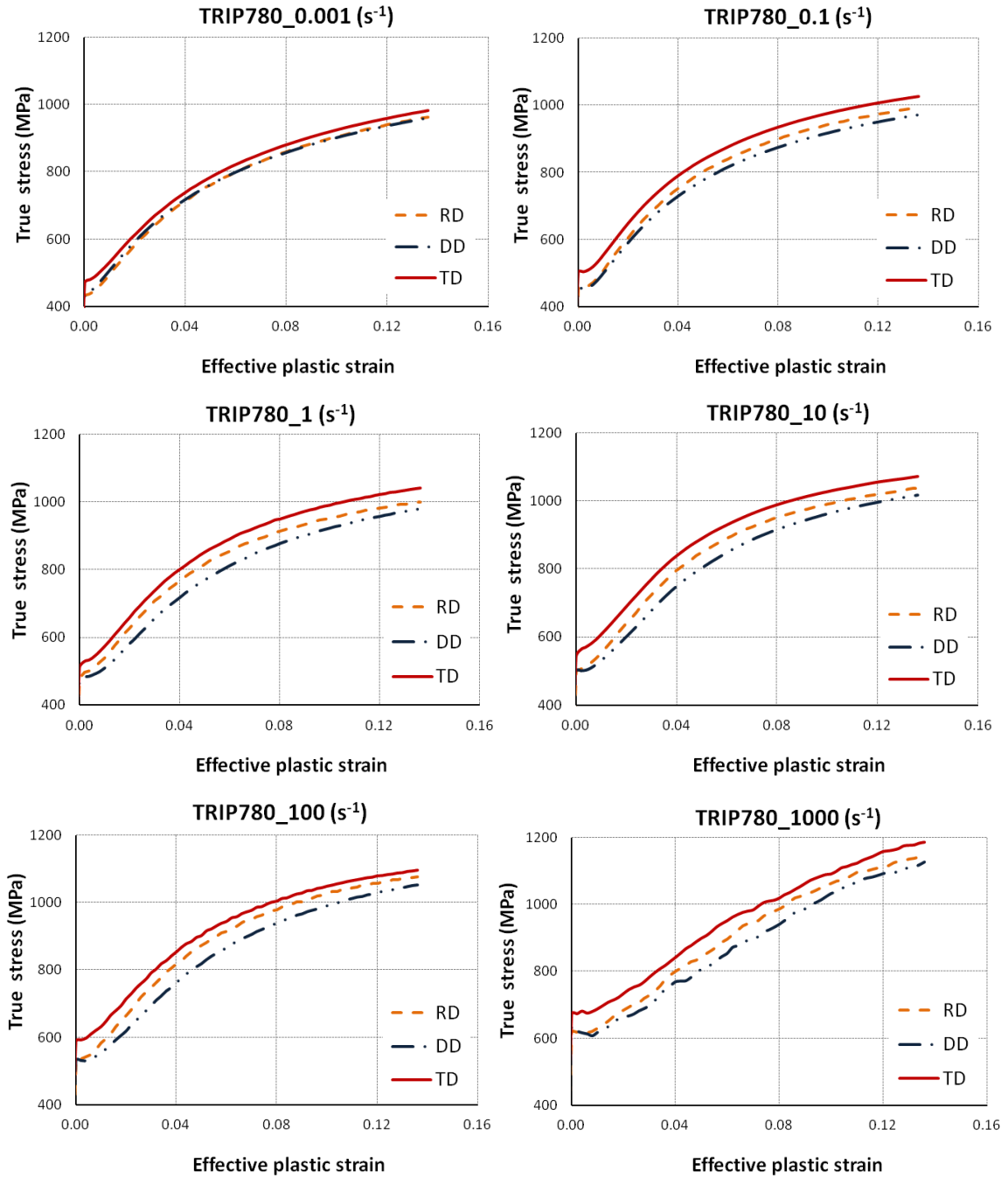


Figure 3-6. TRIP780 true stress versus effective plastic strain curves obtained at various strain rates in RD, DD, and TD

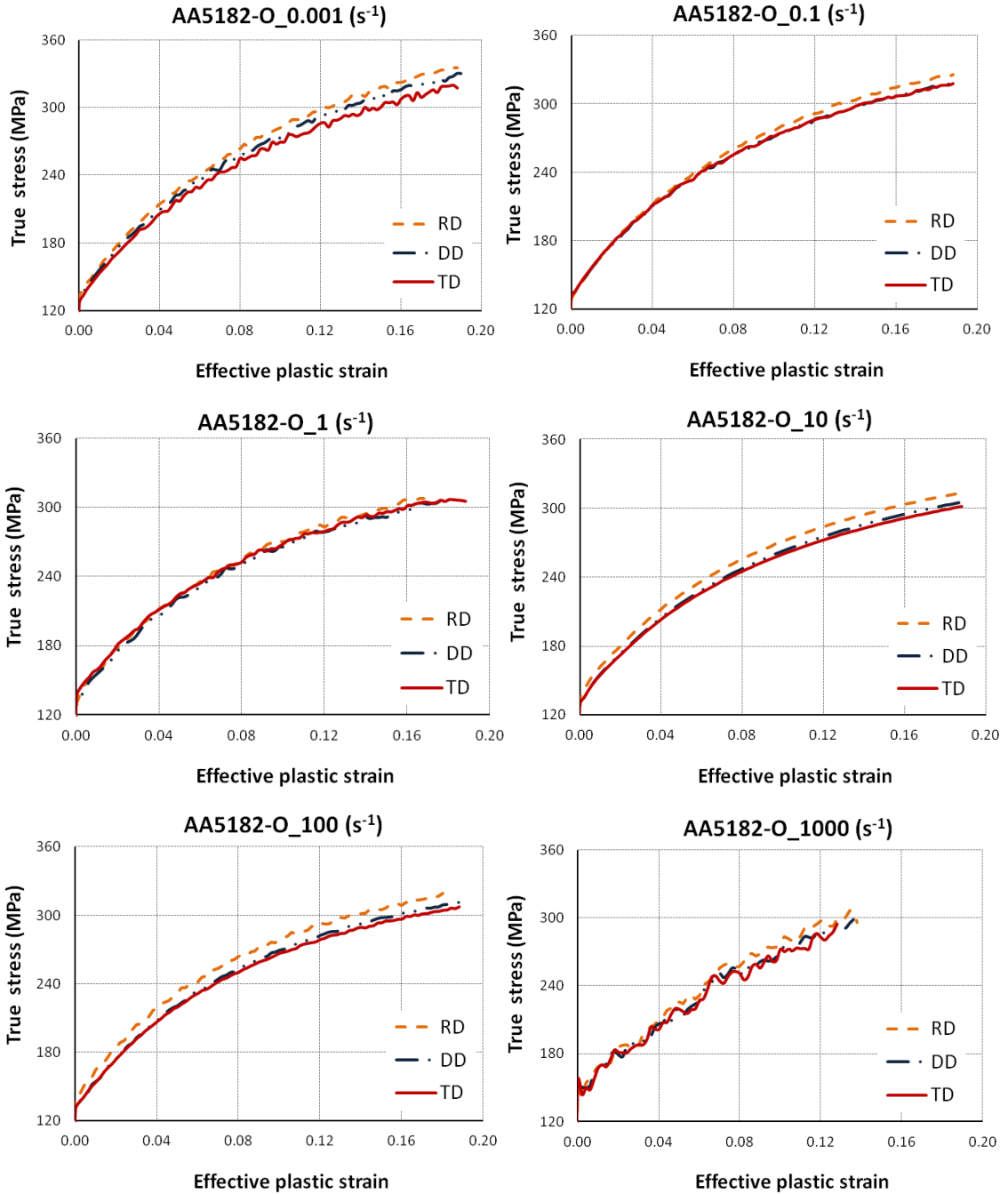


Figure 3-7. AA5182-O true stress versus effective plastic strain curves obtained at various strain rates in RD, DD, and TD

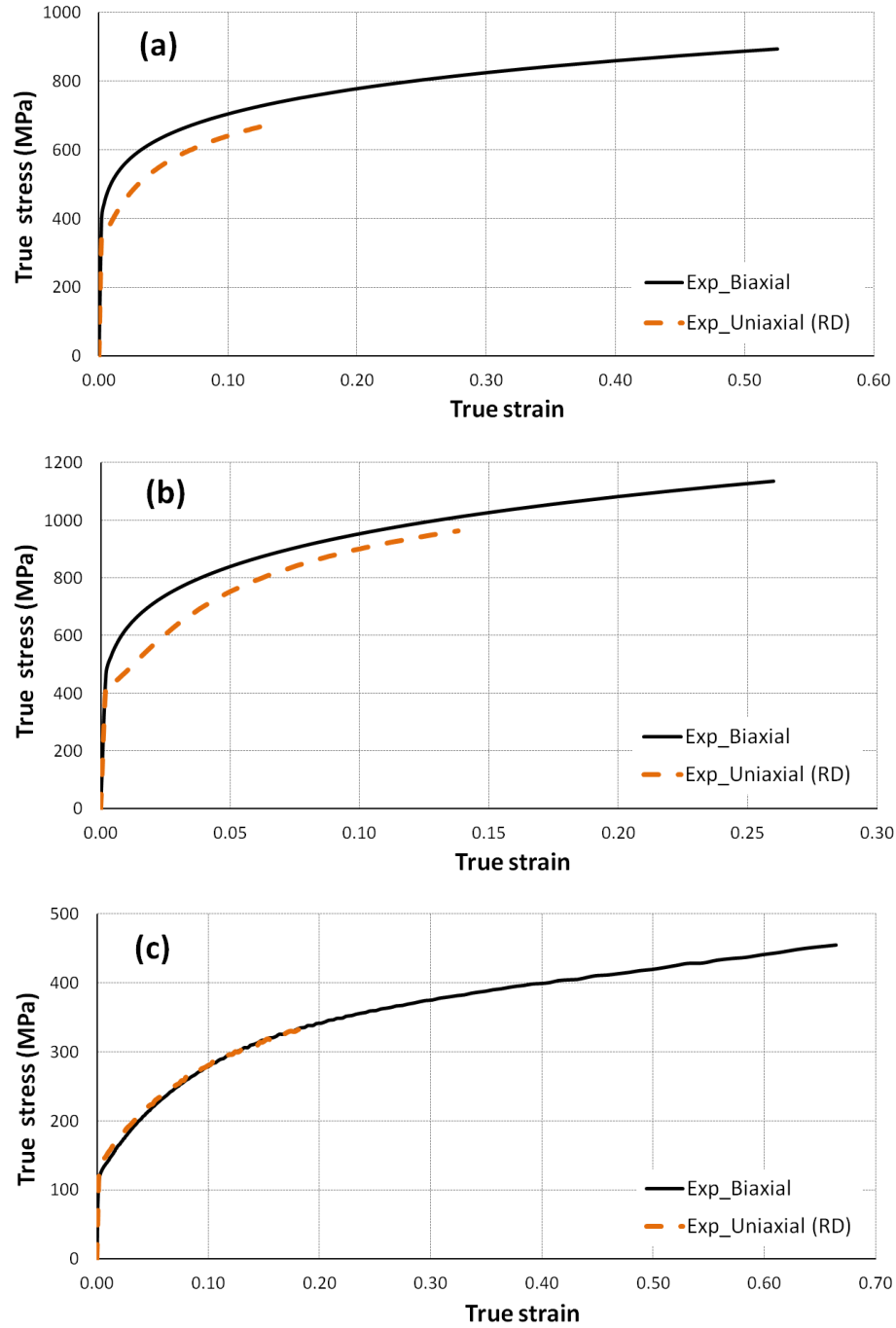


Figure 3-8. Biaxial and uniaxial true stress versus effective plastic strain curves at 0.001 s^{-1} for a) DP600 b) TRIP780 c) AA5182-O

3.2.3.2 r-value

In addition to the flow stresses, r-values in different orientations are required to comprehensively describe the material anisotropy. In order to determine the r-values, the engineering elongation in the longitudinal and width directions of specimens was measured, using a biaxial extensometer (below 1 s^{-1}) and the DIC technique (above 1 s^{-1}). By converting the measurements to true strains and applying the volume constancy assumption, the r-value can be calculated as follows

$$r = -\frac{\varepsilon_w/\varepsilon_l}{1 + \varepsilon_w/\varepsilon_l} \quad (3-32)$$

where ε_w and ε_l are the width and longitudinal true strains, respectively. The ratio $\varepsilon_w/\varepsilon_l$ is the slope of the first-order equation fitted to the width versus longitudinal true strain curve over a certain strain range. Therefore, in materials with small variations of width strain versus longitudinal strain, the r-value that is calculated based on Eq. (3-32) provides a good representation of the material anisotropy. In this work, this approach was used to calculate the r-values of DP600, TRIP780, and AA5182-O in the rolling (RD), diagonal (DD), and transverse (TD) directions over a range of strains between 0.01 and 0.14 (Figure 3-9-Figure 3-11).

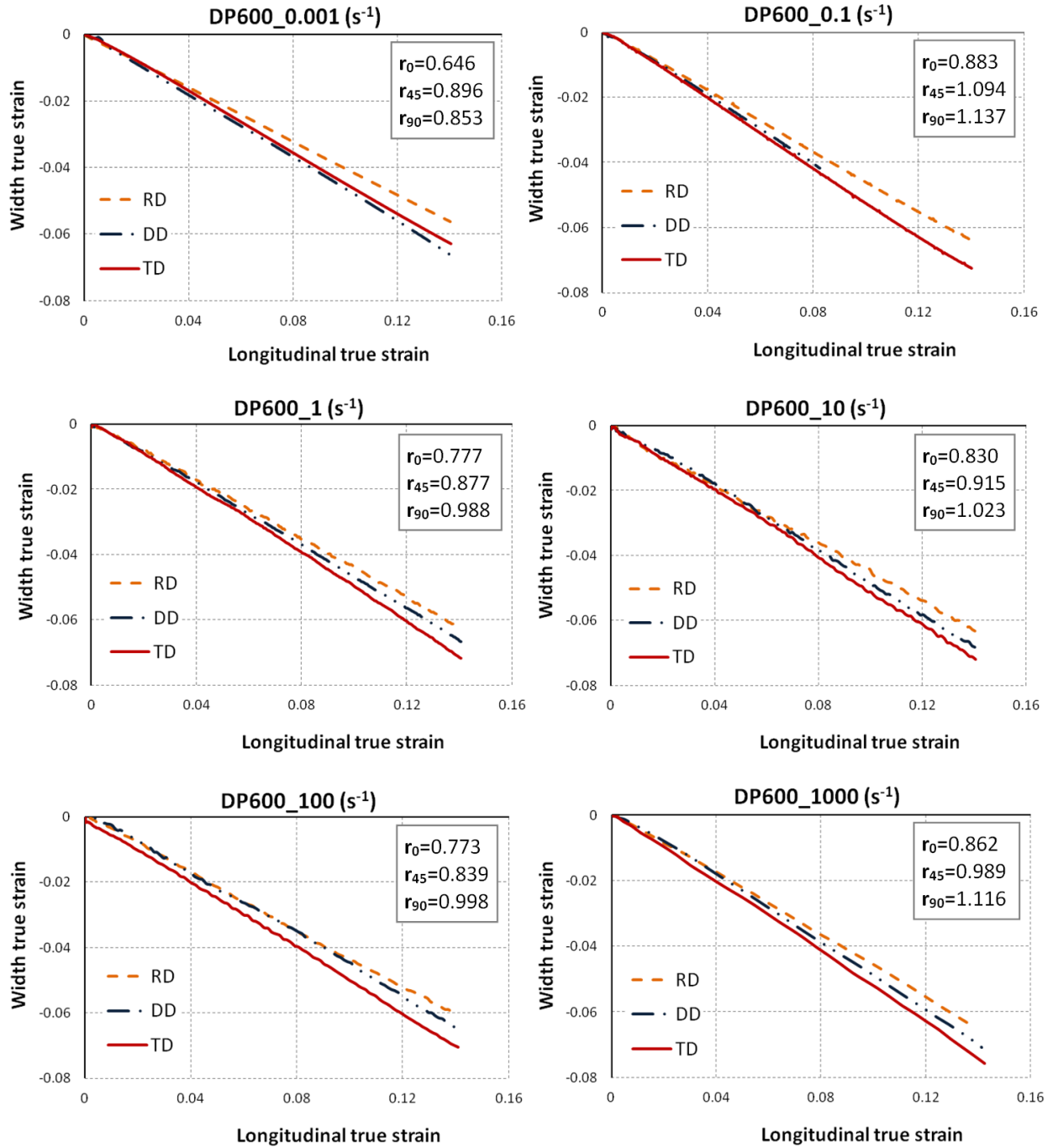


Figure 3-9. DP600 width versus longitudinal true strain curves obtained from uniaxial tension in RD, DD and TD at various strain rates

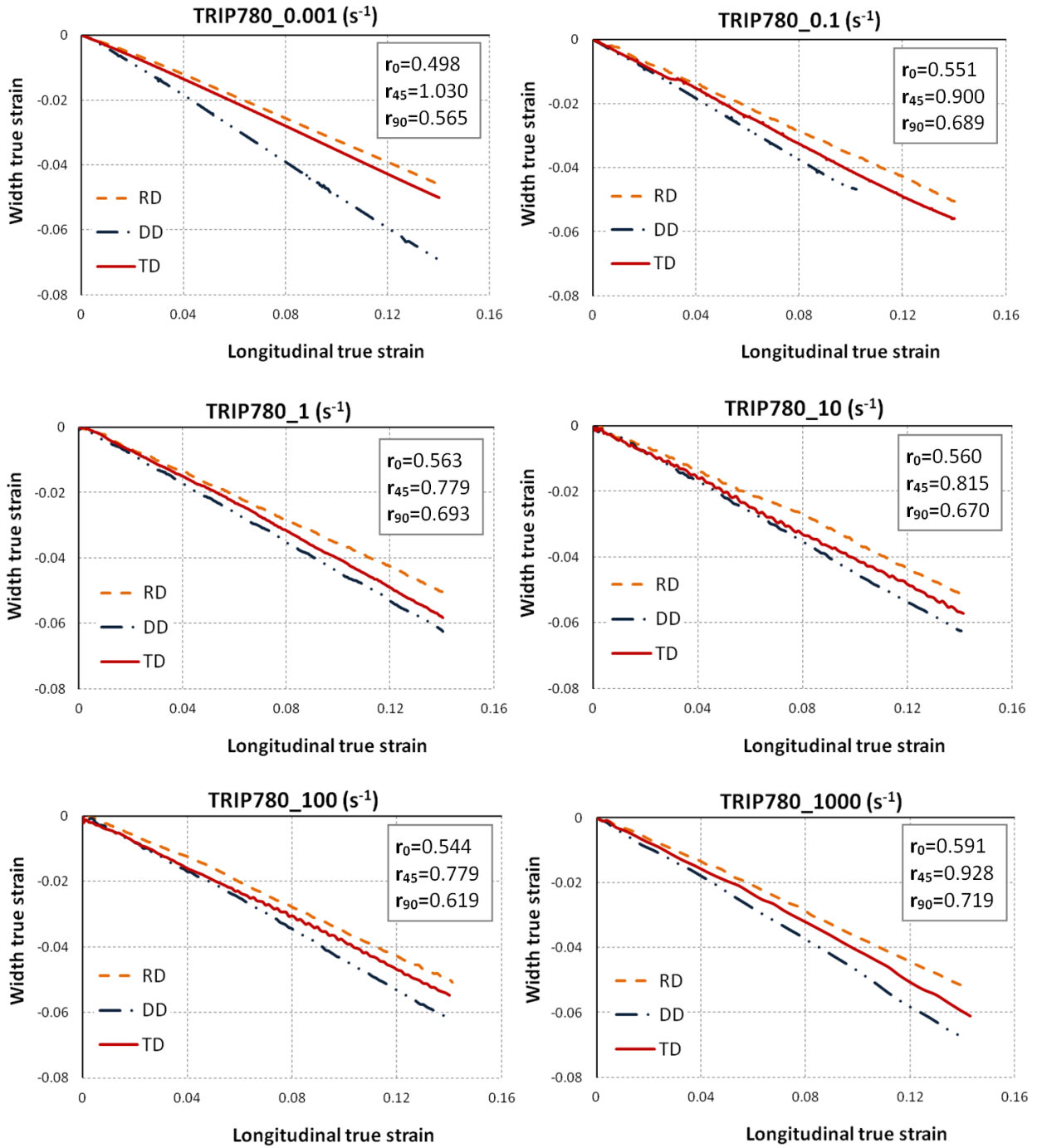


Figure 3-10. TRIP780 width versus longitudinal true strain curves obtained from uniaxial tension in RD, DD and TD at various strain rates

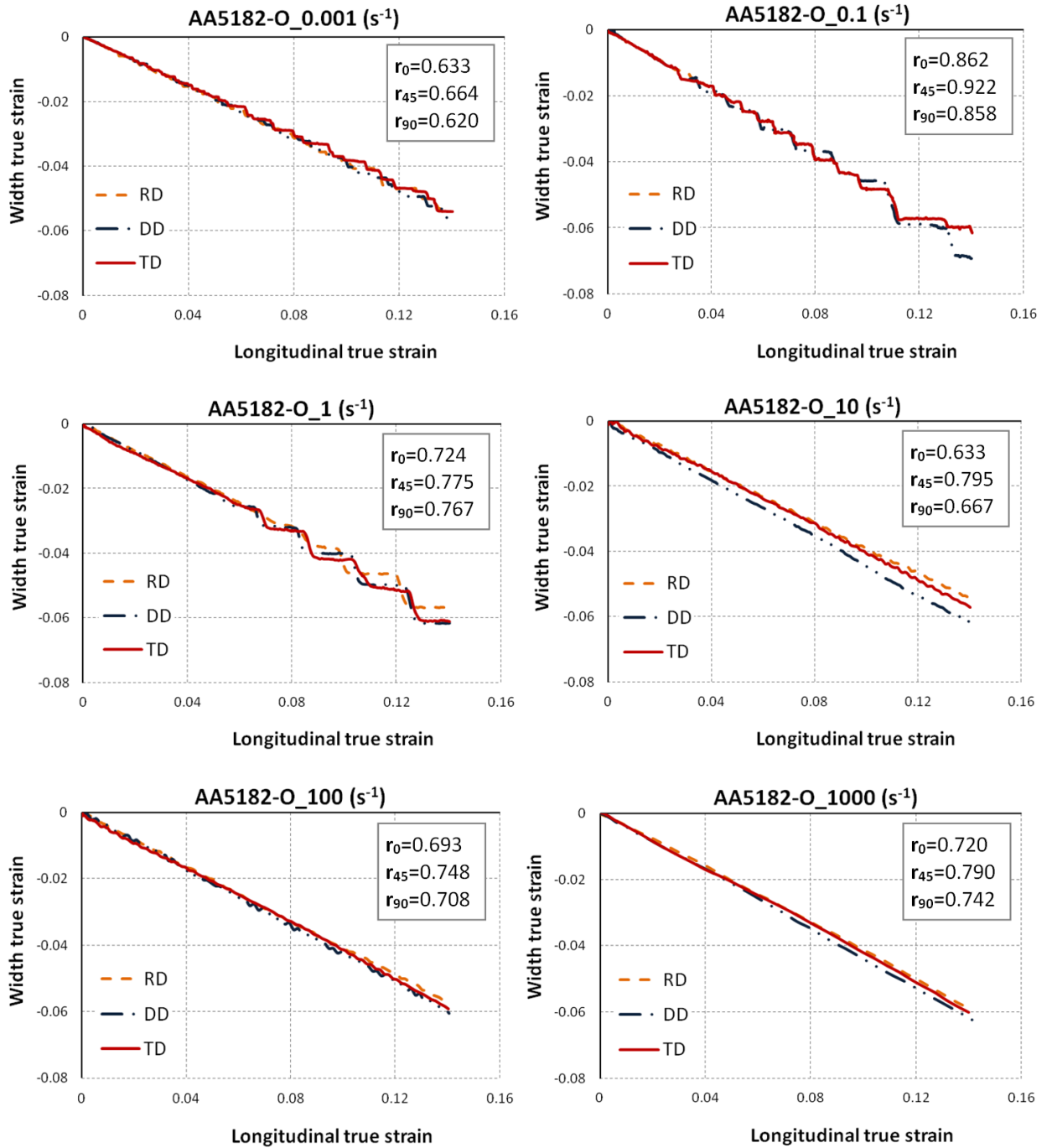


Figure 3-11. AA5182-O width versus longitudinal true strain curves obtained from uniaxial tension in RD, DD and TD at various strain rates

3.3 Anisotropy coefficients

In rate-dependent forming processes, in addition to the size of the flow surface (that is determined by a rate-dependent hardening model), the shape of the flow surface can change due to variations in the flow stresses and r-values. In order to investigate the effect of strain rate on the material flow behaviour, the yield function anisotropy coefficients must be determined for each effective strain rate and not merely for the initial quasi-static condition. In this work, based on procedures that will be discussed in the next sections, the anisotropy coefficients for several yield functions have been obtained at various strain rates (0.001, 0.1, 1.0, 10, 100, and 1000 s^{-1}). The set of anisotropy coefficients of a yield function for each effective strain rate can be used to update the anisotropy coefficients according to strain rate. This may improve the accuracy of FE simulations of strain rate sensitive processes, such as EHF.

3.3.1 Evolution of flow stresses

Anisotropy coefficients are independent of strain in yield functions, therefore it is necessary to select certain flow stresses (as input data) for uniaxial and biaxial stress states so as to calibrate the anisotropy coefficients at certain effective plastic strain (or plastic work). In many publications, the initial yield stresses (at zero plastic strain) are selected as the input data, which can cause substantial inaccuracy because in this region of the stress-strain curve the slope is the steepest. In addition, a large amount of plastic strain is expected in sheet metal forming simulations, but the initial yield stress is only associated with a very small plastic strain (almost zero) and anisotropy coefficients calibrated at or near zero plastic strain may not reflect the anisotropy of the material at higher strain levels. For these reasons, the flow stresses have been selected based on a comprehensive investigation of the normalized flow stress variation in the uniaxial (DD, TD) and biaxial (Biax) conditions for each corresponding strain rate.

Figure 3-12-Figure 3-14 show the normalized flow curves for DP600, TRIP780, and AA5182-O, in which the uniaxial flow stress in the diagonal direction (DD), the uniaxial flow stress in the transverse direction (TD) and the biaxial flow stress (Biax), were normalized relative to the flow stress in the rolling direction (RD) at each corresponding

strain rate. It should be noted that the flow stress in the rolling direction is extrapolated up to large strain values (greater than the ultimate effective plastic strain value obtained from the uniaxial test) using the biaxial flow stress data. The biaxial flow stress data was used to calculate a more accurate work hardening exponent rather than simply extrapolating the uniaxial flow curve based on a hardening model such as a power-law, JC, KHL, or etc. It should be noted that due to the limitations of existing experimental testing equipment and procedures, there is no reliable testing method to obtain experimental biaxial flow stress at intermediate and high strain rates. Here, an analytical procedure was used to obtain flow curves for all three materials, the details of which are discussed in the next section. In Figures 3-12 to 3-14, the expression “Exp_Biax” is related to the experimental biaxial flow stress which is only available at 0.001 s^{-1} , and the expression “Cal_Biax” represents the biaxial flow stresses at $0.1, 1.0, 10, 100, \text{ and } 1000 \text{ s}^{-1}$, that were calculated using this analytical procedure. In this work, since large strain values (greater than 0.3 or even 0.4 true major strain) are anticipated from the EHF simulations, the flow stresses for uniaxial and biaxial cases were combined to achieve a more accurate and general material flow behaviour prediction.

The normalized flow curves for DP600 (Figure 3-12) show significant variations in both the diagonal and transverse directions (DD and TD) for small strain values, which emphasizes that the initial yield stress is not a good representation of the anisotropic behaviour of DP600 at larger strain values. At almost all strain rates, the DD and TD uniaxial normalized flow stresses for DP600 saturate in the strain range from 0.1 to 0.14. Therefore, the DD and TD normalized flow stresses were selected based on average values in this range, and these are given in Table 3.2. Also, the normalized biaxial flow stress (Biax) for DP600 was selected based on an average value in the strain range from 0.2 to 0.5, since the normalized biaxial flow stresses saturate at strains above 0.2 for almost all strain rates. This procedure of identifying the normalized flow stress is very reasonable, since larger strains are obtained in biaxial EHF simulations compared to the uniaxial and plane-strain conditions. In addition, the procedure of selecting flow stresses at higher strain values gives a more precise indication of material flow behaviour because

the flow stress obtained from the biaxial bulge test (at 0.001 s^{-1}) is not as accurate for small strain values.

The normalized flow curves for TRIP780 (Figure 3-13) show that the DD and TD uniaxial normalized flow stresses do not vary significantly after 0.1 strain for almost all strain rates. Therefore, similar to DP600, the normalized flow stresses for the uniaxial cases were obtained based on average values in the strain range from 0.1 to 0.14, and are given in Table 3.9. The TRIP780 biaxial normalized flow stresses saturate after effective plastic strains of 0.1 for almost all strain rates. Therefore, the Biax normalized value is calculated based on the average value in the strain range 0.15 to 0.25. Similar to DP600, the significant variation in the normalized flow stresses at low strains shows that selecting the initial yield stress as an input value to calibrate anisotropy coefficients is a very inaccurate approach to describe the material anisotropy behaviour of TRIP780. In contrast with DP600 and TRIP780, a significant variation can be seen in the normalized DD and TD uniaxial flow stresses of AA5182-O at almost all strain rates (Figure 3-14). These variations make it difficult to decide which strain range to consider in order to select the normalized flow stresses that best describe the anisotropy of AA5182-O. In order to maintain consistency with the other materials, the DD and TD normalized flow stresses were calculated based on average values for the strain range of 0.1-0.18. The normalized biaxial flow stresses of AA5182-O were calculated based on average values in the strain range of 0.2-0.6, due to the very small variation after 0.2 strain in almost all strain rates.

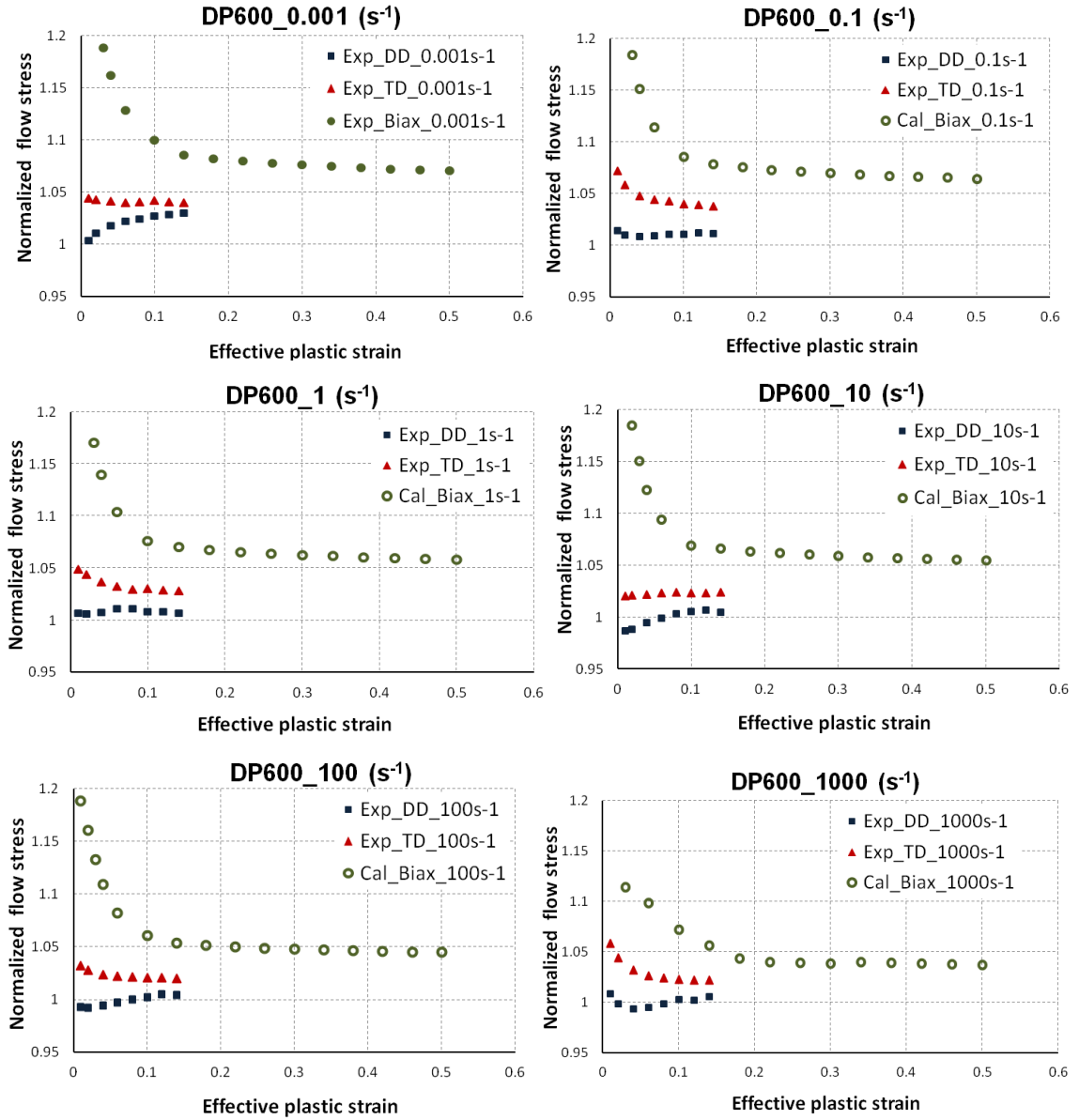


Figure 3-12. Evolution of DP600 uniaxial and biaxial flow stresses normalized to the uniaxial flow stress in the RD at various strain rates

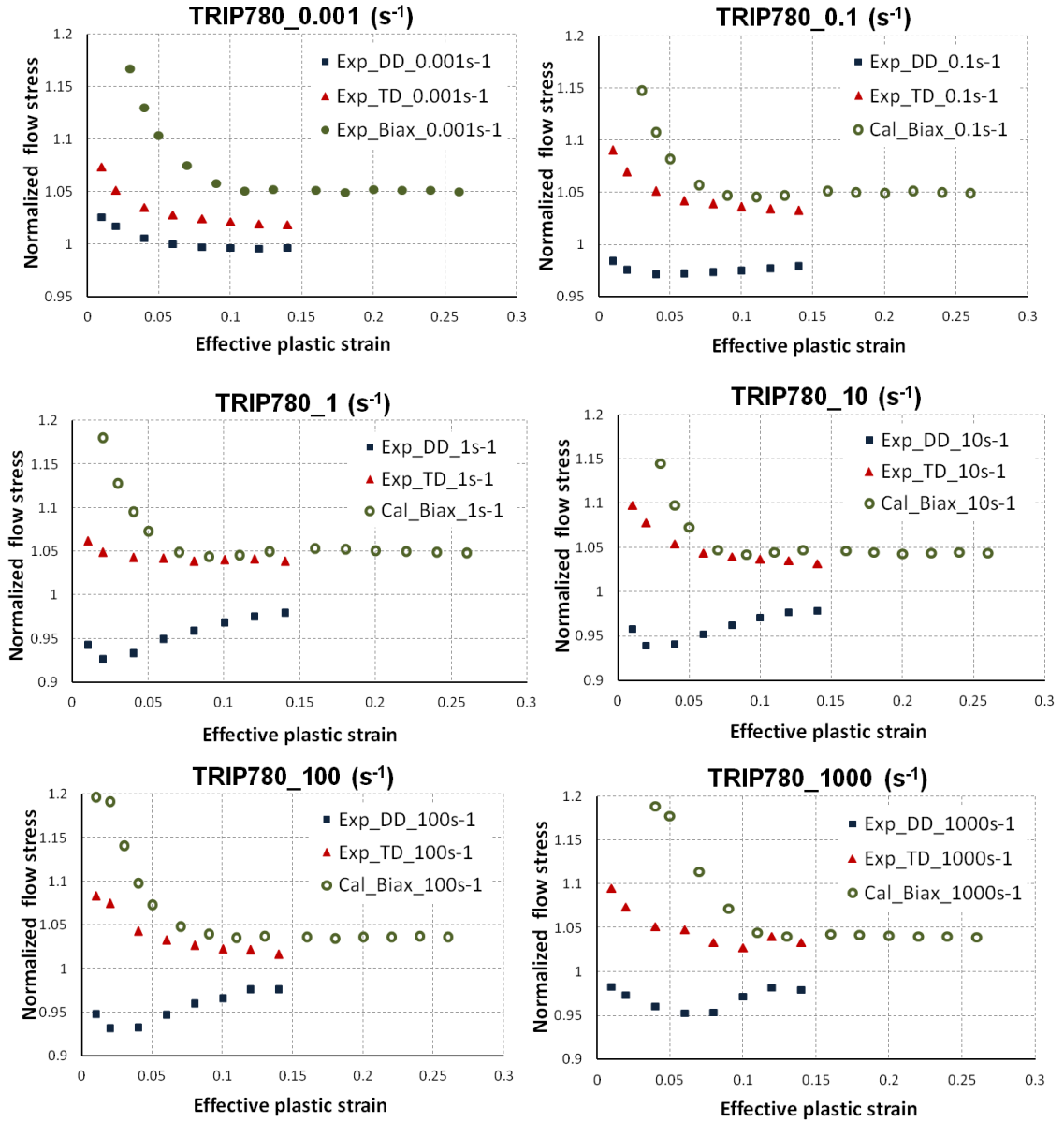


Figure 3-13. Evolution of TRIP780 uniaxial and biaxial flow stresses normalized to the uniaxial flow stress in the RD at various strain rates

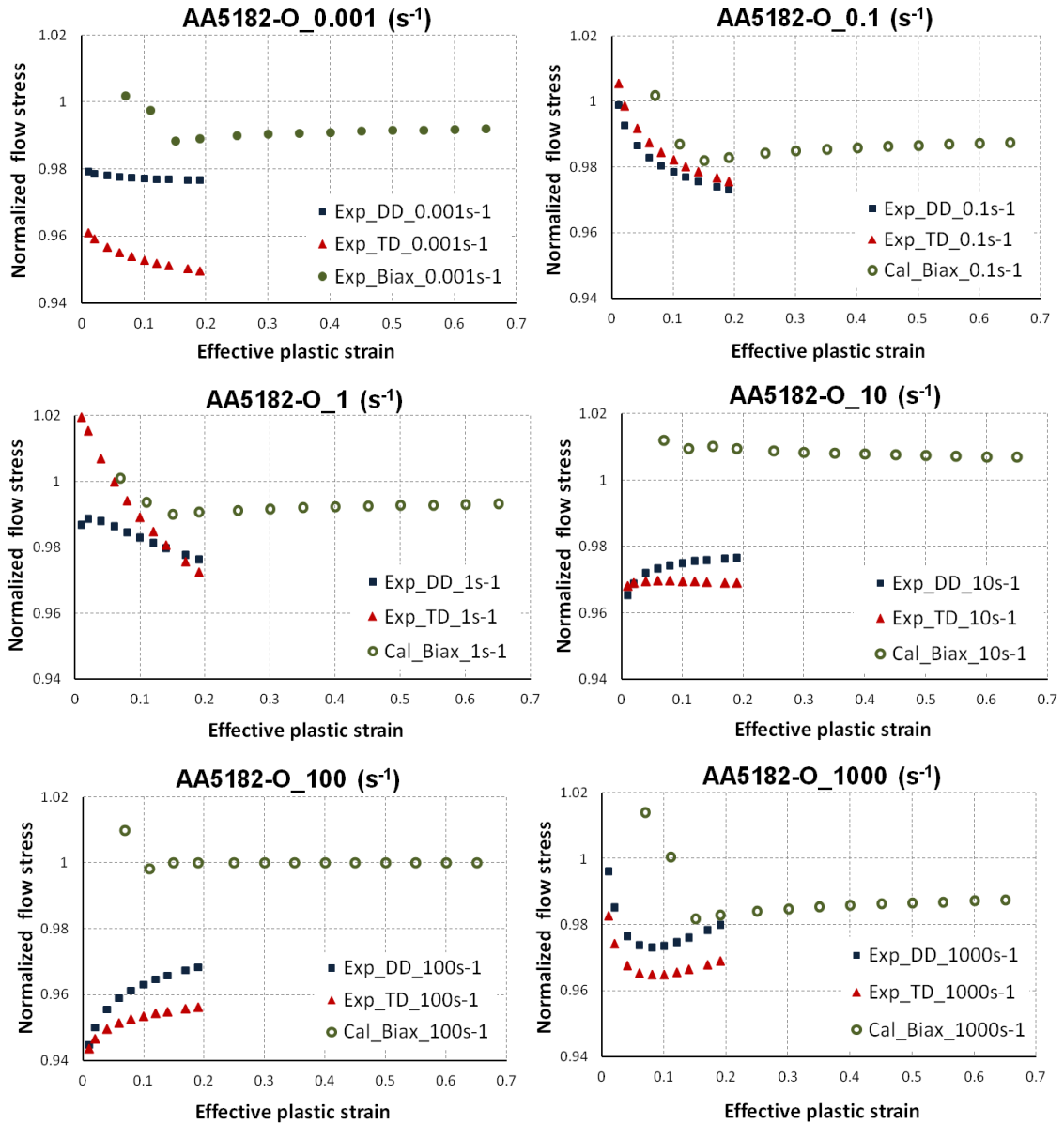


Figure 3-14. Evolution of AA5182-O uniaxial and biaxial flow stresses normalized to the uniaxial flow stress in the RD at various strain rates

3.3.2 Calculation of biaxial flow stress at higher strain rates

To describe the changes in material anisotropy w.r.t. strain rates, the uniaxial flow stresses and r -values were obtained from uniaxial tension tests in three different orientations for a wide range of strain rates ($0.001 - 1000 \text{ s}^{-1}$). In addition, the biaxial flow stresses at various strain rates are also needed for the calibration of most yield functions. As mentioned before, due to the limitations of existing testing methods, it is only possible to obtain experimental biaxial flow stress in the quasi-static condition (0.001 s^{-1}). In order to obtain the missing data, an analytical procedure was developed to calculate the biaxial flow stresses for strain rates of 0.1, 1, 10, 100 and 1000 s^{-1} .

In this procedure, it was assumed that the calculated biaxial flow curves (Cal_Biax) at strain rates greater than 0.001 s^{-1} , have the same trend as the experimental biaxial flow curve (Exp_Biax) at 0.001 s^{-1} . Based on this assumption, the biaxial flow curve only shifts up or down with changes in strain rate, depending upon the strain-rate sensitivity of the material. The strain-rate sensitivity of the material was calculated based on a superposition approach applied to the uniaxial flow stresses in the RD, DD, and TD. In this approach, it was assumed that the average strain rate sensitivity in uniaxial tension in RD, DD and TD, is a good representation of the biaxial strain-rate sensitivity.

Figure 3-15a shows the DP600 uniaxial flow stresses in the RD, DD, and TD at 0.1, 0.12, and 0.14 strains and for each strain rate. These points were selected because the DP600 uniaxial flow stresses are almost saturated for strains above 0.1 (Figure 3-12). By calculating an average flow stress for the three material orientations, a single point is obtained for each strain rate (Figure 3-15b). Then, by fitting a polynomial equation to the average points and shifting the fitted curve upwards so that it passes through the experimental biaxial flow stress point at 0.001 s^{-1} , a trend can be obtained which represents the strain-rate sensitivity of the biaxial flow stress. Figure 3-15b shows a substantial increase in the average strain-rate sensitivity rate of DP600 above 1 s^{-1} . Also, Figure 3-15c shows the calculated biaxial (Cal_Biax) flow curves of DP600 at various strain rates. The calculated biaxial flow curves were calculated based on the average

strain-rate sensitivity and assuming no changes in the biaxial work hardening rate with increasing strain rates.

The same procedure was used to calculate the biaxial flow curves for TRIP780 at strain rates of 0.1, 1, 10, 100 and 1000 s^{-1} . Figure 3-16b shows the average strain-rate sensitivity of TRIP780 is lower compared to DP600. The calculated biaxial (Cal_Biax) flow curves of TRIP780 for various strain rates are shown in Figure 3-16c. The biaxial flow curves for AA5182-O (Figure 3-17) show that the near-zero strain-rate sensitivity of AA5182-O in the uniaxial condition results in an almost strain rate independency of the biaxial flow stress. Many previous researchers have reported zero or a small negative strain-rate sensitivity for AA5182-O based on solely the uniaxial flow stress in the rolling direction, whereas this work presents a more general and reliable conclusion.

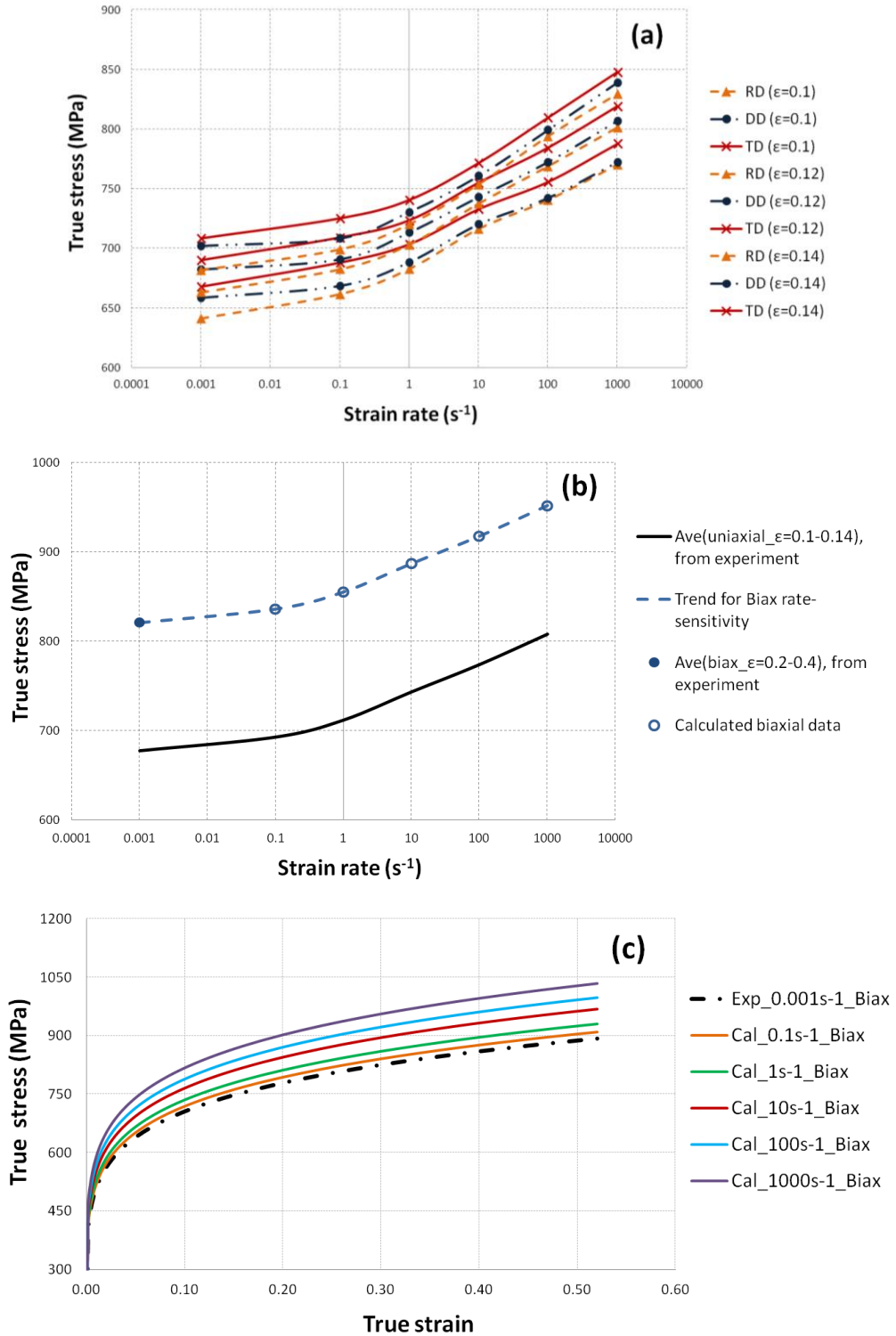


Figure 3-15. Calculation of DP600 biaxial flow curves at strain rates of 0.1, 1, 10, 100 and 1000 s^{-1}

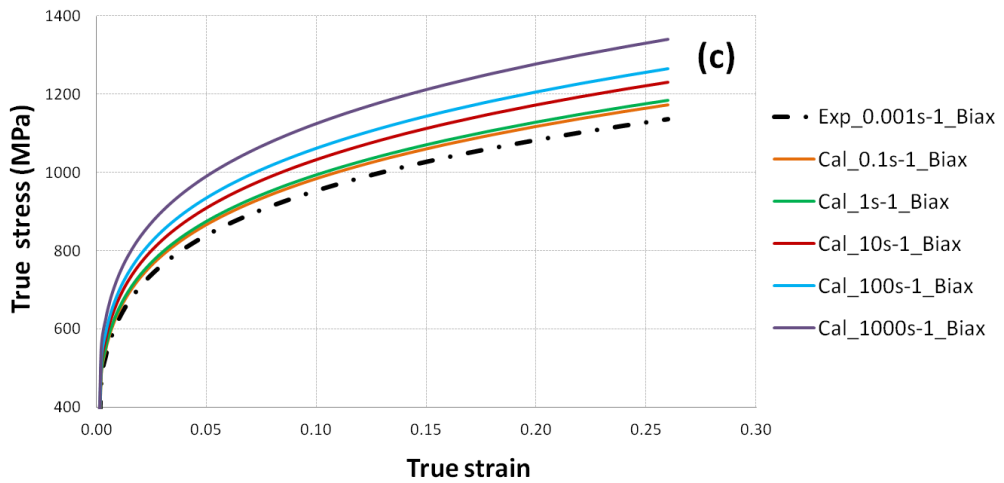
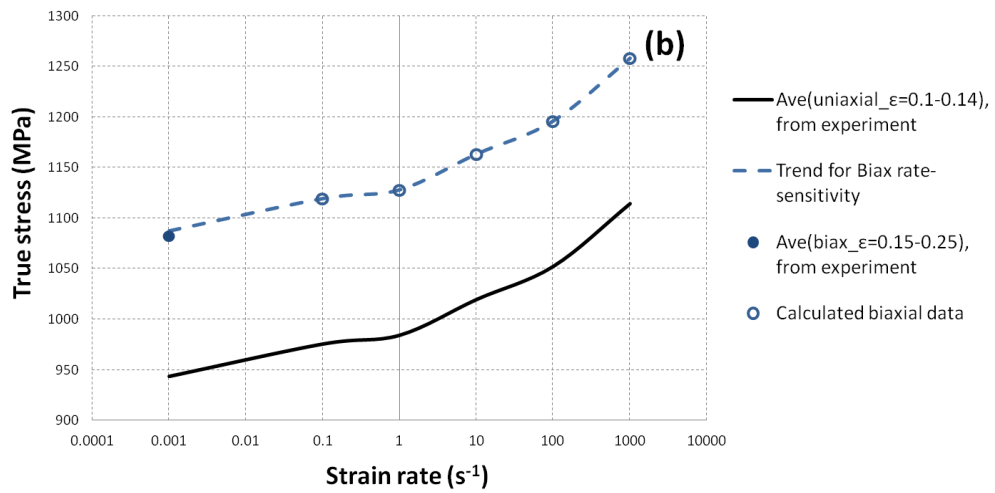
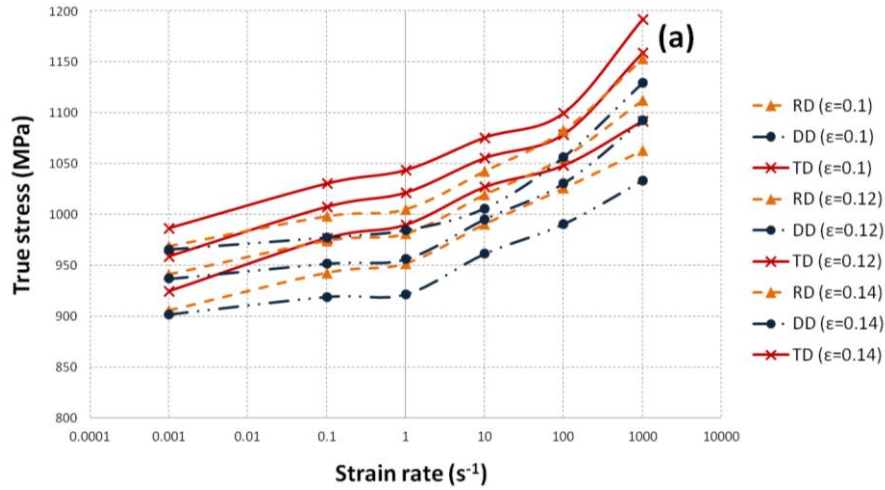


Figure 3-16. Calculation of TRIP780 biaxial flow curves at strain rates of 0.1, 1, 10, 100 and 1000 s^{-1}

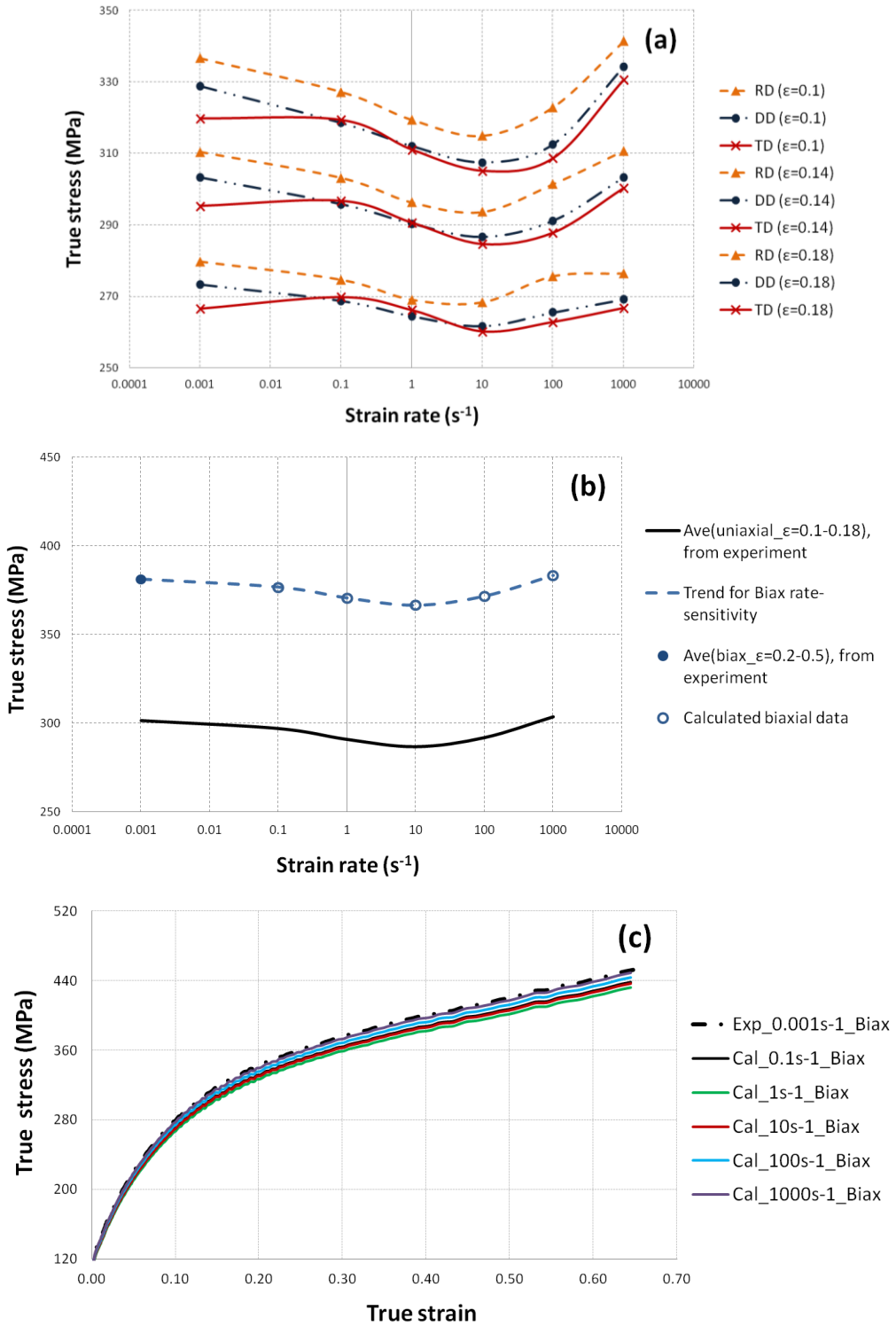


Figure 3-17. Calculation of AA5182-O biaxial flow curves at strain rates of 0.1, 1, 10, 100 and 1000 s^{-1}

3.3.3 Determination of anisotropy coefficients for different yield functions

Figure 3-18 shows the variations of the normalized flow stress (discussed in section 3.3.1) and r-value (discussed in section 3.2.3.2) w.r.t. strain rate for DP600. Results show a continuous decrease in the flow stresses with increasing strain rate. i.e., the anisotropy effect associated with the flow stress decreases with strain rate. The r-value variations show oscillations with the same trend in different orientations (r_0, r_{45}, r_{90}). Figure 3-19 shows the variations in the flow stresses and r-values of TRIP780 w.r.t. strain rate. The trends do not show a smooth or continuous increase or decrease w.r.t. strain rate, which makes it difficult to draw a conclusion on the effect of strain rate on the anisotropy behaviour of TRIP780. Compared to DP600 and TRIP780, AA5182-O shows greater oscillations in the normalized flow stresses w.r.t. strain rate (Figure 3-20). Also, similar to DP600, a similar trend for r_0, r_{45} and r_{90} can be observed in AA5182-O.

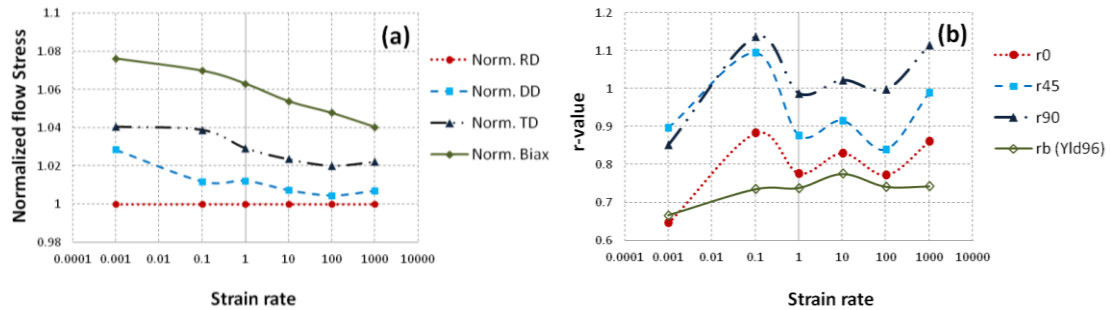


Figure 3-18. Anisotropy variation w.r.t. strain rate for DP600;
a) normalized flow stress b) r-value

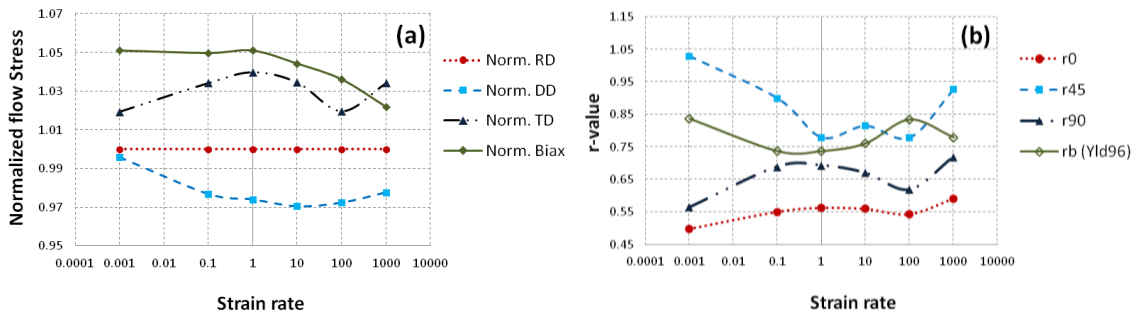


Figure 3-19. Anisotropy variation w.r.t. strain rate for TRIP780;
a) normalized flow stress b) r-value

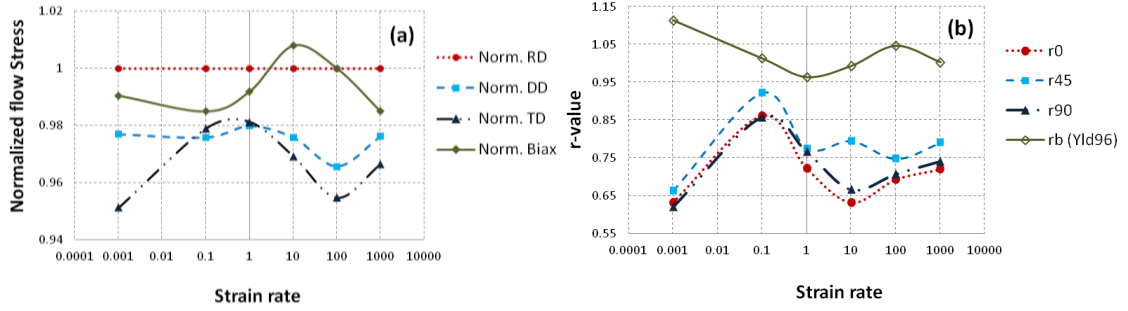


Figure 3-20. Anisotropy variation w.r.t. strain rate for AA5182-O;
a) normalized flow stress b) r-value

The input data required to calibrate the different anisotropic yield functions and the corresponding anisotropy coefficients for DP600, TRIP780, and AA5182-O at various strain rates are given in Tables 3.2-3.8, Tables 3.9-3.15, and Tables 3.16-3.22, respectively. It should be emphasized that for all cases, the flow stresses are normalized w.r.t. the uniaxial flow stress in the RD ($\bar{\sigma} = \sigma_0$).

Table 3.2. DP600 input data at various strain rates; for calibration of different yield functions

DP600	Strain rate (s ⁻¹)					
	0.001	0.1	1	10	100	1000
Experimental data						
$\sigma_0/\bar{\sigma}$	1.000	1.000	1.000	1.000	1.000	1.000
$\sigma_{45}/\bar{\sigma}$	1.028	1.012	1.012	1.007	1.004	1.007
$\sigma_{90}/\bar{\sigma}$	1.041	1.039	1.029	1.024	1.020	1.022
$\sigma_b/\bar{\sigma}$	1.076	1.070	1.063	1.054	1.048	1.040
r_0	0.646	0.883	0.777	0.830	0.773	0.862
r_{45}	0.896	1.094	0.877	0.915	0.839	0.989
r_{90}	0.853	1.137	0.988	1.023	0.998	1.116
Calculated from Yld2000-2d						
$\sigma_{15}/\bar{\sigma}$	1.005	1.001	1.001	1.000	1.000	1.000
$\sigma_{30}/\bar{\sigma}$	1.016	1.004	1.005	1.002	1.000	1.003
$\sigma_{60}/\bar{\sigma}$	1.036	1.023	1.020	1.014	1.011	1.013
$\sigma_{75}/\bar{\sigma}$	1.040	1.034	1.026	1.021	1.017	1.019
r_{15}	0.685	0.917	0.790	0.841	0.778	0.879
r_{30}	0.790	1.003	0.826	0.871	0.797	0.926
r_{60}	0.921	1.142	0.931	0.965	0.903	1.052
r_{75}	0.879	1.144	0.972	1.006	0.969	1.099
Calculated r_b from Yld96						
r_b (Yld96)	0.666	0.735	0.738	0.776	0.742	0.743

Table 3.3. Hill48 coefficients for DP600 at various strain rates

DP600	Strain rate (s ⁻¹)					
	0.001	0.1	1	10	100	1000
Hill48-r.value						
G	0.608	0.531	0.563	0.546	0.564	0.537
F	0.460	0.412	0.443	0.443	0.437	0.415
H	0.392	0.469	0.437	0.454	0.436	0.463
N	1.491	1.504	1.384	1.401	1.340	1.418
Hill48-stress						
G	0.470	0.473	0.470	0.473	0.475	0.484
F	0.393	0.400	0.414	0.427	0.436	0.440
H	0.530	0.527	0.530	0.527	0.525	0.516
N	1.460	1.517	1.510	1.521	1.527	1.511

Table 3.4. Hill90 coefficients for DP600 at various strain rates

DP600	Strain rate (s ⁻¹)					
	0.001	0.1	1	10	100	1000
Hill90-r.value						
m	1.804	1.912	1.782	1.819	1.771	1.902
a	-0.140	-0.126	-0.120	-0.104	-0.127	-0.129
b	-0.271	-0.183	-0.011	0.002	0.052	-0.030
Hill90-stress						
m	1.804	1.912	1.782	1.819	1.771	1.902
a	-0.069	-0.075	-0.048	-0.040	-0.032	-0.041
b	0.058	-0.055	-0.014	-0.030	-0.036	-0.030

Table 3.5. Barlat89 coefficients for DP600 at various strain rates (exponent $a = 6$)

DP600	Strain rate (s ⁻¹)					
	0.001	0.1	1	10	100	1000
Barlat89-r.value						
a	1.150	1.001	1.068	1.042	1.067	1.012
c	0.850	0.999	0.932	0.958	0.933	0.988
h	0.923	0.939	0.938	0.947	0.934	0.937
p	0.998	0.981	0.960	0.963	0.945	0.960
Barlat89-stress						
a	1.115	1.003	1.063	1.048	1.068	1.007
c	0.885	0.997	0.937	0.952	0.932	0.993
h	0.961	0.963	0.972	0.977	0.980	0.978
p	0.969	0.991	0.990	0.994	0.998	0.995

Table 3.6. Yld96 coefficients for DP600 at various strain rates (exponent $a = 6$)

DP600	Strain rate (s^{-1})					
	0.001	0.1	1	10	100	1000
c_1	0.767	0.837	0.828	0.860	0.871	0.911
c_2	0.782	0.885	0.841	0.869	0.852	0.903
c_3	1.006	1.023	1.020	1.022	1.018	1.015
c_6	0.888	0.968	0.965	0.980	0.985	0.988
α_x	2.55	1.52	1.82	1.57	1.56	1.21
α_y	3.4	1.73	2.28	1.92	2.15	1.63
α_{z0}	1	1	1	1	1	1
α_{z1}	1.52	1.12	0.98	0.96	0.89	0.978
Calculation of r_b from Yld96						
r_b (Yld96)	0.666	0.735	0.738	0.776	0.742	0.743

Table 3.7. Yld2000-2d coefficients for DP600 at various strain rates (exponent $a = 6$)

DP600	Strain rate (s^{-1})					
	0.001	0.1	1	10	100	1000
α_1	0.944	0.996	0.966	0.976	0.956	0.979
α_2	0.919	0.945	0.954	0.964	0.978	0.983
α_3	0.815	0.866	0.854	0.877	0.873	0.899
α_4	0.945	0.939	0.952	0.958	0.960	0.956
α_5	1.001	0.986	0.996	0.995	1.003	1.001
α_6	0.858	0.886	0.888	0.906	0.919	0.948
α_7	0.951	0.986	0.963	0.973	0.966	0.985
α_8	1.057	1.047	1.082	1.074	1.090	1.041

Table 3.8. Yld2004-18P coefficients for DP600 at various strain rates (exponent $a = 6$)

DP600	Strain rate (s^{-1})					
	0.001	0.1	1	10	100	1000
c'_{12}	0.765	0.898	1.305	1.072	1.286	0.832
c'_{13}	0.272	0.888	0.931	0.853	0.978	0.709
c'_{21}	0.889	1.185	0.998	0.853	0.777	1.407
c'_{23}	0.376	0.941	0.589	0.395	0.546	0.888
c'_{31}	1.058	1.026	0.921	0.805	-0.073	0.846
c'_{32}	0.901	0.723	1.159	0.892	1.039	0.991
c'_{44}	1.814	1.022	2.103	1.204	1.628	1.183
c'_{55}	1.445	1.165	1.585	1.156	1.478	1.089
c'_{66}	0.990	1.035	1.231	0.948	1.189	1.144
c''_{12}	0.944	0.836	0.329	0.952	0.192	0.713
c''_{13}	1.082	0.505	0.152	1.132	0.950	0.534
c''_{21}	1.054	0.879	0.822	0.930	0.696	0.846
c''_{23}	1.053	0.290	0.684	1.136	0.386	0.704
c''_{31}	0.980	1.222	1.296	1.042	1.214	1.515
c''_{32}	1.071	1.113	1.361	1.136	1.372	1.161
c''_{44}	1.272	0.790	0.979	1.287	1.832	0.616
c''_{55}	1.197	1.945	1.903	1.205	1.522	1.512
c''_{66}	0.862	0.917	0.681	0.972	0.722	0.825

Table 3.9. TRIP780 input data at various strain rates; for calibration of different yield functions

TRIP780	Strain rate (s ⁻¹)					
	0.001	0.1	1	10	100	1000
Experimental data						
$\sigma_0/\bar{\sigma}$	1.000	1.000	1.000	1.000	1.000	1.000
$\sigma_{45}/\bar{\sigma}$	0.996	0.977	0.974	0.971	0.972	0.978
$\sigma_{90}/\bar{\sigma}$	1.020	1.034	1.040	1.035	1.020	1.034
$\sigma_b/\bar{\sigma}$	1.051	1.050	1.051	1.044	1.036	1.022
r_0	0.498	0.551	0.563	0.560	0.544	0.591
r_{45}	1.030	0.900	0.779	0.815	0.779	0.928
r_{90}	0.565	0.689	0.693	0.670	0.619	0.719
Calculated from Yld2000-2d						
$\sigma_{15}/\bar{\sigma}$	1.000	0.993	0.991	0.992	0.992	0.993
$\sigma_{30}/\bar{\sigma}$	0.997	0.980	0.976	0.977	0.977	0.980
$\sigma_{60}/\bar{\sigma}$	1.005	0.994	0.994	0.986	0.986	0.995
$\sigma_{75}/\bar{\sigma}$	1.016	1.021	1.025	1.009	1.009	1.021
r_{15}	0.586	0.618	0.607	0.594	0.594	0.657
r_{30}	0.835	0.778	0.704	0.704	0.704	0.812
r_{60}	0.903	0.872	0.778	0.751	0.751	0.899
r_{75}	0.661	0.752	0.724	0.664	0.664	0.781
Calculated r_b from Yld96						
r_b (Yld96)	0.837	0.738	0.738	0.761	0.834	0.780

Table 3.10. Hill48 coefficients for TRIP780 at various strain rates

TRIP780	Strain rate (s ⁻¹)					
	0.001	0.1	1	10	100	1000
Hill48-r.value						
G	0.667	0.645	0.640	0.641	0.648	0.629
F	0.589	0.515	0.520	0.535	0.569	0.517
H	0.333	0.355	0.360	0.359	0.352	0.372
N	1.922	1.624	1.483	1.547	1.556	1.635
Hill48-stress						
G	0.471	0.486	0.490	0.491	0.485	0.511
F	0.434	0.421	0.415	0.425	0.446	0.446
H	0.529	0.514	0.510	0.509	0.515	0.489
N	1.563	1.642	1.655	1.665	1.649	1.613

Table 3.11. Hill90 coefficients for TRIP780 at various strain rates

TRIP780	Strain rate (s ⁻¹)					
	0.001	0.1	1	10	100	1000
Hill90-r.value						
m	1.876	1.745	1.650	1.682	1.677	1.830
a	-0.065	-0.115	-0.106	-0.092	-0.067	-0.100
b	-0.909	-0.466	-0.235	-0.314	-0.306	-0.484
Hill90-stress						
m	1.876	1.745	1.650	1.682	1.677	1.830
a	-0.036	-0.052	-0.053	-0.048	-0.028	-0.055
b	-0.102	-0.256	-0.257	-0.274	-0.218	-0.266

Table 3.12. Barlat89 coefficients for TRIP780 at various strain rates (exponent $a = 6$)

TRIP780	Strain rate (s ⁻¹)					
	0.001	0.1	1	10	100	1000
Barlat89-r.value						
a	1.307	1.239	1.232	1.241	1.266	1.212
c	0.693	0.761	0.768	0.759	0.734	0.788
h	0.960	0.933	0.938	0.946	0.960	0.943
p	1.152	1.051	1.013	1.035	1.046	1.053
Barlat89-stress						
a	1.075	1.033	1.017	1.032	1.074	1.039
c	0.925	0.967	0.983	0.968	0.926	0.961
h	0.981	0.967	0.962	0.966	0.981	0.967
p	1.009	1.038	1.043	1.047	1.043	1.037

Table 3.13. Yld96 coefficients for TRIP780 at various strain rates (exponent $a = 6$)

TRIP780	Strain rate (s^{-1})					
	0.001	0.1	1	10	100	1000
c_1	0.736	0.771	0.771	0.778	0.785	0.836
c_2	0.743	0.786	0.786	0.806	0.792	0.869
c_3	0.977	0.982	0.982	0.979	0.981	0.973
c_6	0.838	0.940	0.965	0.977	0.960	0.962
α_x	4.250	3.000	3.000	2.900	3.150	2.130
α_y	4.800	3.700	3.700	3.350	3.600	2.420
α_{z0}	1.000	1.000	1.000	1.000	1.000	1.000
α_{z1}	2.820	1.400	1.070	1.070	1.150	1.300
Calculation of r_b from Yld96						
r_b (Yld96)	0.837	0.738	0.738	0.761	0.834	0.780

Table 3.14. Yld2000-2d coefficients for TRIP780 at various strain rates (exponent $a = 6$)

TRIP780	Strain rate (s^{-1})					
	0.001	0.1	1	10	100	1000
α_1	0.893	0.920	0.934	0.937	0.921	0.950
α_2	0.901	0.913	0.898	0.898	0.913	0.917
α_3	0.843	0.856	0.862	0.870	0.876	0.923
α_4	0.989	0.970	0.967	0.974	0.991	0.980
α_5	1.015	1.014	1.013	1.015	1.017	1.021
α_6	0.856	0.883	0.883	0.894	0.896	0.942
α_7	0.996	0.994	0.976	0.987	0.982	1.004
α_8	1.073	1.147	1.184	1.174	1.169	1.101

Table 3.15. Yld2004-18P coefficients for TRIP780 at various strain rates (exponent $a = 6$)

TRIP780	Strain rate (s^{-1})					
	0.001	0.1	1	10	100	1000
C'_{12}	1.171	1.431	1.359	1.014	0.918	1.011
C'_{13}	0.968	1.537	0.830	1.647	0.965	1.084
C'_{21}	0.776	0.913	1.291	0.539	1.026	1.029
C'_{23}	0.577	0.953	0.544	1.197	0.953	0.988
C'_{31}	0.193	0.878	0.900	0.902	1.348	1.087
C'_{32}	0.944	1.496	1.191	0.930	1.524	0.739
C'_{44}	1.276	1.093	1.210	1.291	0.732	3.087
C'_{55}	1.091	1.027	1.897	2.659	2.435	1.083
C'_{66}	1.040	1.235	1.415	0.828	1.036	1.040
C''_{12}	1.030	0.913	0.568	1.178	0.736	0.898
C''_{13}	1.060	0.507	0.444	0.564	0.071	0.580
C''_{21}	0.530	0.345	0.313	0.795	0.898	0.659
C''_{23}	1.141	0.450	0.596	0.915	0.322	0.152
C''_{31}	1.261	0.667	1.389	0.497	1.209	1.059
C''_{32}	1.132	0.871	1.445	0.395	0.967	1.151
C''_{44}	1.305	1.352	1.025	1.077	1.032	1.013
C''_{55}	1.340	1.658	1.196	-0.199	0.748	-0.451
C''_{66}	0.930	0.720	0.479	1.084	0.897	0.938

Table 3.16. AA5182 input data at various strain rates; for calibration of different yield functions

AA5182-O	Strain rate (s ⁻¹)					
	0.001	0.1	1	10	100	1000
Experimental data						
$\sigma_0/\bar{\sigma}$	1.000	1.000	1.000	1.000	1.000	1.000
$\sigma_{45}/\bar{\sigma}$	0.977	0.976	0.980	0.976	0.966	0.976
$\sigma_{90}/\bar{\sigma}$	0.951	0.979	0.981	0.969	0.955	0.967
$\sigma_b/\bar{\sigma}$	0.991	0.985	0.992	1.008	1.000	0.985
r_0	0.633	0.862	0.724	0.633	0.693	0.720
r_{45}	0.664	0.922	0.775	0.795	0.748	0.790
r_{90}	0.620	0.858	0.767	0.667	0.708	0.742
Calculated from Yld2000-2d						
$\sigma_{15}/\bar{\sigma}$	0.997	0.995	0.996	0.996	0.994	0.996
$\sigma_{30}/\bar{\sigma}$	0.989	0.984	0.987	0.986	0.980	0.986
$\sigma_{60}/\bar{\sigma}$	0.964	0.974	0.978	0.971	0.958	0.970
$\sigma_{75}/\bar{\sigma}$	0.955	0.977	0.980	0.969	0.955	0.967
r_{15}	0.642	0.878	0.735	0.671	0.707	0.737
r_{30}	0.659	0.909	0.757	0.751	0.734	0.771
r_{60}	0.649	0.904	0.778	0.762	0.738	0.779
r_{75}	0.629	0.873	0.771	0.697	0.718	0.754
Calculated r_b from Yld96						
r_b (Yld96)	1.114	1.013	0.963	0.993	1.046	1.003

Table 3.17. Hill48 coefficients for AA5182-O at various strain rates

AA5182-O	Strain rate (s ⁻¹)					
	0.001	0.1	1	10	100	1000
Hill48-r.value						
G	0.612	0.537	0.580	0.613	0.591	0.581
F	0.625	0.539	0.547	0.581	0.578	0.564
H	0.388	0.463	0.420	0.388	0.409	0.419
N	1.440	1.531	1.438	1.546	1.459	1.478
Hill48-stress						
G	0.457	0.494	0.489	0.460	0.451	0.480
F	0.562	0.537	0.527	0.524	0.549	0.551
H	0.543	0.506	0.511	0.540	0.549	0.520
N	1.586	1.585	1.575	1.609	1.645	1.583

Table 3.18. Hill90 coefficients for AA5182-O at various strain rates

AA5182-O	Strain rate (s ⁻¹)					
	0.001	0.1	1	10	100	1000
Hill90-r.value						
m	1.700	1.917	1.796	1.761	1.719	1.817
a	0.010	0.002	-0.030	-0.027	-0.011	-0.015
b	-0.058	-0.116	-0.051	-0.238	-0.075	-0.101
Hill90-stress						
m	1.700	1.917	1.796	1.761	1.719	1.817
a	0.071	0.038	0.030	0.049	0.068	0.055
b	0.012	-0.100	-0.068	-0.055	-0.068	-0.044

Table 3.19. Barlat89 coefficients for AA5182-O at various strain rates (exponent a = 8)

AA5182-O	Strain rate (s ⁻¹)					
	0.001	0.1	1	10	100	1000
Barlat89-r.value						
a	1.230	1.075	1.146	1.213	1.176	1.156
c	0.770	0.925	0.854	0.787	0.824	0.844
h	1.006	1.001	0.983	0.984	0.994	0.992
p	1.013	1.015	0.997	1.029	1.008	1.009
Barlat89-stress						
a	1.246	1.152	1.144	1.186	1.235	1.195
c	0.754	0.848	0.856	0.814	0.765	0.805
h	1.051	1.021	1.019	1.032	1.047	1.035
p	1.023	1.030	1.025	1.029	1.041	1.028

Table 3.20. Yld96 coefficients for AA5182-O at various strain rates (exponent $a = 8$)

AA5182-O	Strain rate (s^{-1})					
	0.001	0.1	1	10	100	1000
c_1	0.967	1.023	0.983	0.931	0.971	1.004
c_2	0.819	0.953	0.908	0.821	0.821	0.888
c_3	1.027	1.005	1.007	1.025	1.036	1.014
c_6	0.972	1.020	1.010	0.970	1.000	0.995
α_x	2.140	1.110	1.440	2.200	1.880	1.440
α_y	3.320	1.390	1.940	3.330	3.100	2.150
α_{z0}	1.000	1.000	1.000	1.000	1.000	1.000
α_{z1}	1.160	0.980	0.930	1.305	1.055	1.093
	Calculation of r_b from Yld96					
r_b (Yld96)	1.114	1.013	0.963	0.993	1.046	1.003

Table 3.21. Yld2000-2d coefficients for AA5182-O at various strain rates (exponent $a = 8$)

AA5182-O	Strain rate (s^{-1})					
	0.001	0.1	1	10	100	1000
α_1	0.909	0.965	0.949	0.920	0.914	0.934
α_2	1.057	1.035	1.024	1.030	1.066	1.049
α_3	0.933	0.995	0.968	0.912	0.920	0.967
α_4	1.047	1.022	1.020	1.025	1.035	1.032
α_5	1.021	1.014	1.018	1.015	1.016	1.021
α_6	0.985	1.024	1.005	0.961	0.978	1.017
α_7	0.987	1.017	0.998	1.000	1.004	1.004
α_8	1.097	1.048	1.071	1.099	1.121	1.069

Table 3.22. Yld2004-18P coefficients for AA5182-O at various strain rates (exponent $a = 8$)

AA5182-O	Strain rate (s^{-1})					
	0.001	0.1	1	10	100	1000
c'_{12}	1.316	0.979	1.079	1.166	1.184	0.667
c'_{13}	1.086	0.758	1.153	1.226	1.302	0.793
c'_{21}	1.090	0.844	0.437	1.098	1.314	0.898
c'_{23}	1.035	0.879	0.773	1.197	1.314	1.046
c'_{31}	0.564	0.917	0.877	1.018	0.862	0.777
c'_{32}	0.485	1.047	1.001	0.845	0.972	0.657
c'_{44}	1.272	0.488	0.695	0.982	1.328	2.238
c'_{55}	0.751	1.199	2.365	1.351	1.020	1.069
c'_{66}	1.193	0.923	0.834	1.150	1.265	0.799
c''_{12}	0.754	1.156	1.252	0.908	0.737	0.994
c''_{13}	1.363	1.228	1.327	0.835	0.862	1.381
c''_{21}	0.554	0.979	1.026	0.619	0.637	1.332
c''_{23}	1.321	1.058	1.200	0.555	0.888	1.419
c''_{31}	0.927	1.011	0.355	0.884	0.855	0.957
c''_{32}	1.114	1.048	0.814	1.013	0.855	0.959
c''_{44}	1.030	1.163	0.939	1.154	0.822	0.771
c''_{55}	1.084	1.294	0.856	1.102	1.323	0.544
c''_{66}	0.675	1.090	1.158	0.818	0.724	1.174

3.3.4 Updating Yld2000-2d anisotropy coefficients w.r.t. strain rate

Figures 3.21, 3.22, and 3.23 show the variation of Yld2000-2d anisotropy coefficients ($\alpha_1 - \alpha_8$) w.r.t. strain rate for DP600, TRIP780, and AA5182-O, respectively. In order to apply these variations to EHF simulations and update the anisotropy coefficients, 4th-order polynomial equations were fitted to the α coefficients. These equations are given in Tables 3.23, 3.24, and 3.25 for DP600, TRIP780, and AA5182-O, respectively, and were implemented into the author's user-defined material model that will be presented in Chapter 5. It should be mentioned that the variable " x " represents " $\log \dot{\epsilon}$ " in these polynomial equations.

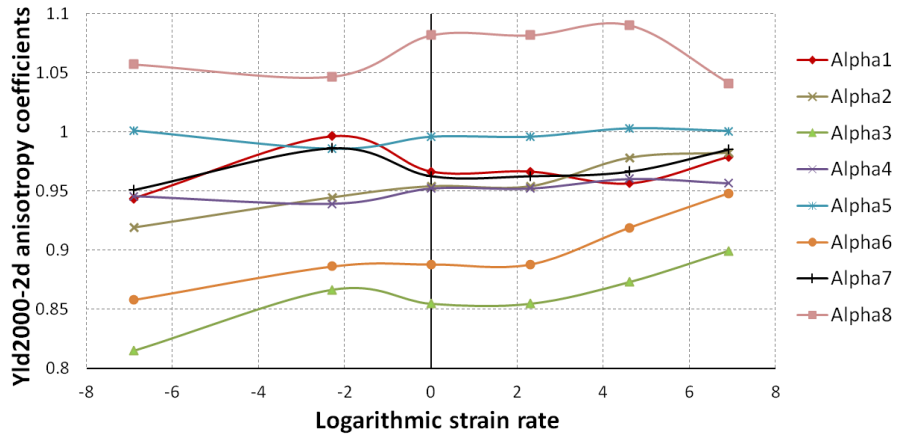


Figure 3.21. Variation of Yld2000-2d anisotropy coefficients w.r.t. strain rate for DP600

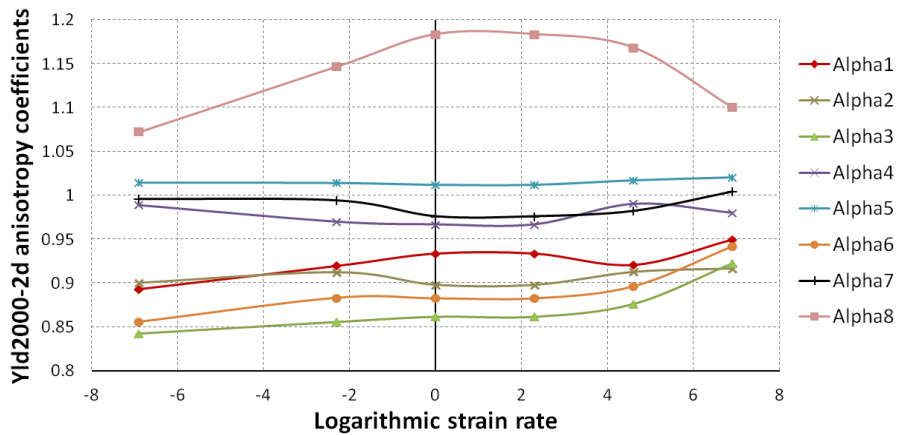


Figure 3.22. Variation of Yld2000-2d anisotropy coefficients w.r.t. strain rate for TRIP780

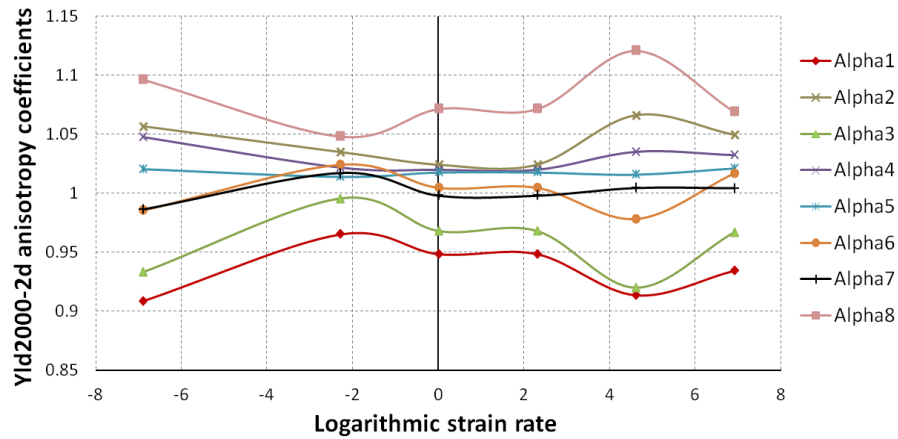


Figure 3.23. Variation of Yld2000-2d anisotropy coefficients w.r.t. strain rate for AA5182-O

Table 3.23. 4th-order equations fitted to Yld2000-2d coefficients for DP600

$$\alpha_1 = -0.00002x^4 + 0.0002x^3 + 0.0006x^2 - 0.0089x + 0.97$$

$$\alpha_2 = -0.00002x^4 + 0.00004x^3 + 0.0008x^2 + 0.0026x + 0.94$$

$$\alpha_3 = -0.00002x^4 + 0.0002x^3 + 0.0012x^2 - 0.0036x + 0.85$$

$$\alpha_4 = 0.000005x^4 - 0.00006x^3 - 0.0002x^2 + 0.0037x + 0.94$$

$$\alpha_5 = 0.000005x^4 - 0.00006x^3 - 0.00008x^2 + 0.0029x + 0.99$$

$$\alpha_6 = -0.00002x^4 + 0.0001x^3 + 0.0012x^2 + 0.0003x + 0.88$$

$$\alpha_7 = -0.00002x^4 + 0.0002x^3 + 0.0012x^2 - 0.0067x + 0.96$$

$$\alpha_8 = 0.00002x^4 - 0.0002x^3 - 0.0006x^2 + 0.0102x + 1.07$$

Table 3.24. 4th-order equations fitted to Yld2000-2d coefficients for TRIP780

$$\alpha_1 = 0.00004x^4 + 0.00003x^3 - 0.0022x^2 + 0.0026x + 0.94$$

$$\alpha_2 = -0.00003x^4 + 0.0001x^3 + 0.0016x^2 - 0.0035x + 0.90$$

$$\alpha_3 = 0.00002x^4 + 0.0001x^3 - 0.0003x^2 + 0.0009x + 0.86$$

$$\alpha_4 = -0.00003x^4 - 0.00001x^3 + 0.00194x^2 + 0.00009x + 0.96$$

$$\alpha_5 = -0.000005x^4 + 0.00002x^3 + 0.0004x^2 - 0.0004x + 1.01$$

$$\alpha_6 = 0.000007x^4 + 0.0002x^3 + 0.00002x^2 - 0.001x + 0.88$$

$$\alpha_7 = -0.00001x^4 + 0.0001x^3 + 0.001x^2 - 0.0049x + 0.98$$

$$\alpha_8 = 0.000002x^4 - 0.0002x^3 - 0.002x^2 + 0.0096x + 1.18$$

Table 3.25. 4th-order equations fitted to Yld2000-2d coefficients for AA5182-O

$$\alpha_1 = 0.00002x^4 + 0.0002x^3 - 0.0017x^2 - 0.006x + 0.95$$

$$\alpha_2 = -0.00006x^4 + 0.00002x^3 + 0.0035x^2 - 0.0013x + 1.01$$

$$\alpha_3 = 0.00003x^4 + 0.0003x^3 - 0.0023x^2 - 0.0097x + 0.98$$

$$\alpha_4 = -0.00001x^4 - 0.00003x^3 + 0.0011x^2 + 0.0002x + 1.01$$

$$\alpha_5 = 0.00001x^4 - 0.00002x^3 - 0.0004x^2 + 0.0009x + 1.01$$

$$\alpha_6 = 0.00002x^4 + 0.0002x^3 - 0.0013x^2 - 0.0067x + 1.01$$

$$\alpha_7 = -0.00002x^4 + 0.0001x^3 + 0.0014x^2 - 0.0051x + 0.99$$

$$\alpha_8 = -0.00005x^4 - 0.0002x^3 + 0.0027x^2 + 0.0085x + 1.05$$

3.4 Rate-dependent hardening models

The material work hardening behaviour, which is usually defined as a scalar function of plastic strain, represents the mechanical response of a material and also determines the expansion ratio of the flow surface in stress space during plastic deformation. The original hardening models, such as Power-law or Voce-law, were solely dependent on the plastic strain. However, in many forming processes, the actual strain hardening behaviour of materials is more complicated. The strain hardening behaviour is not only dependent on strain, but also on strain rate and temperature. Therefore, for an accurate prediction of plastic material flow in a finite element simulation of a rate-dependent forming process, the work hardening behaviour of the material must be determined more precisely over wide ranges of strain rates and temperatures. To this end, many phenomenological rate-dependent hardening models have been proposed to predict the strain hardening effect together with the strain rate hardening (or softening) and thermal softening of the material (Johnson and Cook, 1983; Zerilli and Armstrong, 1987; Liang and Khan, 1999; Paul, 2012). In most of these proposed hardening models, the strain hardening, strain rate, and thermal effects are generally presented as decoupled terms and the stress response is expressed as a multiplicative form of these terms. In this work, three phenomenological rate-dependent hardening models, JC, KHL, and SKP (Johnson and Cook, 1983; Liang and Khan, 1999; Paul, 2012), were selected because they are widely used, easy to implement into a FE code, and have been justified for a variety of steel and aluminum sheet metal alloys over a wide range of strain rates.

3.4.1 Johnson-Cook (JC)

Johnson and Cook (1983) introduced a model (JC) to describe the hardening behaviour of metals subjected to large strains over wide ranges of strain rates and temperatures. This model is implemented into many FE codes, such as ABAQUS and LS-DYNA, and is able to successfully capture the hardening behaviour of different steel grades and aluminum alloys. The JC model can be written as

$$\sigma = [A + B\varepsilon_p^n] \left[1 + C \ln \left(\frac{\dot{\varepsilon}}{\dot{\varepsilon}_0} \right) \right] \left[1 - \left(\frac{T - T_r}{T_m - T_r} \right)^m \right] \quad (3-33)$$

where ε_p is the equivalent plastic strain, $\dot{\varepsilon}$ and $\dot{\varepsilon}_0$ are the instantaneous and reference strain rates, respectively, T , T_r , and T_m are the current, room, and melting temperatures, respectively, and A , B , n , C , and m are the material constants, which are given in Table 3.26 for DP600, TRIP780, and AA5182-O. The JC equation includes three separate terms; the strain hardening term which is an expression of Power-law, the strain rate hardening term which represents the instantaneous strain-rate sensitivity of the material, and the thermal softening term. However, there is an inherent deficiency in the JC model in that it is not able to accurately describe the work hardening behaviour of some metals at high strain rates. Indeed, the decoupling of the strain rate and thermal softening terms in the JC model causes the work hardening rate ($d\sigma/d\varepsilon$) to remain constant over all strain rates, i.e., the stress-strain curve can only shift up or down when the strain rate changes. Experimental observations for some materials show a decrease in the work hardening rate with increasing the strain rate (Chen and Gray, 1995), and therefore the JC model fails to represent the actual behaviour of these materials.

3.4.2 Khan-Huang-Liang (KHL)

Extensive experimental observations for many metals have shown that the work hardening rate can indeed be dependent on the strain rate and temperature. In order to overcome the shortcomings of the JC model, Khan and Liang (1999) proposed a hardening model (also referred to as KHL), which can incorporate the change in work hardening rate as a function of strain rate and temperature. Many modifications have been applied to the KHL model to adjust it for BCC, FCC, and HCP metals (Khan et al., 2004, 2007). In this study, the general modified format of the KHL model that is widely applied to BCC and FCC metals was used. This version of the KHL model can be written as

$$\sigma = \left[A + B\varepsilon_p^{n_0} \left(1 - \frac{\ln \dot{\varepsilon}}{\ln D_0^p} \right)^{n_1} \right] \left(\frac{\dot{\varepsilon}}{\dot{\varepsilon}_0} \right)^c \left(\frac{T_m - T}{T_m - T_r} \right)^m \quad (3-34)$$

where ε_p is the equivalent plastic strain, $\dot{\varepsilon}$ and $\dot{\varepsilon}_0$ are the instantaneous and reference strain rates, respectively, T , T_r , and T_m are the current, room, and melting temperatures, respectively, D_0^p is a constant equal to 10^6 s^{-1} which is applied to non-dimensionalize the $(1 - \ln\dot{\varepsilon}/\ln D_0^p)$ term, and A , B , n_0 , n_1 , C and m are material constants, which are given in Table 3.27 for DP600, TRIP780, and AA5182-O. In the KHL model, the changes in the work hardening rate as a function of strain rate can be accommodated through the constant n_1 . It should be noted that, the term $(1 - \ln\dot{\varepsilon}/\ln D_0^p)^\beta$ is always greater than one, which causes the KHL model to predict a higher work hardening rate compared to the JC model.

3.4.3 Surajit Kumar Paul (SKP)

Paul (2012) proposed a new hardening model (so-called SKP), which is more general in nature compared to the JC and KHL models, as discussed in Section 2.3. This model is able to predict the hardening behaviour for a variety of metals (with BCC, FCC, or HCP crystal structures), over a large range of strain rates and temperatures. The general form of the SKP model can be expressed as

$$\sigma = \sigma_0 e^{A \ln\left(\frac{\dot{\varepsilon}}{\dot{\varepsilon}_0}\right) - k(T - T_a)} + [B\varepsilon_p + C(1 - e^{-\beta\varepsilon_p})] \left(1 - H \ln\left(\frac{\dot{\varepsilon}}{\dot{\varepsilon}_0}\right)\right) (1 - G(T - T_a)) \quad (3-35)$$

where ε_p is the equivalent plastic strain, $\dot{\varepsilon}$ and $\dot{\varepsilon}_0$ are the instantaneous and reference strain rates, respectively, T and T_a are the current and absolute temperatures, respectively, and σ_0 , A , k , B , C , β , H and G are material constants, which are given in Table 3.28 for DP600, TRIP780, and AA5182-O. In the absence of temperature effect, the SKP model reduces to

$$\sigma = \sigma_0 \left(\frac{\dot{\varepsilon}}{\dot{\varepsilon}_0}\right)^A + [B\varepsilon_p + C(1 - e^{-\beta\varepsilon_p})] \left(1 - H \ln\left(\frac{\dot{\varepsilon}}{\dot{\varepsilon}_0}\right)\right) \quad (3-36)$$

The reduced equation includes the yield stress, quasi-static, and strain rate sensitive terms. The strain rate effect is engaged in all three terms independently, which makes

SKP a flexible model that can reproduce the hardening behaviour of a variety of materials over a wide range of strain rates.

3.5 Determination of constants for different hardening models

Many researchers have fitted the hardening models to the experimental uniaxial flow curve up to uniform elongation (ultimate point), without verifying the work hardening rate beyond the ultimate point. The accurate prediction of material hardening behaviour beyond the ultimate point is necessary to precisely predict the plastic deformation at very large plastic strains, in particular for EHF simulations of biaxial stretching. In this work, the experimental uniaxial flow curve at each strain rate was extrapolated beyond the uniform elongation, according to the corresponding experimental or calculated biaxial flow curve (obtained in Section 3.3.2). The JC, KHL, and SKP hardening models were fitted to the uniaxial flow curves over a wide range of strain rates, after they were extrapolated to large strains based on the biaxial data (Figures 3.24-3.26).

The least-squares method combined with a constrained optimization procedure in MATLAB was used to optimize the material constants. It should be noted that, the temperature effect was ignored in the calibration of all aforementioned hardening models. The material constants in the JC, KHL, and SKP hardening models are given in Tables 3.26-3.28 for DP600, TRIP780, and AA5182-O.

Table 3.26. Constants in the JC hardening model for DP600, TRIP780, and AA5182-O

	A (MPa)	B (MPa)	n	C	$\dot{\epsilon}_0$ (s^{-1})
DP600	335	614	0.33	0.015	0.001
TRIP780	433	1236	0.46	0.012	0.001
AA5182-O	108	419	0.39	-0.002	0.001

Table 3.27. Constants in the KHL hardening model for DP600, TRIP780, and AA5182-O

	A (MPa)	B (MPa)	n_0	n_1	C	$\dot{\epsilon}_0$ (s^{-1})
DP600	323	603	0.34	0.078	0.018	0.001
TRIP780	382	1227	0.41	0.011	0.012	0.001
AA5182-O	72	487	0.32	-0.24	-0.016	0.001

Table 3.28. Constants in the SKP hardening model for DP600, TRIP780, and AA5182-O

	σ_0 (MPa)	A	B (MPa)	n	C (MPa)	β	H	$\dot{\epsilon}_0$ (s^{-1})
DP600	318	0.029	354	0.54	258	15.6	0.0015	0.001
TRIP780	379	0.031	752	0.92	489	19.3	0.003	0.001
AA5182-O	91	0.011	584	0.47	873	-0.2	0.004	0.001

Figure 3-24 shows the correlation of the experimental data (uniaxial flow curves extrapolated based on the biaxial flow curves) with the fitted results for JC, KHL, and SKP hardening models at different strain rates for DP600. Results show that, although the correlations with KHL and SKP models are reasonably good, the KHL model is better able to represent the response of DP600 over the entire range of strain and strain rate. The results predicted by the JC model show a slight deviation from the experimental data points for almost all strain rate regimes, which is due to its limited flexibility compared to the other two models. Figure 3-25 shows a poor prediction of the JC model at different strain rates for TRIP780. Similar to DP600, results show that the KHL model delivers the best results for TRIP780, under quasi-static, intermediate and high strain rate regimes for almost the entire range of strains. Also, except for a slightly poor correlation at the highest strain rate ($1000 s^{-1}$), the SKP model predictions are in good agreement with the experimental response of TRIP780 for the entire range of strains and strain rates. Both DP600 and TRIP780 exhibit positive strain-rate sensitivity, as given in Tables 3.26, 3.27, and 3.28 for JC, KHL, and SKP models, respectively.

As shown in Figure 3-26, AA5182-O exhibits slightly negative or almost zero strain-rate sensitivity, in which the calibrated constants are given in Table 3.26-Table 3.28.

Almost all three models are shown to correlate and predict the observed responses similar. It should be noted that experimental observations by Picu et al. (2005) showed similar behaviour for AA5182-O. They concluded that the small negative strain-rate sensitivity was due to the interaction of solute atoms with dislocations, where the interactions are associated with the dynamic strain aging (DSA) of AA5182-O. The DSA mechanism can lead to clustering of solute atoms which produces resistance to dislocation motion. The average size of clusters is smaller in size at higher strain rates and cannot produce the same resistance to dislocation motion as can large clusters. i.e., at lower strain rate regimes there is enough time to form large clusters which provide resistance to dislocation motion giving rise to a faster increase of strain hardening at lower strain rates. Finally, it can be concluded that for the examined strain rate range of uniaxial tensile tests (from 0.001 s^{-1} to 1000 s^{-1}), there is no reason to apply a rate-dependent hardening model in the FE simulation of AA5182-O.

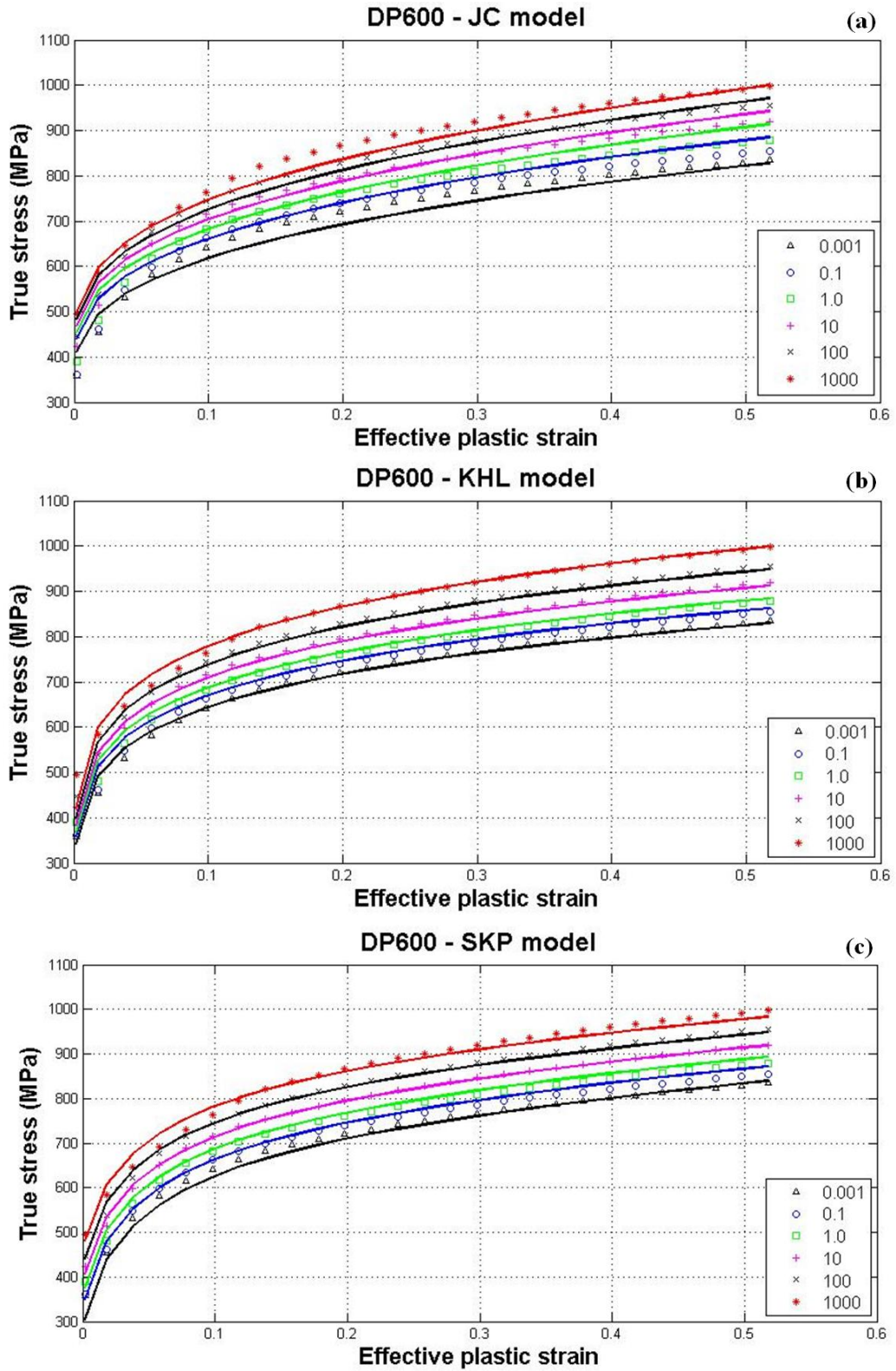


Figure 3-24. Flow curves predicted by JC, KHL, and SKP models for DP600

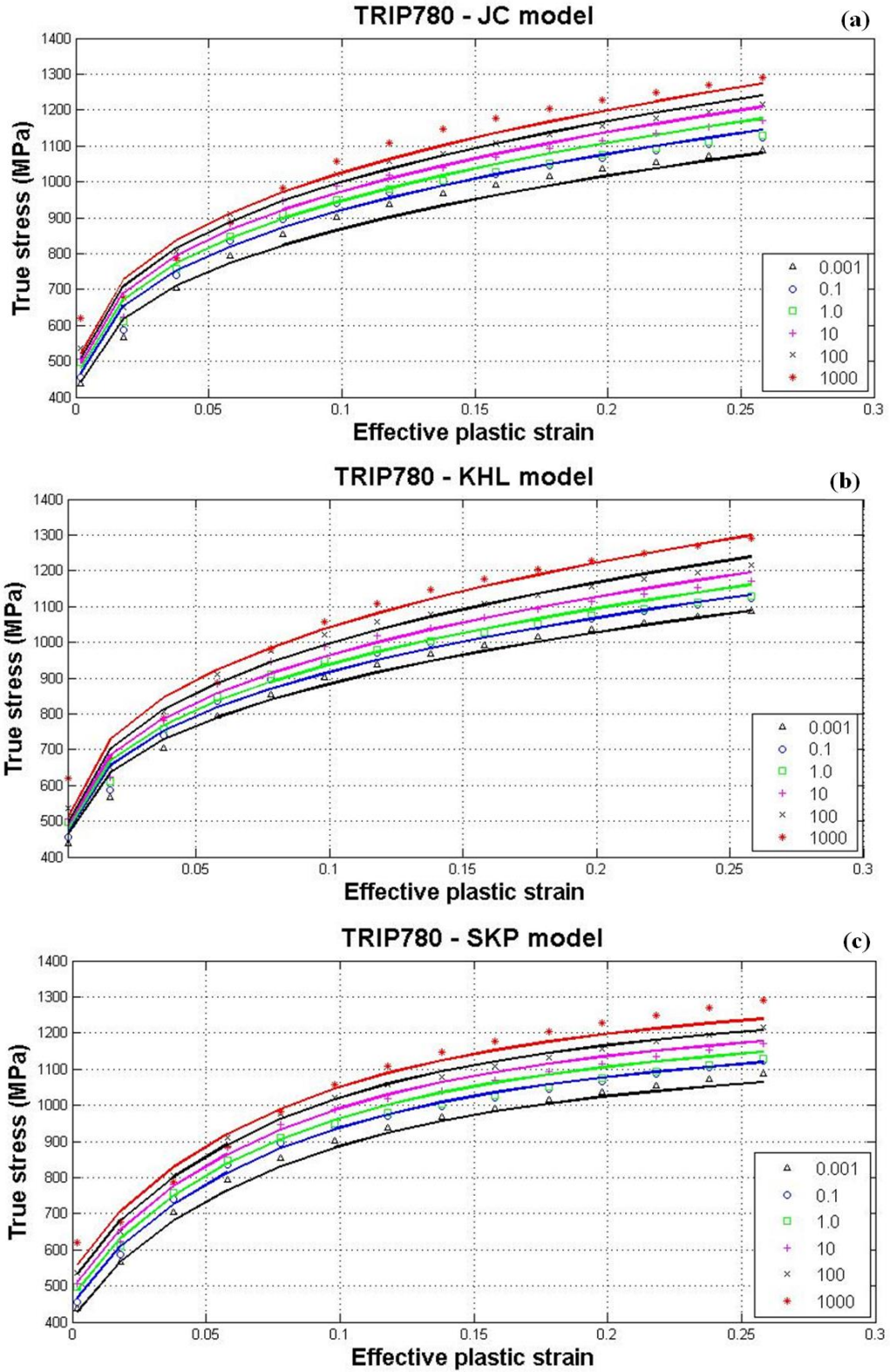


Figure 3-25. Flow curves predicted by JC, KHL, and SKP models for TRIP780

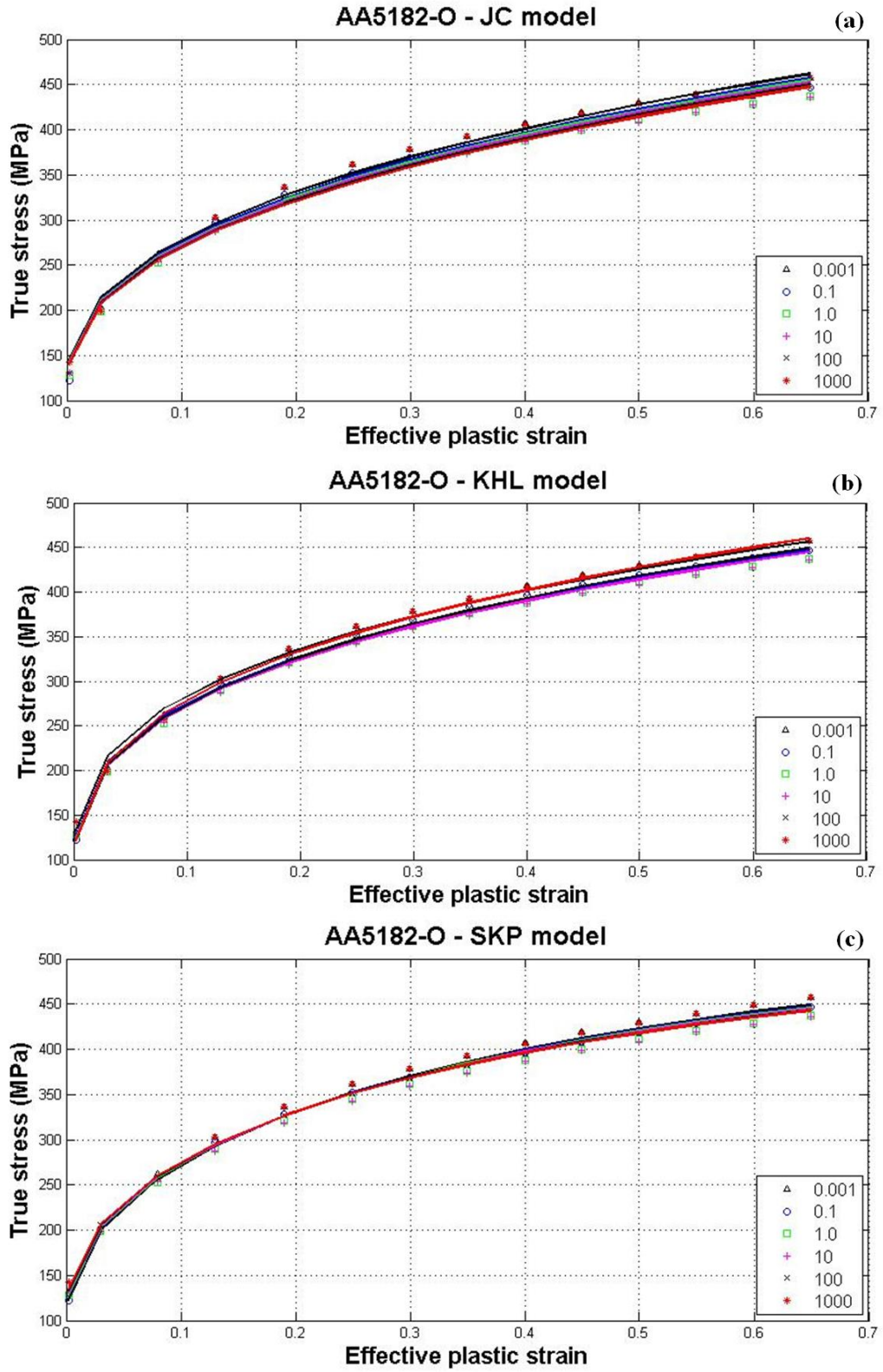


Figure 3-26. Flow curves predicted by JC, KHL, and SKP models for AA5182-O

4 Effect of Updating Anisotropy Coefficients on the Flow Surface

4.1 Planar Distribution of Anisotropic Data (uniaxial flow stress and r-value)

Sheet metals generally exhibit a substantial anisotropy of mechanical properties due to the cold-rolling process and the consequent crystallographic texture. The rolling process induces a particular anisotropy in the sheet material characterised by the symmetry of the mechanical properties w.r.t. three orthogonal planes. The intersection lines of the symmetry planes are the orthotropy axes, which are expressed by RD, DD, and TD (rolling, diagonal and, transverse directions, respectively), as shown in Figure 4-1.

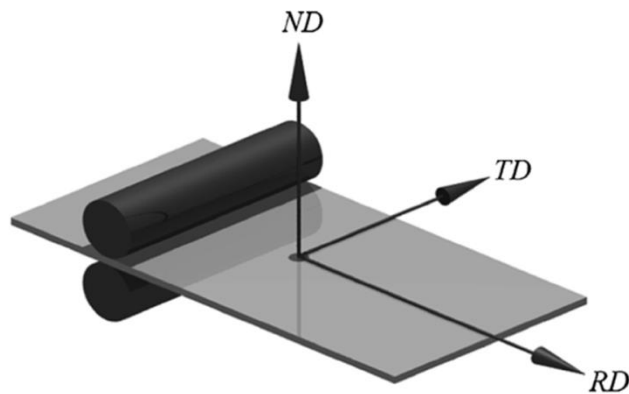


Figure 4-1. Orthotropy axes of the rolled sheet metals

The variation of the plastic flow behaviour with direction can be assessed by the Lankford coefficient (r-value). The value of the Lankford coefficient depends on the direction (or material orientation) in the plane of the sheet (r_θ), and is determined by conducting uniaxial tension tests in various directions (θ), as shown in Figure 4-2b. The

subscript " θ " specifies the angle between the axis of the specimen and the rolling direction. For instance, r_0 , r_{45} , and r_{90} represent the r-values in the rolling (RD), diagonal (DD), and transverse (TD) directions, respectively, and were obtained for DP600, TRIP780, and AA5182-O, as discussed in Section 3.2.3.2.

Another important element characterising the performance of a yield function is the capability to predict the variations of the uniaxial flow stress in the plane of the sheet metal (σ_θ). The experimental uniaxial flow stresses in the rolling, diagonal, and transverse directions were determined in Section 3.3.1 for DP600, TRIP780, and AA5182-O. In order to assess the capability of a yield function, the relationships defining the dependence of the parameters with the material anisotropy (r_θ and σ_θ) on the angle θ measured from the rolling direction shall be established. In the case of a uniaxial tension condition (Figure 4-2a), the components of the stress tensor can be written as follows

$$\sigma_{11} = \sigma_\theta \cos^2\theta, \quad \sigma_{22} = \sigma_\theta \sin^2\theta, \quad \sigma_{12} = \sigma_{21} = \sigma_\theta \cos\theta \sin\theta \quad (4-1)$$

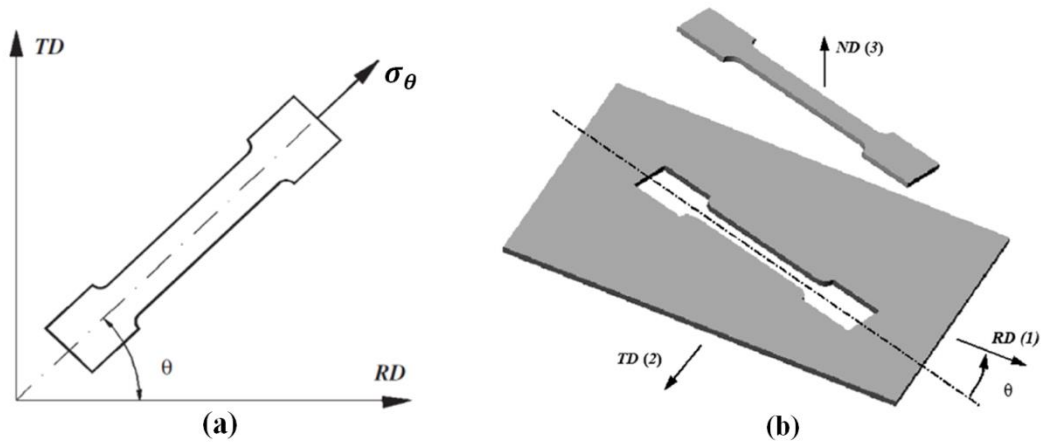


Figure 4-2. a) Uniaxial flow stress corresponding to a direction in the plane of the sheet metal, b) Tensile specimen extracted at the angle θ ; measured from the rolling direction

By replacing Eq. (4-1) in the relationship defining the effective stress and taking into account the homogeneity assumption, we have

$$\sigma_{\theta} = \sigma_{ref}/F_{\theta} \quad (4-2)$$

where σ_{ref} is the reference flow stress which is usually selected to be that in the rolling direction (σ_0), and F_{θ} is a function of the angle θ , which is related to the yield function adopted in the constitutive material model. Eq. (4-2) expresses the uniaxial flow stress (σ_{θ}) corresponding to the planar direction identified by the angle θ .

In a similar way, the relationship defining the variation of the r-value (r_{θ}) in the plane of the sheet metal can be established. Let us consider the specimen inclined at the angle θ w.r.t. the rolling direction (Fig. 4.2b). According to the definition of the plastic flow, the instantaneous anisotropy coefficients can be expressed by

$$r_{\theta} = \frac{\dot{\epsilon}_{22}}{\dot{\epsilon}_{33}} = \frac{\dot{\epsilon}_{\theta+90}}{\dot{\epsilon}_{33}} \quad (4-3)$$

Taking into account the volume constancy assumption ($\dot{\epsilon}_{11} + \dot{\epsilon}_{22} + \dot{\epsilon}_{33} = 0$), as well as the expressions of the strain rate components along the principal directions, we have

$$r_{\theta} = \frac{\dot{\epsilon}_{11} \cos^2\theta + \dot{\epsilon}_{22} \sin^2\theta + \dot{\epsilon}_{12} \cos\theta \sin\theta}{\dot{\epsilon}_{11} + \dot{\epsilon}_{22}} \quad (4-4)$$

According to the associated flow rule (AFR), Eq. (4-4) can be rewritten in terms of the stress components as follows

$$r_{\theta} = \frac{\sigma_{11}(\partial\sigma/\partial\sigma_{11}) + \sigma_{22}(\partial\sigma/\partial\sigma_{22}) + \sigma_{12}(\partial\sigma/\partial\sigma_{12})}{\sigma_{11}(\partial\sigma/\partial\sigma_{11}) + \sigma_{22}(\partial\sigma/\partial\sigma_{22})} \quad (4-5)$$

Finally, by coupling Eq. (4-5) with Euler's identity and replacing Eq.(4-2), we have

$$r_{\theta} = \frac{F_{\theta}}{\partial\sigma/\partial\sigma_{11} + \partial\sigma/\partial\sigma_{22}} - 1 \quad (4-6)$$

Eq. (4-6) expresses the anisotropy associated with the material plastic flow as a dependence of the specimen inclination. In order to evaluate the performance of a yield function in describing the anisotropy behaviour of a sheet material, both F_{θ} and the stress derivatives ($\partial\sigma/\partial\sigma_{11}$ and $\partial\sigma/\partial\sigma_{22}$) are required to be specified in Eqs. (4-2) and (4-6).

The determination of the function F_θ and the stress derivatives are presented in the following section for several yield functions.

4.1.1 Uniaxial Anisotropic Data Formulation

4.1.1.1 Hill48

Taking into account Eq. (3-1) (Hill, 1948), Eq. (4-1), and Eq. (4-2), F_θ can be defined by

$$F_\theta = [G\cos^4\theta + F\sin^4\theta + H(\cos^2\theta - \sin^2\theta)^2 + 2N\cos^2\theta \sin^2\theta]^{1/2} \quad (4-7)$$

where G, F, H, and N are the anisotropy coefficients, which are given in Table 3.3, Table 3.10, and Table 3.17 for DP600, TRIP780, and AA5182-O, respectively. By replacing Eq. (4-7) in Eq (4-6) and taking the stress derivatives, r_θ can be written as

$$r_\theta = \frac{G\cos^4\theta + F\sin^4\theta + H\cos^2 2\theta + (1/2)N\sin^2 2\theta}{G\cos^2\theta + F\sin^2\theta} - 1 \quad (4-8)$$

4.1.1.2 Hill90

By using Eq. (3-4) (Hill, 1990), Eq. (4.1), and Eq. (4-2), F_θ can be written as follows

$$F_\theta = \left[\frac{1}{2} \left(1 + \left(\frac{\sigma_b}{\tau} \right)^m - 2a \cos 2\theta + b \cos^2 2\theta \right) \right]^{1/m} \quad (4-9)$$

where m , a , and b are the anisotropy coefficients, which are given in Tables 3.4, 3.11, and 3.18 for DP600, TRIP780, and AA5182-O, respectively. By replacing Eq. (4-9) in Eq (4-6) and taking the stress derivatives, r_θ can be written as

$$r_\theta = \frac{\left(\frac{\sigma_b}{\tau} \right)^m - 1 + (2/m)b \cos^2 2\theta}{2 - 2a \cos 2\theta + ((m - 2)/m)b \cos^2 2\theta} \quad (4-10)$$

4.1.1.3 Barlat89

Taking into account Eq. (3-10) (Barlat and Lian, 1989), Eq. (4-1), and Eq. (4-2), F_θ can be written as follows

$$F_\theta = [a(F_1 + F_2)^M + a(F_1 - F_2)^M + (1 - a)(2F_2)^M]^{1/M} \quad (4-11)$$

where

$$F_1 = \frac{\cos^2\theta + h \sin^2\theta}{2}, \quad F_2 = \left[\left(\frac{\cos^2\theta - h \sin^2\theta}{2} \right)^2 + p^2 \cos^2\theta \sin^2\theta \right]^{1/2} \quad (4-12)$$

where a , h , and p are the anisotropy coefficients, which are given in Tables 3.5, 3.12, and 3.19 for DP600, TRIP780, and AA5182-O, respectively. It should be noted that in all Barlat's yield functions (Barlat89, Yld2000-2d, and Yld2004-18p), the exponent (M or a) is set to 6 and 8 for BCC and FCC metals, respectively. By replacing Eq. (4-12) in Eq (4-6) and taking the stress derivatives, r_θ can be written as

$$r_\theta = \frac{[a(F_1 + F_2)^M + a(F_1 - F_2)^M + (1 - a)(2F_2)^M]^{1/M}}{a(k_1 + k_2)^{M-1}(t_1 + t_2) + a(k_1 - k_2)^{M-1}(t_1 - t_2) + 2(a - 1)(2k_2)^{M-1}t_2} - 1 \quad (4-13)$$

where

$$k_1 = F_1 \cdot \sigma_\theta; \quad k_2 = F_2 \cdot \sigma_\theta$$

$$t_1 = \frac{a(k_1 + k_2)^{M-1} + a(k_1 - k_2)^{M-1}}{\bar{\sigma}^{M-1}}; \quad (4-14)$$

$$t_2 = \frac{a(k_1 + k_2)^{M-1} - a(k_1 - k_2)^{M-1} + 2(a - 1)(2k_2)^{M-1}}{\bar{\sigma}^{M-1}}$$

4.1.1.4 Yld2000-2d

Taking into account Eq. (3-20) (Barlat et al., 2003), Eq. (4-1), and Eq. (4-2), F_θ can be written as follows

$$F_{\theta} = \left[\frac{1}{2} \left(\left| \sqrt{\Delta'} \right|^a + \left| \frac{1}{2} \left(\Delta_1'' - \sqrt{\Delta_2''} \right) \right|^a + \left| \frac{1}{2} \left(\Delta_1'' + \sqrt{\Delta_2''} \right) \right|^a \right) \right]^{1/a} \quad (4-15)$$

where

$$\begin{cases} \Delta' = (L_3' \cos^2 \theta + L_4' \sin^2 \theta)^2 + 2L_{66}'^2 \sin^2 2\theta \\ \Delta_1'' = 3(L_1'' \cos^2 \theta + L_2'' \sin^2 \theta) \\ \Delta_2'' = (L_3'' \cos^2 \theta + L_4'' \sin^2 \theta)^2 + 2L_{66}''^2 \sin^2 2\theta \end{cases} \quad (4-16)$$

where parameters L_i' and L_i'' are defined as below

$$\begin{cases} L_1' = L_{11}' + L_{21}' & L_1'' = L_{11}'' + L_{21}'' \\ L_2' = L_{12}' + L_{22}' & L_2'' = L_{12}'' + L_{22}'' \\ L_3' = L_{11}' - L_{21}' & L_3'' = L_{11}'' - L_{21}'' \\ L_4' = L_{12}' - L_{22}' & L_4'' = L_{12}'' - L_{22}'' \end{cases} \quad (4-17)$$

where L_{ij}' and L_{ij}'' are the components of the two linear tensors defined in Eq. (3-22), expressing the anisotropy of the material as functions of α_1 to α_8 . α_k coefficients are given in Tables 3.7, 3.14, and 3.21 for DP600, TRIP780, and AA5182-O, respectively.

By using Eq. (3.20), the effective stress for Yld2000-2d can be expressed by

$$\sigma = \left(\frac{1}{2} \phi \right)^{1/a} = \left(\frac{1}{2} \right)^{1/a} \left[\left| \Lambda_2' \right|^{a/2} + \left| \frac{1}{2} \left(\Lambda_1'' - \sqrt{\Lambda_3''} \right) \right|^a + \left| \frac{1}{2} \left(\Lambda_1'' + \sqrt{\Lambda_3''} \right) \right|^a \right]^{1/a} \quad (4-18)$$

where

$$\begin{cases} \Lambda_1' = L_3' \sigma_{11} + L_4' \sigma_{22} \\ \Lambda_2' = \Lambda_1'^2 + 4L_{66}'^2 \sigma_{12}^2 \\ \Lambda_1'' = (L_1'' \sigma_{11} + L_2'' \sigma_{22}) \\ \Lambda_2'' = (L_3'' \sigma_{11} + L_4'' \sigma_{22}) \\ \Lambda_3'' = \Lambda_2''^2 + 4L_{66}''^2 \sigma_{12}^2 \end{cases} \quad (4-19)$$

By replacing Eq. (4-19) in Eq. (4-18) and taking the derivative, we have

$$\begin{aligned}
\frac{\partial \sigma}{\partial \sigma_{11,22}} = & \left(\frac{1}{2}\right)^{1/a} \left[(L'_{3,4} \Lambda'_1) |\Lambda'_2|^{\left(\frac{a}{2}-1\right)} \cdot \text{sign}(\Lambda'_2) \right. \\
& + \frac{1}{2} \left(3L''_{1,2} - L''_{3,4} \Lambda''_2 / \sqrt{\Lambda''_3} \right) \left| \frac{1}{2} \left(3\Lambda''_1 - \sqrt{\Lambda''_3} \right) \right|^{(a-1)} \cdot \text{sign} \left(\frac{1}{2} \left(3\Lambda''_1 \right. \right. \\
& \left. \left. - \sqrt{\Lambda''_3} \right) \right) \\
& + \frac{1}{2} \left(3L''_{1,2} + L''_{3,4} \Lambda''_2 / \sqrt{\Lambda''_3} \right) \left| \frac{1}{2} \left(3\Lambda''_1 + \sqrt{\Lambda''_3} \right) \right|^{(a-1)} \cdot \text{sign} \left(\frac{1}{2} \left(3\Lambda''_1 \right. \right. \\
& \left. \left. + \sqrt{\Lambda''_3} \right) \right) \left. \right] \cdot \phi^{\left(\frac{1}{a}-1\right)}
\end{aligned} \tag{4-20}$$

Finally, by replacing $\partial \sigma / \partial \sigma_{11}$ and $\partial \sigma / \partial \sigma_{11}$ in Eq. (4.6), r_θ associated to Yld2000-2d can be calculated.

4.1.1.5 Yld2004-18p

Taking into account Eq. (3-28) (Barlat et al., 2005), Eq. (4-1), and Eq. (4-2), F_θ can be written as follows

$$F_\theta = \left[\frac{1}{4} (\Gamma 1 + \Gamma 2 + \Gamma 3 + \Gamma 4 + \Gamma 5 + \Gamma 6 + \Gamma 7 + \Gamma 8 + \Gamma 9) \right]^{1/a} \tag{4-21}$$

Where

$$\begin{aligned}
\Gamma 1 &= \left| \frac{1}{2} (\Delta'_1 + \sqrt{\Delta'_2} - \Delta''_1 - \sqrt{\Delta''_2}) \right|^\alpha & \Gamma 2 &= \left| \frac{1}{2} (\Delta'_1 + \sqrt{\Delta'_2} - \Delta''_1 + \sqrt{\Delta''_2}) \right|^\alpha \\
\Gamma 3 &= \left| \frac{1}{2} (\Delta'_1 + \sqrt{\Delta'_2} - \Delta'_3) \right|^\alpha & \Gamma 4 &= \left| \frac{1}{2} (\Delta'_1 - \sqrt{\Delta'_2} - \Delta''_1 - \sqrt{\Delta''_2}) \right|^\alpha \\
\Gamma 5 &= \left| \frac{1}{2} (\Delta'_1 - \sqrt{\Delta'_2} - \Delta''_1 + \sqrt{\Delta''_2}) \right|^\alpha & \Gamma 6 &= \left| \frac{1}{2} (\Delta'_1 - \sqrt{\Delta'_2} - \Delta'_3) \right|^\alpha \\
\Gamma 7 &= \left| \frac{1}{2} (\Delta'_3 - \Delta''_1 - \sqrt{\Delta''_2}) \right|^\alpha & \Gamma 8 &= \left| \frac{1}{2} (\Delta'_3 - \Delta''_1 + \sqrt{\Delta''_2}) \right|^\alpha \\
\Gamma 9 &= \left| \frac{1}{2} (\Delta'_3 - \Delta''_3) \right|^\alpha
\end{aligned} \tag{4-22}$$

where Δ'_i and Δ''_i are defined as below

$$\begin{cases} \Delta'_1 = L'_1 \cos^2\theta + L'_2 \sin^2\theta \\ \Delta'_2 = \Delta_4'^2 + 2L_{66}'^2 \sin^2 2\theta \\ \Delta'_3 = L'_{31} \cos^2\theta + L'_{32} \sin^2\theta \\ \Delta'_4 = L'_3 \cos^2\theta + L'_4 \sin^2\theta \end{cases} \quad \begin{cases} \Delta''_1 = L''_1 \cos^2\theta + L''_2 \sin^2\theta \\ \Delta''_2 = \Delta_4''^2 + 2L_{66}''^2 \sin^2 2\theta \\ \Delta''_3 = L''_{31} \cos^2\theta + L''_{32} \sin^2\theta \\ \Delta''_4 = L''_3 \cos^2\theta + L''_4 \sin^2\theta \end{cases} \quad (4-23)$$

where parameters L'_i and L''_i are defined based on Eq. (4-17). Also, L'_{ij} and L''_{ij} are the components of the two linear transformation matrices incorporating the anisotropy coefficients, c'_{ij} and c''_{ij} , which were described in Section 3.1.6 The 18 anisotropy coefficients are given in Table 3.8, Table 3.15, and Table 3.22 for DP600, TRIP780, and AA5182-O, respectively.

By using Eqs. (3-28) and (4-22), the effective stress for Yld2004-18p can be expressed by

$$\sigma = \left(\frac{1}{4}\phi\right)^{1/a} = \left(\frac{1}{4}\right)^{1/a} [\Gamma_1 + \Gamma_2 + \Gamma_3 + \Gamma_4 + \Gamma_5 + \Gamma_6 + \Gamma_7 + \Gamma_8 + \Gamma_9]^{1/a} \cdot \sigma_\theta^a \quad (4-24)$$

By replacing Eq. (4-22) in Eq. (4-24), and taking the derivative, we have

$$\frac{\partial \sigma}{\partial \sigma_{11,22}} = \left(\frac{1}{4}\right)^{1/a} [\Pi_{1,2} + \Pi_{2,1,2} + \Pi_{3,1,2} + \Pi_{4,1,2} + \Pi_{5,1,2} + \Pi_{6,1,2} + \Pi_{7,1,2} + \Pi_{8,1,2} + \Pi_{9,1,2}] \cdot \phi^{\left(\frac{1}{a}-1\right)} \quad (4-25)$$

Where

$$\Pi_{1,2} = \frac{\partial}{\partial \sigma_{11,22}} |S'_1 - S''_1|^a = \left(\frac{1}{2}L'_{1,2} + \frac{1}{2}L'_{3,4}\Delta'_4/\sqrt{\Delta'_2} - \frac{1}{2}L''_{1,2} - \frac{1}{2}\frac{L''_{3,4}\Delta''_4}{\sqrt{\Delta''_2}} \right) \cdot \left[\frac{1}{2}\Delta'_1 + \frac{1}{2}\sqrt{\Delta'_2} - \frac{1}{2}\Delta''_1 - \frac{1}{2}\sqrt{\Delta''_2} \right]^{(a-1)} \cdot \text{sign} \left(\frac{1}{2}\Delta'_1 + \frac{1}{2}\sqrt{\Delta'_2} - \frac{1}{2}\Delta''_1 - \frac{1}{2}\sqrt{\Delta''_2} \right) \quad (4-26a)$$

$$\begin{aligned} \Pi_{2,1,2} &= \frac{\partial}{\partial \sigma_{11,22}} |S'_1 - S''_2|^a = \left(\frac{1}{2} L'_{1,2} + \frac{1}{2} L'_{3,4} \Delta'_4 / \sqrt{\Delta'_2} - \frac{1}{2} L''_{1,2} + \frac{\frac{1}{2} L''_{3,4} \Delta''_4}{\sqrt{\Delta''_2}} \right) \\ &\cdot \left| \frac{1}{2} \Delta'_1 + \frac{1}{2} \sqrt{\Delta'_2} - \frac{1}{2} \Delta''_1 + \frac{1}{2} \sqrt{\Delta''_2} \right|^{(a-1)} \cdot \text{sign} \left(\frac{1}{2} \Delta'_1 + \frac{1}{2} \sqrt{\Delta'_2} - \frac{1}{2} \Delta''_1 \right. \\ &\quad \left. + \frac{1}{2} \sqrt{\Delta''_2} \right) \end{aligned} \quad (4.26b)$$

$$\begin{aligned} \Pi_{3,1,2} &= \frac{\partial}{\partial \sigma_{11,22}} |S'_1 - S''_2|^a = \left(\frac{1}{2} L'_{1,2} + \frac{1}{2} L'_{3,4} \Delta'_4 / \sqrt{\Delta'_2} - L''_{31,32} \right) \\ &\cdot \left| \frac{1}{2} \Delta'_1 + \frac{1}{2} \sqrt{\Delta'_2} - \Delta''_3 \right|^{(a-1)} \cdot \text{sign} \left(\frac{1}{2} \Delta'_1 + \frac{1}{2} \sqrt{\Delta'_2} - \Delta''_3 \right) \end{aligned} \quad (4.26c)$$

$$\begin{aligned} \Pi_{4,1,2} &= \frac{\partial}{\partial \sigma_{11,22}} |S'_2 - S''_1|^a = \left(\frac{1}{2} L'_{1,2} - \frac{1}{2} L'_{3,4} \Delta'_4 / \sqrt{\Delta'_2} - \frac{1}{2} L''_{1,2} - \frac{\frac{1}{2} L''_{3,4} \Delta''_4}{\sqrt{\Delta''_2}} \right) \\ &\cdot \left| \frac{1}{2} \Delta'_1 - \frac{1}{2} \sqrt{\Delta'_2} - \frac{1}{2} \Delta''_1 - \frac{1}{2} \sqrt{\Delta''_2} \right|^{(a-1)} \cdot \text{sign} \left(\frac{1}{2} \Delta'_1 - \frac{1}{2} \sqrt{\Delta'_2} - \frac{1}{2} \Delta''_1 \right. \\ &\quad \left. - \frac{1}{2} \sqrt{\Delta''_2} \right) \end{aligned} \quad (4.26d)$$

$$\begin{aligned} \Pi_{5,1,2} &= \frac{\partial}{\partial \sigma_{11,22}} |S'_2 - S''_2|^a = \left(\frac{1}{2} L'_{1,2} - \frac{1}{2} L'_{3,4} \Delta'_4 / \sqrt{\Delta'_2} - \frac{1}{2} L''_{1,2} + \frac{\frac{1}{2} L''_{3,4} \Delta''_4}{\sqrt{\Delta''_2}} \right) \\ &\cdot \left| \frac{1}{2} \Delta'_1 - \frac{1}{2} \sqrt{\Delta'_2} - \frac{1}{2} \Delta''_1 + \frac{1}{2} \sqrt{\Delta''_2} \right|^{(a-1)} \cdot \text{sign} \left(\frac{1}{2} \Delta'_1 - \frac{1}{2} \sqrt{\Delta'_2} - \frac{1}{2} \Delta''_1 \right. \\ &\quad \left. + \frac{1}{2} \sqrt{\Delta''_2} \right) \end{aligned} \quad (4.26e)$$

$$\begin{aligned} \Pi_{6,2} = \frac{\partial}{\partial \sigma_{11,22}} |S'_2 - S''_3|^a &= \left(\frac{1}{2} L'_{1,2} - \frac{1}{2} L'_{3,4} \Delta'_4 / \sqrt{\Delta'_2} - L''_{31,32} \right) \\ &\cdot \left| \frac{1}{2} \Delta'_1 - \frac{1}{2} \sqrt{\Delta'_2} - \Delta''_3 \right|^{(a-1)} \cdot \text{sign} \left(\frac{1}{2} \Delta'_1 - \frac{1}{2} \sqrt{\Delta'_2} - \Delta''_3 \right) \end{aligned} \quad (4.26f)$$

$$\begin{aligned} \Pi_{7,2} = \frac{\partial}{\partial \sigma_{11,22}} |S'_3 - S''_1|^a &= \left(L'_{31,32} - \frac{1}{2} L''_{1,2} - \frac{\frac{1}{2} L''_{3,4} \Delta''_4}{\sqrt{\Delta''_2}} \right) \\ &\cdot \left| \Delta'_3 - \frac{1}{2} \Delta''_1 - \frac{1}{2} \sqrt{\Delta''_2} \right|^{(a-1)} \cdot \text{sign} \left(\Delta'_3 - \frac{1}{2} \Delta''_1 - \frac{1}{2} \sqrt{\Delta''_2} \right) \end{aligned} \quad (4.26g)$$

$$\begin{aligned} \Pi_{8,2} = \frac{\partial}{\partial \sigma_{11,22}} |S'_3 - S''_2|^a &= \left(L'_{31,32} - \frac{1}{2} L''_{1,2} + \frac{\frac{1}{2} L''_{3,4} \Delta''_4}{\sqrt{\Delta''_2}} \right) \\ &\cdot \left| \Delta'_3 - \frac{1}{2} \Delta''_1 + \frac{1}{2} \sqrt{\Delta''_2} \right|^{(a-1)} \cdot \text{sign} \left(\Delta'_3 - \frac{1}{2} \Delta''_1 + \frac{1}{2} \sqrt{\Delta''_2} \right) \end{aligned} \quad (4.26h)$$

$$\Pi_{9,2} = \frac{\partial}{\partial \sigma_{11,22}} |S'_3 - S''_3|^a = (L'_{31,32} - L''_{31,32}) |\Delta'_3 - \Delta''_3|^{(a-1)} \cdot \text{sign}(\Delta'_3 - \Delta''_3) \quad (4.26i)$$

Finally, by replacing $\partial\sigma/\partial\sigma_{11}$ and $\partial\sigma/\partial\sigma_{11}$ in Eq. (4-6), r_θ associated to Yld2004-18p can be calculated.

4.1.2 Predicted Anisotropic Data (flow stress and r-value)

By replacing the defined F_θ , $\partial\sigma/\partial\sigma_{11}$, and $\partial\sigma/\partial\sigma_{22}$ for each yield function in Eqs. (4-2) and (4-6), the distribution of the flow stress ratio (normalized w.r.t. the flow stress in the rolling direction) and r-value can be predicted. Figure 4-3-Figure 4-20 show a comprehensive comparison between the results predicted using Hill's family (Hill48 and Hill90) and Barlat's family (Barlat89, Yld2000-2d, and Yld2004-18p) of yield functions, and the experimental data for DP600, TRIP780, and AA5182-O, at different strain rates.

It should be noted that for Hill48 (Section 3.1.1.1), Hill90 (Section 3.1.2.1), and Barlat89 (Section 3.1.3.1) two calibration procedures were used, and the results of both are presented here. The experimental input data presented in the following graphs are summarized in Table 3.2, Table 3.9, and Table 3.16 for DP600, TRIP780, and AA5182-O, respectively, for different strain rates. It is unfortunate that the experimental data were only available for 0°, 45°, and 90°, and not for every 15 degrees from the RD. However, unlike the HCP metals, a smooth and continuous variation of anisotropic data w.r.t. the tension angle is expected to be observed for BCC and FCC metals (the three used sheet materials in this study).

The purpose of this work is to update the anisotropy coefficients w.r.t. strain rate in the rate-dependent constitutive material model, so it is important to demonstrate the flexibility of each yield function at different strain rate regimes. Therefore, the experimental and predicted in-plane distribution of the flow stress and the r-value are shown in Figure 4-3-Figure 4-20, for 0.001, 0.1, 1, 10, 100 and 1000 s⁻¹ strain rates. It should be noted that, since the experimental data were used to identify the anisotropy coefficients, the calculations are not completely predictive. However, the main point of these graphs is to evaluate the ability of each yield function to describe the whole set of anisotropic data (flow stresses and r-values) at various strain rates.

Figure 4-3a,b-Figure 4-20a,b show the results predicted by Hill's family of yield functions at various strain rates. In all cases, the results show that Hill48-r.value (calibrated based on r-values) and Hill48-stress (calibrated based on flow stresses) are not able to reproduce the variation of the experimental flow stresses and the r-value, respectively. The inability of Hill's family of yield functions to reproduce the experimental trends was expected due to the nature of the procedures used to calibrate these models. Results show that Hill90-stress is somewhat able to capture the average variation of experimental r-value, which is an advantage of this model compared to Hill48-stress. Also, Hill90-r.value is more or less able to predict the average flow stress variation, which makes this model superior to Hill48-r.value. Among all Hill's family of yield functions, it is shown that flow stress and r-value directionalities are best described by Hill90-stress for the entire range of strain rate and for all three materials.

Figure 4-3c,d-Figure 4-20c,d show experimental normalized flow stress and r-value anisotropies in addition to values predicted with Barlat's family of yield functions. As shown in these figures, Yld2000-2d and Yld2004-18p best capture both flow stress and r-value anisotropies, while Barlat89-r.value and Barlat89-stress underestimate or overestimate the flow stress and r-value. In contrast with Barlat89, both Yld2000-2d and Yld2004-18p result in an accurate simulation of the experimental normalized uniaxial flow stress as well as the r-value distribution. A close agreement can be seen between the distribution curves of Yld2004-18p and Yld2000-2d, since the additional data points (15° , 30° , 60° , and 75°) required for the calibration of Yld2004-18p were calculated using Yld2000-2d, as indicated in Table 3.2, Table 3.9, and Table 3.16, for DP600, TRIP780, and AA5182-O, respectively. It should be noted that, in the event that the experimental input data was available every 15 degrees, it would be expected that Yld2004-18p would be in better agreement with the experimental values compared to Yld2000-2d, due to its more flexible formulation and more comprehensive calibration scheme. However, if only three data points (0° , 45° , and 90°) are available, Yld2000-2d is able to exactly predict the experimental data, while Yld2004-18p may not be as accurate as Yld2000-2d, due to only minimizing a single error function instead of solving a system of equations (like Yld2000-2d). These small differences can be seen more clearly in Figure 4-5c,d, Figure 4-12 c,d, and Figure 4-17 c,d, for DP600, TRIP780, and AA5182-O, respectively. The strong performance of Yld2000-2d and Yld2004-18p is associated with their formulations and calibration procedures.

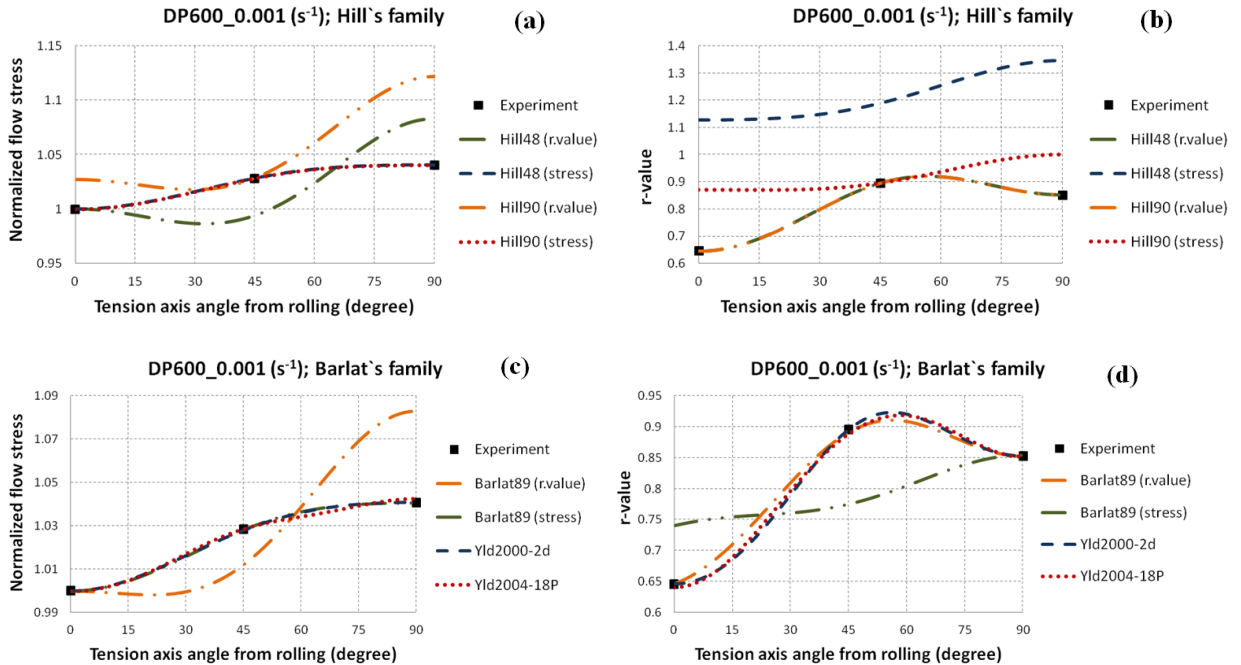


Figure 4-3. Measured and predicted anisotropy of the flow stress and the r-value; for DP600 at 0.001 s^{-1}

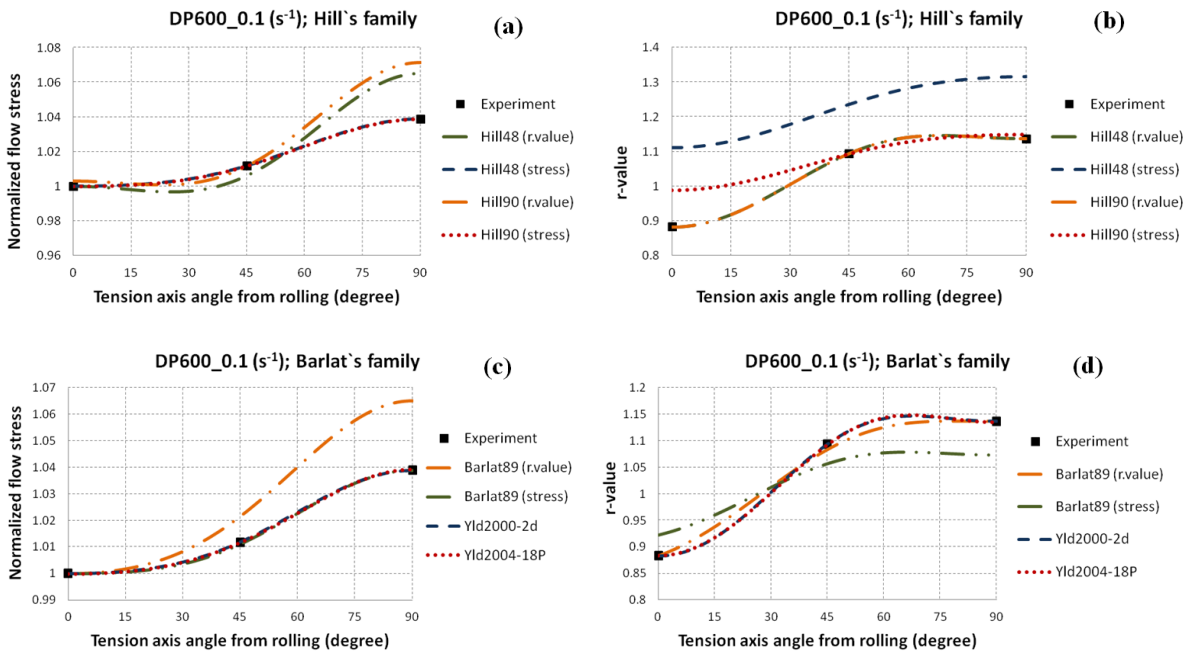


Figure 4-4. Measured and predicted anisotropy of the flow stress and the r-value; for DP600 at 0.1 s^{-1}

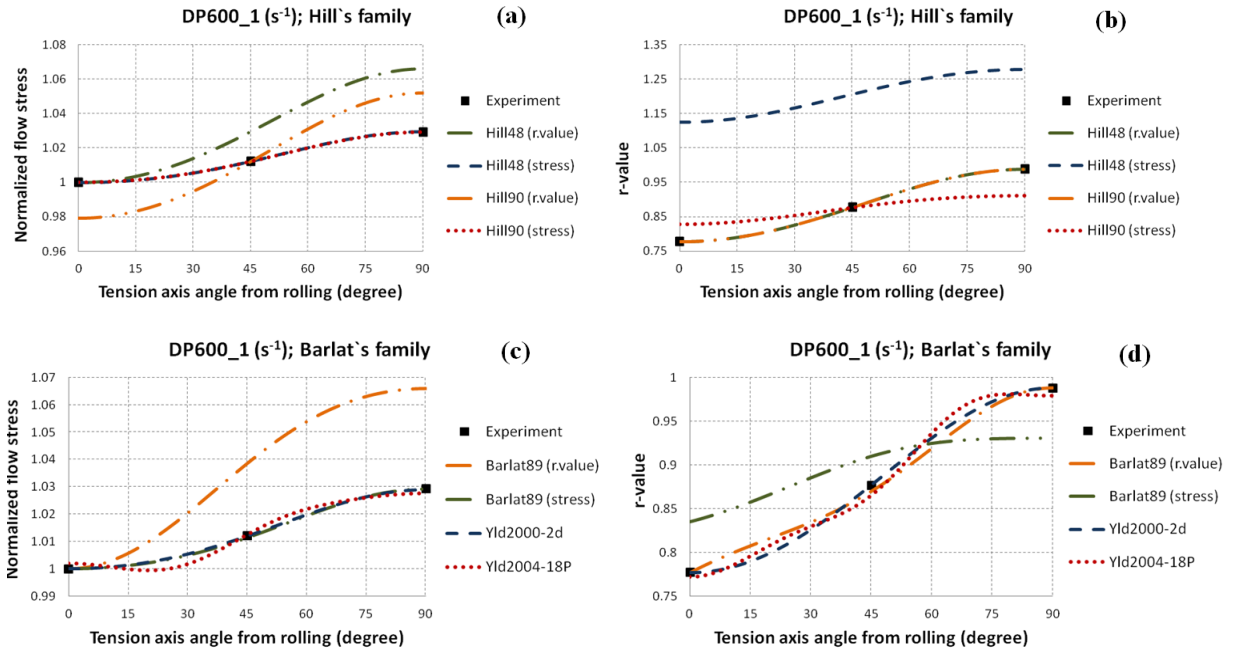


Figure 4-5. Measured and predicted anisotropy of the flow stress and the r -value; for DP600 at 1 s^{-1}

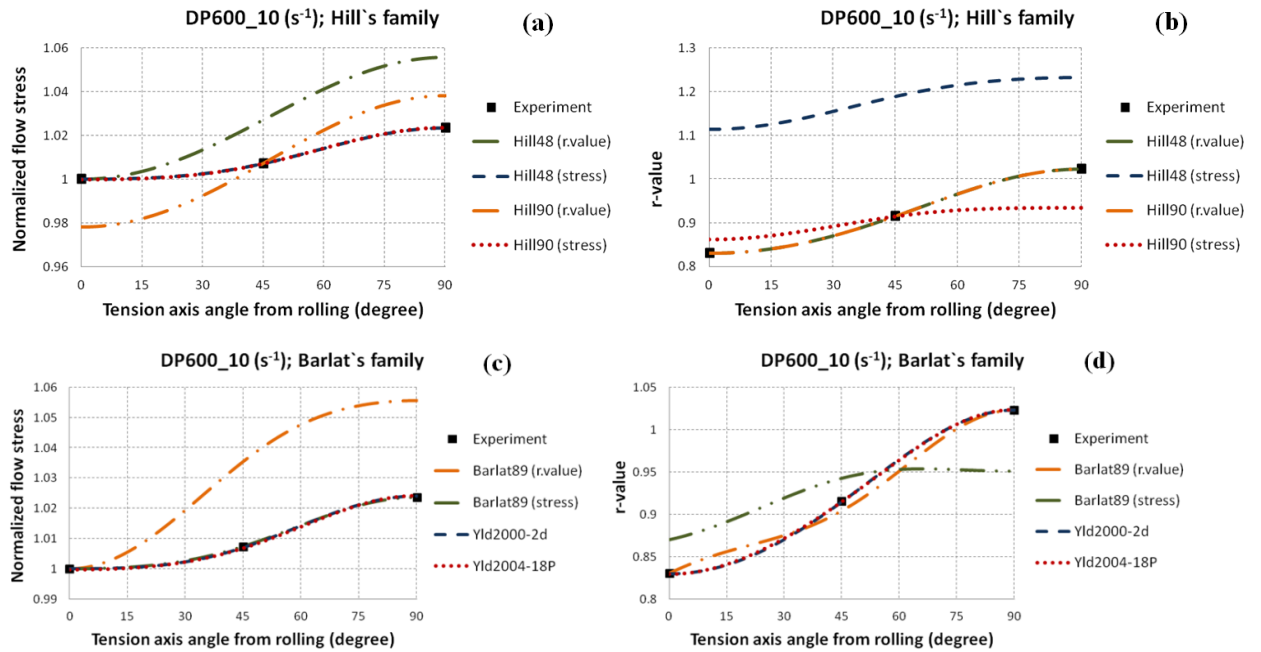


Figure 4-6 Measured and predicted anisotropy of the flow stress and the r -value; for DP600 at 10 s^{-1}

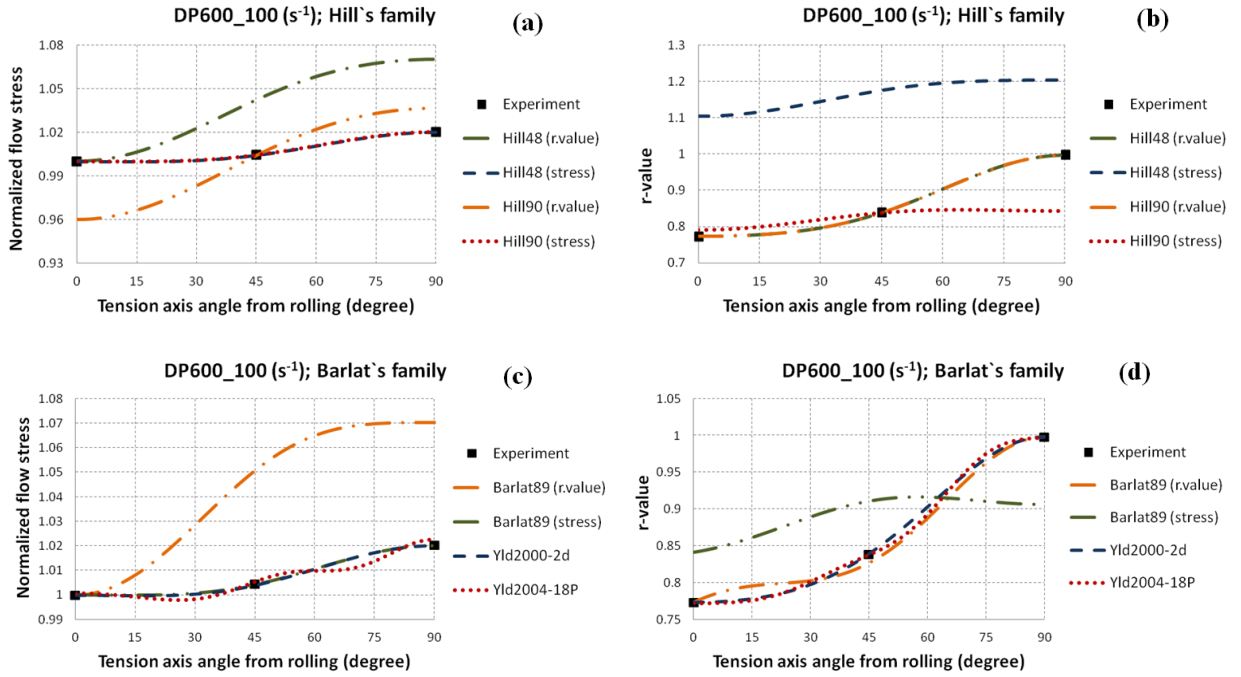


Figure 4-7 Measured and predicted anisotropy of the flow stress and the r-value; for DP600 at 100 s^{-1}

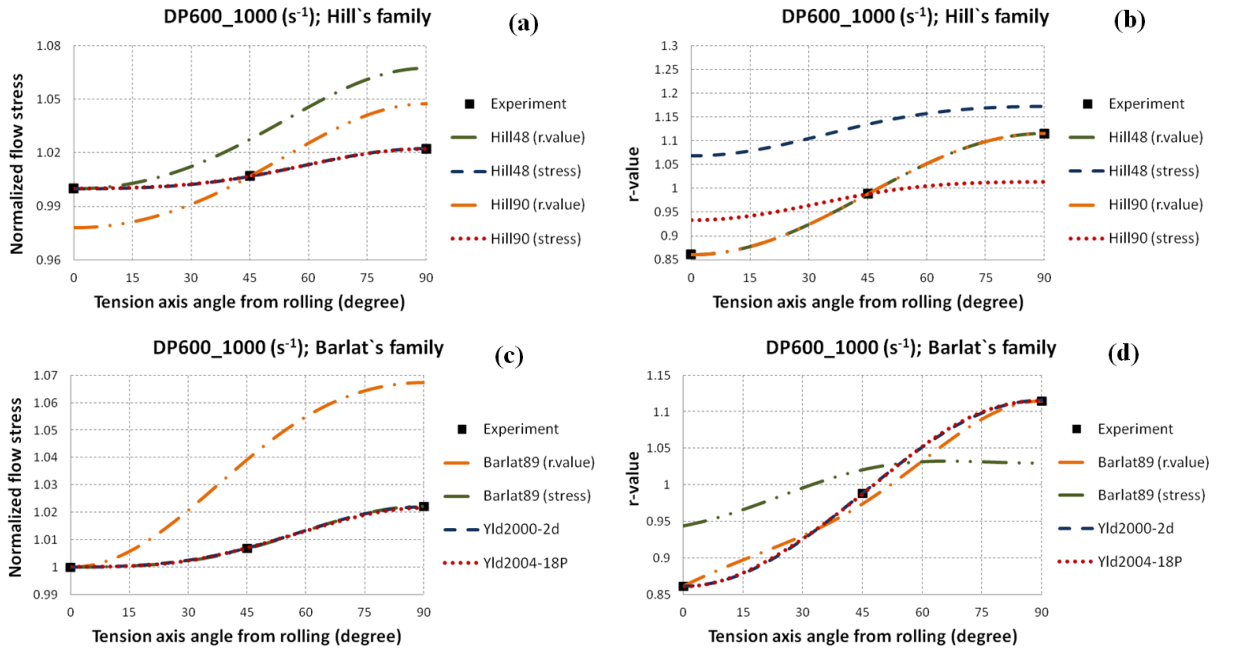


Figure 4-8 Measured and predicted anisotropy of the flow stress and the r-value; for DP600 at 1000 s^{-1}

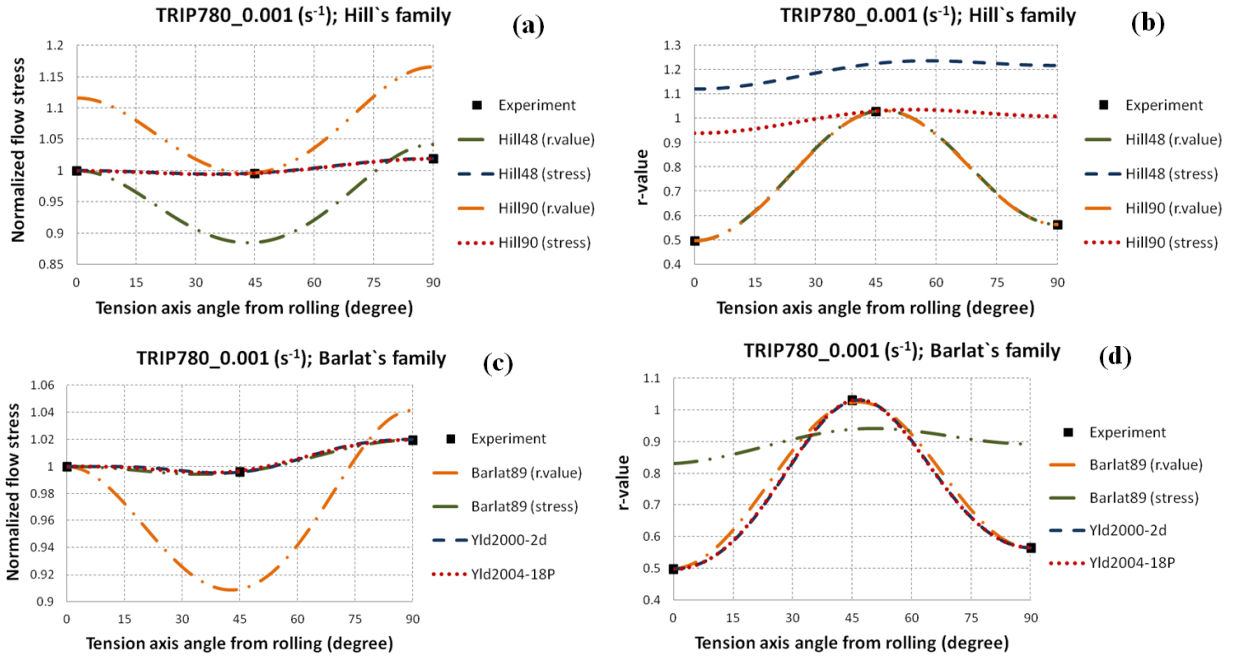


Figure 4-9 Measured and predicted anisotropy of the flow stress and the r-value; for TRIP780 at 0.001 s^{-1}

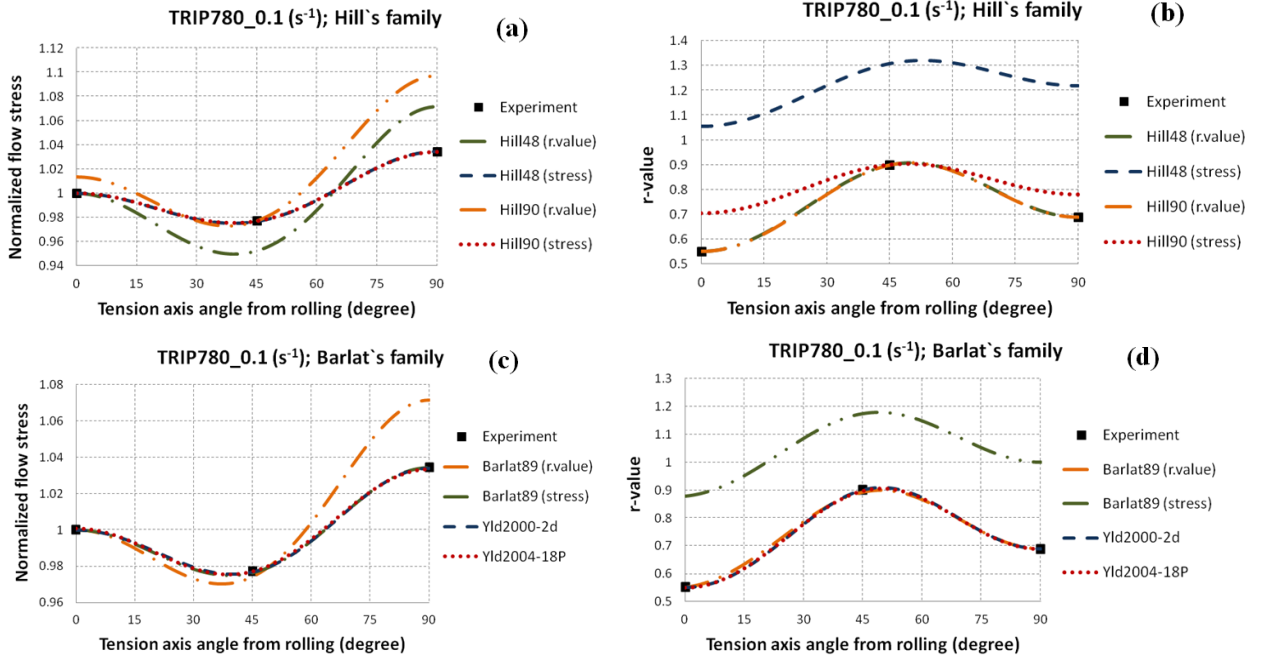


Figure 4-10 Measured and predicted anisotropy of the flow stress and the r-value; for TRIP780 at 0.1 s^{-1}

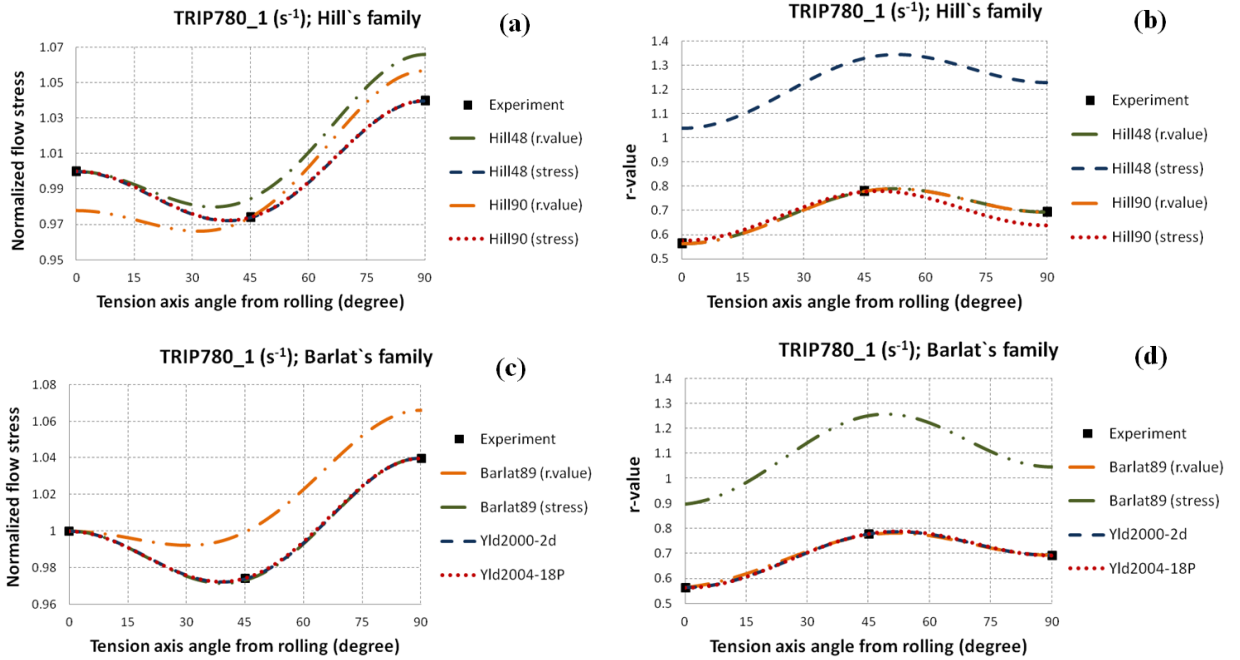


Figure 4-11 Measured and predicted anisotropy of the flow stress and the r -value; for TRIP780 at 1 s^{-1}

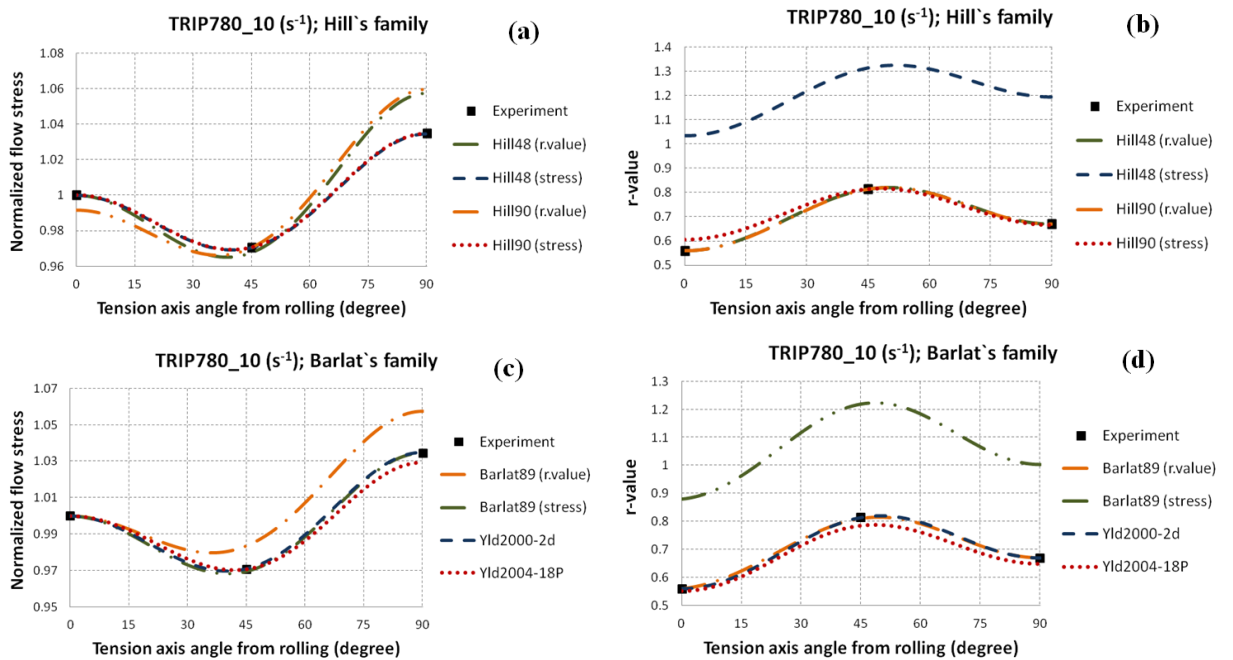


Figure 4-12 Measured and predicted anisotropy of the flow stress and the r -value; for TRIP780 at 10 s^{-1}

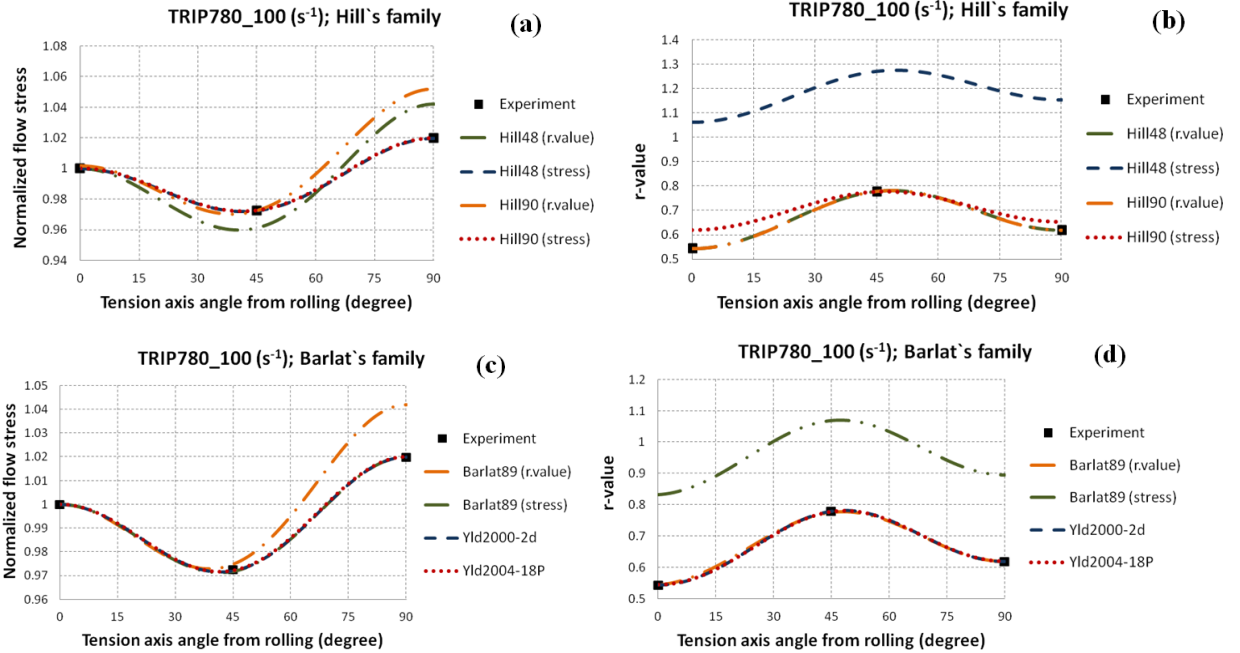


Figure 4-13 Measured and predicted anisotropy of the flow stress and the r-value; for TRIP780 at 100 s^{-1}

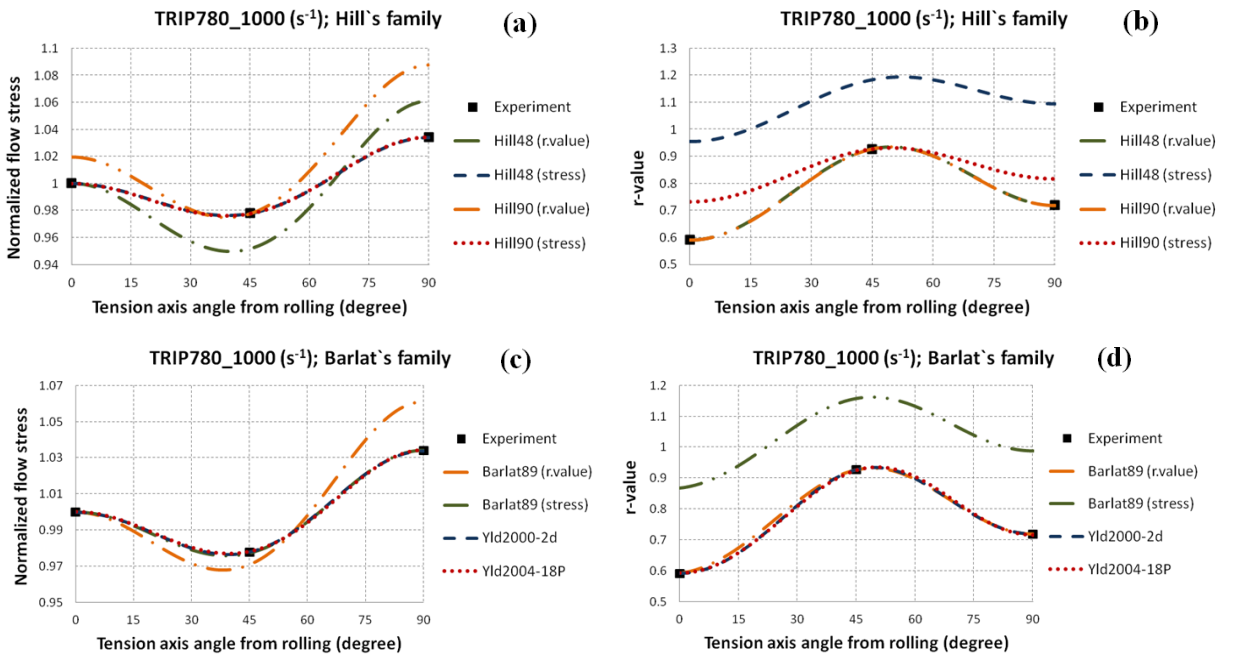


Figure 4-14 Measured and predicted anisotropy of the flow stress and the r-value; for TRIP780 at 1000 s^{-1}

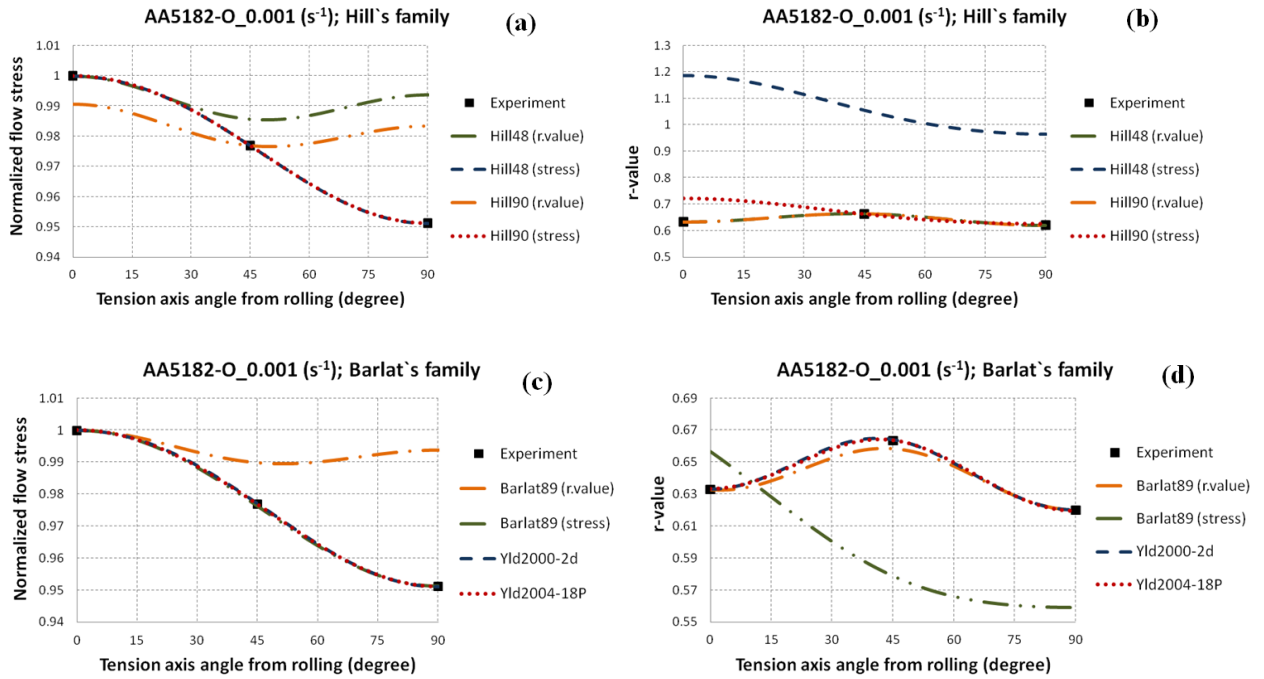


Figure 4-15 Measured and predicted anisotropy of the flow stress and the r-value; for AA5182-O at 0.001 s^{-1}

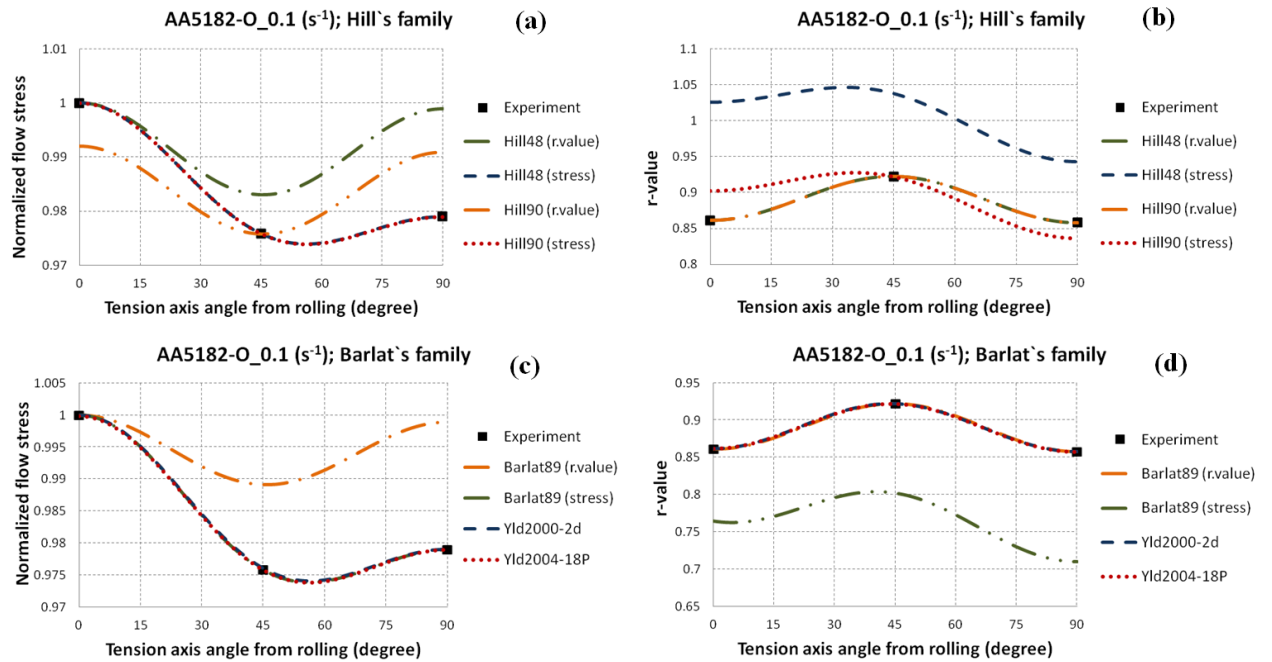


Figure 4-16 Measured and predicted anisotropy of the flow stress and the r-value; for AA5182-O at 0.1 s^{-1}

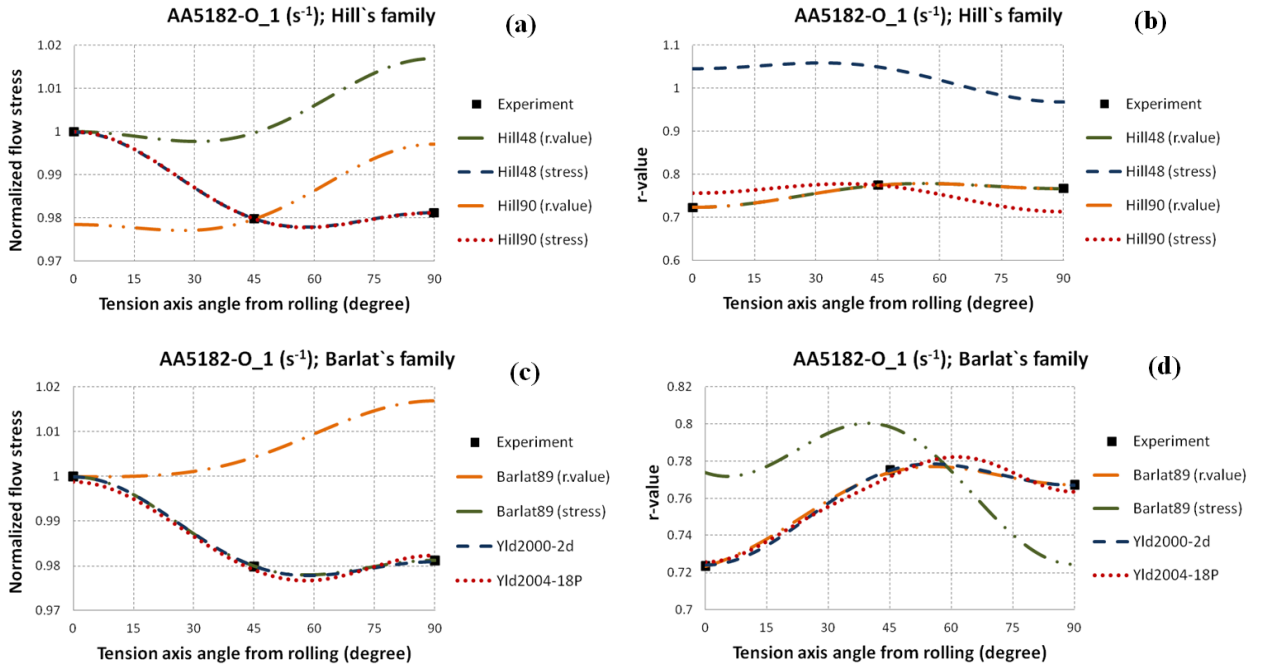


Figure 4-17 Measured and predicted anisotropy of the flow stress and the r-value; for AA5182-O at 1 s^{-1}

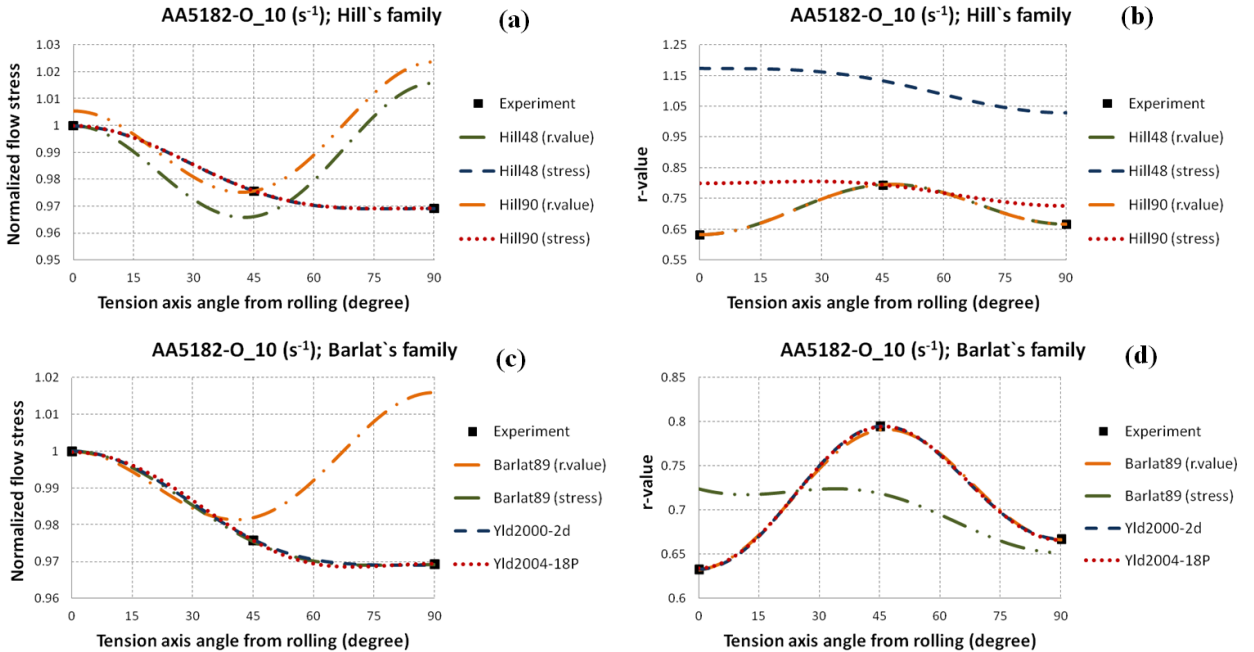


Figure 4-18 Measured and predicted anisotropy of the flow stress and the r-value; for AA5182-O at 10 s^{-1}

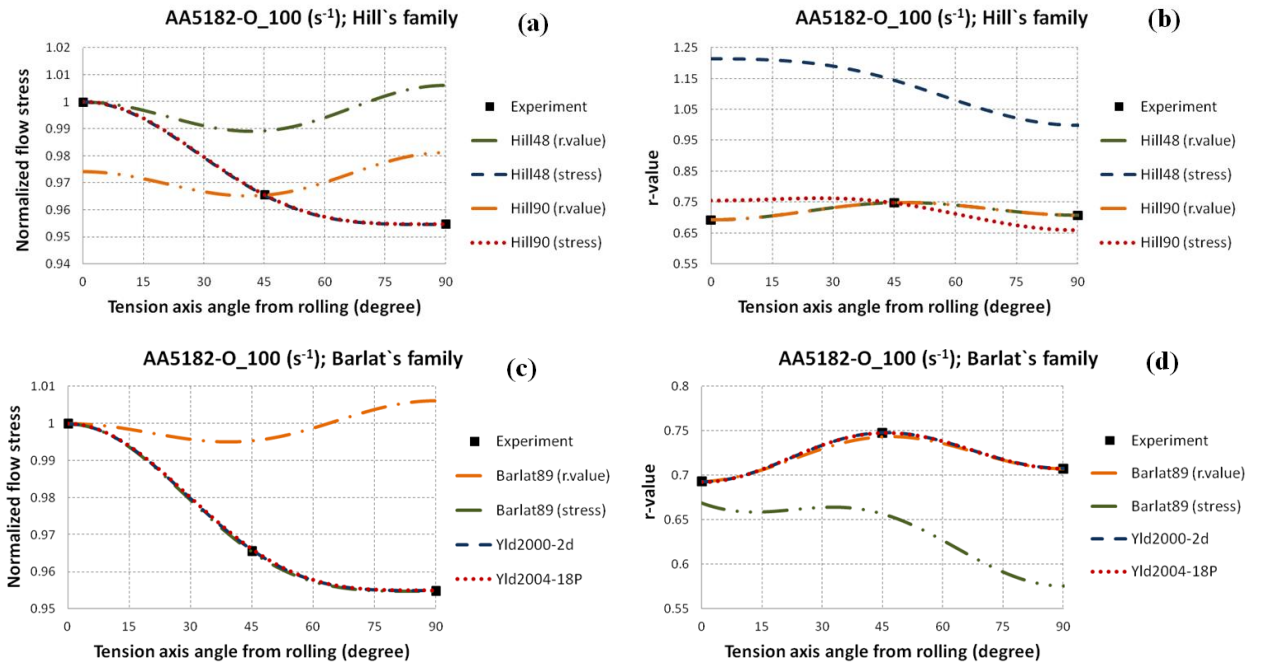


Figure 4-19 Measured and predicted anisotropy of the flow stress and the r-value; for AA5182-O at 100 s^{-1}

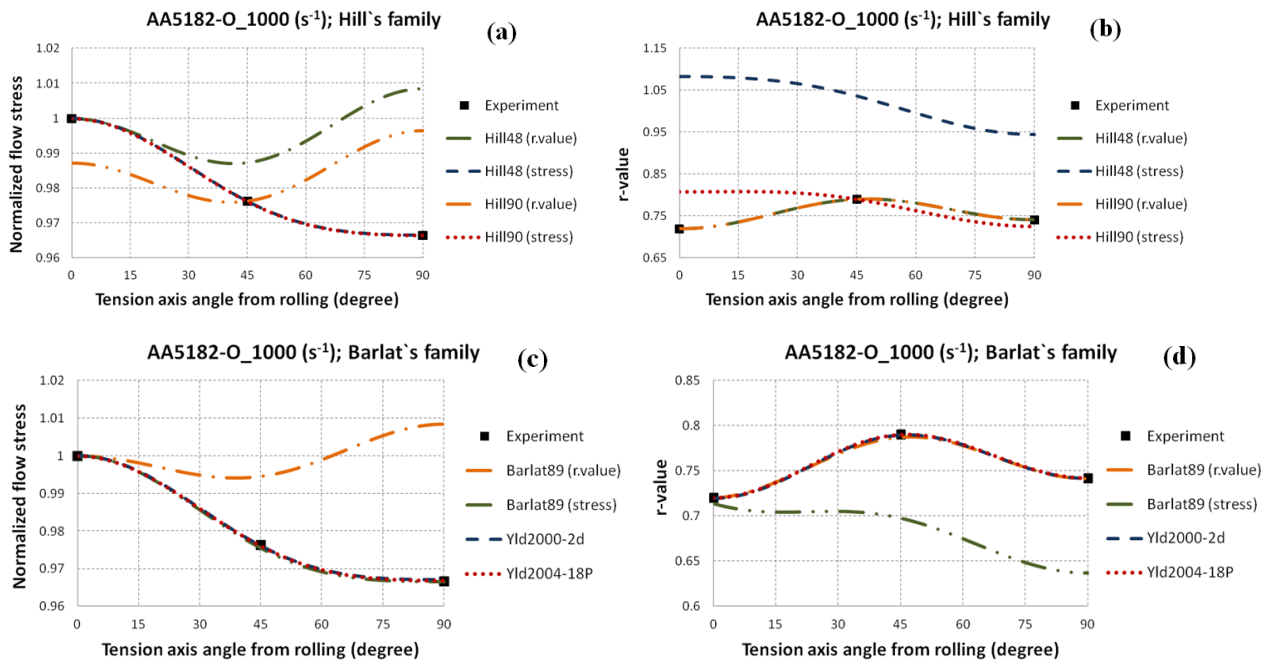


Figure 4-20 Measured and predicted anisotropy of the flow stress and the r-value; for AA5182-O at 1000 s^{-1}

Based on this comprehensive study of the performance of different yield functions, it was found that Yld2000-2d and Yld2004-18p best capture the anisotropic behaviour of

DP600, TRIP780, and AA5182-O at all strain rates. In order to show the effect of strain rate on the predicted anisotropic data, Yld2000-2d was selected as the preferred yield function. Figure 4-21-Figure 4-23 show the distribution curves predicted by Yld2000-2d at different strain rates for the three materials. Due to the ability of Yld2000-2d to exactly capture the anisotropic data at 0° , 45° and 90° to the RD, the change in these curves is a good indication of the effect of strain rate on the anisotropy of the material. Figure 4-21 a shows that by increasing the strain rate, the uniaxial flow stress of DP600 decreases for the entire range of orientations from 0° to 90° , which emphasizes the importance of updating the anisotropy coefficients of DP600 w.r.t. strain rate (by applying the 4th-order polynomial functions, as given in Table 3.23 for DP600). Also, Figure 4-22a and Figure 4-23a show the changes of the predicted flow stress w.r.t. strain rate for TRIP780 and AA5182-O, respectively. In comparison with DP600, these two materials show less sensitivity of the Yld2000-2d anisotropy coefficients to strain rate, in-particular at 1000 s^{-1} . It can be observed that Figure 4-21b and Figure 4-23b show a sudden increase in the r-values from 0.001 s^{-1} to 0.1 s^{-1} for the entire range of orientations, whereas no continuous increase or decrease can be seen for the entire range of strain rates.

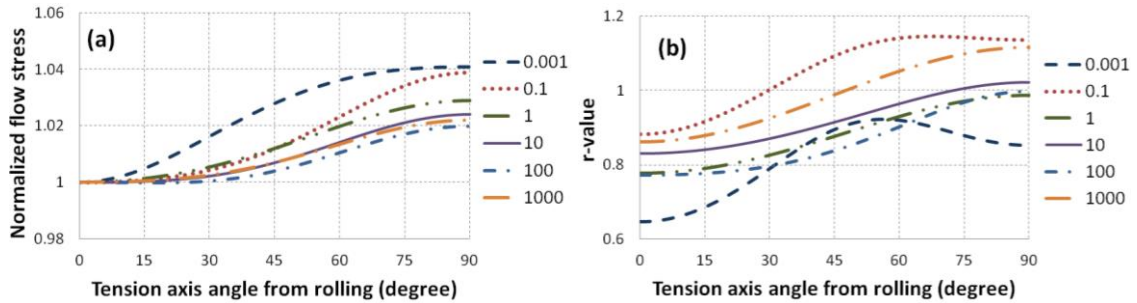


Figure 4-21 Anisotropy variation for DP600 as predicted by Yld2000-2d at various strain rates; a) normalized flow stress b) r-value

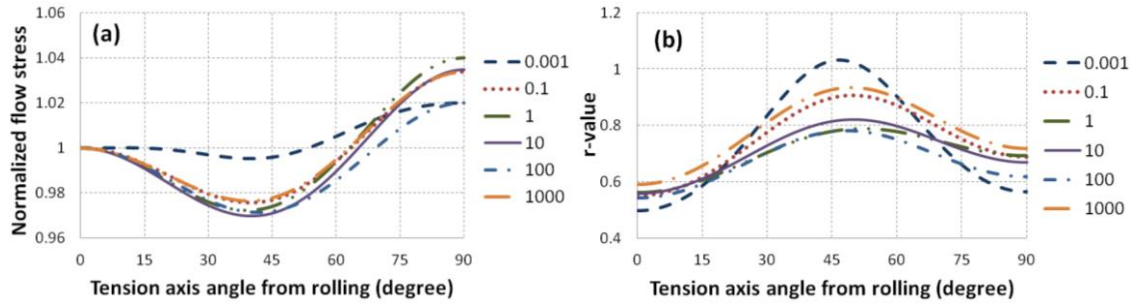


Figure 4-22 Anisotropy variation for TRIP780 as predicted by Yld2000-2d at various strain rates; a) normalized flow stress b) r-value

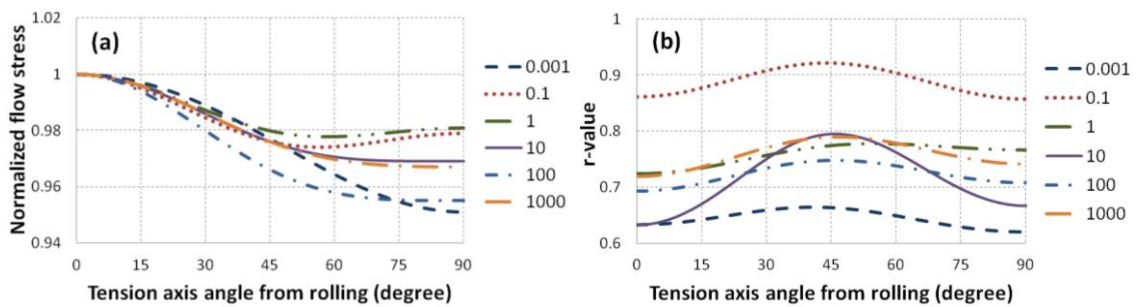


Figure 4-23 Anisotropy variation for AA5182-O as predicted by Yld2000-2d at various strain rates; a) normalized flow stress b) r-value

4.2 Effect of Updating Anisotropy Coefficients on the Flow Surface

In order to understand the influence of updating anisotropy for the three materials (DP600, TRIP780, and AA5182-O), the flow surfaces were derived and plotted in two-dimensional (2D) principal stress space for each strain rate by assuming the principal axes of stress and anisotropy coincide. This is an effective way to visualize the initial/subsequent flow state (flow surface shape) of a material in sheet metal forming processes where the strain rate may vary. For the sake of brevity, due to the accuracy of Yld2000-2d and the wide spread use of Hill48-r.value, only the influence of updating anisotropy coefficients on the flow surfaces predicted by Yld2000-2d and Hill48-r.value are presented here. However, a comprehensive comparison was completed to investigate the difference between Hill's and Barlat's families of yield functions when the anisotropy coefficients are updated according to the strain rate. Also, in order to consider the effect of the shear term the flow surfaces predicted by Yld2000-2d have been plotted for every 0.1 increment of normalized shear stress.

It should be noted that in all graphs the term “Quasistatic” represents the experimental or predicted results at 0.001 s^{-1} (the lowest strain rate) and the term “Updated” refers to the results obtained by adjusting the anisotropy coefficients at the current level of strain rate. For instance, if the graph is showing the results for 10 s^{-1} , the “Quasistatic” is associated with the results for 0.001 s^{-1} , while the “Updated” represents the results at 10 s^{-1} . Apart from the graphs showing the flow surfaces for every 0.1 increment of normalized shear stress, all other graphs represent the experimental and predicted data for two different normalized shear stress values: first, 0, and secondly, the value of the ratio of the flow stress in the diagonal direction w.r.t. the rolling direction (σ_{45}/σ_0) for each corresponding strain rate. It is noticeable that the value for σ_{45}/σ_0 can be changed from material to material and from strain rate to strain rate.

4.2.1 Comparison between the Updated and Quasistatic Yld2000-2d

Figures 4-24 to 4-26 show the differences in the flow surfaces of the three sheet materials predicted by Yld2000-2d in two different ways: Quasistatic and Updated anisotropy coefficients, for each level of strain rate. In these figures, the solid-line represents the flow surfaces using anisotropy coefficients associated with each corresponding strain rate (Updated), whereas the dotted-line represents the flow surfaces at 0.001 s^{-1} (Quasistatic).

Figure 4-24 shows an increasing effect of updating the anisotropy coefficients of DP600 in biaxial stress states, in-particular for strain rates above 100 s^{-1} . A non-negligible difference in the flow surfaces can be seen at higher strain rates for biaxial stress states, while this difference is smaller for the uniaxial stress state in TD. These differences emphasise the importance of updating anisotropy coefficients according to the strain rate for DP600 in FE simulations of rate-dependent sheet metal forming processes. Compared to DP600, the flow surfaces predicted by Yld2000-2d for TRIP780 show less sensitivity of the flow stresses to strain rate in biaxial stress states, as shown in Figure 4-25.

Figure 4-26 shows no difference between the Updated and Quasistatic flow surfaces in the biaxial stress states and only minor differences in the uniaxial stress state in TD, in

particular at intermediate strain rates (0.1, 1, and 10 s^{-1}) for AA5182-O. By comparing the predicted flow surfaces with the experimental data points, Figures 4-24 to 4-26 show that Yld2000-2d is able to accurately describe the anisotropy of the three materials at various strain rates under different stress-states. This is not surprising since Yld2000-2d is calibrated using all experimental uniaxial and biaxial data points, simultaneously.

4.2.2 Comparison between the Updated and Quasistatic Hill48-r.value

Figures 4-27 to 4-29 show the flow surfaces predicted by Hill48-r.value for the three materials in the given range of strain rate. The comparison between the predicted flow surfaces and the experimental data shows the inability of Hill48-r.value to accurately capture the anisotropic data of these three materials at various strain rates. However, results show that updating the anisotropy coefficients w.r.t. strain rate can help to improve the performance of the Hill48-r.value function, in-particular for the biaxial stress states. This improvement is more evident for DP600 and TRIP780 when the shear stress term is non-zero ($\sigma_{xy} = \sigma_{xx} = \sigma_{yy} = \sigma_{45}/2$), as shown in Figures 4-27 and 4-28. It can be concluded that, although Hill48-r.value is not a suitable yield function, its overall performance can be slightly improved by updating its anisotropy coefficients.

4.2.3 Comparison between the Updated Hill's family and Updated Barlat's family

Figures 4-30 to 4-32 show the flow surfaces of DP600, TRIP780, and AA5182-O predicted by Hill's and Barlat's families of yield functions when the anisotropy parameters are updated for each level of strain rate. Among Hill's family, Hill48-stress and Hill90-stress functions show a better correlation between the experimental data and the predicted flow surfaces for the above-mentioned materials at various strain rates, which is because the experimental flow stresses were used in the calibration procedure. A difference can be seen in the curvature of the flow surfaces predicted by Hill48-stress and by Hill90-stress, which is due to the different formulations and exponents of these two functions. For all strain rate regimes, this difference is more significant for the plane-strain, pure-shear stress states, as well as when the shear stress ratio is non-zero.

Figures 4-30 to 4-32 show that among Barlat's family of yield functions, Barlat89 is not able to reproduce the experimental data for biaxial stress states at various strain rates. In addition to the inaccuracy in the biaxial stress state, Barlat89-r.value shows a remarkable deviation from the uniaxial flow stress data in the TD at almost all strain rates and for all three materials. Results show that Yld2000-2d and Yld2004-18p best capture the experimental data points for all three materials for the entire range of strain rates. A small difference in the curvatures of the flow surfaces predicted by these two yield functions can be seen at several strain rates (for instance, DP600_0.001 s-1, TRIP780_10 s-1, AA5182-O_0.001 s-1), in particular in the pure-shear and plane-strain stress states, as well as when the shear stress ratio is increased. This is due to the difference in the mathematical formulation and calibration approach of these two functions. It should be noted that Figure 4-32 shows a sharper curvature in the biaxial stress state for the flow surfaces of AA5182-O, compared to the flow surfaces of DP600 and TRIP780, which is basically caused by the difference of the exponent values for these materials ($a = 6$ for DP600 and TRIP780 and $a = 8$ for AA5182-O). These values are widely accepted as reliable exponents for these materials based on the extensive experimental work that has been carried out to develop and validate the different Barlat yield functions (Barlat et al., 2003; 2005). It is noticeable that, generally, the Hill's family of flow surfaces have more rounded shapes than Barlat's family of flow surfaces, due to the difference in the exponent of these yield functions. This difference is more significant for AA5182-O, since Barlat's yield functions have the highest exponent value ($a = 8$).

In order to select the most accurate yield function among the Hill90, Yld2000-2d, and Yld2004, additional experimental data points, particularly in pure-shear and plane-strain stress states are needed at various strain rates. However, acquiring the required experimental data points at intermediate and high strain rate regimes is very challenging, if not impossible, and advanced machines, tooling, and specific testing procedures are required. In order to evaluate the predicted flow surfaces by these three yield functions, some comments can still be made in spite of the lack of a complete set of experimental data points. The curvatures of the computed Yld2000-2d and Yld2004-18p flow surfaces are sharper, particularly in the biaxial stress state, as compared with the flow surfaces predicted by Hill90-stress at various strain rates. Also, compared to Yld2000-2d and

Yld2004-18p, the flow surfaces calculated by Hill90-stress show a smaller radius of curvature, in-particular in the pure-shear stress state.

Since uniaxial and biaxial flow stresses and r-values are required in the calibration of both Updated Yld2000-2d and Yld2004-18p, it can be concluded that these functions are more robust compared to the Updated Hill90-stress. In addition, experimental observations for the quasi-static condition for different steel grades and aluminum alloys (Barlat et al., 2003; 2005) showed that the Updated Yld2000-2d and Yld2004-18p flow surfaces correlate better with the experimental data for different stress states, such as pure-shear and plane-strain (which are not available here). This conclusion for the quasi-static condition can be extended to higher strain rate regimes, if the yield functions are calibrated accurately for each corresponding strain rate, i.e., the anisotropy coefficients are updated w.r.t. strain rate. Therefore, it can be concluded that the Updated flow surfaces predicted by both Yld2000-2d and Yld2004-18p show the most accurate initial and subsequent flow surface shapes at various strain rates.

4.2.4 Comparison between the Updated Yld2000-2d and von Mises

Figures 4-33 to 4-35 show the comparison between the flow surfaces predicted by Updated Yld2000-2d and von Mises for DP600, TRIP780, and AA5182-O at various strain rates. As discussed above, the Updated flow surfaces computed by Yld2000-2d are considered to accurately describe the anisotropy of these sheet materials and therefore can be considered as references to compare with the von Mises flow surfaces. Figures 4-33 and 4-34 show some difference between the Yld2000-2d and von Mises flow surfaces in biaxial and plane-strain stress states for both DP600 and TRIP780. These differences decrease with increasing strain rate, but still remain considerable.

Figure 4-35 shows a substantial discrepancy between the flow surfaces predicted by Yld2000-2d and von Mises for AA5182-O, particularly in plane-strain stress states, and also when the shear stress ratio is high ($\sigma_{xy} = \sigma_{45}/2$). These differences are associated with the much higher exponent value ($a = 8$) of Yld2000-2d compared to the von Mises exponent value ($a = 2$). In contrast with DP600 and TRIP780, the predicted flow surfaces coincide with each other in the biaxial stress state due to the similar flow stresses

of AA5182-O in uniaxial tension in RD and in biaxial tension. Also, the same flow stresses are predicted by both Yld2000-2d and von Mises in pure shear for DP600, but small differences can be observed in the computed flow surfaces for TRIP780 and AA5182-O.

According to the observations from Figures 4-33 to 4-35, it can be concluded that in the FE simulations of EHF (or any other rate-dependent sheet metal forming process), updating the anisotropy according to strain rate can have a significant influence on the accuracy of the prediction of the sheet deformation history. For instance, significantly different residual strains and stresses would be expected in EHF simulations of DP600 and TRIP780, by using the updated Yld2000-2d instead of von Mises, when biaxial or plane-strain stress states tend to dominate. Even more significant differences would be expected in the predictions for AA5182-O in plane-strain stress states or when the shear stress ratio is significant. It should be noted that for DP600 and TRIP780, if the Yld2000-2d coefficients are not updated (only using the initial or Quasistatic anisotropy coefficients), the overestimation in the EHF simulation results would become less significant, since the differences between the updated Yld2000-2d and von Mises flow surfaces decrease with increasing strain rates.

4.2.5 Comparison between the Updated and Quasistatic Yld2000-2d at different levels of normalized shear stress

In order to more comprehensively investigate the effect of updating anisotropy coefficients, a comparison is now made between the Updated and Quasistatic flow surfaces predicted by Yld2000-2d at 0, 0.1, 0.2, 0.3, 0.4, and 0.5 levels of normalized shear stress (w.r.t. the uniaxial flow stress in RD) for DP600, TRIP780, and AA5182-O at various strain rates, as shown in Figures 4-36 to 4-38. As can be seen from Figure 4-36, for almost all strain rates, the difference between the Updated and Quasistatic flow surfaces becomes more significant as the value of the shear stress increases. Another observation is that for TRIP780 the difference between the Updated and Quasistatic flow surfaces is almost constant for the entire range of normalized shear stress at almost all strain rates, as shown in Figure 4-37. Also, Figure 4-38 shows that the difference between the Updated and Quasistatic flow surfaces is very small for AA5182-O for the entire

range of normalized shear stress increments and for almost all strain rates. The reason can be explained by the small difference between flow stress and r-value anisotropy in AA5182-O. Finally, it can be concluded that in the case of DP600 and TRIP780, there is a critical need to describe anisotropy behaviour of these materials accurately considering the wide range of strain rates that exist in the EHF process. An improvement in the FE results, such as residual stresses and strains, is expected by applying Updated Yld2000-2d. Observations showed that the anisotropy coefficients of Yld2000-2d for AA5182-O are much less sensitive to strain rate, compared to DP600 and TRIP780. Therefore, it is expected that only applying a Quasistatic Yld2000-2d in the EHF simulations of AA5182-O can be used to predict accurate results.

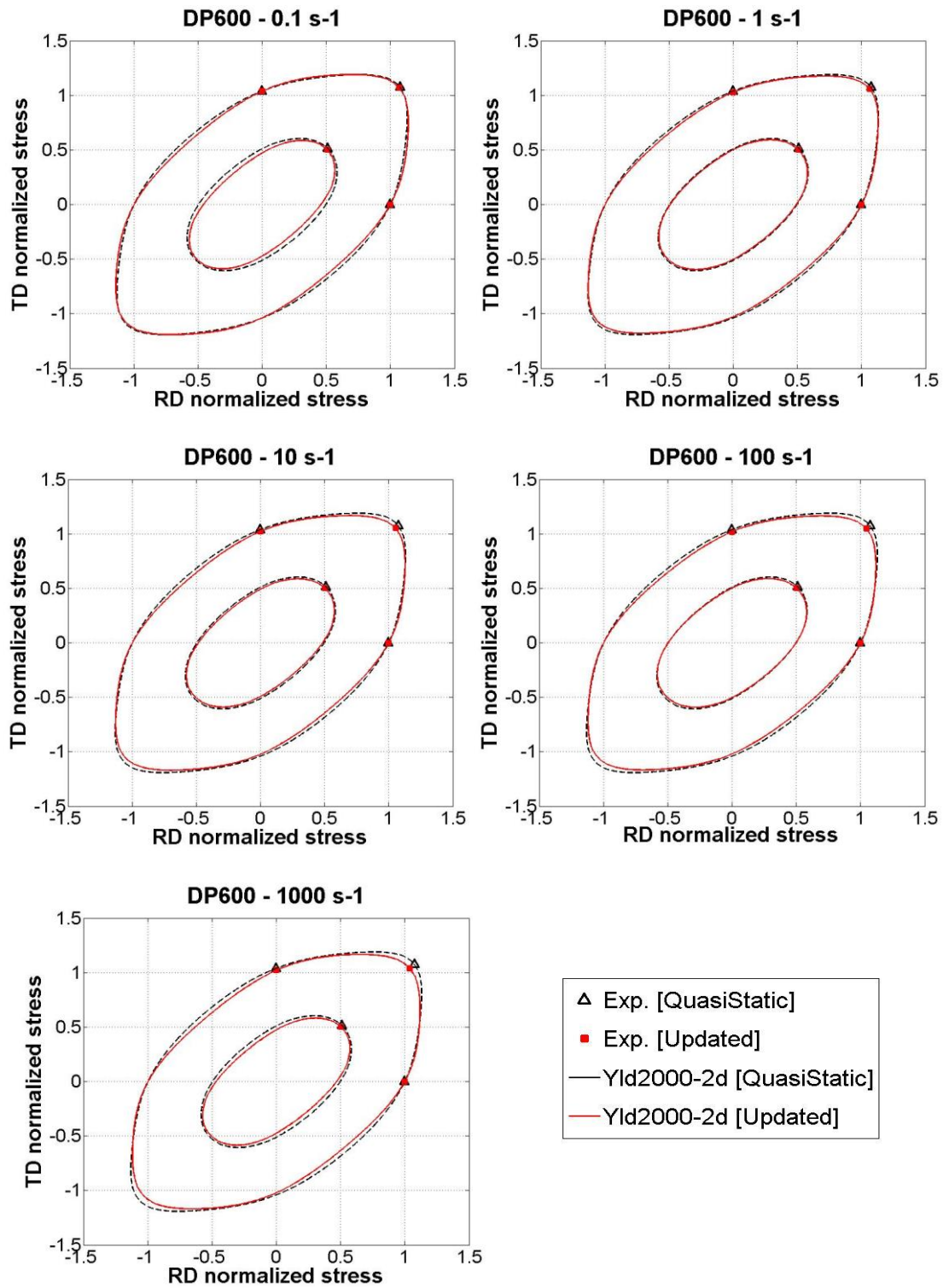


Figure 4-24 Flow surface for DP600 predicted by Yld2000-2d at various strain rates; using initial and updated anisotropy coefficients

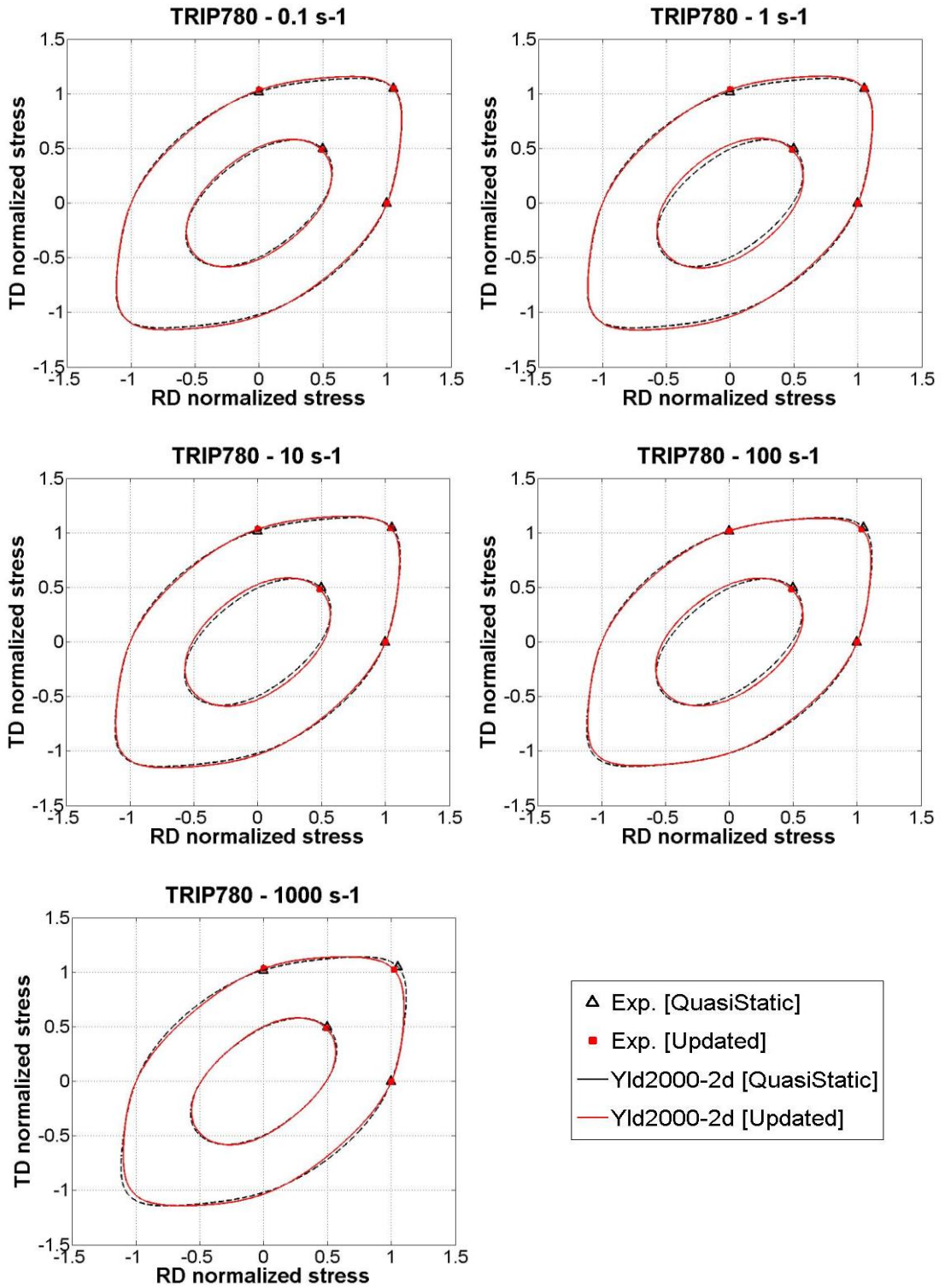


Figure 4-25 Flow surface for TRIP780 predicted by Yld2000-2d at various strain rates; using initial and updated anisotropy coefficients

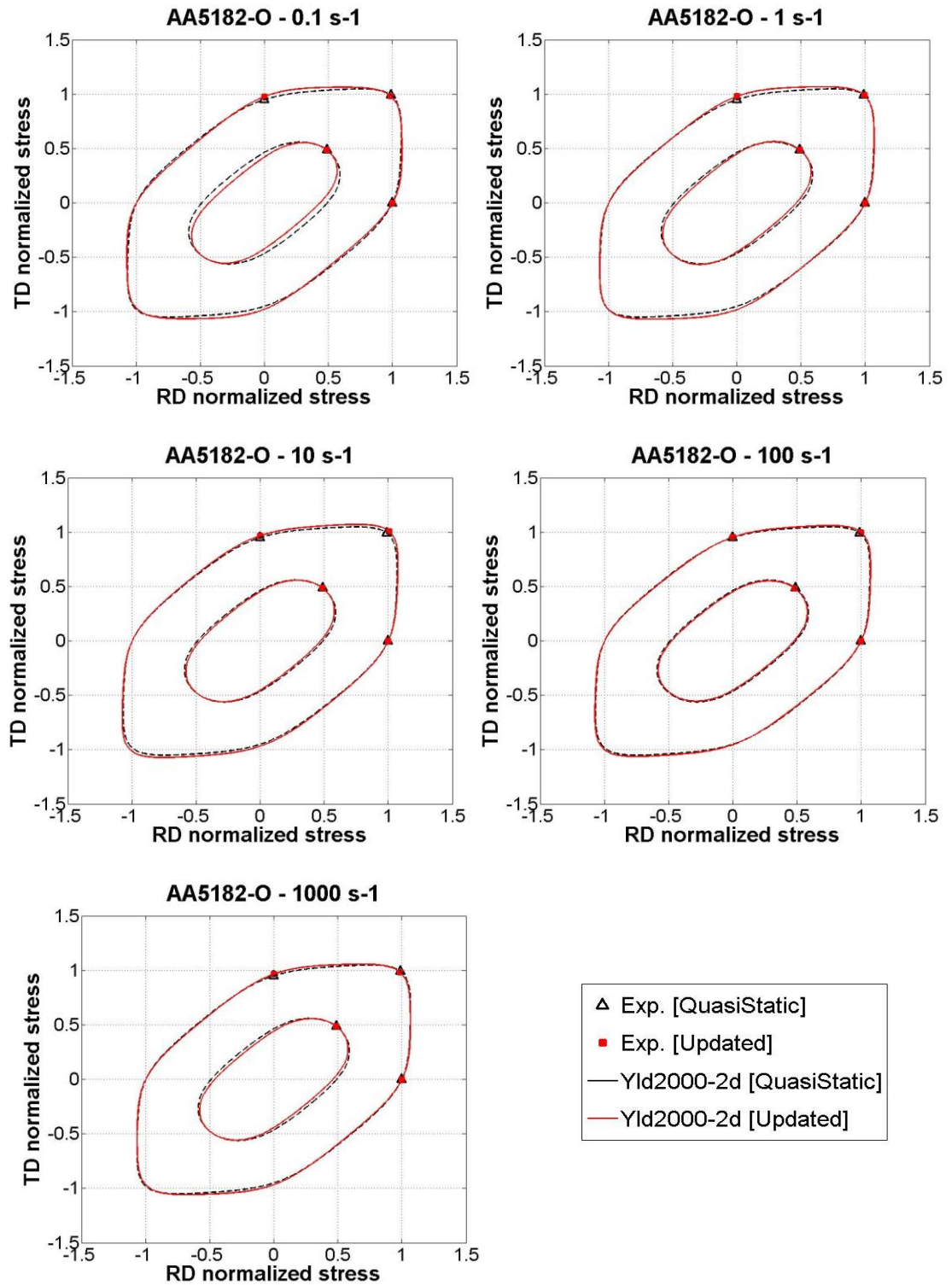


Figure 4-26 Flow surface for AA5182-O predicted by Yld2000-2d at various strain rates; using initial and updated anisotropy coefficients

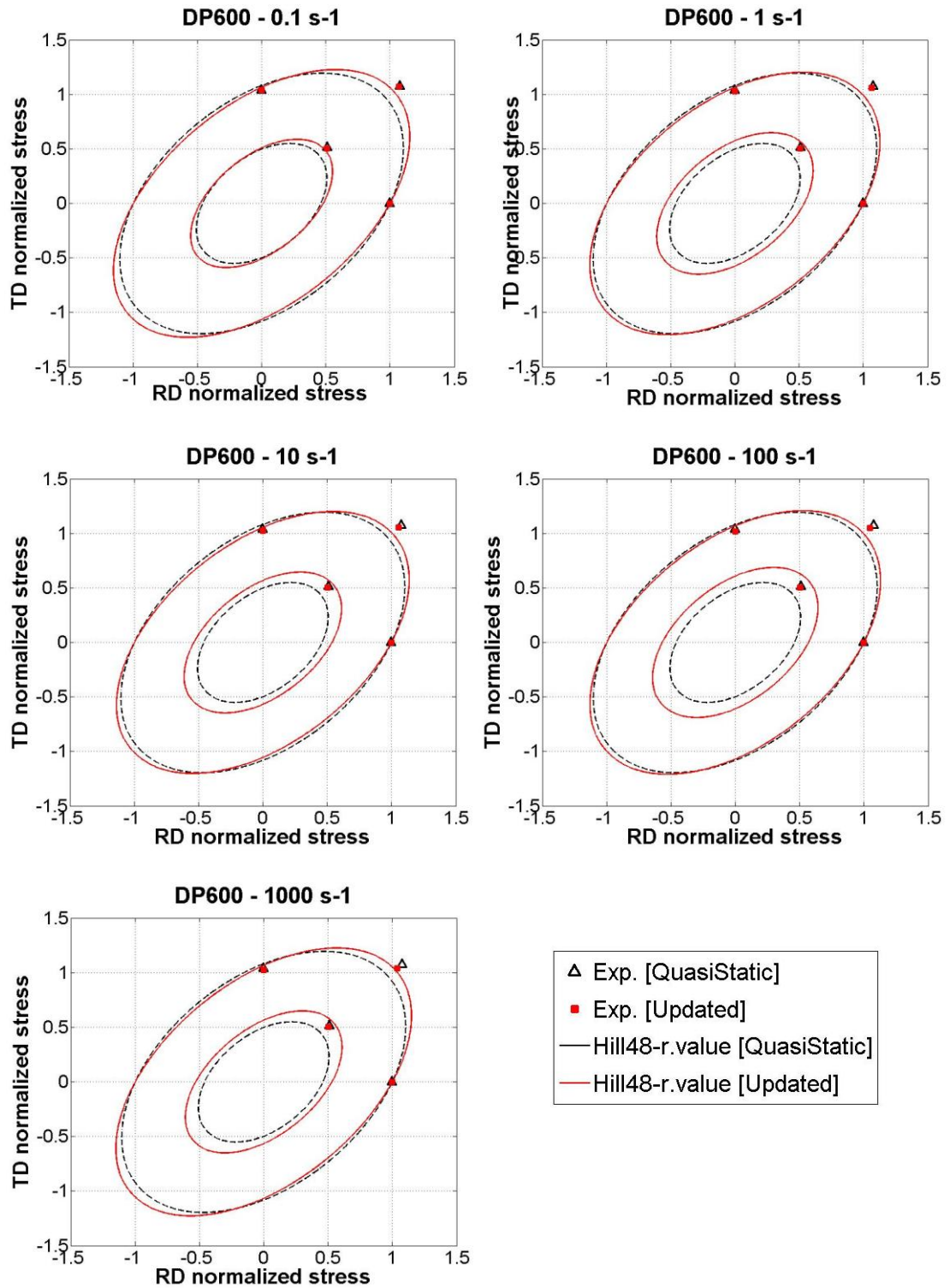


Figure 4-27 Flow surface for DP600 predicted by Hill48.r-value at various strain rates; using initial and updated anisotropy coefficients

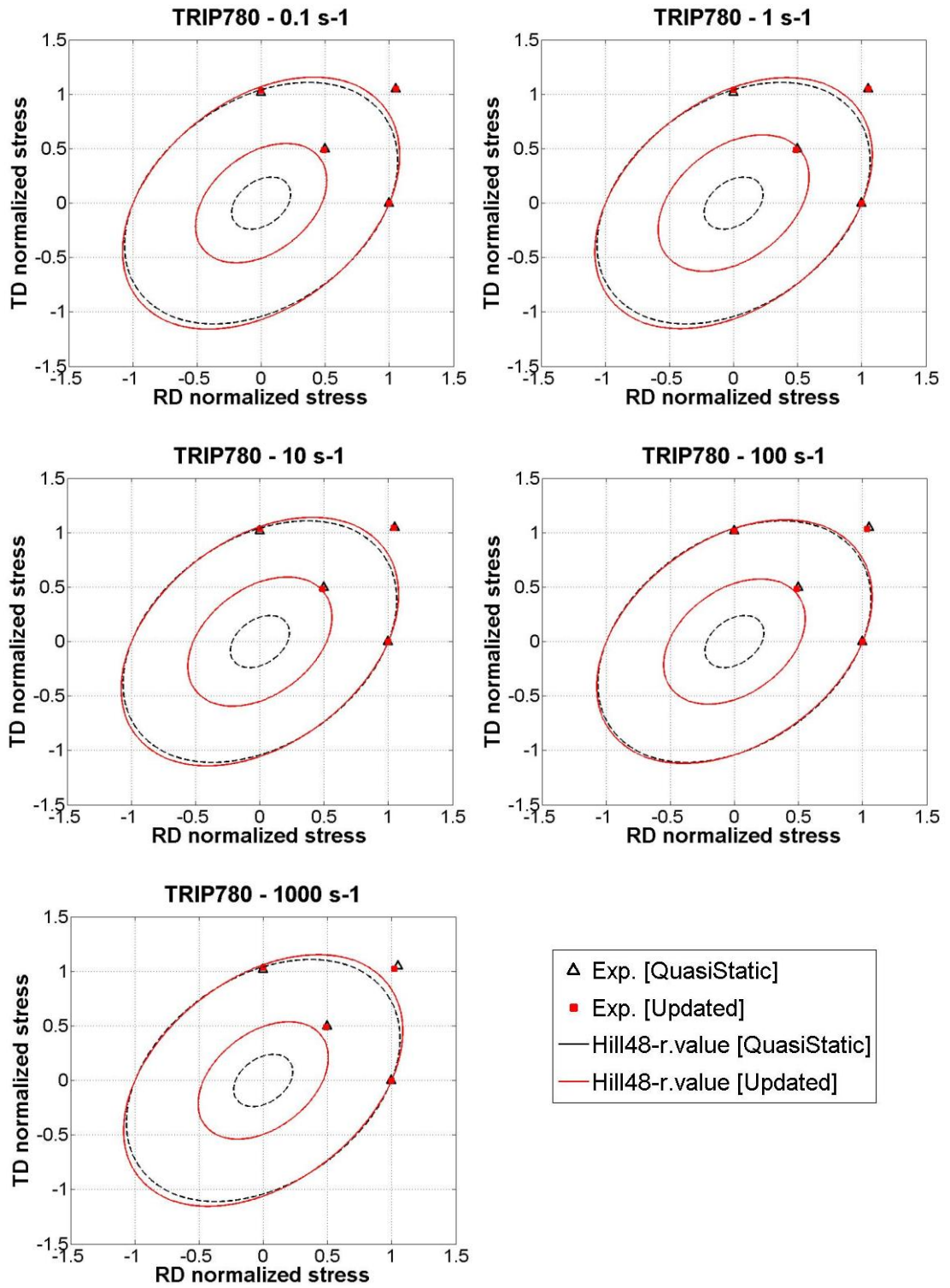


Figure 4-28 Flow surface for TRIP780 predicted by Hill48.r-value at various strain rates; using initial and updated anisotropy coefficients

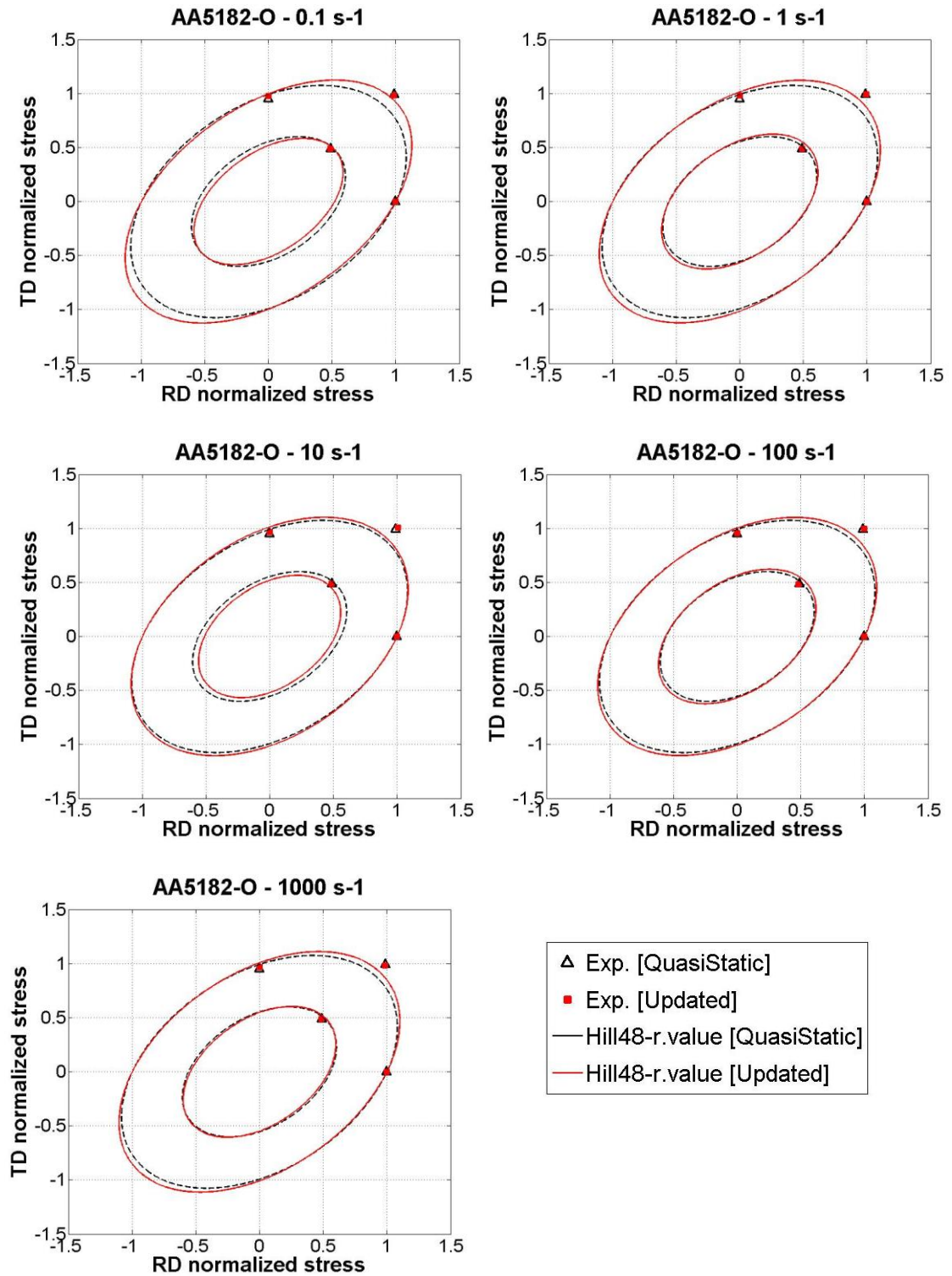
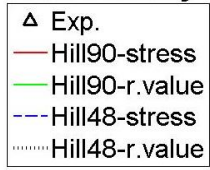


Figure 4-29 Flow surface for AA5182-O predicted by Hill48-r-value at various strain rates; using initial and updated anisotropy coefficients

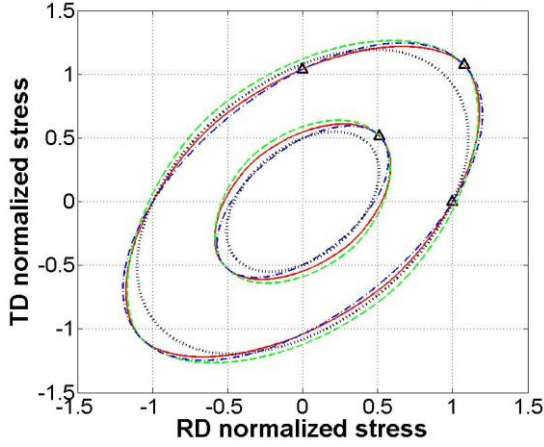
Hill's family



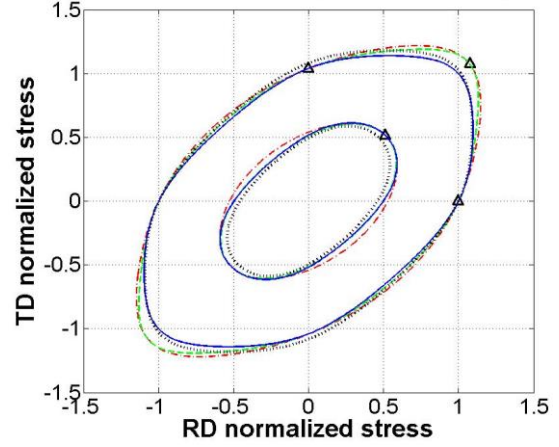
Barlat's family



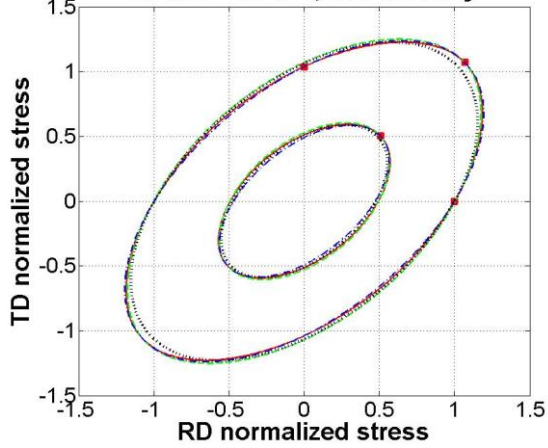
DP600 - 0.001 s⁻¹; Hill's family



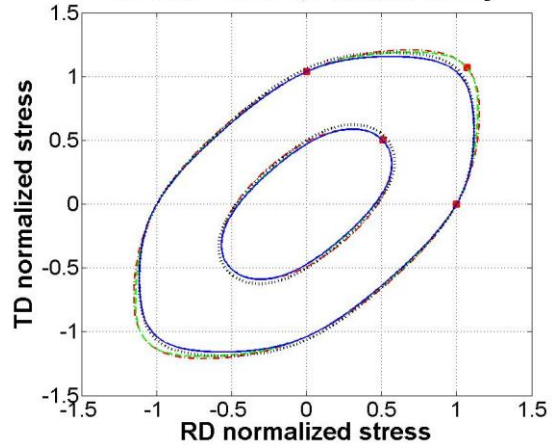
DP600 - 0.001 s⁻¹; Barlat's family



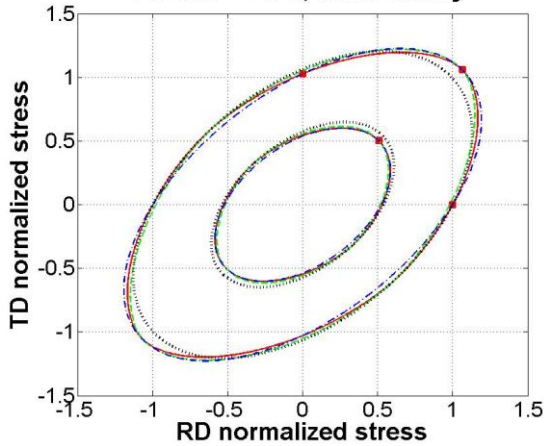
DP600 - 0.1 s⁻¹; Hill's family



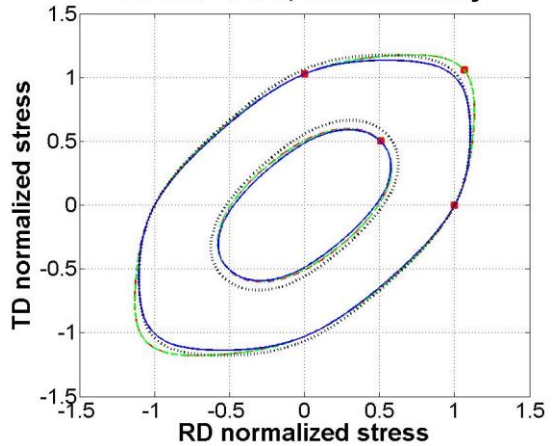
DP600 - 0.1 s⁻¹; Barlat's family



DP600 - 1 s⁻¹; Hill's family



DP600 - 1 s⁻¹; Barlat's family



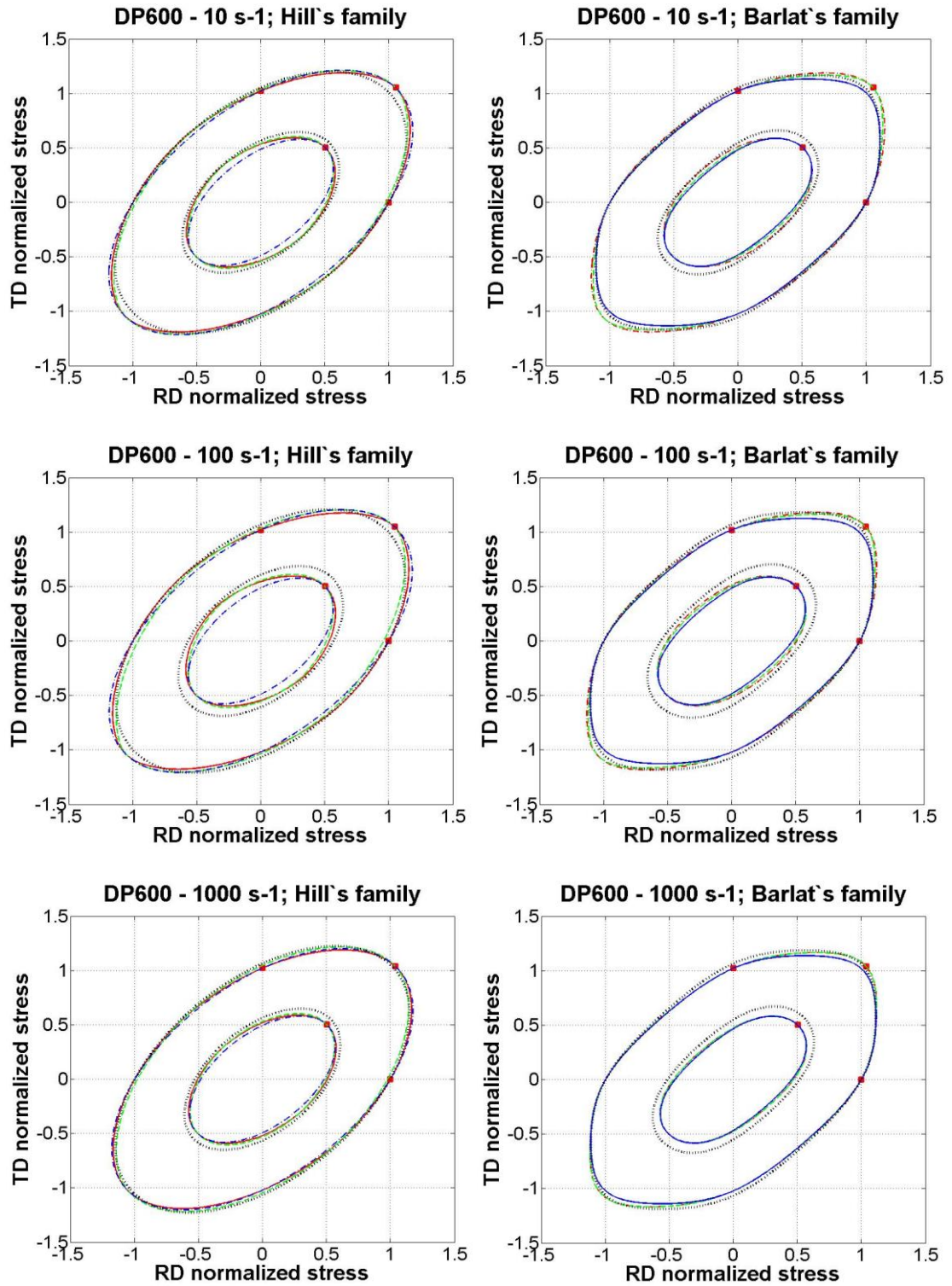
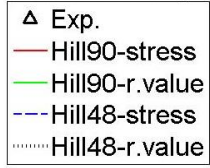
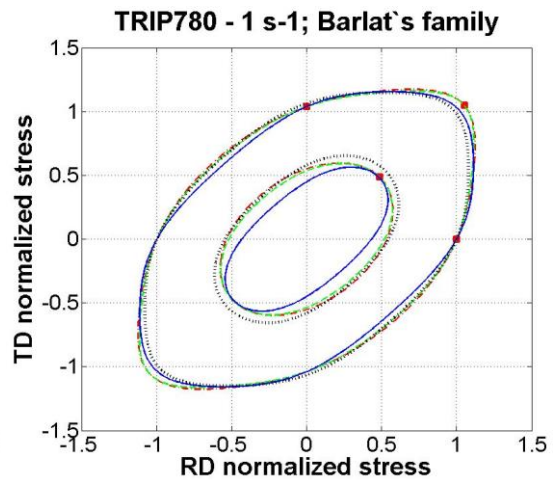
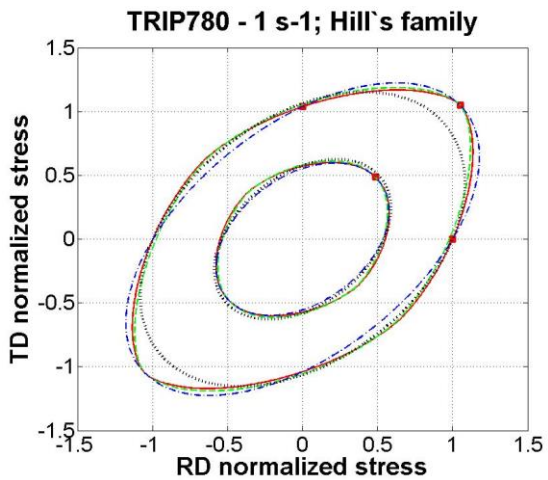
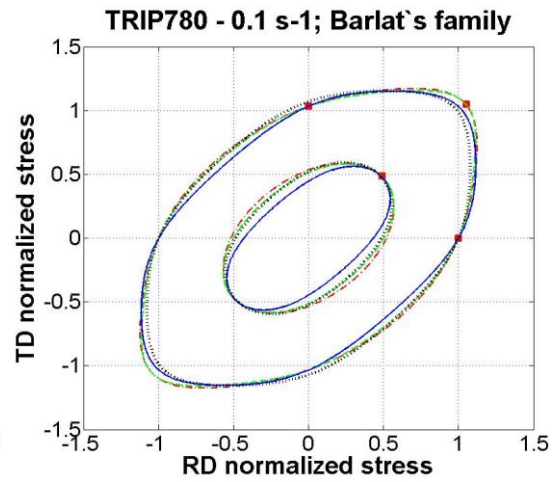
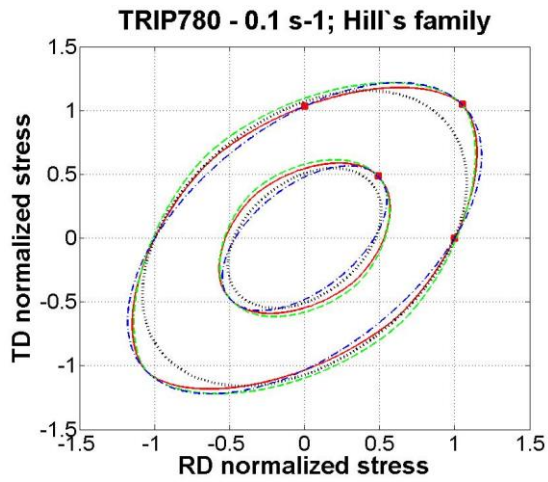
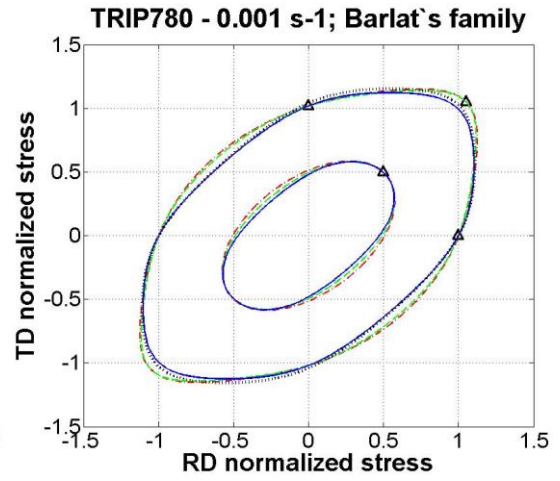
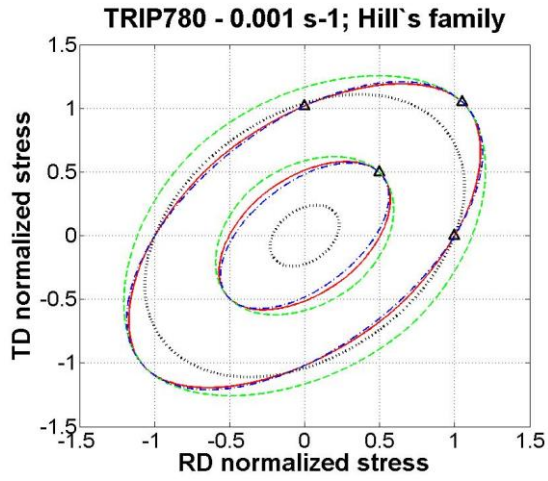


Figure 4-30 Comparison between the flow surfaces for DP600 predicted by Hill's and Barlat's families at various strain rates; using updated anisotropy coefficients

Hill's family



Barlat's family



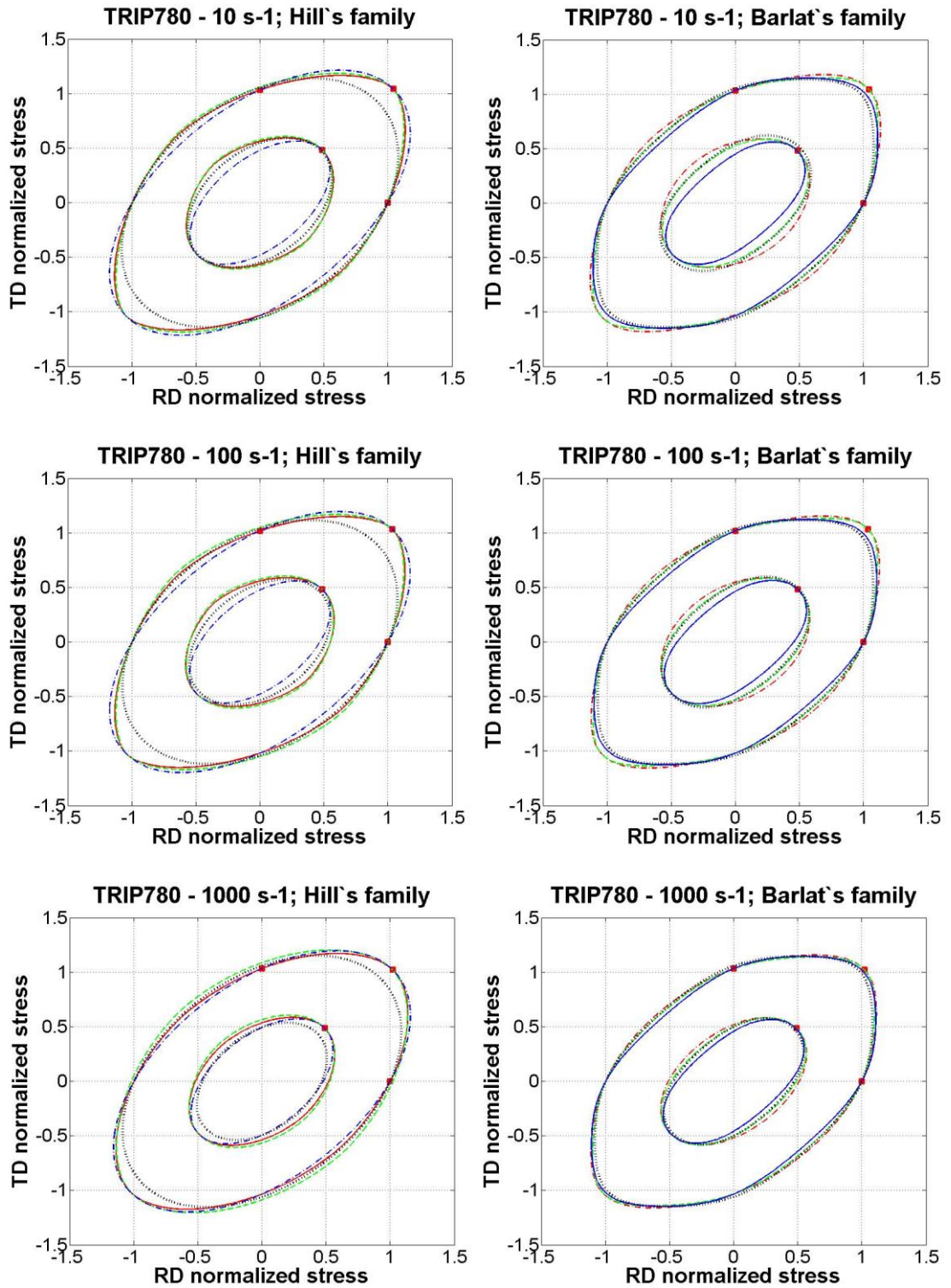
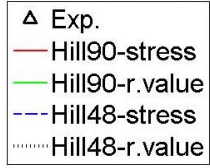
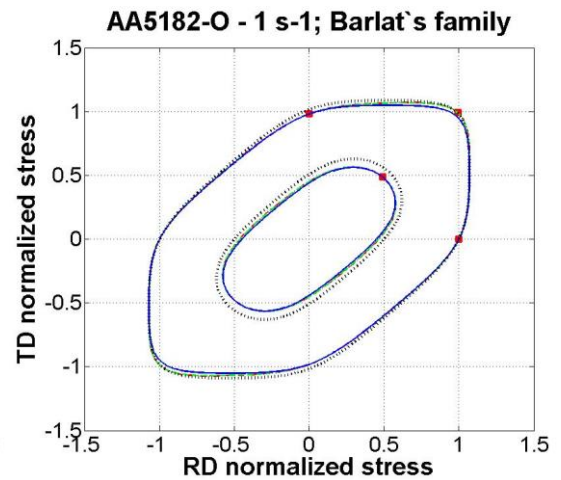
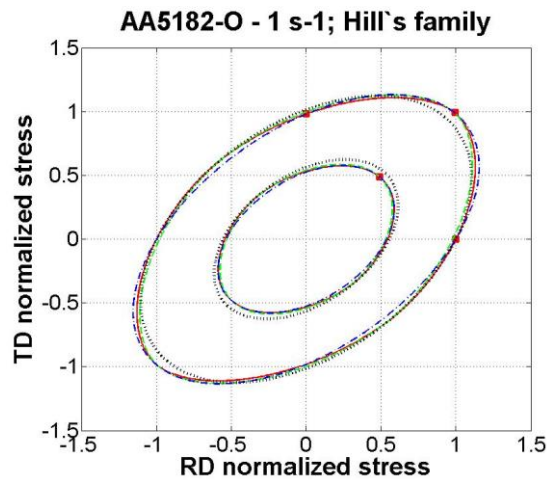
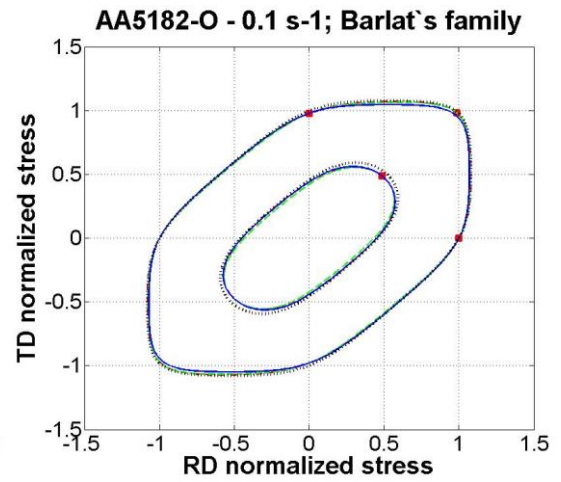
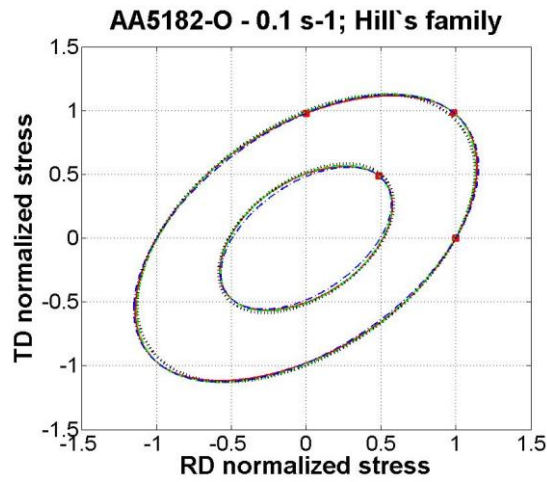
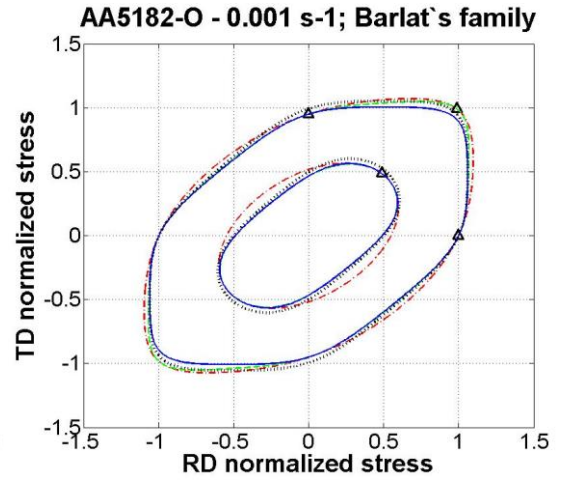
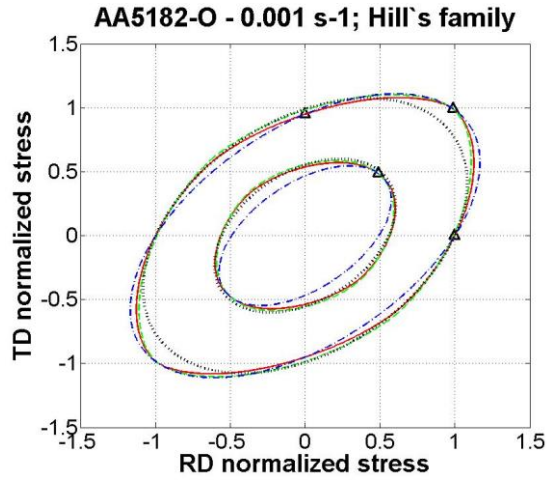


Figure 4-31 Comparison between the flow surfaces for TRIP780 predicted by Hill's and Barlat's families at various strain rates; using updated anisotropy coefficients

Hill's family



Barlat's family



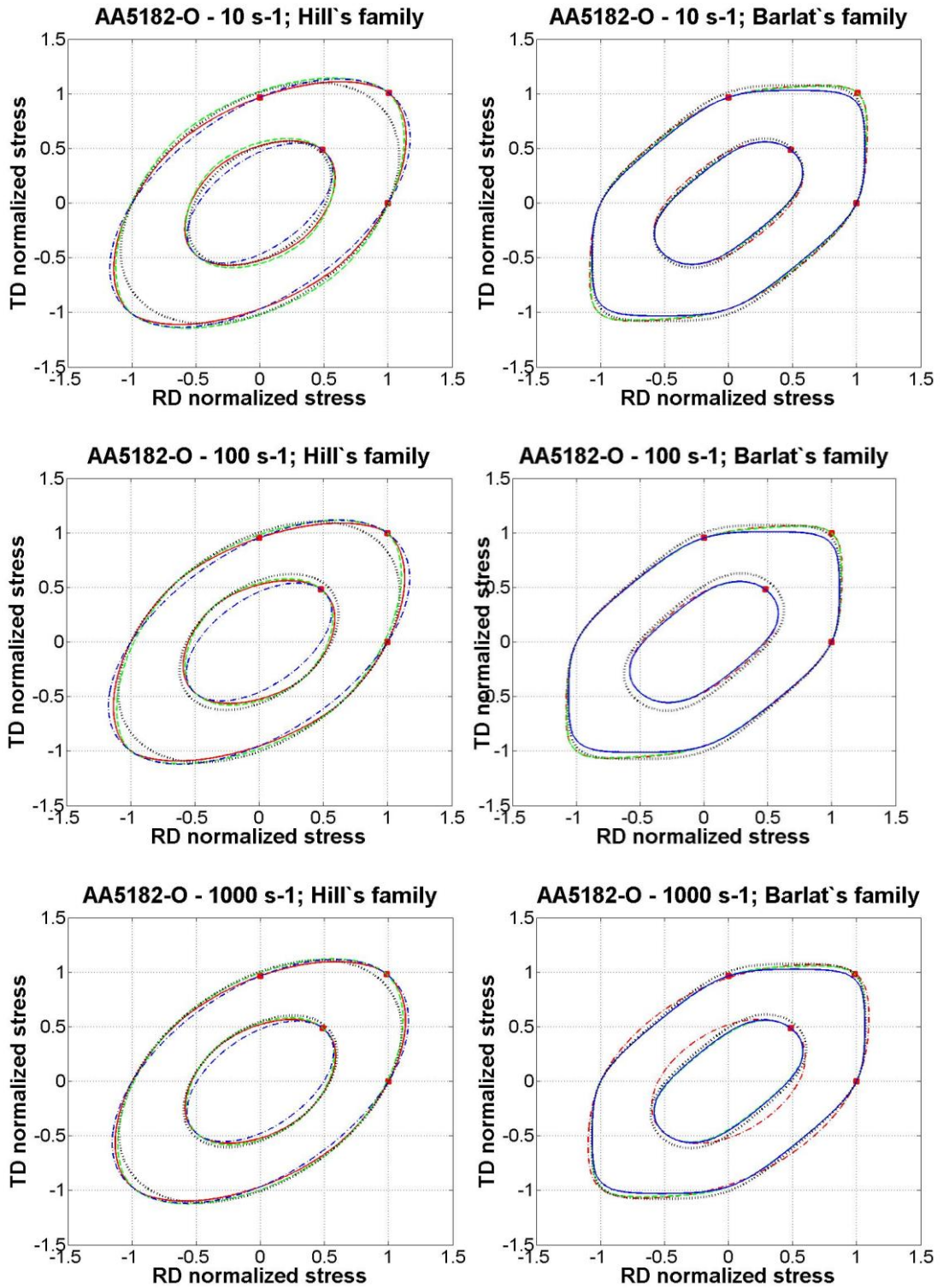


Figure 4-32 Comparison between the flow surfaces for AA5182-O predicted by Hill's and Barlat's families at various strain rates; using updated anisotropy coefficients

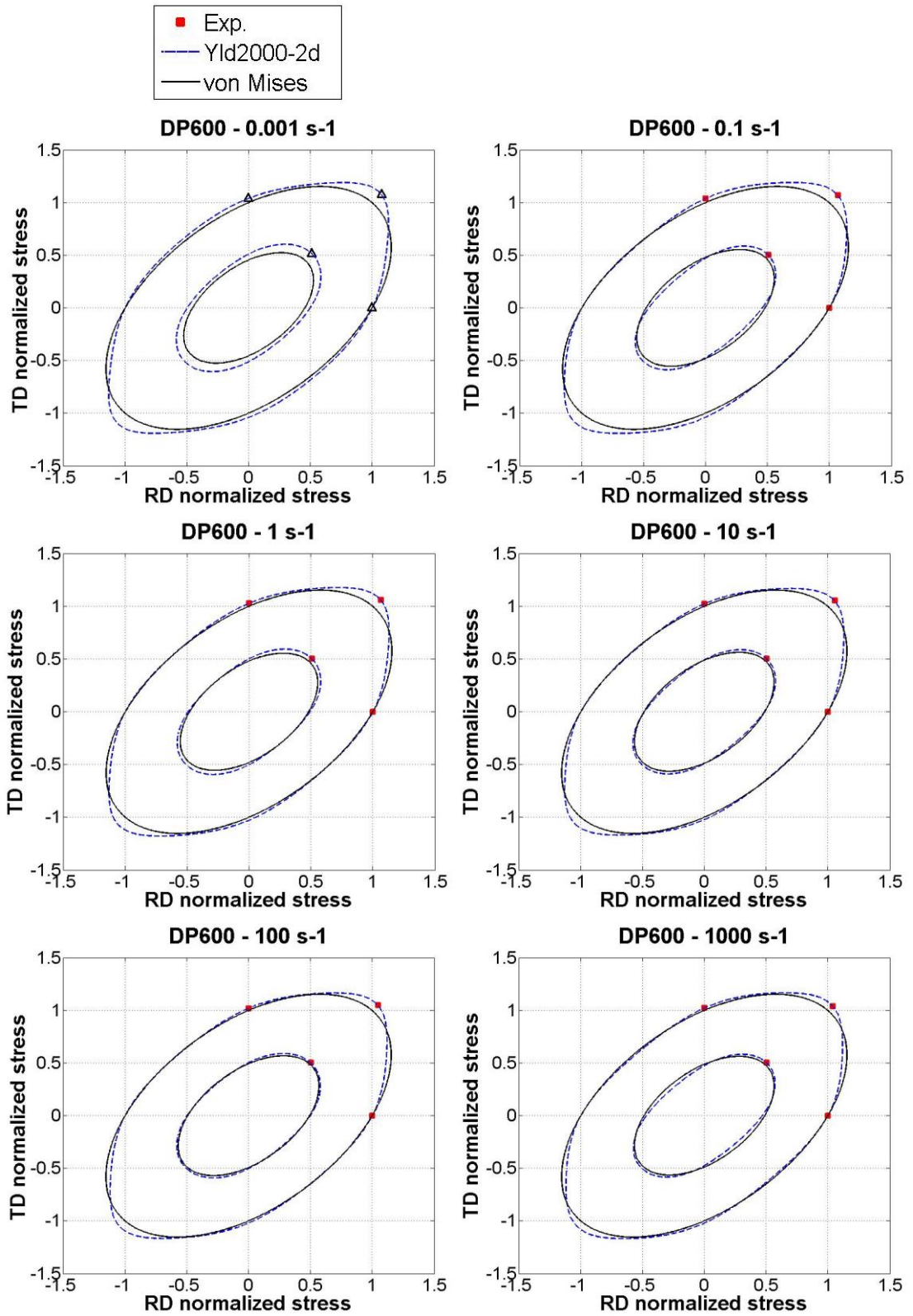


Figure 4-33 Comparison between the flow surfaces for DP600 predicted by Yld2000-2d and von Mises at various strain rates; using updated anisotropy coefficients for Yld2000-2d

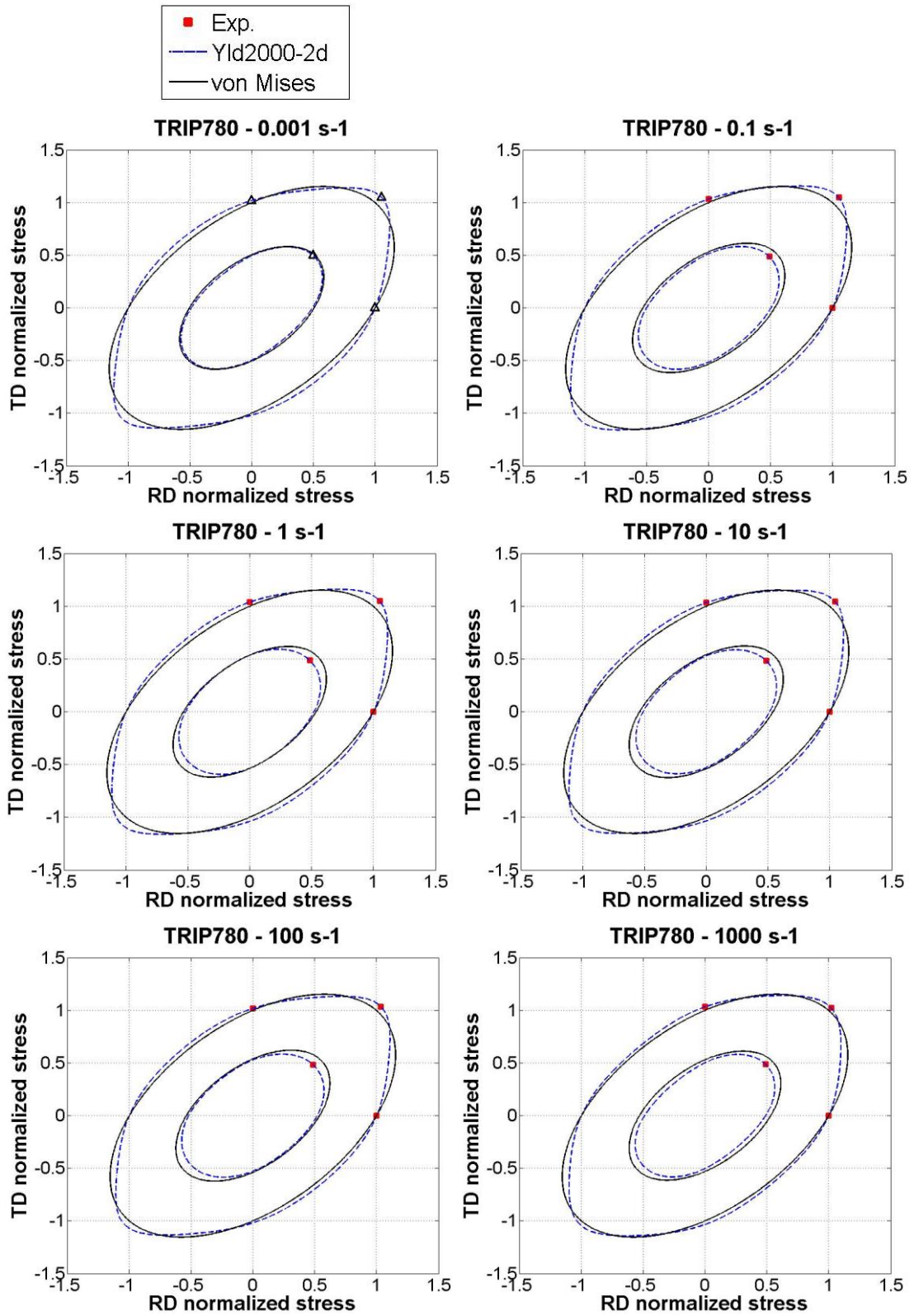


Figure 4-34 Comparison between the flow surfaces for TRIP780 predicted by Yld2000-2d and von Mises at various strain rates; using updated anisotropy coefficients for Yld2000-2d

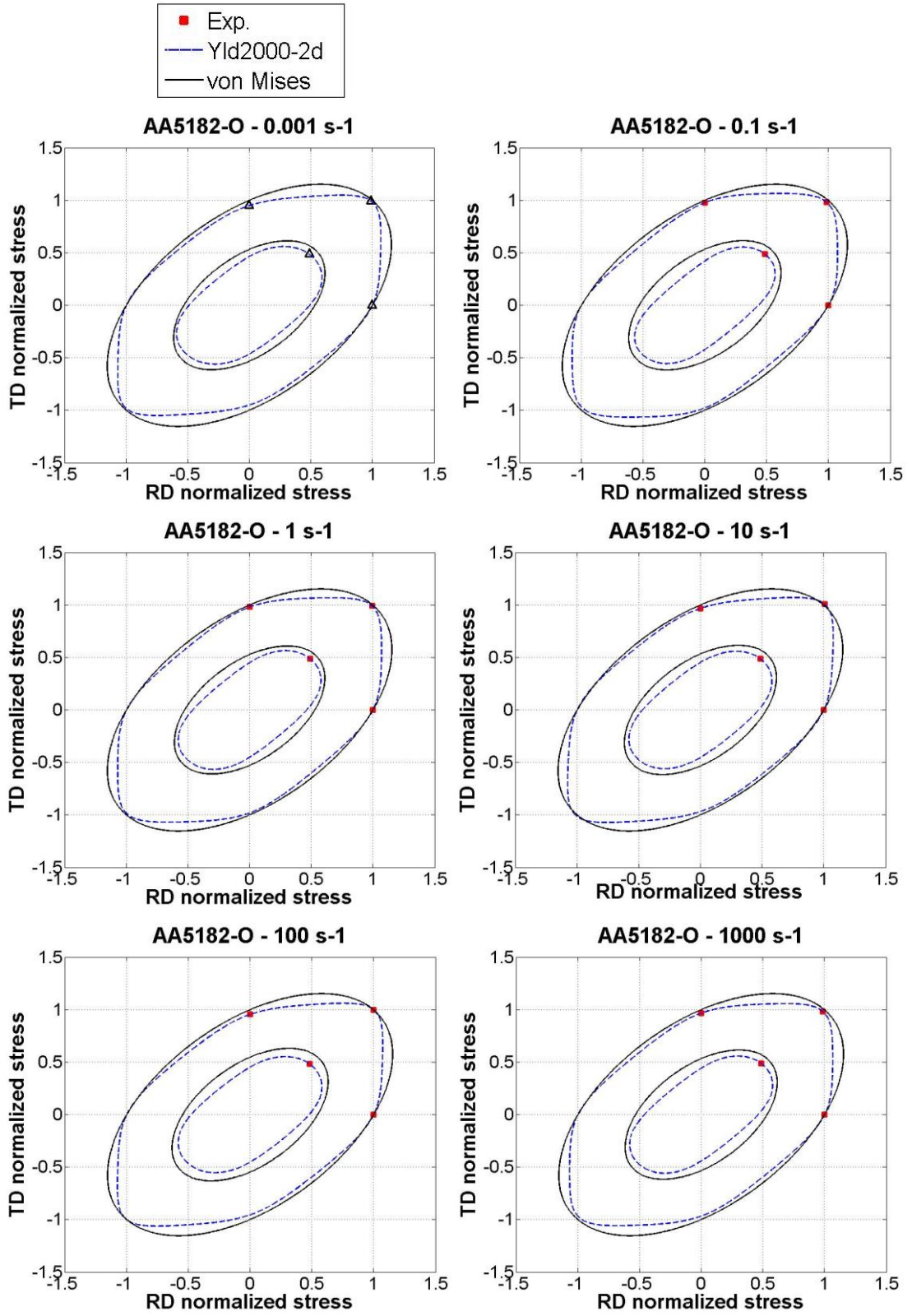


Figure 4-35 Comparison between the flow surfaces for AA5182-O predicted by Yld2000-2d and von Mises at various strain rates; using updated anisotropy coefficients for Yld2000-2d

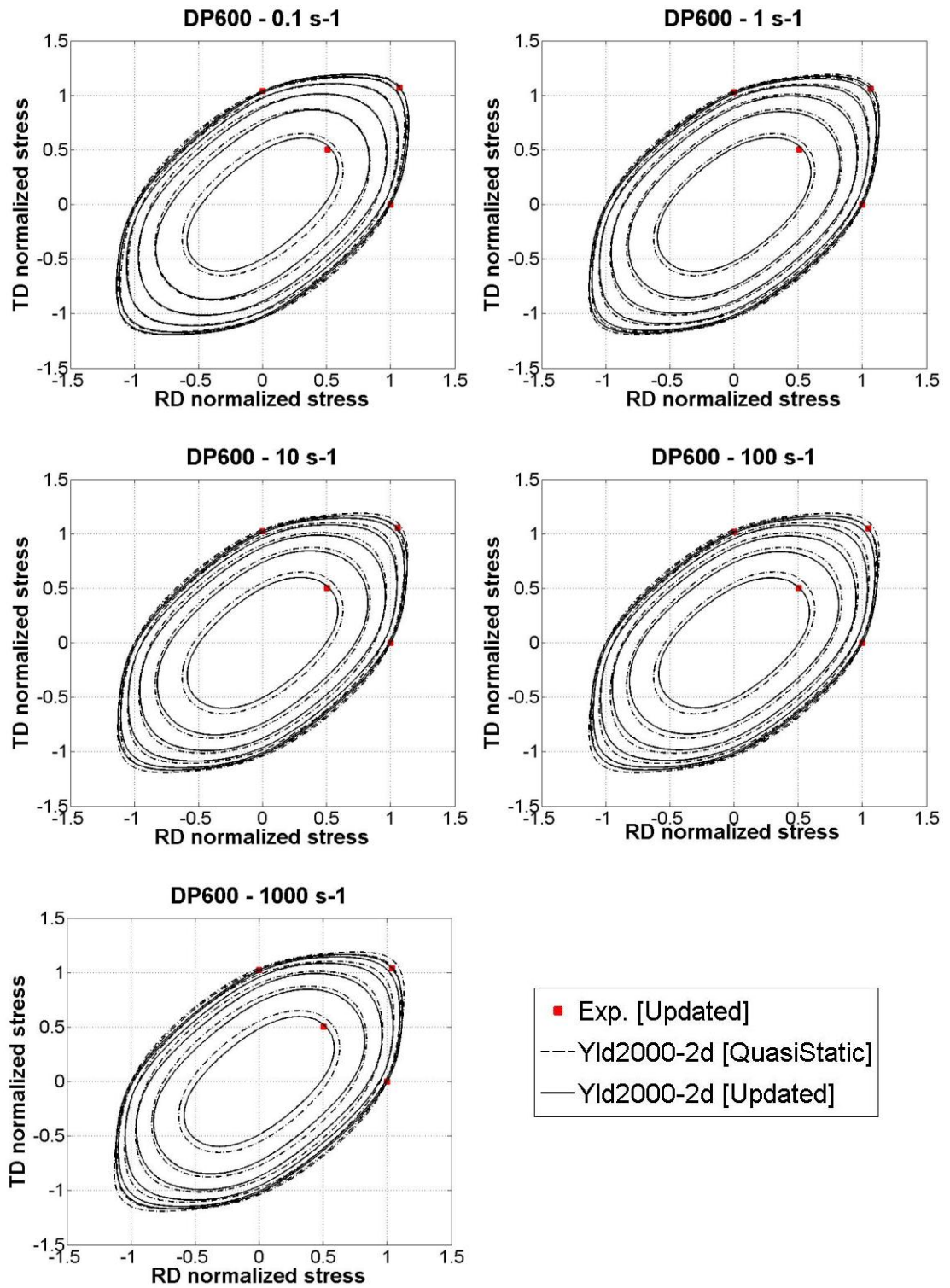


Figure 4-36 Flow surfaces for DP600 predicted by Yld2000-2d with contours of normalized shear stress in 0.1 increments from 0 to 0.5 at various strain rates; using initial and updated anisotropy coefficients

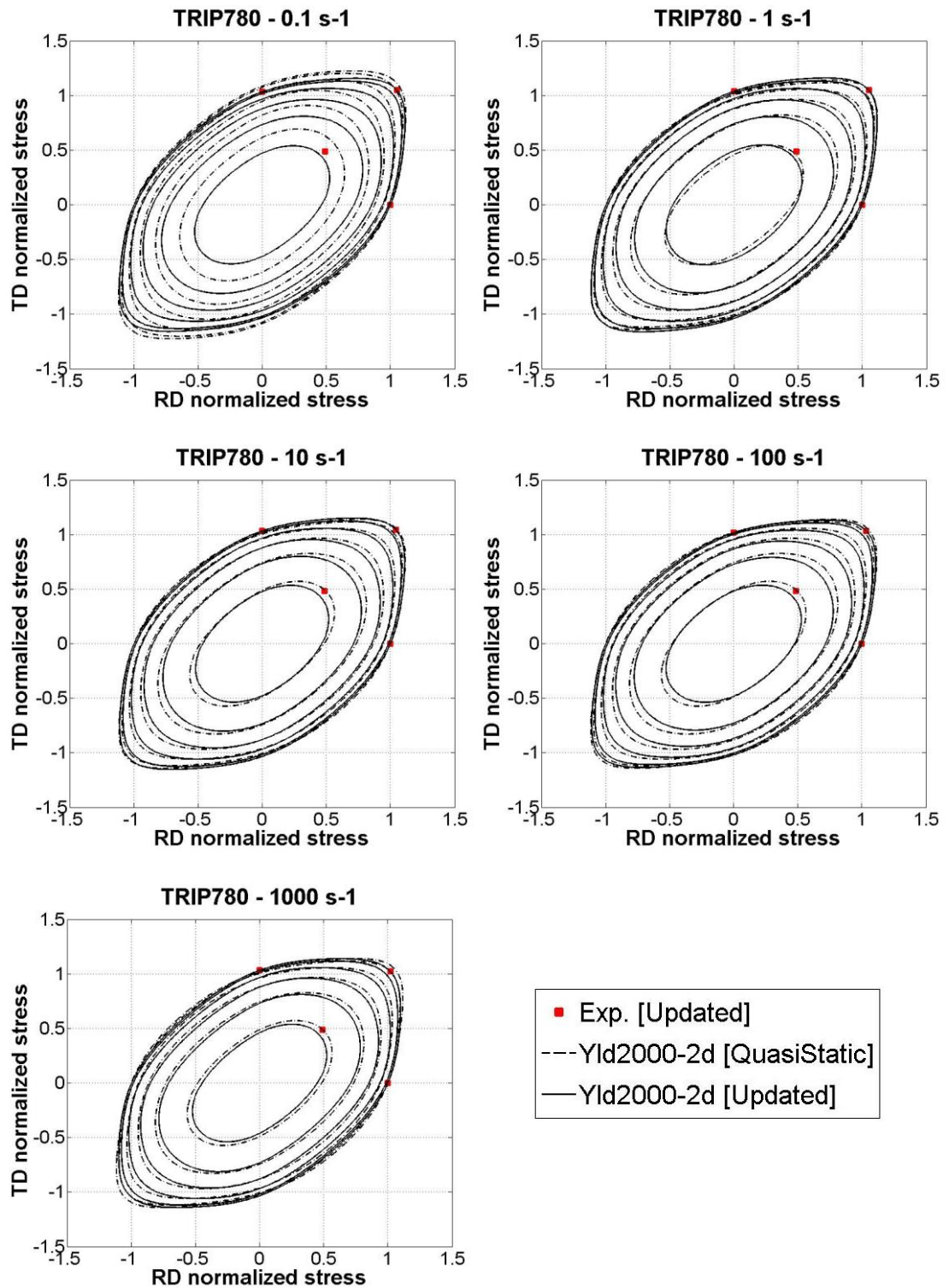


Figure 4-37 Flow surfaces for TRIP780 predicted by Yld2000-2d with contours of normalized shear stress in 0.1 increments from 0 to 0.5 at various strain rates; using initial and updated anisotropy coefficients

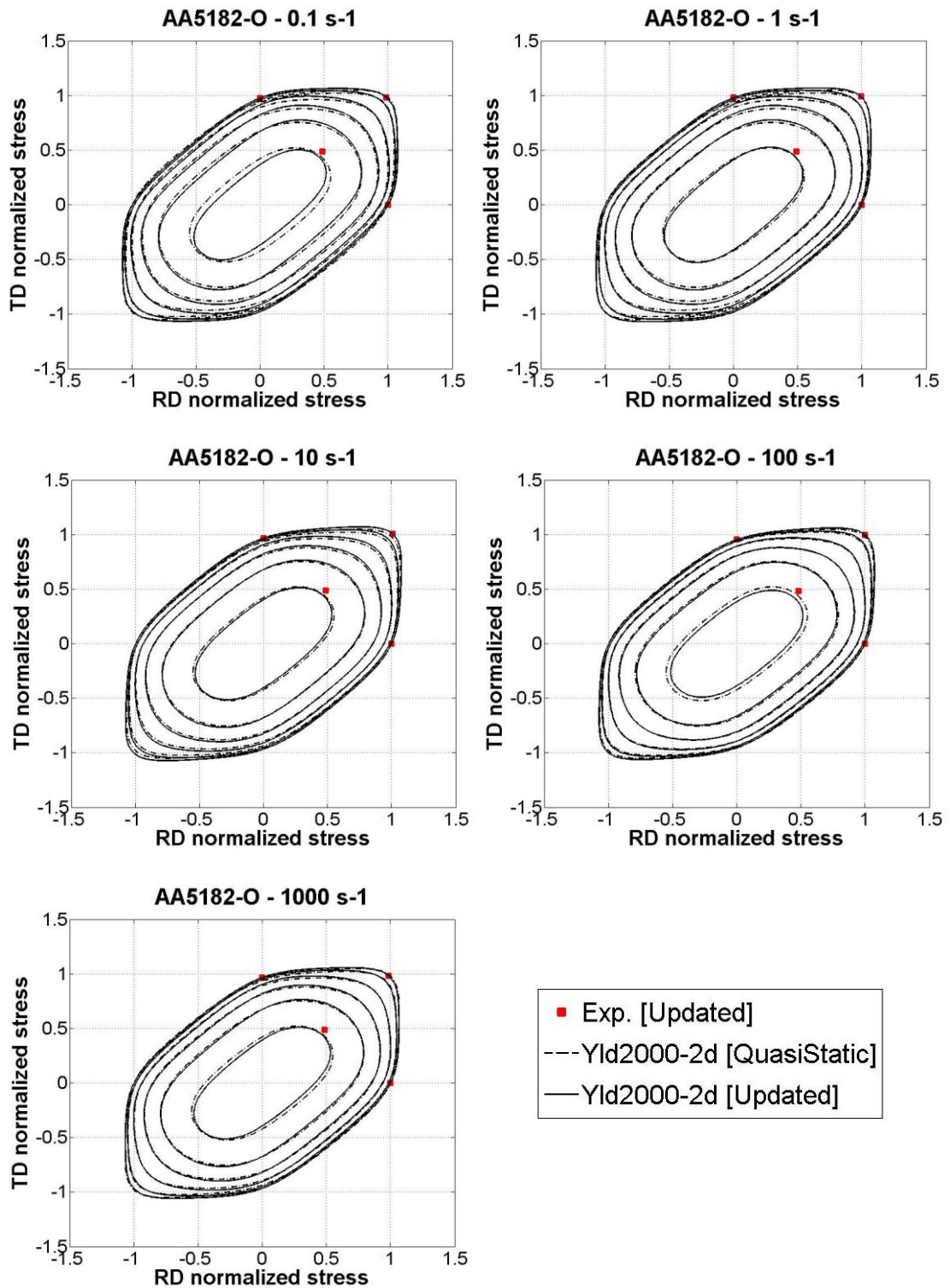


Figure 4-38 Flow surfaces for AA5182-O predicted by Yld2000-2d with contours of normalized shear stress in 0.1 increments from 0 to 0.5 at various strain rates; using initial and updated anisotropy coefficients

5 Rate-dependent Implicit Stress Integration Scheme

5.1 Introduction

A material constitutive model describes the mechanical behaviour of sheet metals and determines the strain and stress distributions in the formed part. The role of a constitutive material model can be more significant in a rate-dependent forming process, because in addition to its dependence on strain, the flow surface shape and size can be substantially affected by the strain rate. In this chapter, an implicit integration scheme is presented to integrate all equations incorporated in a rate-dependent constitutive model. A numerical algorithm, using the return mapping procedure, was developed for implementation of this model into a FE code and is applicable to any general anisotropic yield function and rate-dependent hardening model.

Three main components are required for implementing a rate-dependent constitutive model into a FE code: a) a plastic potential (which was taken to be the yield function due to the associated flow rule, AFR, assumption) which expresses the stress components relationship when plastic yielding occurs, b) a plastic flow formulation and its incremental integration (AFR) which describes the incremental strain and stress relationship, and c) a rate-dependent hardening model that describes the evolution of the initial flow stress throughout the deformation history. A great deal of research has been dedicated to developing and/or modifying new rate-dependent hardening models to improve the results of rate-dependent forming processes (Khan and Liang, 1999; Khan et al, 2004, 2007). From a computational point of view, Simo and Taylor (1985; 1986) proposed the idea of a return mapping algorithm for computational plasticity. Zeng et al.

(1996) and Kojic (2002) reviewed some numerical procedures for stress integration of inelastic material models including basic rate-independent hardening rules. Recently, Haowen (2011) implemented an associative constitutive model based on the von Mises yield function and modified the KHL hardening model using the formulation of Yoon et al. (1999a,b) for simulation of intermediate and high speed multi-axial loading conditions. To the best of the author's knowledge, a comprehensive study to evaluate the influence of strain rate on the prediction of a sheet deformation history in a high-speed metal forming process where a rate-dependent yield function (updating the anisotropy coefficients w.r.t. strain rate) and a rate-dependent hardening model are simultaneously implemented has not been done before. Almost all the developed rate-dependent constitutive models were consisted of rate-dependent hardening models combined with isotropic yield functions (Khan et al, 2004; 2007).

In this work, among all the anisotropic yield functions and rate-dependent hardening models presented in Chapter 3, the Hill48, Yld2000-2d and Yld2004-18p yield functions, and JC, KHL, and SKP were identified as being the most suitable to implement in rate-dependent hardening models. The anisotropic yield functions were combined with rate-dependent hardening models to develop user-defined material subroutines for ABAQUS/Explicit (VUMAT) for the plane stress and general stress conditions. It should be noted that in the developed VUMATs, in order to describe the strain rate effect on the material anisotropy behaviour more accurately, the anisotropy coefficients were updated w.r.t. strain rate, based on the 4th-order polynomial functions introduced in Section 3.3.4. Yld2000-2d was selected due to its ability to accurately describe the anisotropy of most sheet materials, and in particular DP600, TRIP780 and AA5182-O, presented in Sections 4.2.1 and 4.2.2. As discussed in Section 3.5, the KHL model is in a better agreement with the experimental stress-strain curves up to large deformations and over a wide range of strain rates, compared to the JC model. However, in addition to the KHL model, the implicit integration equation for the JC and SKP models were also derived due to their wide-spread use and implementation.

At the end of this chapter, the VUMAT verification is demonstrated under different loading conditions. For verification of the rate-dependent hardening model, the uniaxial

experimental flow curves in the rolling and transverse directions are compared with the stress-strain responses of a VUMAT (combined of Yld2000-2d yield function and KHL hardening model) at different strain rates. For the flow rule verification, the RD and TD uniaxial and biaxial flow stresses at various strain rates are compared with the corresponding experiments. Also, simulations of the bending of a cantilever beam and of loading under combined tension-shear were carried out to evaluate the accuracy of the developed numerical integration algorithm in the VUMAT compared with the ABAQUS built-in material model (combination of Hill48 yield function and JC hardening model).

5.2 Stress Integration

The implementation of a constitutive model into a nonlinear FE code involves the integration of the state of the material at an integration point over a time increment. In order to numerically integrate the stress and state variables (internal variables) over an increment, different methods have been proposed. Simo and Hughes (1998) proposed an algorithm called radial return-mapping which is a particular case of elastic predictor/plastic corrector algorithms. This algorithm works when a purely elastic trial stress is followed by a plastic corrector phase, which is here extended to the rate-dependent condition and is called the elastic predictor/visco-plastic corrector algorithm. The purpose of the latter is to satisfy the consistency condition at the end of each time step in a manner consistent with the prescribed flow rule.

The stresses and all state variables (such as total strain increment) are assumed to be known (which is typical for commercial software, such as ABAQUS and LS-DYNA) at the beginning of each time step based on the determined values from the last time increment and the assumption that the system is in global equilibrium. According to the return mapping algorithm, first the trial stress tensor is calculated based on the incremental displacement gradient field (or discrete total strain increment) over the time $[t_n, t_{n+1}]$. Then, the radial return mapping algorithm (or elastic predictor/visco-plastic corrector method) is used to satisfy the stress state on the subsequent flow surface. In this chapter, all the formulations are developed for plane stress conditions and are written in such a way that they can be easily extended to a three-dimensional (3D) stress state by

simply replacing the elastic and anisotropic matrices. In the following equations, subscript n denotes a quantity at the beginning of the time step and the subscript $n + 1$ (which represents a quantity at the end of the time increment) is eliminated for the sake of brevity. All the stresses, strains and state variables (internal state variables) are expressed in the local material coordinate system. It is more convenient to use a co-rotational coordinate system, where the base system rotates with the material (Yoon et al., 1999a). The implicit (Euler backward) method is used to integrate all plasticity equations. In order to distinguish between tensors and scalars, tensors are denoted by bold fonts and scalars are denoted by normal fonts.

When the stress reaches the yield point of the material, the transition from the elastic state to the plastic state occurs. The yield point is generally established using the uniaxial flow curves of the material at different strain rates. It is more complex to define a yield criterion when a multi-axial stress state is used to represent the transition of the material from the elastic to the plastic state. To this end, an implicit function (so-called yield function) is defined by expressing the relationship between the principal stresses at which the plastic flow occurs. The yield criterion, as a function of all state variables, can be written in a generic form as

$$\phi = \bar{\sigma}(\boldsymbol{\sigma}) - \sigma_y(\bar{\epsilon}^p, \dot{\epsilon}) = 0 \quad (5-1)$$

where $\bar{\sigma}(\boldsymbol{\sigma})$ is a continuously differentiable function of the stress components, and σ_y is a scalar function (usually taken to be the flow stress in uniaxial tension) of state variables including effective plastic strain ($\bar{\epsilon}^p$) and strain rate ($\dot{\epsilon}$), in rate-dependent hardening models (in this work, the temperature effect is ignored in all derived equations). In general, the mathematical formulation of a phenomenological rate-dependent hardening model can be written as a multiplication of two separate terms; the first term, is a function of the effective plastic strain ($\bar{\epsilon}^p$) and/or strain rate ($\dot{\epsilon}$) and is denoted by $\sigma_{y_1}(\bar{\epsilon}^p, \dot{\epsilon})$, and the second term, is only a function of the strain rate ($\dot{\epsilon}$) and is denoted by $\sigma_{y_2}(\dot{\epsilon})$. Therefore, the general form of a rate-dependent hardening model can be written as follows

$$\sigma_y(\bar{\epsilon}^p, \dot{\epsilon}) = \left[\sigma_{y_1}(\bar{\epsilon}^p, \dot{\epsilon}) \right] \left[\sigma_{y_2}(\dot{\epsilon}) \right] \quad (5-2)$$

Eq. (5-1) is a mathematical formulation of a surface (so-called flow surface) in the 3D space of the principal stresses, which must be closed and convex. In the case of plane stress conditions ($\sigma_3 = 0$), the 3D flow surface reduces to a planar curve in the plane of the principal stresses σ_1 and σ_2 . During plastic deformation, the initial and subsequent geometrical characterizations of the flow surface are expressed by $\bar{\sigma}(\boldsymbol{\sigma})$, and the initial size and subsequent expansion of the flow surface are determined by σ_y . Points located inside the surface ($\phi < 0$) are related to the elastic state, whereas they are related to a plastic state when located on the surface ($\phi = 0$). It should be noted that there is no physical meaning when the points are located outside of the surface ($\phi > 0$). These are known as the Kuhn-Tucker conditions which can be briefly described by the following equations

$$\phi \leq 0, \Delta p \geq 0 \Rightarrow \Delta p \phi = 0 \quad (5-3)$$

where Δp denotes the effective plastic strain increment. According to the associated flow rule (AFR) and the consistency condition, the increment of plastic strain can be obtained by taking the derivative of the yield function w.r.t. stress, as follows

$$\Delta \boldsymbol{\epsilon}^p = \Delta p \frac{\partial \bar{\sigma}(\boldsymbol{\sigma})}{\partial \boldsymbol{\sigma}} = \Delta p \mathbf{m} \quad (5-4)$$

where Δp can be obtained by solving the yield function equation using the return mapping method and \mathbf{m} represents the normal to the flow surface at the current (unknown) configuration. In the implicit (Euler backward) method, the variation of \mathbf{m} must be taken into consideration during the return mapping procedure, resulting in a more complex method, but also more accurate results compared to the explicit (Euler forward) method. The main disadvantage of the explicit stress integration algorithm is that it is only conditionally stable, which requires a very small time increment for each time step. Compared with the explicit algorithm, the implicit method is unconditionally stable and a more accurate solution can be obtained with larger time increments. In the implicit

method, the radial return mapping procedure is applied to ensure the calculated stress, strain, and any other internal state variables simultaneously satisfy the consistency condition and the yield condition.

In the return mapping procedure, the total strain increment is initially assumed to be fully elastic. Then, the effective stress (so-called trial stress) is calculated based on the yield equation $\bar{\sigma}(\boldsymbol{\sigma})$. If the calculated effective stress is less than, or equal to, the flow stress (calculated based on the hardening equation, σ_y), then the trial stress is accepted as the solution and the deformation is fully elastic. But if the effective stress is larger than the flow stress, the effective plastic strain and all internal state variables are corrected and the new stress is updated by subtracting the increment of plastic strain from the total strain increment. For every single time step, this iteration continues until the updated stress state satisfies the yield function equation. The Newton-Raphson method is usually used to solve the yield function equation for the effective plastic strain increment, Δp . The mathematical return mapping formulation can be written as follows

$$\boldsymbol{\sigma} = \boldsymbol{\sigma}^{Tr} - \mathbf{D}[\Delta \boldsymbol{\varepsilon}^p] \quad (5-5)$$

where $\boldsymbol{\sigma}^{Tr}$ denotes the trial stress which is a purely elastic deformation (so-called elastic predictor), $\boldsymbol{\sigma}$ is the stress at the end of the time increment (t_{n+1}), and \mathbf{D} is the elasticity tensor which is written for plane stress conditions as follows

$$\mathbf{D} = \frac{E}{1-\nu^2} \begin{bmatrix} 1 & \nu & 0 \\ \nu & 1 & 0 \\ 0 & 0 & \frac{1-\nu}{2} \end{bmatrix} \quad (5-6)$$

where E is the elastic modulus and ν is Poisson's ratio. It should be emphasized that the incremental formulation is expressed in an embedded (co-rotational) material coordinate system, which is objective w.r.t. material rotation. By assuming the total strain increment is elastic, the trial stress can be calculated as follows

$$\boldsymbol{\sigma}^{Tr} = \boldsymbol{\sigma}_n + \mathbf{D}[\Delta \boldsymbol{\varepsilon}^p] \quad (5-7)$$

At the beginning of the $n + 1$ time increment, the plastic strain increments, $\Delta\boldsymbol{\varepsilon}^p$, is assumed to be zero and will be updated later if plastic deformation occurs at the Gauss integration point. In a plastic deformation, the trial stress is outside the flow surface and it will be modified by a visco-plastic corrector to satisfy the yield condition. By substituting the plastic strain increment (Δp) from Eq. (5-4) into Eq. (5-5), the updated stress is obtained as follows

$$\boldsymbol{\sigma} = \boldsymbol{\sigma}^{Tr} - \mathbf{D}[\Delta p \mathbf{m}] \quad (5-8)$$

By replacing Eq. (5-2) into Eq. (5-1), then based on the yield condition at the end of the time increment, the effective stress can be calculated from the updated stress as follows

$$\phi = \bar{\sigma}(\boldsymbol{\sigma}^{Tr} - \Delta p \mathbf{D} \mathbf{m}) - \sigma_{y_1}(\Delta p, \Delta p / \Delta t) \cdot \sigma_{y_2}(\Delta p / \Delta t) = 0 \quad (5-9)$$

By dividing Eq. (5-9) by $\sigma_{y_2}(\Delta p / \Delta t)$, the yield criterion for the rate-dependent condition, can be rewritten as follows

$$\psi = \phi \cdot \left[\frac{1}{\sigma_{y_2}(\Delta p / \Delta t)} \right] = \bar{\sigma}(\boldsymbol{\sigma}^{Tr} - \Delta p \mathbf{D} \mathbf{m}) \cdot \left[\frac{1}{\sigma_{y_2}(\Delta p / \Delta t)} \right] - \sigma_{y_1}(\Delta p, \Delta p / \Delta t) = 0 \quad (5-10)$$

Figure 5-1 shows a schematic view of the multi-step return mapping algorithm used for the AFR in the plane stress (2D) state.

Eq. (5-10) is a closed-form nonlinear function of Δp that can be solved by any efficient numerical method. In this work, the Newton-Raphson method is used to solve the yield equation in each iteration to find the Δp value, which is used as a reference for the next time increment. It is usually difficult to find the solution of Eq. (5-10) numerically, if the yield function has an advanced non-quadratic formulation and/or if the strain increment is not sufficiently small. In order to solve this issue, Yoon et al. (1999b) proposed a multi-step return mapping algorithm which is applicable to advanced anisotropic yield functions and general hardening models without the need of a line-search algorithm, even for relatively large strain increments (Yoon et al., 2004). This multi-step algorithm is

applied in this work to control the residual and guarantee the convergence to the solution. In an iterative scheme, for sub-step k , the Eq. (5-10) can be modified as follows

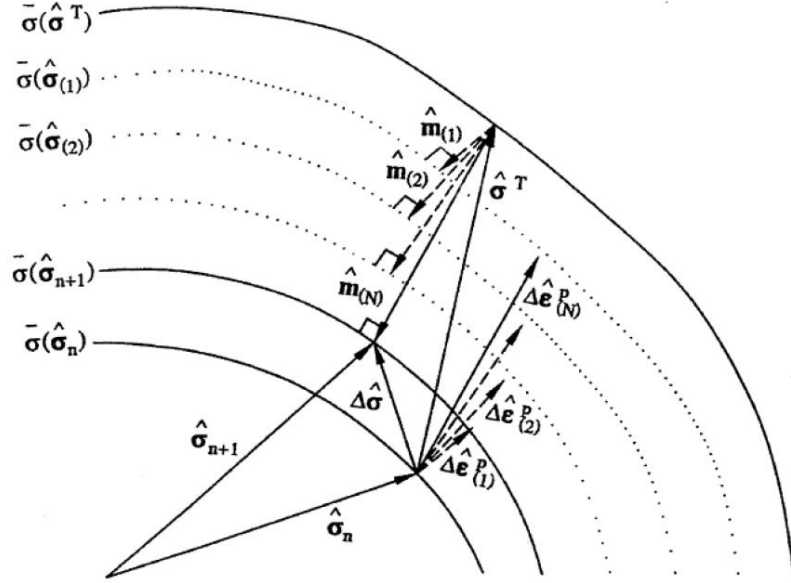


Figure 5-1 Schematic of a multi-steps return mapping procedure for AFR in the 2D stress space

$$\psi_k = \psi(\Delta p_k) = \bar{\sigma}(\hat{\sigma}^{Tr} - \Delta p_k \mathbf{D} \mathbf{m}_k) \cdot \left[\frac{1}{\sigma_{y_2}(\Delta p_k / \Delta t)} \right] - \sigma_{y_1}(\Delta p_k, \Delta p_k / \Delta t) \quad (5-11)$$

where ψ_k ($k = 1$ to $R-1$), is a rate-dependent residual for each sub-step and has a prescribed value. It is supposed that R sub-steps are required to reach to the final solution ($\phi_R \approx 0$), which mathematically can be expressed by

$$\psi_0 = \psi(\Delta p_0 = 0), \quad \{\psi_k | \psi_0 > \psi_1 > \dots > \psi_k > \dots > \psi_R (\psi_R \approx 0), k = 0 \sim R\}, \quad (5-12)$$

$$\Delta \psi = (\psi_{k-1} - \psi_k) < \sigma_y$$

Figure 5-1 shows that, the \mathbf{m} (normal to the flow surface) in each sub-step, is first estimated from its direction in the previous sub-step. Then, the exact \mathbf{m} is determined by solving Eq. (5-11) based on the Euler backward (implicit) method. By rearranging Eqs. (5-11) and (5-8), the following residual functions (g_1 and g_2) can be written as follows for sub-step (k),

$$\begin{cases} g_1 = \bar{\sigma}(\boldsymbol{\sigma}_k) \left[\frac{1}{\sigma_{y_2}(\Delta p_k/\Delta t)} \right] - \sigma_{y_1}(\Delta p_k, \Delta p_k/\Delta t) - \psi_k = 0 \\ g_2 = \mathbf{D}^{-1}[\boldsymbol{\sigma}_k - \boldsymbol{\sigma}^{Tr}] + \Delta p_k \mathbf{m}_k = 0 \end{cases} \quad (5-13)$$

where $\boldsymbol{\sigma}_k = \boldsymbol{\sigma}^{Tr} - \Delta p_k \mathbf{D} \mathbf{m}_k$, is the calculated stress at each iteration. The residual functions (g_1 and g_2) must be linearized around the current values of the state variables to numerically obtain the correction of each internal state variable at each iteration and consequently the stress tensor. By applying Taylor's series expansion at the current configuration and by ignoring the non-linear terms, the linear residuals can be written as follows

$$\begin{cases} g_1 + \mathbf{m} : d\boldsymbol{\sigma} : \left[\frac{1}{\sigma_{y_2}(\Delta p/\Delta t)} \right] + \bar{\sigma}(\boldsymbol{\sigma}_k) \frac{d}{d\Delta p} \left[\frac{1}{\sigma_{y_2}(\Delta p/\Delta t)} \right] d\Delta p - H d\Delta p = 0 \\ g_2 + \left[\mathbf{D}^{-1} + \Delta p \frac{\partial \mathbf{m}}{\partial \boldsymbol{\sigma}} \right] : d\boldsymbol{\sigma} + \mathbf{m} d\Delta p = 0 \end{cases} \quad (5-14)$$

where H is the first derivative of σ_{y_1} w.r.t. Δp ($H = \partial \sigma_{y_1} / \partial \Delta p$), which was calculated for JC, KHL, and SKP hardening models and will be presented in Section 5.2.1. The correction for the effective plastic strain ($d\Delta p$) can be found by solving the above system of equations. After some mathematical arrangements in the system of Eq. (5-14), the correction for the effective plastic strain ($d\Delta p$) can be obtained by

$$d\Delta p = \frac{g_1 - \mathbf{m} : \mathbf{X}_i^{-1} : g_2 [1/\sigma_{y_2}(\Delta p/\Delta t)]}{\mathbf{m} : \mathbf{X}_i^{-1} : \mathbf{m} [1/\sigma_{y_2}(\Delta p/\Delta t)] - \bar{\sigma}(\boldsymbol{\sigma}_k) \frac{d}{d\Delta p} [1/\sigma_{y_2}(\Delta p/\Delta t)] + H} \quad (5-15)$$

Where

$$\mathbf{X}_i^{-1} = \left[\mathbf{D}^{-1} + \Delta p \frac{\partial \mathbf{m}}{\partial \boldsymbol{\sigma}} \right]^{-1} \quad (5-16)$$

Eq. (5-15) gives $d\Delta p$ and consequently each variable can be updated, and iterations continue until the convergence is achieved within a small prescribed

tolerance (usually 10^{-6}). The incremental plastic strain can be updated for step (k) as follows

$$\Delta p_k^{i+1} = \Delta p_k^i + d\Delta p_k \quad (5-17)$$

Based on the new value of the plastic strain increment, the total effective plastic strain ($\bar{\epsilon}^p$), stress tensor, and the rate-dependent hardening function (flow stress) can also be updated as follows

$$\begin{cases} \bar{\epsilon}^p = \bar{\epsilon}_n^p + \Delta p \\ \boldsymbol{\sigma} = \boldsymbol{\sigma}_n + \Delta \boldsymbol{\sigma} \\ \sigma_y = \sigma_y(\bar{\epsilon}^p, \Delta p / \Delta t) \end{cases} \quad (5-18)$$

where $\bar{\epsilon}_n^p$ is the total effective plastic strain from the previous time increment (t_n). The overall algorithm (flow chart) of the implicit rate-dependent numerical algorithm used in the VUMAT is summarized in Appendix-2. Using this algorithm, general rate-dependent user-material subroutines (VUMAT) were developed for ABAQUS/Explicit, which include different anisotropic yield functions (Hill48 and Yld2000-2d) and rate-dependent hardening models (JC, KHL, and SKP), to simulate the EHF process.

5.2.1 Derivatives of Hardening Functions

In order to calculate the correction for the effective plastic strain ($d\Delta p$) from Eq. (5-15), the first derivatives of the JC, KHL, and SKP hardening models w.r.t. Δp ($\partial \sigma_{y_1} / \partial \Delta p$ and $\partial \sigma_{y_2} / \partial \Delta p$) are required.

5.2.1.1 JC

The JC hardening equation can be expressed in multiplicative form by

$$\sigma_y = \sigma_{y_1} \cdot \sigma_{y_2}, \quad \sigma_{y_1} = A + B(\bar{\epsilon}^p)^n, \quad \sigma_{y_2} = 1 + C \ln \left(\frac{\Delta p / \Delta t}{\dot{\epsilon}_0} \right) \quad (5-19)$$

where A , B , n , and C are material constants. The first derivatives of σ_{y_1} and σ_{y_2} functions w.r.t. Δp are as follows

$$H = \frac{d}{d\Delta p} \left(\frac{1}{\sigma_{y_1}(\Delta p, \Delta p/\Delta t)} \right) = Bn(\bar{\varepsilon}^p)^{n-1} \quad (5-20a)$$

$$\frac{d}{d\Delta p} \left(\frac{1}{\sigma_{y_2}(\Delta p/\Delta t)} \right) = -\frac{C}{\Delta p} \left(\frac{1}{1 + C \ln \left(\frac{\Delta p/\Delta t}{\dot{\varepsilon}_0} \right)} \right)^2 = -\frac{C}{\Delta p \sigma_{y_2}^2}, \quad (5.20b)$$

By replacing Eqs. (5-19), (5-20a), and (5.20b) into Eq. (5-15), the correction for the effective plastic strain ($d\Delta p$) can be obtained for a constitutive model with the JC hardening model.

5.2.1.2 KHL

The KHL hardening equation is given by

$$\sigma_y = \sigma_{y_1} \cdot \sigma_{y_2}, \quad \sigma_{y_1} = A + B(\bar{\varepsilon}^p)^{n_0} \left(1 - \frac{\ln(\Delta p/\Delta t)}{\ln D_0^p} \right)^{n_1}, \quad \sigma_{y_2} = \left(\frac{\Delta p/\Delta t}{\dot{\varepsilon}_0} \right)^C \quad (5-21)$$

where A , B , n_0 , n_1 , and C are material constants and $D_0^p = 10^6 \text{ s}^{-1}$. The first derivatives of σ_{y_1} and σ_{y_2} functions w.r.t. Δp are obtained as follows

$$\begin{aligned} H &= \frac{d}{d\Delta p} \left(\frac{1}{\sigma_{y_1}(\Delta p, \Delta p/\Delta t)} \right) \\ &= B(\bar{\varepsilon}^p)^{n_0} \left(1 - \frac{\ln(\Delta p/\Delta t)}{\ln D_0^p} \right)^{n_1} \left[\frac{n_0}{\bar{\varepsilon}^p} \right. \\ &\quad \left. - \frac{n_1}{\ln D_0^p \Delta p} \left(\frac{\ln D_0^p}{\ln D_0^p - \ln(\Delta p/\Delta t)} \right) \right] \end{aligned} \quad (5-22a)$$

$$\frac{d}{d\Delta p} \left(\frac{1}{\sigma_{y_2}(\Delta p/\Delta t)} \right) = -\frac{C}{\Delta p} \left(\frac{\dot{\varepsilon}_0}{(\Delta p/\Delta t)} \right)^C = -\frac{C}{\Delta p \sigma_{y_2}}, \quad (5.22b)$$

By replacing Eqs. (5-21), (5-22a) and (5.22b) into Eq. (5-15), the correction for the effective plastic strain ($d\Delta p$) can be obtained for a constitutive model with KHL hardening model.

5.2.1.3 SKP

The SKP hardening equation can be written as follows

$$\sigma_y = \sigma_{y_1} \cdot \sigma_{y_2},$$

$$\sigma_{y_1} = \sigma_0 \left[\left(\frac{\Delta p / \Delta t}{\dot{\epsilon}_0} \right)^A \left/ \left(1 - H \cdot \ln \left(\frac{\Delta p / \Delta t}{\dot{\epsilon}_0} \right) \right) \right] + [B \bar{\epsilon}^p + C(1 - \exp(-\beta \bar{\epsilon}^p))], \quad (5-23)$$

$$\sigma_{y_2} = 1 - H \cdot \ln \left(\frac{\Delta p / \Delta t}{\dot{\epsilon}_0} \right)$$

where σ_0 , A , k , B , C , β , and H are material constants. The first derivatives of σ_{y_1} and σ_{y_2} functions w.r.t. Δp are obtained as follows

$$H = \frac{d}{d\Delta p} \left(\frac{1}{\sigma_{y_1}(\Delta p, \Delta p / \Delta t)} \right) =$$

$$\frac{\sigma_0}{\Delta p} \left(\frac{\Delta p / \Delta t}{\dot{\epsilon}_0} \right)^A \left[A \left(1 - H \cdot \ln \left(\frac{\Delta p / \Delta t}{\dot{\epsilon}_0} \right) \right) + H \right] \left(\frac{1}{1 - H \cdot \ln \left(\frac{\Delta p / \Delta t}{\dot{\epsilon}_0} \right)} \right)^2 + C\beta \exp(-\beta p) \quad (5-24a)$$

$$\frac{d}{d\Delta p} \left(\frac{1}{\sigma_{y_2}(\Delta p / \Delta t)} \right) = \frac{H}{\Delta p} \left(\frac{1}{1 - H \cdot \ln \left(\frac{\Delta p / \Delta t}{\dot{\epsilon}_0} \right)} \right)^2 = \frac{H}{\Delta p \sigma_{y_2}^2}, \quad (5.24b)$$

By replacing Eqs. (5-23), (5-24a), and (5.24b) into Eq. (5-15), the correction for the effective plastic strain ($d\Delta p$) can be obtained for a constitutive model with SKP hardening model.

5.2.2 Derivatives of Yield Functions

Eq. (5-15) shows that, in addition to the first derivative of the hardening equation, the first and second derivatives of the yield function ($\mathbf{m}, \partial\mathbf{m}/\partial\boldsymbol{\sigma}$) must be defined to obtain the correction for the effective plastic strain ($d\Delta p$). The developed numerical procedure can be easily used with any advanced anisotropic yield function whose first and second derivatives can be explicitly defined. Here, for the sake of brevity, the derivatives for only two yield functions, Hill48 and Yld2000-2d, which were used to develop the user material subroutines, are presented.

5.2.2.1 Hill48

The yield condition for the Hill48 can be written as follows

$$\left(\frac{3}{2}\boldsymbol{\sigma}^T \mathbf{M} \boldsymbol{\sigma}\right)^{1/2} - \sigma_y = 0 \quad (5-25)$$

where \mathbf{M} is the anisotropic tensor which for the plane stress condition is defined by

$$\mathbf{M} = \frac{2}{3}\sigma_0^2 \begin{bmatrix} H + G & -H & 0 \\ -H & H + F & 0 \\ 0 & 0 & 2N \end{bmatrix} \quad (5-26)$$

where F, G, H, and N are the Hill48 anisotropy coefficients, described in Section 3.1.1.2 or 3.1.1.3. The effective stress can be defined as follows

$$\bar{\sigma} = \left(\frac{3}{2}\boldsymbol{\sigma}^T \mathbf{N} \boldsymbol{\sigma}\right)^{1/2} \quad (5-27)$$

According to Eqs. (5-4) and (5-27), the normal to the yield surface (\mathbf{m}) is obtained by

$$\mathbf{m} = \frac{\partial\bar{\sigma}(\boldsymbol{\sigma})}{\partial\boldsymbol{\sigma}} = \frac{3}{2} \frac{\mathbf{N}\boldsymbol{\sigma}}{\bar{\sigma}} \quad (5-28)$$

By differentiating Eq. (5-28), the second derivative ($\partial\mathbf{m}/\partial\boldsymbol{\sigma}$) of the Hill48 yield function can be defined as follows

$$\frac{\partial \mathbf{m}}{\partial \boldsymbol{\sigma}} = \frac{(3/2)\mathbf{N} - \mathbf{m} \otimes \mathbf{m}}{\bar{\sigma}} \quad (5-29)$$

5.2.2.2 Yld2000-2d

The first and second derivatives of the Yld2000-2d function are straightforward but considerably more lengthy than the Hill48 derivatives. The formulation and anisotropy coefficients of Yld2000-2d are described in detail in Section 3.1.5, and are not repeated here for the sake of brevity. Using the chain rule, the first derivative of the Yld2000-2d function can be expressed as

$$\mathbf{m} = \frac{\partial \bar{\sigma}(\boldsymbol{\sigma})}{\partial \boldsymbol{\sigma}} = [2a\bar{\sigma}^{(a-1)}]^{-1} \left[\frac{\partial \phi'}{\partial X'} \frac{\partial X'}{\partial X'_{\alpha\beta}} \frac{\partial X'_{\alpha\beta}}{\partial \boldsymbol{\sigma}} + \frac{\partial \phi''}{\partial X''} \frac{\partial X''}{\partial X''_{\alpha\beta}} \frac{\partial X''_{\alpha\beta}}{\partial \boldsymbol{\sigma}} \right] \quad (5-30)$$

where $\alpha\beta$ stands for 11, 22 and 12. By differentiating, each term in the above equation can be calculated as follows

$$\frac{\partial \phi'}{\partial X'} = \begin{bmatrix} \frac{\partial \phi'}{\partial X'_1} \\ \frac{\partial \phi'}{\partial X'_2} \end{bmatrix} = \begin{bmatrix} a(X'_1 - X'_2)^{(a-2)} |X'_1 - X'_2| \\ -a(X'_1 - X'_2)^{(a-2)} |X'_1 - X'_2| \end{bmatrix} \quad (5-31)$$

$$\begin{aligned} \frac{\partial \phi''}{\partial X''} &= \begin{bmatrix} \frac{\partial \phi''}{\partial X''_1} \\ \frac{\partial \phi''}{\partial X''_2} \end{bmatrix} \\ &= \begin{bmatrix} a(2X''_2 + X''_1)^{(a-2)} |2X''_2 + X''_1| + 2a(2X''_1 + X''_2)^{(a-2)} |2X''_1 + X''_2| \\ 2a(2X''_2 + X''_1)^{(a-2)} |2X''_2 + X''_1| + a(2X''_1 + X''_2)^{(a-2)} |2X''_1 + X''_2| \end{bmatrix} \end{aligned} \quad (5-32)$$

$$\begin{aligned} \frac{\partial X'}{\partial X'_{\alpha\beta}} &= \begin{bmatrix} \frac{\partial X'_1}{\partial X'_{11}} & \frac{\partial X'_1}{\partial X'_{22}} & \frac{\partial X'_1}{\partial X'_{12}} \\ \frac{\partial X'_2}{\partial X'_{11}} & \frac{\partial X'_2}{\partial X'_{22}} & \frac{\partial X'_2}{\partial X'_{12}} \end{bmatrix} \\ &= \begin{bmatrix} \frac{1}{2} \left(1 + \frac{X'_{11} - X'_{22}}{\sqrt{\Delta'}} \right) & \frac{1}{2} \left(1 - \frac{X'_{11} - X'_{22}}{\sqrt{\Delta'}} \right) & \frac{2X'_{12}}{\sqrt{\Delta'}} \\ \frac{1}{2} \left(1 - \frac{X'_{11} - X'_{22}}{\sqrt{\Delta'}} \right) & \frac{1}{2} \left(1 + \frac{X'_{11} - X'_{22}}{\sqrt{\Delta'}} \right) & -\frac{2X'_{12}}{\sqrt{\Delta'}} \end{bmatrix} \end{aligned} \quad (5-33)$$

$$\begin{aligned} \frac{\partial X''}{\partial X''_{\alpha\beta}} &= \begin{bmatrix} \frac{\partial X''_1}{\partial X''_{11}} & \frac{\partial X''_1}{\partial X''_{22}} & \frac{\partial X''_1}{\partial X''_{12}} \\ \frac{\partial X''_2}{\partial X''_{11}} & \frac{\partial X''_2}{\partial X''_{22}} & \frac{\partial X''_2}{\partial X''_{12}} \end{bmatrix} \\ &= \begin{bmatrix} \frac{1}{2} \left(1 + \frac{X''_{11} - X''_{22}}{\sqrt{\Delta''}} \right) & \frac{1}{2} \left(1 - \frac{X''_{11} - X''_{22}}{\sqrt{\Delta''}} \right) & \frac{2X''_{12}}{\sqrt{\Delta''}} \\ \frac{1}{2} \left(1 - \frac{X''_{11} - X''_{22}}{\sqrt{\Delta''}} \right) & \frac{1}{2} \left(1 + \frac{X''_{11} - X''_{22}}{\sqrt{\Delta''}} \right) & -\frac{2X''_{12}}{\sqrt{\Delta''}} \end{bmatrix} \end{aligned} \quad (5-34)$$

$$\frac{\partial X'_{\alpha\beta}}{\partial \sigma} = \mathbf{L}', \quad \frac{\partial X''_{\alpha\beta}}{\partial \sigma} = \mathbf{L}'' \quad (5-35)$$

where,

$$\Delta' = (X'_{11} - X'_{22})^2 + 4X'_{12}{}^2, \quad \Delta'' = (X''_{11} - X''_{22})^2 + 4X''_{12}{}^2 \quad (5-36)$$

By replacing Eqs. (5-31)-(5-35) into Eq. (5-30), the first derivative of Yl2000-2d is obtained. A similar procedure is followed to obtain the second derivative of Yl2000-2d, by making derivation from Eq. (5-30) based on the chain rule

$$\frac{\partial \mathbf{m}}{\partial \sigma} = \frac{\partial^2 \bar{\sigma}}{\partial \sigma^2} = \frac{\bar{\sigma}^{(a-1)}}{2a} \frac{\partial^2 \phi}{\partial \sigma^2} - \frac{1-a}{\bar{\sigma}} \mathbf{m} \otimes \mathbf{m} \quad (5-37)$$

By differentiating from the Yld2000-2d equation, $\partial^2 \phi / \partial \sigma^2$ can be written based on the chain rule as follows

$$\begin{aligned} \frac{\partial^2 \phi}{\partial \sigma^2} &= \left[\left(\frac{\partial^2 \phi'}{\partial X' \partial X'} \frac{\partial X'}{\partial X'_{\alpha\beta}} \frac{\partial X'_{\alpha\beta}}{\partial \sigma} \right) \frac{\partial X'}{\partial X'_{\alpha\beta}} \frac{\partial X'_{\alpha\beta}}{\partial \sigma} + \left(\frac{\partial^2 \phi''}{\partial X'' \partial X''} \frac{\partial X''}{\partial X'_{\alpha\beta}} \frac{\partial X'_{\alpha\beta}}{\partial \sigma} \right) \frac{\partial X''}{\partial X'_{\alpha\beta}} \frac{\partial X'_{\alpha\beta}}{\partial \sigma} \right] \\ &+ \left[\frac{\partial \phi'}{\partial X'} \left(\frac{\partial^2 X'}{\partial X'_{\alpha\beta} \partial X'_{\alpha\beta}} \frac{\partial X'_{\alpha\beta}}{\partial \sigma} \right) \frac{\partial X'_{\alpha\beta}}{\partial \sigma} + \frac{\partial \phi''}{\partial X''} \left(\frac{\partial^2 X''}{\partial X'_{\alpha\beta} \partial X'_{\alpha\beta}} \frac{\partial X'_{\alpha\beta}}{\partial \sigma} \right) \frac{\partial X'_{\alpha\beta}}{\partial \sigma} \right] \end{aligned} \quad (5-38)$$

where,

$$\begin{aligned} \frac{\partial^2 \phi'}{\partial X' \partial X'} &= \begin{bmatrix} \frac{\partial \phi'}{\partial X'_1 \partial X'_1} & \frac{\partial \phi'}{\partial X'_1 \partial X'_2} \\ \frac{\partial \phi'}{\partial X'_2 \partial X'_1} & \frac{\partial \phi'}{\partial X'_2 \partial X'_2} \end{bmatrix} \\ &= a(a-1) |X'_1 - X'_2|^{(a-2)} \text{sign}(X'_1 - X'_2) \begin{bmatrix} 1 & -1 \\ -1 & 1 \end{bmatrix} \end{aligned} \quad (5-39)$$

$$\begin{aligned} \frac{\partial^2 \phi''}{\partial X'' \partial X''} &= \begin{cases} \frac{\partial \phi''}{\partial X''_1 \partial X''_1} = a(a-1) [|2X''_2 + X''_1|^{(a-2)} \text{sign}(2X''_2 + X''_1) + 4|2X''_1 + X''_2|^{(a-2)} \text{sign}(2X''_1 + X''_2)] \\ \frac{\partial \phi''}{\partial X''_1 \partial X''_2} = a(a-1) [2|2X''_2 + X''_1|^{(a-2)} \text{sign}(2X''_2 + X''_1) + 2|2X''_1 + X''_2|^{(a-2)} \text{sign}(2X''_1 + X''_2)] \\ \frac{\partial \phi''}{\partial X''_2 \partial X''_1} = a(a-1) [2|2X''_2 + X''_1|^{(a-2)} \text{sign}(2X''_2 + X''_1) + 2|2X''_1 + X''_2|^{(a-2)} \text{sign}(2X''_1 + X''_2)] \\ \frac{\partial \phi''}{\partial X''_2 \partial X''_2} = a(a-1) [4|2X''_2 + X''_1|^{(a-2)} \text{sign}(2X''_2 + X''_1) + |2X''_1 + X''_2|^{(a-2)} \text{sign}(2X''_1 + X''_2)] \end{cases} \end{aligned} \quad (5-40)$$

$$\left[\frac{\partial^2 X_1'}{\partial X'_{\alpha\beta} \partial X'_{\alpha\beta}} \right] = - \left[\frac{\partial^2 X_2'}{\partial X'_{\alpha\beta} \partial X'_{\alpha\beta}} \right] =$$

$$\begin{bmatrix} \left(\frac{1}{4\Delta'} - \frac{(X'_{11} - X'_{22})^2}{16\Delta'^3} \right) & \left(-\frac{1}{4\Delta'} + \frac{(X'_{11} - X'_{22})^2}{16\Delta'^3} \right) & \left(-\frac{(X'_{11} - X'_{22})X'_{12}}{4\Delta'^3} \right) \\ \left(-\frac{1}{4\Delta'} + \frac{(X'_{11} - X'_{22})^2}{16\Delta'^3} \right) & \left(\frac{1}{4\Delta'} - \frac{(X'_{11} - X'_{22})^2}{16\Delta'^3} \right) & \left(\frac{(X'_{11} - X'_{22})X'_{12}}{4\Delta'^3} \right) \\ \left(-\frac{(X'_{11} - X'_{22})X'_{12}}{4\Delta'^3} \right) & \left(\frac{(X'_{11} - X'_{22})X'_{12}}{4\Delta'^3} \right) & \left(\frac{1}{\Delta'} - \frac{X_{12}'^2}{\Delta'^3} \right) \end{bmatrix} \quad (5-41)$$

$$\left[\frac{\partial^2 X_1''}{\partial X''_{\alpha\beta} \partial X''_{\alpha\beta}} \right] = - \left[\frac{\partial^2 X_2''}{\partial X''_{\alpha\beta} \partial X''_{\alpha\beta}} \right] =$$

$$\begin{bmatrix} \left(\frac{1}{4\Delta''} - \frac{(X''_{11} - X''_{22})^2}{16\Delta''^3} \right) & \left(-\frac{1}{4\Delta''} + \frac{(X''_{11} - X''_{22})^2}{16\Delta''^3} \right) & \left(-\frac{(X''_{11} - X''_{22})X''_{12}}{4\Delta''^3} \right) \\ \left(-\frac{1}{4\Delta''} + \frac{(X''_{11} - X''_{22})^2}{16\Delta''^3} \right) & \left(\frac{1}{4\Delta''} - \frac{(X''_{11} - X''_{22})^2}{16\Delta''^3} \right) & \left(\frac{(X''_{11} - X''_{22})X''_{12}}{4\Delta''^3} \right) \\ \left(-\frac{(X''_{11} - X''_{22})X''_{12}}{4\Delta''^3} \right) & \left(\frac{(X''_{11} - X''_{22})X''_{12}}{4\Delta''^3} \right) & \left(\frac{1}{\Delta''} - \frac{X''_{12}{}^2}{\Delta''^3} \right) \end{bmatrix} \quad (5-42)$$

It should be mentioned that for the sake of brevity the derivatives of the Yld2004-18p yield function are not presented here and the interested readers are referred to the work of Barlat et al. (2005). The rate-dependent implicit integration algorithm developed in this chapter is completely defined for two different anisotropic yield functions (Hill48 and Yld2000-2d) and three different hardening models (JC, KHL, and SKP). In order to apply the developed VUMAT into finite-strain shell elements in ABAQUS/Explicit, the transverse shear stiffness must also be calculated.

5.3 Transverse Shear Stiffness

For finite-shell elements, ABAQUS/Explicit will automatically calculate the transverse shear stiffness values in each time increment. However, the user must specify the transverse shear stiffness values manually as part of the shell section, when applying a user-defined material subroutine (VUMAT). ABAQUS computes the transverse shear

stiffness by matching the shear response for the case of shell bending about one axis to that of a three-dimensional solid, using a parabolic variation of transverse shear stress in each layer. In order to calculate the transverse shear stiffness values, ABAQUS assumes that the bending about one principal direction is not enforcing a restraining moment about the other direction. This assumption may cause inaccuracy for composite shells with orthotropic layers that are not symmetric about the shell mid-surface, in which the shell section directions may not be the principal bending directions. Since ABAQUS computes the transverse shear stiffness values only once at the beginning of an analysis based on the material initial linear elastic stiffness, any changes to the transverse shear stiffness values during an analysis are ignored. For a homogeneous shell element made of a linear, orthotropic elastic material, the transverse shear stiffness values are obtained as follows

$$K_{11}^{ts} = \frac{5}{6} G_{13}^E t, \quad K_{22}^{ts} = \frac{5}{6} G_{23}^E t, \quad K_{12}^{ts} = K_{21}^{ts} = 0 \quad (5-43)$$

where G_{13}^E and G_{23}^E are the material's shear moduli in the out-of-plane directions, and t is the average element thickness. "5/6" is the shear correction factor which results from matching the transverse shear energy of a shell element to that of a three-dimensional solid element in pure bending (ABAQUS 6.12 user's manual).

5.4 Verification of the User Material Subroutine (VUMAT)

In this section, the validity and accuracy of the developed rate-dependent user-defined subroutines are verified for several loading conditions at various strain rates, using two different VUMATs. The first VUMAT is based on the Yld2000-2d yield function and the KHL hardening model and the second one is a combination of Hill48 yield function and JC hardening model. The material used in these simulations is the DP600 that was described in Chapter 3 and the Yld2000-2d anisotropy coefficients and the KHL material constants are given in Tables 3.7 and 3.27, respectively. The first VUMAT was used to simulate the uniaxial tension (in the rolling and transverse directions) and biaxial tension of a single element. The simulation results are compared with the corresponding experimental flow curves to evaluate the VUMAT, qualitatively and quantitatively.

The second VUMAT was used to simulate the bending of a cantilever beam and loading under combined tension-shear. The VUMAT results are compared with the ABAQUS built-in material model to evaluate the accuracy of the developed rate-dependent numerical integration algorithm. It should be noted that it is not possible to combine an anisotropic yield function with a rate-dependent hardening model using the built-in constitutive material models in ABAQUS/Explicit. Therefore, in the second VUMAT, the Hill48 anisotropy coefficients were set to values which represent an isotropic material and the JC material constants for DP600 (given in Table 3.26) were used to compare the results of the VUMAT with the ABAQUS built-in material model (based on von Mises yield function and JC hardening model).

5.4.1 Uniaxial tension at various strain rates

As a very simple test, the uniaxial tension test can be used to verify the first rate-dependent VUMAT (based on Yld2000-2d and KHL). This type of loading is attractive as it causes a homogenous material deformation and only one single element can be used in the simulation. The main advantage of using a single element is the mesh-independency of the solution. To this end, the uniaxial tension of a 1 mm by 1 mm square plane-stress element was simulated in the rolling (RD) and transverse (TD) directions at various strain rates. As shown in Figure 5-2, the left or the bottom side of the element was fixed in the X or Y-direction, respectively, to simulate the uniaxial tension in the rolling and transverse directions. Also, the node located at the bottom left corner of the element was fixed in both X and Y-directions in both cases. Then, in order to produce various strain rate regimes, different constant velocities were applied to the right side or the top of the element to simulate the uniaxial tension in the rolling and transverse directions, respectively. The element was selected as CPS4R, a first-order quadrilateral reduced integration element type.

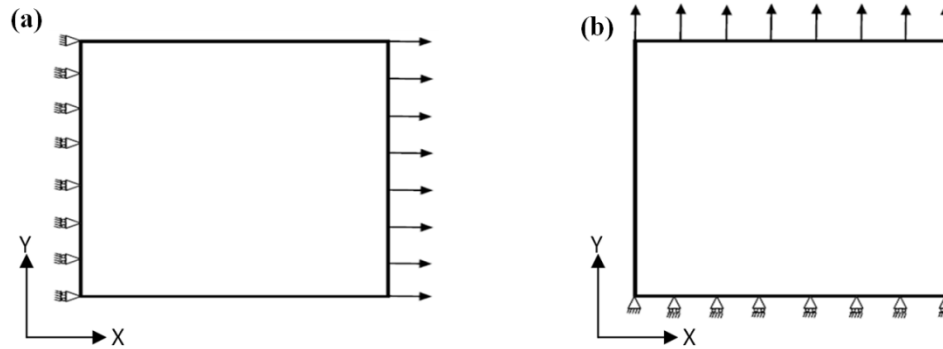


Figure 5-2. Schematic of the single element model for the uniaxial tension in a) RD b) TD

Figure 5-3 shows that the rate-dependent VUMAT is able to reproduce the experimental flow stresses in uniaxial tension at various strain rates (here, only strain rates of 10, 100, and 1000 s^{-1} are shown). It should be noted that the appropriate extrapolation was applied at each strain rate to extend the uniaxial flow curves to the same level as the experimental or calculated equibiaxial curves (as discussed in Section 3.5). Except for the initial small strain values (which are not really in the strain range of interest, since the EHF process leads to much higher strain values), the predicted flow stresses correlate well with the corresponding experimental curves. It can be concluded that both Yld2000-2d yield function and KHL hardening model correctly predict the behaviour of DP600 in uniaxial tension. The discrepancy between the experimental and predicted uniaxial flow stresses for the small strain values ($0 - 0.05$) are related to the procedure used to determine the normalized flow stresses for calibration of different yield functions. Based on the calibration procedure discussed in Section 3.3.1, the normalized flow stresses were selected when they saturate (after certain level of strain), which guarantees that, apart from the initial small strain values, the predicted flow stresses will match with the corresponding experiments for a wide range of strain values, as can be seen in Figure 5-3.

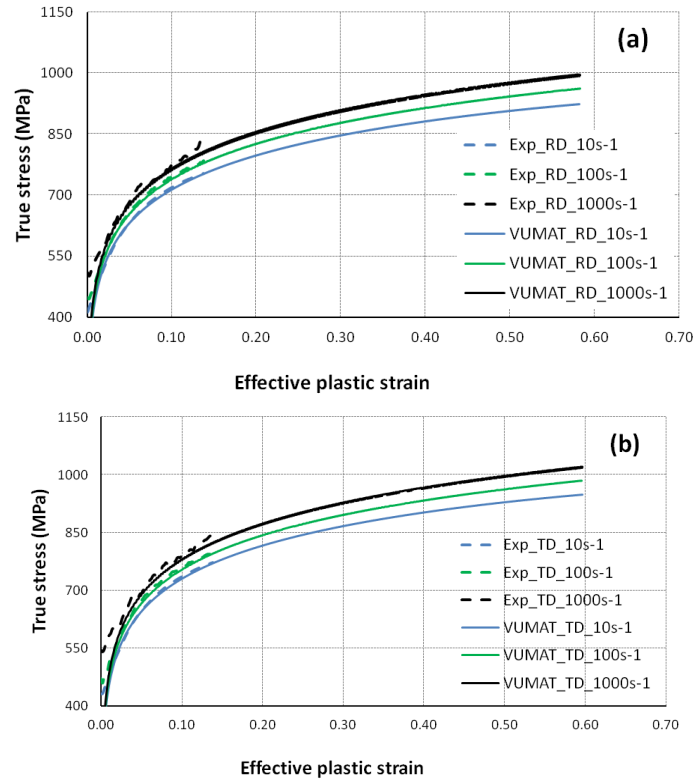


Figure 5-3. Comparison between experimental and predicted DP600 uniaxial flow curves; at various strain rates, a) RD b) TD

5.4.2 Biaxial loading at various strain rates

Uniaxial tension simulations serve to validate the VUMAT in uni-directional loading, however, actual forming processes usually lead to multiaxial loading conditions. The biaxial bulge test is one of the most popular examples of biaxial loading in sheet metal forming, and was used to evaluate the VUMAT in biaxial tension. To this end, a 1 mm by 1 mm square element (CPS4R element type) was subjected to equibiaxial loading using the first VUMAT. As shown in Figure 5-4, the bottom and left sides of the element were fixed in both X and Y-directions, respectively. Then, different velocities were applied simultaneously to the top and right sides of the element to produce various strain rates.

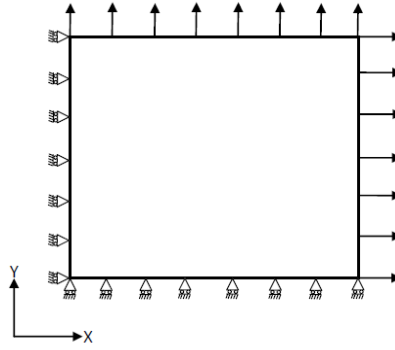


Figure 5-4. Schematic of the single element model for biaxial tension

Figure 5-5 shows the comparison between the predicted biaxial flow stresses and the corresponding calculated ones (obtained based on the procedure discussed in Section 3.3.2). As expected, considering to the biaxial normalized flow stress determination procedure (presented in Section 3.3.1), the VUMAT is able to predict the biaxial flow stresses quite well after approximately 0.2 strain, at each level of strain rate. The VUMAT slightly underestimates the biaxial flow stresses at various strain rate regimes in the plastic strain range of 0 – 0.2.

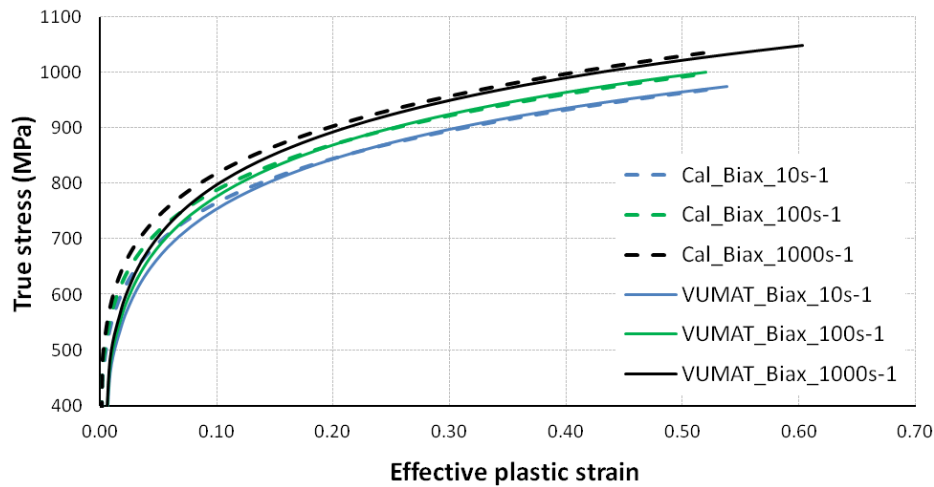


Figure 5-5 Comparison between experimental and predicted DP600 biaxial flow curves; at various strain rates

Figure 5-6 shows an overall comparison between experimental/calculated and predicted uniaxial and biaxial flow curves at various strain rates. For all strain rate regimes, results show that the developed rate-dependent user-defined material model is

able to describe the DP600 material anisotropy accurately in both uniaxial and biaxial loading conditions. It is noticeable that a minor discrepancy for the uniaxial condition can be observed, at the beginning of the plastic strain region (below 0.05), while this discrepancy is more significant for a larger strain range (below 0.2) in the biaxial case. These discrepancies are considered acceptable considering the main objective of this work is to predict the behaviour of sheet materials up to larger strain values in biaxial stress states in high strain rate forming processes, such as EHF.

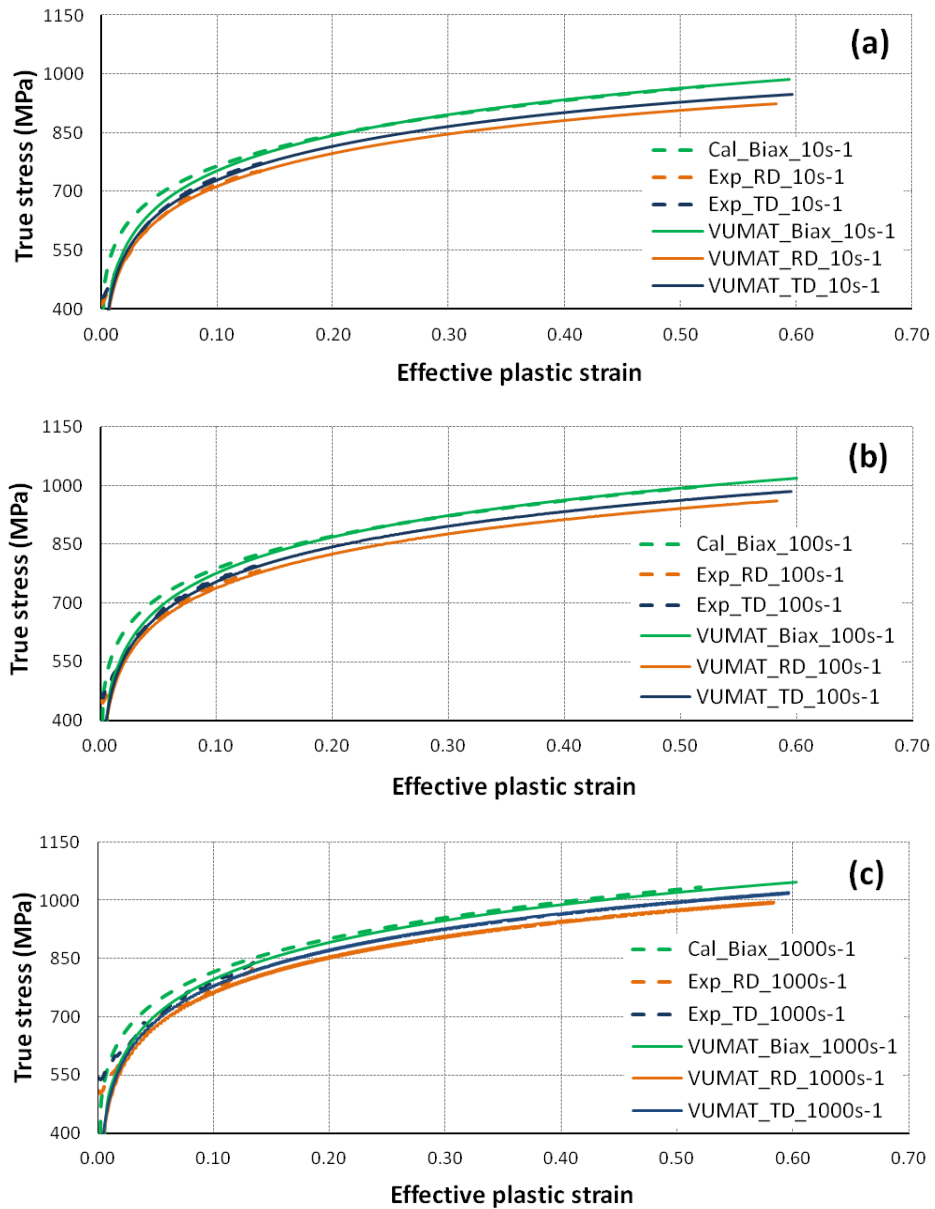


Figure 5-6. Comparison between experimental and predicted uniaxial and biaxial DP600 flow curves; a) 10 s^{-1} b) 100 s^{-1} c) 1000 s^{-1}

5.4.3 Bending of a cantilever beam

In order to verify the accuracy of the developed rate-dependent implicit integration method with the ABAQUS integration algorithm, the second VUMAT was used to simulate the bending of a cantilever beam. Once again, it should be emphasized that due to the inability of applying a built-in anisotropic rate-dependent constitutive model into the simulations in ABAQUS/Explicit, isotropic behaviour was assumed for DP600 in the second VUMAT. Therefore, Hill48 was reduced to the von Mises function, which makes the second VUMAT exactly identical to the rate-dependent ABAQUS built-in material model based on von Mises yield function and JC hardening model. As shown in Figure 5-7, a 1 mm by 10 mm rectangle was fixed at one end and loaded with a downward velocity of $V_y = 1000 \text{ mm/s}$ at the other end. CPS4R elements of 0.25 mm by 0.25 mm were used to discretize the beam.

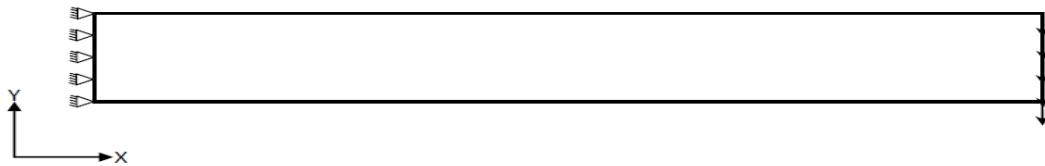


Figure 5-7. Schematic of the cantilever beam model

Figure 5-8 shows the predicted effective stress variation along the top surface of the beam obtained by the VUMAT and the ABAQUS built-in material model. The comparison shows the same results for both the VUMAT and the ABAQUS built-in material model, which represents the capability of the developed rate-dependent numerical implicit integration algorithm to predict the same flow stress as the ABAQUS built-in algorithm, when assuming isotropic behaviour. Figure 5-9 also shows the effective stress contours in the deformed beam as predicted by the VUMAT and the ABAQUS built-in material model.

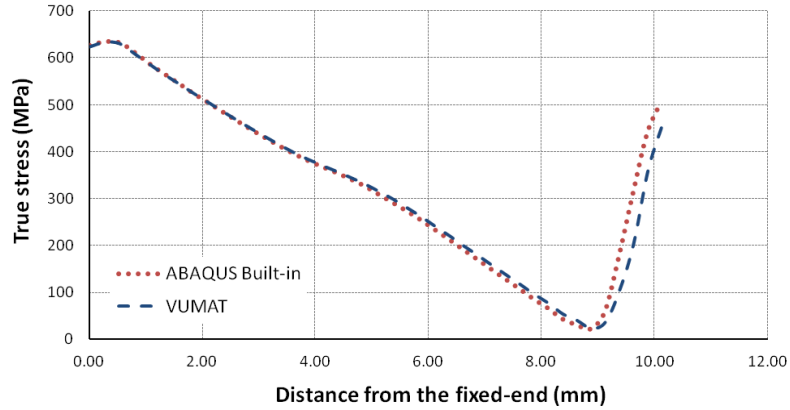


Figure 5-8. Effective stress variation along the top surface of a DP600 beam

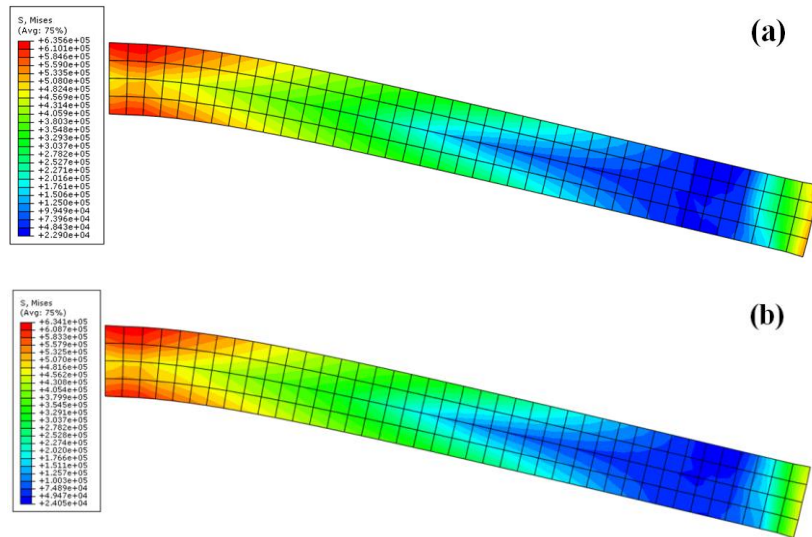


Figure 5-9. Effective stress contours in the deformed DP600 beam; a) VUMAT, b) ABAQUS built-in material model

5.4.4 Combined tension-shear

The second VUMAT was again used to simulate a combined tension-shear loading to verify the developed rate-dependent implicit integration algorithm. Similar to the uniaxial and biaxial cases, a 1 mm by 1 mm square was meshed with CPS4R elements. As shown in Figure 5-10, the bottom side of the element was fixed in the X and Y-directions and two different sets of velocities were applied to the top side, separately. In the first set, $V_x = 5 \text{ mm/s}$ and $V_y = 7.5 \text{ mm/s}$ were selected as the velocities in the X and Y-

directions, respectively. In the second set, these values were increased to $V_x = 500 \text{ mm/s}$ and $V_y = 7500 \text{ mm/s}$ to simulate a higher strain rate regime.

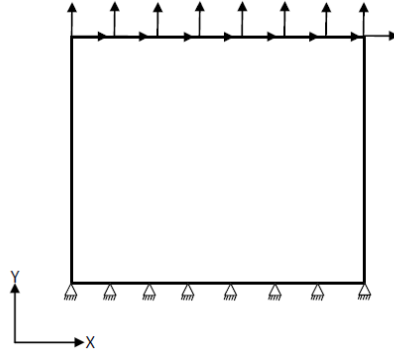


Figure 5-10. Schematic of the combined tension-shear model

Figure 5-11 compares the effective flow stresses of DP600 predicted by the VUMAT and the ABAQUS built-in material model. For the two different sets of velocities, the same stress-strain responses were obtained, which confirms the accuracy of the rate-dependent VUMAT under a multiaxial loading condition.

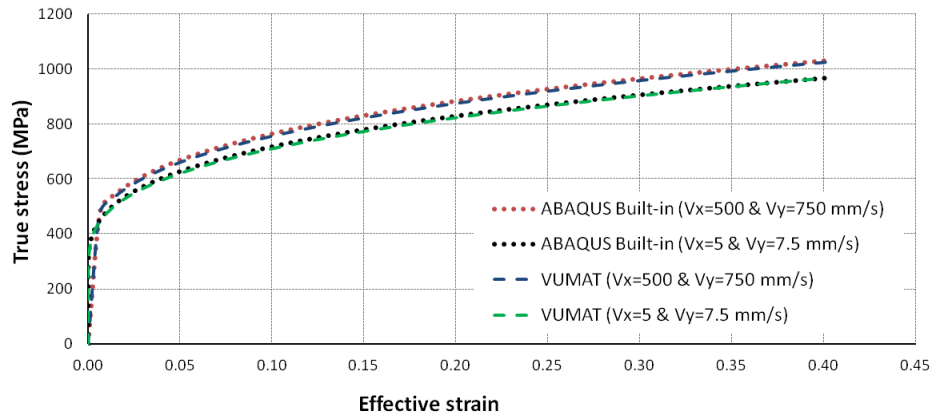


Figure 5-11. Comparison between the predicted flow stresses obtained by the VUMAT and the ABAQUS built-in material model; at two different sets of velocities

According to the above simulations, the developed rate-dependent user-defined material models are able to accurately predict the stress field of DP600 in several loading conditions such as uniaxial tension, biaxial tension, bending, and combined tension-shear. Therefore, it can be concluded that the user-defined material subroutines have been

correctly implemented and are expected to work properly for more complex loading conditions such as actual sheet metal forming simulations. The results of EHF simulations, using rate-dependent anisotropic user-defined material models, will be discussed in the next chapter.

6 Finite Element Simulation of Electrohydraulic Forming

6.1 Introduction

Substantial efforts have been dedicated to the finite element (FE) analysis of pulsed forming processes (Golovashchenko et al., 2013, Imbert and Worswick, 2011 and Melander et al., 2011). However, the role of material anisotropy and its effects on different aspects of sheet material deformation have not yet been clearly understood due to the complexity of the experimental and numerical work required for such an investigation.

This chapter presents quantitative anisotropy results of electrohydraulic forming (EHF) process for DP600 steel and AA5182-O aluminum sheets, based upon experimental measurements and finite element (FE) predictions of major/minor (principal) strain distributions. To this end, four specimens with optimized geometries, representing four different strain paths (uniaxial, intermediate draw, plane strain and biaxial) were safely formed under electrohydraulic free-forming (EHFF) conditions. A new FE model using ABAQUS/Explicit code was developed, applying the ignition-and-growth model to a small spherical volume as an equivalent of the actual plasma channel. The developed rate-dependent (KHL hardening model) isotropic (von Mises) and anisotropic (Yld2000-2d) constitutive material models (VUMATs) were used to simulate the EHFF process. These FE predictions are presented and compared to the measured strain distributions to investigate the effect of sheet material anisotropy at intermediate and high strain rate regimes. Also, the developed VUMATs were applied to a single element to calculate the difference in the effective plastic strain predicted by isotropic and anisotropic yield

functions at various strain rates. Finally, electrohydraulic die-forming (EHDF) using a conical-die was simulated for DP600. The developed general rate-dependent anisotropic material model (VUMAT, which is the combination KHL hardening model and Yld2004-18p yield function) was applied to consider the effect of anisotropy in a general (three-dimensional) stress state. Details of both the experimental work and the FE modelling technique, as well as the results are presented in the following sections.

6.2 Experimental work

In electrohydraulic forming (EHF), two or more electrodes are located in a water-filled chamber and a high-voltage discharge across the electrodes creates a plasma channel. The plasma channel expands and generates a shockwave that propagates through a fluid (generally water) and forms the sheet at the acoustic velocity of the fluid. The parameters that affect the efficiency of the EHF process are the distance between the electrodes and the blank (stand-off distance), the number and the mutual position of the electrodes, the electrical properties of the liquid, the capacitance of the circuit, the input voltage, the inductance and resistance of the equipment, and the shape and the volume of the chamber. The main pieces of equipment required for EHF tests are a pulse unit, a forming tool, a chamber, and a press. Interested readers are referred to Golovashchenko et al. (2013) for more details on the experimental EHF process, equipment and tooling design. A schematic of typical EHF tooling and setup that were used in both EHFF and EHDF tests is shown in Figure 6-1.

In order to verify the FE modeling approach of EHF and determine the role of material anisotropy at intermediate and high strain rate regimes, Electrohydraulic free-forming (EHFF) tests were carried out for DP600 steel and AA5182-O aluminum sheets. Different specimen geometries were designed and optimized particularly to determine the experimental forming limits in EHFF for specific strain paths. To this end, new open-window dies were built and some existing tools were modified by Maris (2014) to ensure the effective operation of EHFF experiments. Also, due to the greater interest to apply this technology in die-forming conditions, electrohydraulic die-forming (EHDF) tests were also carried out with DP600 sheets to investigate the effect of anisotropy in a

general stress state at high strain rate regimes. All experiments were performed at Ford's Research & Advanced Engineering laboratory.

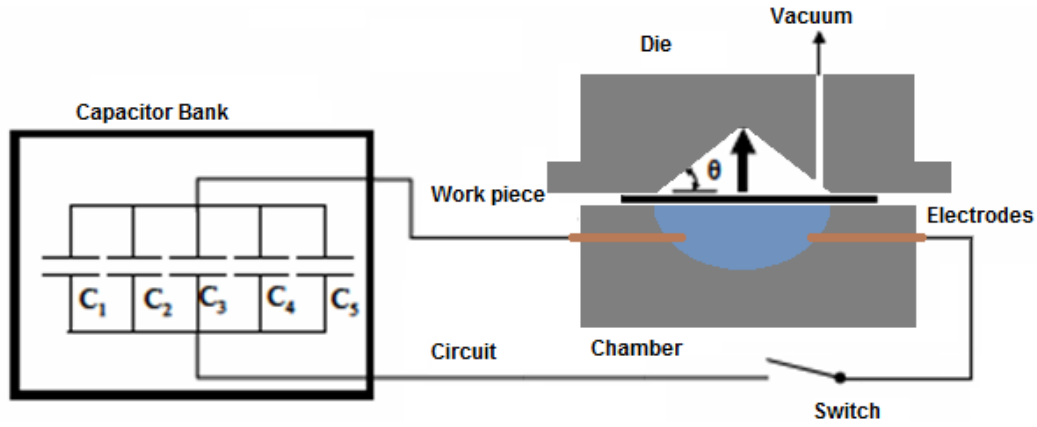


Figure 6-1. Schematic of a typical EHDF setup (Maris, 2014)

6.2.1 EHF Tooling

6.2.1.1 Pulse Unit

The Magnepress pulse unit was used to provide the electrical energy for the EHF tests. The duration of the discharge and the energy delivered to the chamber are internal characteristics of the pulse unit, which have a significant effect on the outcome of the experiments. The Magnepress has a total capacitance of $200\mu\text{F}$ and can deliver a maximum input voltage of 15kV , and a corresponding maximum energy of 22.5kJ . The measurements showed an approximately constant discharge time of $120\mu\text{s}$ with a sinusoidal shape, with a total forming time on the order of $100\text{-}350\mu\text{s}$ for different sheet metals. It should be noted that all specimens were formed with a single pulse of energy in both EHFF and EHDF to produce higher strain rate regimes. With both the conical die and open window die, a hydraulic press was used to clamp the upper dies to the chamber during EHF experiments with a clamping force of 100 tons. This amount of clamping force ensured that there was no drawing in of the sheet into the die cavity.

The portion of the released electrical energy that is actually delivered to the sheet depends on many factors associated with the experimental set-up and the electrical

efficiency of tooling and cables. Due to various types of energy losses in the EHF process, repeating the process to obtain the very same maximum height in the safe deformed specimens is very challenging. Attempts were made by Maris (2014) to experimentally quantify the electrical energy delivered to a hemispherical chamber. Voltages and currents that were measured across the electrodes and inside the Magnepress were used to calculate the power and energy at both the Magnepress and chamber. Results showed that even for successive pulses with consistent experimental set-up, the outcome of the dynamic EHF process can vary based on the amount of energy lost to inefficiencies. Therefore, experimentally measuring the actual energy that is generated within the chamber and the portion which is transferred to the blank can significantly vary from test to test depending on many parameters. Due to the shortage of reliable energy or pressure measurements for each specimen geometry and the variability in the process due to many parameters; it was decided to calibrate the energy in the FE models by measuring the maximum height of safely deformed specimens for each specimen geometry and for each material.

6.2.1.2 Chamber

In both EHFF and EHDF tests a hemispherical chamber with a diameter of 120mm was used. In order to increase the efficiency of the process, a 30mm tall chamber ring was added to increase the total volume of water contained in the chamber to 0.79L. The shape of a chamber is an important factor in the process, since it affects the wave reflection off the chamber walls. The optimization of a chamber design to increase the efficiency of the EHF process as well as result in a desired strain distribution in the deformed sheet material is very complex and requires a deep knowledge of wave propagation, reflection and fluid/solid interaction (FSI); such an optimization was not conducted as this was not the focus of this work.

6.2.1.3 Die

The EHFF specimens were formed without carrier (driver) sheets, which allowed water to pass through the cut-out holes in the specimens. In order to prevent any undesired deformation of the specimens due to rebounding of the water onto the top side of the

specimen, the EHFF specimens were formed into an open window die. In order to form specimens in a state of biaxial strain in EHDF, DP600 steel sheets were formed into a conical die with an apex angle of 112° (34° from the horizontal), a base diameter of 120 mm, an entry radius of 10 mm and a tip radius of 10 mm. An experimental study by Golovashchenko et al., (2013) showed that dies with greater depths were too extreme considering the formability of DP600 sheets. The study by Golovashchenko et al., (2013) also indicated that this die angle was ideal because it allowed for an effective dynamic sheet-die interaction which led to the activation of the beneficial formability enhancement mechanisms associated with die impact in EHDF.

In contrast to traditional stamping, the EHF process does not use a punch, and there is inherently no friction at the sheet/water interface. However, in EHF the friction between the sheet and the die does influence the sheet material deformation, especially in EHDF. In EHFF there is only a friction effect at the entry radius of the open window die, which does not have an influence on the overall material deformation, since the high amount of plastic deformation occurs in the central gauge section of the specimen far from the die entry radius. The friction effect can be considerable when it comes to EHDF, where there is a significant dynamic sheet/die interaction over almost the entire die surface. It should be noted that all EHFF and EHDF experiments were conducted without any lubricant at the sheet/die interface.

6.2.2 Sheet material, geometry and preparation

Two sheet materials of significant interest to the automotive industry, DP600 steel and AA5182-O aluminum were selected for EHFF, but only the DP600 steel sheet was used in EHDF experiments. Both sheet materials were 1.5mm thick and were tested in the as-received condition. The mechanical properties of these materials including r-values and flow stresses in different material orientations at various strain rates were presented in Tables 3.2 and 3.16 for DP600 and AA5182-O, respectively.

In order to carry out EHFF tests in which the sheet material can deform along specific strain paths, four different specimens were developed with cut-out holes of various shapes such that four specific linear strain paths would be generated; uniaxial,

intermediate draw, plane strain and biaxial tension. Based on a comprehensive numerical optimization procedure, the specimens were designed and optimized such that the greatest major strain is located in the center of the specimen while minimizing stress concentrations in the corner radii of the cutouts. The EHFF specimens were safely formed with different energy levels so as to study the effect of anisotropy in different stress states at intermediate and high strain rate regimes.

An important point is that carrier (drivers) blanks, which are normally used in quasi-static tests to create a uniform strain distribution and have been used in the EHFF work of other researchers, were omitted in these EHFF tests. The use of a carrier blank results in a more complex friction condition between the specimen and the carrier sheet which adds a substantial uncertainty to the acquired experimental data, and increases the complexity in the numerical simulation of the forming process. Therefore, the elimination of carrier blanks made for a simple and straightforward test in which friction was minimized, the maximum stress was located at the centre of the gauge area and the strain path was quasi-linear. Also, due to careful optimization of the EHFF specimens, no edge cracking was observed in any of the deformed specimens which ensured the reliability of the experimental data. In addition, the existence of a single gauge section in the centre of each specimen, makes this gauge area an interest zone to concentrate on the effect of anisotropy at high strain rate regimes. The four different specimen geometries were cut out from circular blanks using a CNC mill. For consistency, all the specimens were machined with the rolling direction (RD) of the material parallel to the length of the gauge section such that the major strain was always parallel to the RD. All the specimens were electroetched with a square grid on one side of the blanks, with a size of 2.54mm (0.1in). Figure 6-2 illustrates the four different specimen geometries used in the EHFF experiments and simulations.

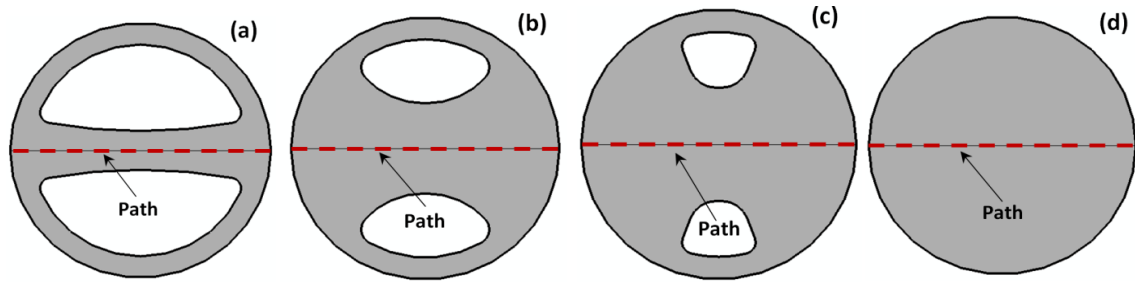


Figure 6-2. Different geometries of specimens used in EHF; a) uniaxial b) intermediate draw c) plane strain d) biaxial

6.2.3 Deformed EHF Specimens

In order to investigate the effect of anisotropy at high strain rate, a total of 27 safely formed specimens were selected from the EHF tests (no necking or fracture were observed); 16 DP600 steel and 11 AA5182-O aluminum sheets. These specimens included all four geometries (uniaxial, intermediate draw, plane strain and biaxial tension) for the two materials. It was difficult to reach the same maximum dome height for the safe specimens in different geometries because EHF is a dynamic process with significant process variability, and accordingly, the exact same conditions do not occur with each electrical discharge. To ensure consistency between specimens and confidence in the measurements, the specimens with almost similar maximum height were selected for comparison with the numerical simulations. A path along the centerline of each specimen (shown in Figure 6-2 for the four specimens) was selected to provide insight into how certain parameters varied from edge to edge within the sheet. In order to evaluate the effect of material anisotropy, the major/minor strain distributions, thickness distributions, and height (vertical or out-of-plane displacement) profile of the selected safe specimens were measured and are presented in section 6.4.2. The height profile (distribution) of the deformed specimens was obtained using a 3D scanner with twin 3.0 Megapixel CMOS image sensors with ± 0.127 mm dimensional accuracy. Also, the energy required to form each specimen was measured at the chamber by Maris (2014) and these measurements are summarized in Table 6.2 and Table 6.3 for DP600 and AA5182-O, respectively. Figure 6-3 shows the selected safe specimens in this study for DP600 and AA5182-O for all four geometries. Also, a safe DP600 biaxial specimen formed into the conical-die is shown in Figure 6-4.

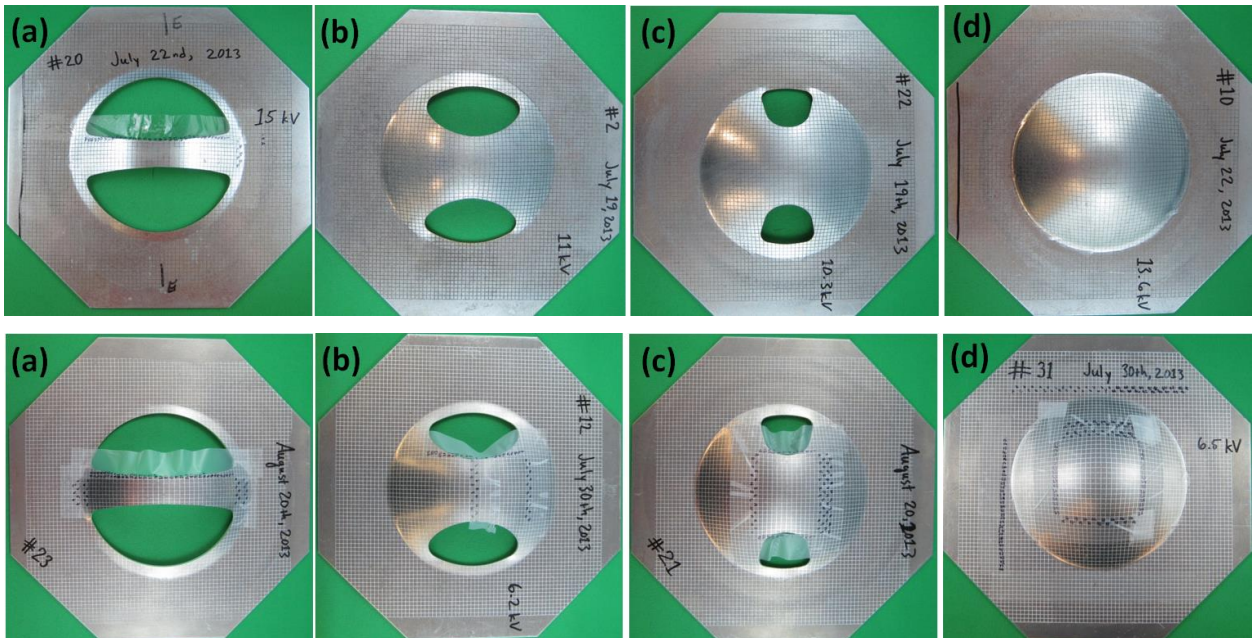


Figure 6-3. Safe EHFF specimens for DP600 (top) and AA5182-O (bottom);
 a) uniaxial b) intermediate draw c) plane strain d) biaxial

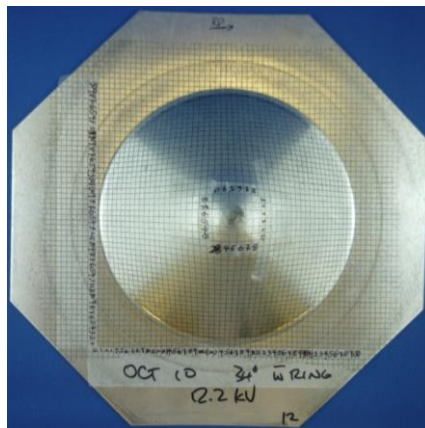


Figure 6-4. Safe EHDF DP600 specimen

6.2.4 Strain measurements

Major and minor strains were measured from the deformed square grids on the EHFF and EHDF specimens using the FMTI grid analyzer model 100U. This apparatus calculates the major and minor strain based on an automatic image processing of the undeformed and deformed grid, using a digital camera and a software package. Ideally, the FMTI tool can be precise to $\pm 0.5\%$ engineering strain (Sklad and Verhaeghe, 2010).

However, the practical accuracy of the measured data strongly depends on the quality of the electroetched grid, among other factors. Based on a study that was conducted in our research lab and reported by Maris (2014), the error of the FMTI grid analyzer was estimated between 2% to 4%, depending on the geometry of the deformed specimen. Also, an Ultrasonic thickness tester was used to measure the thickness of each specimen along the centreline of the gauge area (Figure 6-2).

6.3 Finite element modelling

6.3.1 Single element model

In order to better understand the role of material anisotropy in the prediction of effective plastic strain at various strain rates (0.001, 0.1, 1, 10, 100 and 1000 s^{-1}), a $1\text{ mm} \times 1\text{ mm}$ single shell element was modelled. To this end, three different constitutive models including von Mises, Hill48 (calibrated based on r-values) and Yld2000-2d yield functions were applied, using the appropriate boundary conditions to simulate plane strain and biaxial tension conditions. It should be mentioned that the anisotropy coefficients were updated w.r.t. strain rate and the KHL hardening model was used in each case. By applying the same amount of plastic strain in the rolling direction (RD) for both plane strain and biaxial tension conditions, the error of effective plastic strain at various strain rates predicted by von Mises and Hill48 yield functions were calculated, assuming Yld2000-2d as the reference yield function. The calculations were completed for both DP600 and AA5182-O and the results are presented later in this chapter.

6.3.2 EHF model

The main emphasis of the simulations in this study was to understand the role of material anisotropy on the deformation occurring when the sheet is formed in EHF process. To this end, three-dimensional finite element explicit dynamic simulations were also performed using ABAQUS/Explicit to predict the deformation history of specimens in EHFF and EHDF. One of the most challenging parts of the EHF simulations was to model the input energy released between the electrodes in the water. In many

simulations, the interaction between the water and the sheet is not taken into account, and the input energy is simulated by a pressure history distributed uniformly across the sheet. However, experimental evidence (Rohatgi et al, 2011 and 2012) suggests that the shape and duration of the pressure pulse propagating through the water and the complex interaction between the water and the sheet significantly affect the strain distribution and strain rate history in the sheet throughout its deformation.

In order to simulate every aspect of the actual mechanism of electrical discharge in EHF, in-depth knowledge and sophisticated principles of underwater electrical discharge, plasma channel generation, wave propagation, hydrodynamics and fluid/solid interaction (FSI) are required (Grinenko et al. 2008). A comprehensive approach for FE modelling EHF in LS-DYNA was presented by Golovashchenko et al. (2013) to describe the results of EHF into open round, V-shaped, and conical dies. However, modelling the EHF process using the same approach in ABAQUS was not possible, due to the unavailability of some features, such as the energy-leak equation of state which was used by Golovashchenko as a representative of electrical discharge in EHF process in LS-DYNA.

In this study as an alternative, shockwave generation by underwater electrical discharge was assumed to be nearly similar to that by underwater explosion (UNDEX), except that underwater electrical discharge involves a plasma channel during the electric discharge whereas UNDEX forms vaporized explosive gas bubbles during the explosion as illustrated in Figure 6-5. Based on the idea of similarity between underwater electrical discharge and UNDEX, Wakeland et al. (2003) applied the combination of similitude relation in UNDEX theory (Cole, 1948) and hydrodynamic code to predict the waveform of underwater electrical discharge-induced shockwave, assuming equivalency between electric energy in underwater electrical discharge and combustion energy in UNDEX. Results showed that the mathematical representation of shockwaves by underwater electrical discharge and similitude relation (Cole, 1948) are practically the same.

It should be emphasized that the main purpose of this work was not to create a complex FE model which is able to capture all aspects of physical mechanisms that occur during EHF, but to develop a reliable FE model (which works for a variety of specimen

geometries and materials) that is able to confidently predict the material anisotropy effect in EHF.

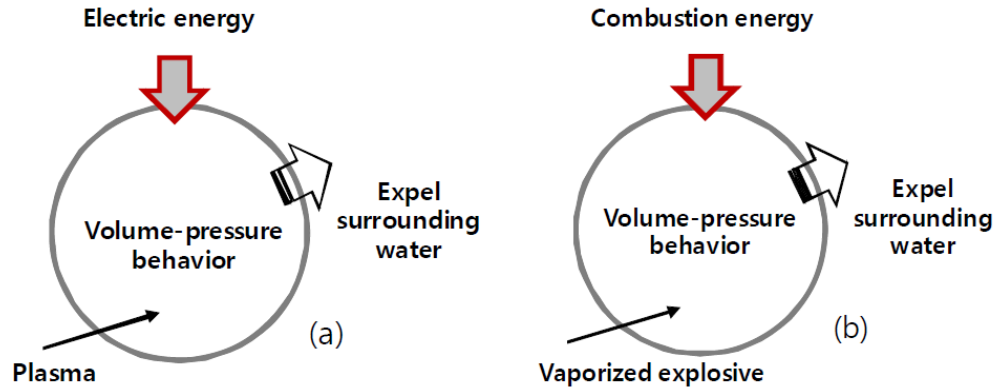


Figure 6-5. Mechanism of shockwave generation by;
a) underwater electrical discharge b) UNDEX

In order to simulate the electrical discharge in this work, the ignition-and-growth equation of state with a specific energy magnitude (which is determined based on the maximum deformed specimen) was assigned to a small spherical volume, which is located in the actual position between the electrodes gap (stand-off distance of 60 mm). It was decided to use the ignition-and-growth model, since the shape of the plasma channel becomes spherical almost at the very beginning of the EHF process based on the investigations reported by Golovashchenko et al. (2013). In order to calculate fluid (water) motion induced by shockwave, Eulerian elements were used to simulate the motion of water using the Mie-Gruneisen (Us-Up) equation of state. In addition, a certain limit (-0.1 MPa) was specified as the cavitation threshold of the water to consider the cavitation phenomenon (free expansion in a constant pressure) when the pressure of water is below that limit. A void property was assigned to the Eulerian elements above the chamber to allow the water to travel into that space as the simulation progressed.

During the EHF process, the heat transfer from the water to the sheet is negligible due to the very short deformation time and very small plasma channel volume compared to the volume of water. However, a local temperature rise (adiabatic thermal softening) does occur due to the plastic work in high-velocity forming. In this work, the thermal softening term was ignored due to insufficient experimental data relative to the effect of a

temperature rise on the flow stress of DP600 and AA5182-O at different strain rates. Therefore, a coupled thermal-structural analysis was reduced to only a structural analysis in this work. Figure 6-6 shows a section view of the developed FE model for EHF simulation. The details of the developed model are described in the following.

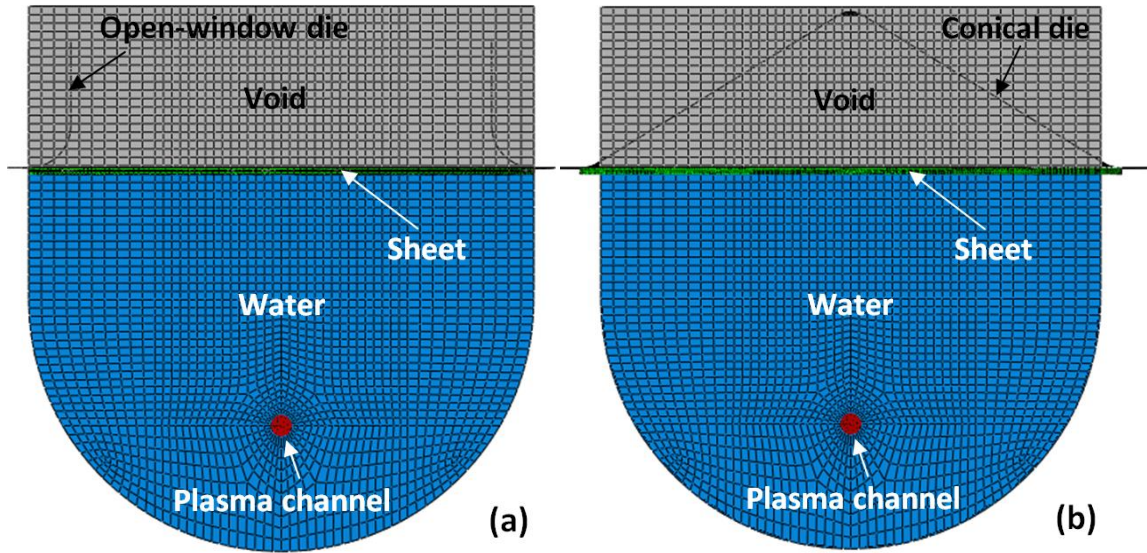


Figure 6-6. Section-view of the EHF finite element model; a) EHF b) EHF

6.3.2.1 Ignition-and-growth model

The ignition-and-growth flow model treats the explosive material as a homogeneous mixture of two distinct constituents, the un-reacted explosive solid and the reacted gaseous product. The Jones-Wilkins-Lee (JWL) equation of state is assigned to each constituent, and a single reaction-rate law is postulated for the conversion of the explosive to products. It is assumed that the two constituents are always in pressure and temperature equilibrium. The pressure in either phase is defined in terms of volume and internal energy as

$$P = A \left(1 - \frac{\omega}{R_1 V} \right) e^{-R_1 V} + B \left(1 - \frac{\omega}{R_2 V} \right) e^{-R_2 V} + \frac{\omega e}{V} \quad (6-1)$$

where P is the pressure, $V = \rho_0 / \rho$ is the relative volume, ω is the Gruneisen parameter, e is the internal energy, and $A, B, R_1,$ and R_2 are constants. The values of the above

constants for a reacted gaseous product are different from those for the unreacted solid explosive. The reaction rate law is expressed as,

$$\begin{aligned} \frac{dF}{dt} = & I[1 - F]^b \left[\frac{\rho}{\rho_0} - 1 - a \right]^x \quad \{0 < F < F_{ig\ max}\} \\ & + G_1[1 - F]^c F^d P^y \quad \{0 < F < F_{G_1\ max}\} \\ & + G_2[1 - F]^e F^g P^z \quad \{F_{G_2\ min} < F < 1\} \end{aligned} \quad (6-2)$$

where F is the fraction reacted, t is time, ρ is the current density, ρ_0 is the initial density, P is pressure, and $I, G_1, G_2, a, b, c, d, e, g, x, y,$ and z are constants. This reaction rate law models the three stages of reaction generally observed during shock initiation of solid explosives. Interested readers are referred to Kapila et al. (2007) for more details on the ignition-and-growth model and formulation.

Based on the experimental and numerical work completed by many researchers (Chen et al., 2007, Urtiew et al., 2006), ignition-and-growth parameters have been optimized for a wide variety of explosive materials. In this work, a parametric study was initially completed on the effect of several explosive materials such as Comp-B, C4, TNT, and LX17 (using the corresponding calibrated ignition-and-growth model) in the prediction of sheet material deformation history in EHF. Results showed a small effect of these materials in the overall deformation histories of different sheets in EHF simulations. Therefore, it was decided to select the calibrated parameters for explosive material Comp-B, calibrated by Schwer (2012). An optimization method was used by Schwer to optimally parameterize the ignition-and-growth reactive flow model to experimental Manganin gauge records. The ignition-and-growth model parameters are provided in Table 6.1.

One of the most important factors in the ignition-and-growth model, which affects the predicted dome height of the formed specimen and consequently the strain distributions, is the specific energy. In this study, the specific energy was determined by correlating the maximum height of the formed specimen predicted by the numerical simulation with that which was measured experimentally, for each strain path and for each sheet material. The magnitude of specific energy was adjusted for each material and specimen geometry in

EHFF simulations, so that the final dome height of the numerical specimens and the associated selected safe experimental specimens corresponded. For the sake of comparison, the amount of experimental input energy and the applied energy in the simulations of different geometries are presented in Table 6.2 and Table 6.3 for DP600 and AA5182-O, respectively.

Table 6.1. Ignition-and-growth parameters for Comp-B

	Un-reacted JWJL	Reacted JWJL	
A (GPa)	4.85×10^4	5.242×10^2	
B (GPa)	-3.9	7.678	
ω	0.893	0.5	
R_1	11.3	4.2	
R_2	1.13	1.1	
ρ_0 (kg/m³)	1.717×10^3		
Reaction rate			
a	0.0367	y	2.0
b	0.667	z	3.0
c	0.667	$F_{ig\ max}$	0.022
d	0.333	$F_{G_1\ max}$	0.7
e	0.222	$F_{G_2\ min}$	0.0
g	1.0	G_1 (GPa⁻²s⁻¹)	1.4×10^4
I (s⁻¹)	4×10^7	G_2 (GPa⁻³s⁻¹)	10^3
x	7.0		

6.3.2.2 Constitutive material model

Numerical simulation results showed a predominance of intermediate and high strain rate regimes during almost the entire EHF process. Since, ABAQUS/Explicit does not support the combined use of anisotropic yield function (such as Hill48, Yld2000-2d and Yld2004-18p) and rate-dependent hardening model (such as JC and KHL) in its library of material models, the user-defined subroutine material model presented earlier was used to model the material behaviour. The subroutine material model was based on Yld2000-2d (for plane stress) and Yld2004-18p (for general stress state) anisotropic yield functions and the KHL hardening model using the implicit integration scheme for ABAQUS/Explicit (VUMAT) (details of the formulations were presented in Chapter 5).

The KHL hardening model was used for all the EHF simulations in this chapter. The KHL constants for DP600 and AA5182-O are presented in Table 3.27. The KHL model was selected due to its ability to accurately describe the response of the DP600 at various strain rates as shown in Figure 4-24b. It should be noted that, as discussed in Section 3.5, compared to the DP600 steel, AA5182-O is almost a strain rate insensitive material throughout the range in which material characterization tests were conducted ($0.001 - 1000 \text{ s}^{-1}$). The main reason for using the KHL hardening model for AA5182-O was to maintain consistency during all the simulations by using the same developed VUMAT for both materials, and by only changing the corresponding material constants. Therefore, no difference in the predicted results is expected for AA5182-O, when applying a rate-independent hardening model.

In the simulations of EHDF using different specimen geometries, due to the prevalence of plane stress conditions in the sheet material, two VUMATs were considered to investigate the effect of anisotropy in EHFF. The first one is the combination of the von-Mises (isotropic) yield function and the KHL model. The second one is the combination of the Yld2000-2d (anisotropic) yield function and the KHL model. The Yld2000-2d anisotropy coefficients were updated for DP600 and AA5182-O based on the equations presented in Table 3.23 and Table 3.25, respectively.

In the simulation of EHDF, the stress state shifts from plane stress to a general (three-dimensional) stress state due to the generation of through-thickness compressive and shear stresses when the sheet impacts the die. Two general VUMATs were developed to consider the anisotropy effect in EHDF. The first VUMAT combines the von Mises yield function and the KHL hardening model. The second one combines Yld2004-18p and the KHL model. As mentioned in Section 3.1.6.1, since pertinent experimental anisotropy data were not available, an isotropic behaviour was assumed through the sheet thickness. Therefore, Yld2004-18p is analogous to Yld2000-2d but offers the added benefit that it is able to account for the through-thickness stresses in solid elements. Similar to Yld2000-2d, the anisotropy coefficients of Yld2004-18p for DP600 were also updated. Finally, due to the unavailability of experimental data above 1000 s^{-1} , it was assumed in the

VUMATs that the anisotropy coefficients remain constant and equal to the values obtained at 1000 s^{-1} .

6.3.2.3 Element Type and mesh convergence

In order to verify the reliability of the FE model, an investigation was carried out to evaluate the effect of numerical parameters such as element type, mesh size and the integration scheme. The use of an isotropic yield function led to a significant decrease in run time which in turn allowed a more detailed mesh convergence study to be conducted. Therefore, the entire mesh convergence study was completed using only the isotropic constitutive model. The Lagrangian and Eulerian meshes were refined to various degrees so as to include coarse, fine and very fine mesh sizes. Major/minor strain and thickness distributions were used as the metrics to check the mesh convergence. Based on the author's investigations it was found that the following conditions yielded the best results.

- In EHFF, the sheet was modelled with three-dimensional quadrilateral (4-node, first-order) Lagrangian shell elements (denoted as S4R) in reduced integration. An average mesh size of 1.5 mm for all geometries represented an appropriate discretization of the model. The number of integration points through the thickness was set to 7 to ensure consistent and accurate deformation.
- In EHDF, the sheet was modelled with three-dimensional hexahedral (8-node, first-order) Lagrangian solid elements (denoted as C3D8R) in reduced integration, which were required for the EHDF calculations to resolve the through-thickness compressive and shear stresses that can be generated due to the dynamic sheet/die interaction. The hourglass energy of the system and the convergence study showed that at least six elements through the thickness were required to accurately capture the stress gradient through the thickness of the sheet. An average in-plane mesh size of 0.75 mm was selected. In view of the small thickness dimension compared to the diameter of the sheet a very small in-plane element size was required, and correspondingly a large number of elements, in order to maintain a reasonable element aspect ratio. Therefore, this parametric

study for EHDF simulations was very time consuming, even when using an isotropic yield function.

- The die (open-window and conical) and chamber were modelled with discrete rigid shell elements (denoted as R3D4). The element size for the rigid parts was selected to be on the same order as the element size of the deformable parts that contact with the rigid parts during the sheet deformation.
- The Eulerian part (including water, spherical volume and void) was discretized with Eulerian elements (denoted as EC3D8R) with reduced integration and hourglass control. The average element size for the water and void sections was 2 mm. The mesh size was reduced to 0.5 mm for the spherical volume, which represents the plasma channel medium. It should be emphasized that the element size of the spherical volume determines the stable increment time of the model, and consequently affects the computation time. Therefore, a very careful consideration was made to select an appropriate element size for the spherical region, by optimizing between the accuracy of the results and computation time.
- A transverse shear stiffness was assigned to the shell element section for DP600 and AA5182-O, by taking into account the formulation presented in Section 5.3.

6.3.2.4 Boundary conditions

The full geometry (i.e. no symmetry conditions) was modeled in both EHFF and EHDF simulations in order to fully consider the complex wave propagation and reflection within the chamber and consequently more accurately describe the fluid/solid interaction. For all specimen geometries, every degree of freedom (translational and rotational) was constrained along the outside perimeter of the sheet to represent the clamping force of the hydraulic press that prevents any material from drawing into the die cavity. The die and chamber were assigned an encastre boundary condition which prevents any translational or rotational movement.

6.3.2.5 Contact algorithm

A general Contact/Explicit was used to define the contact between Lagrangian bodies and Eulerian materials. The Eulerian-Lagrangian contact formulation is based on an enhanced immersed boundary method, in which the contact constraints are enforced using a penalty method where the default penalty stiffness parameter is automatically maximized subject to stability limits. Based on the general contact property, tensile stresses are not transmitted across an Eulerian-Lagrangian contact interface. Therefore, the interface friction coefficient is zero, which signifies that the friction has almost no effect on the predicted strain distribution in EHFF. In contrast, the friction effect can be significant in EHDF simulation, due to contact of the sheet against the conical die. The classical Coulomb friction law in a surface-to-surface contact model utilizing a penalty-based algorithm was used to account for the interaction between the sheet and the die. Following the work of Golovashchenko et al., (2013), static and dynamic friction coefficients of 0.2 and 0.15 were selected for this EHF process.

6.4 Results and Discussion

6.4.1 Single element results

As mentioned before, the effective plastic strain was predicted for two forming conditions (balance biaxial tension and plane strain tension) using a single element. This element was deformed up to a true plastic strain of 1.0 in the RD for the plane strain condition and up to 1.0 in both the RD and TD for the biaxial condition. It should be mentioned that in all simulations in this section, results are presented for both the rolling direction (RD) and the transverse direction (TD). The reason for presenting both sets of results is that the predicted results will be different in plane strain tension depending whether the tension direction is parallel with the RD or the TD. Therefore, it is more comprehensive to present the predicted results in both directions. In all the following graphs in this Section, the term “RD” indicates that the gauge section of the specimen was oriented parallel with the rolling direction in the FE model, whereas “TD” indicates that the gauge section was oriented parallel with the transverse direction. Also, it should be emphasized that the relative error was calculated relative to the results predicted by Yld2000-2d. As shown in Section 4.1.2, the Yld2000-2d is able to describe material anisotropy more accurately than the von Mises or Hill48 yield functions. Therefore, the results using Yld2000-2d were considered the reference from which to measure the relative error.

6.4.1.1 DP600 von Mises error

Figures 6-7a and 6-7b show the comparison between the effective plastic strain predicted for DP600 using Yld2000-2d and von Mises in the equibiaxial and plane strain conditions, respectively. Figure 6-7c shows that the maximum error (4% – 7%) occurs in the biaxial condition for all strain rates. Results show that the discrepancy between the Yld2000-2d and von Mises decreases as the strain rate increases, which is expected since the biaxial flow stress ratio (σ_b/σ_0) decreases with increasing strain rate, as shown in Figure 4-33. Also, the error for the plane strain condition shows a significant dependence on material orientation since it is positive (+3%) in the RD and negative (-3%) in the TD for almost all strain rates.

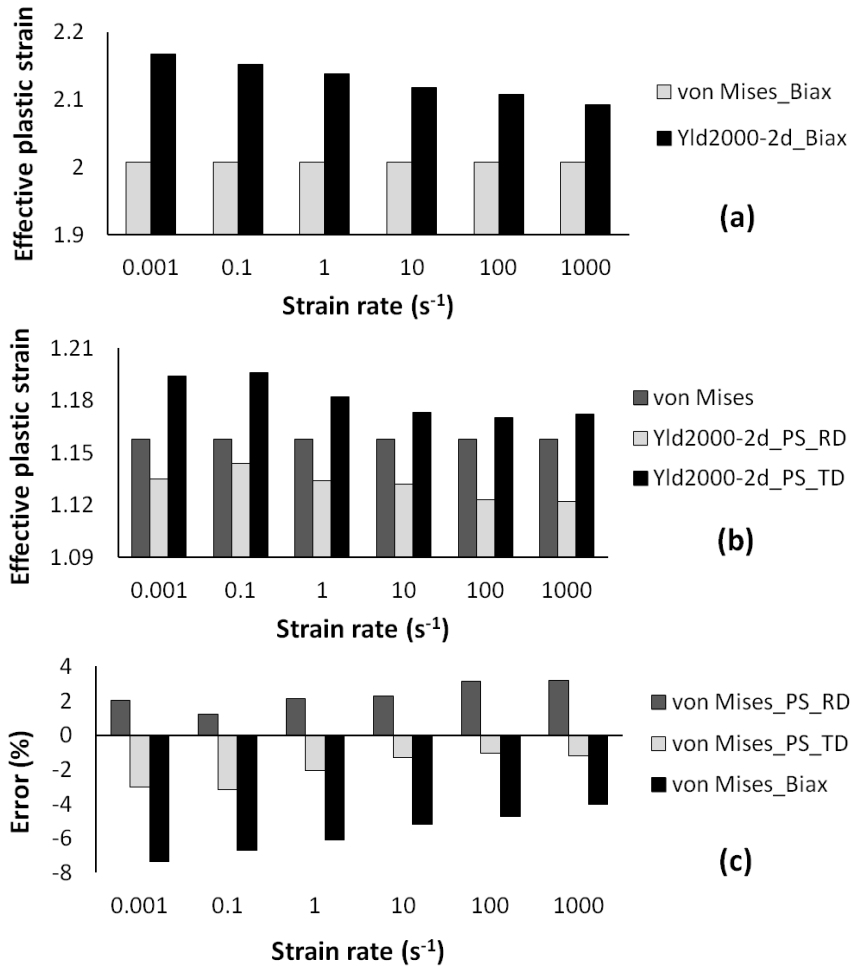


Figure 6-7. Predicted effective plastic strain for DP600 using Yld2000-2d and von Mises yield functions; a) biaxial, b) plane strain, and c) relative error

6.4.1.2 DP600 Hill48 error

Figures 6-8a and 6-8b show the comparison between the effective plastic strain predicted for DP600 using Yld2000-2d and Hill48 in the biaxial and plane strain conditions, respectively. Figure 6-8c shows the relative error calculated based on the corresponding results at each strain rate and for each condition. Biaxial tension results show that as the strain rate increases, the effective plastic strains predicted by Hill48 approach the value predicted with Yld2000-2d (the relative error decreases to less than 2%). In contrast, the error increases with the strain rate (3% – 5%) for the plane strain condition.

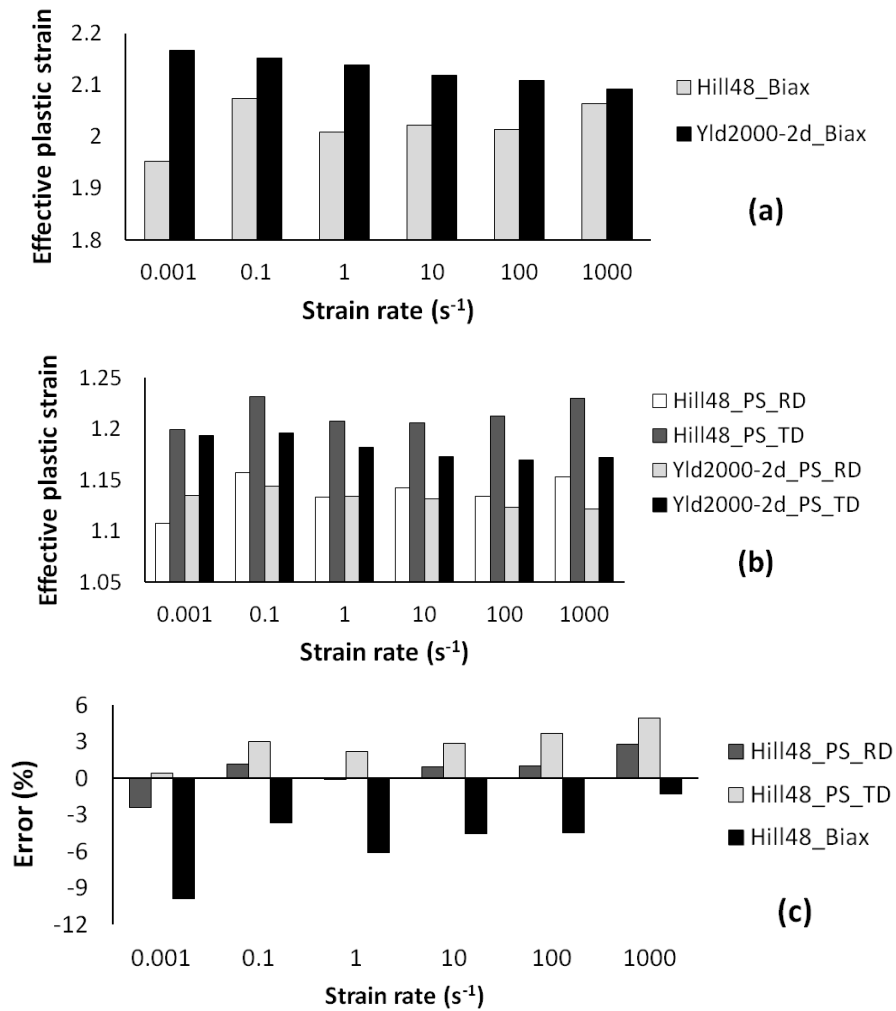


Figure 6-8. Predicted effective plastic strain for DP600 using Yld2000-2d and Hill48 yield functions; a) biaxial, b) plane strain and c) relative error

6.4.1.3 TRIP780 von Mises error

Figures 6-9a and 6-9b show the comparison between the effective plastic strain predicted for TRIP780 using Yld2000-2d and von Mises in biaxial and plane strain conditions, respectively. Figure 6-9c shows that the maximum relative error (3% – 7%) occurs in both balance biaxial tension and plane strain (RD) conditions for almost all strain rates. Similar to DP600, the error in the balanced biaxial condition decreases with increasing strain rate which is expected considering Figure 4-34. Also, plane strain results show that the relative error slightly increases when the strain rate increases.

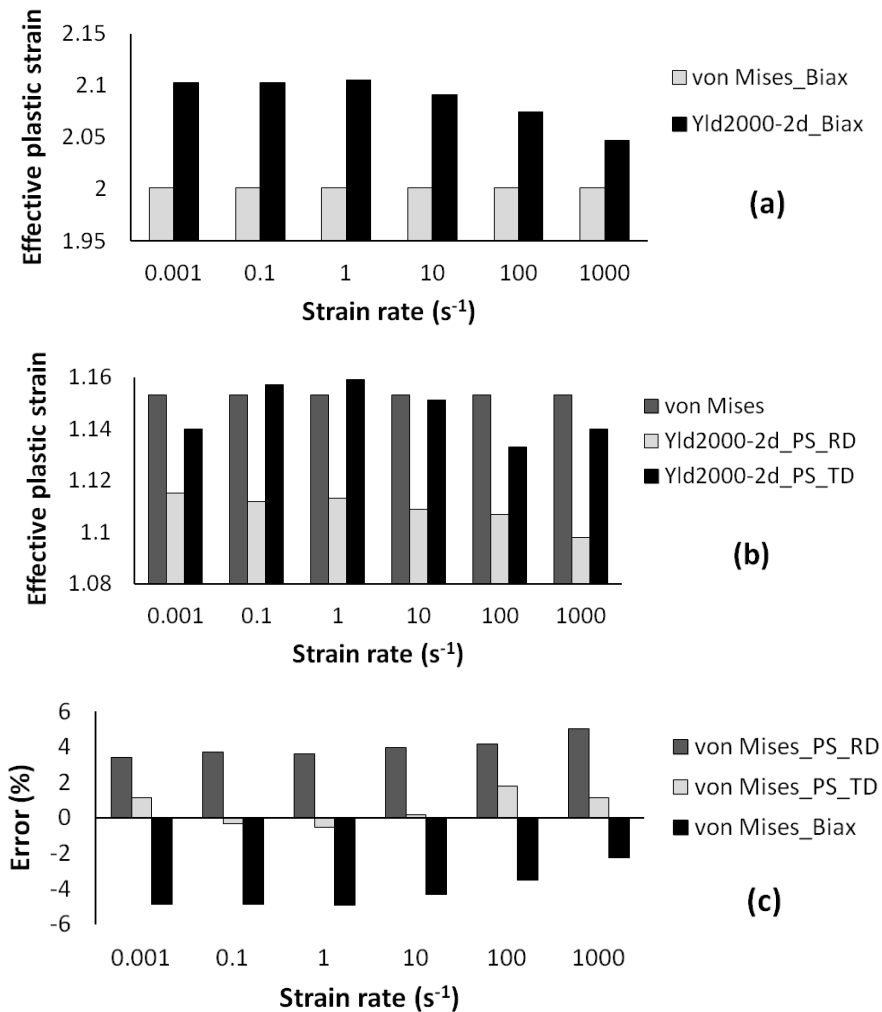


Figure 6-9 Predicted effective plastic strain for TRIP780 using Yld2000-2d and von Mises yield functions; a) biaxial, b) plane strain and c) relative error

6.4.1.4 TRIP780 Hill48 error

Figures 6-10a and 6-10b show the comparison between the effective plastic strain predicted for TRIP780 using Yld2000-2d and Hill48 in the biaxial and plane strain conditions, respectively. Figure 6-10c shows a significant error (8% – 15%) in the biaxial condition for all strain rates using Hill48. The error decreases with increasing strain rate but still remains considerable. Results in plane strain show a much lower error (3% – 4%) for almost all strain rates. Moreover, the relative error decreases with strain rate and the predicted effective plastic strain is practically the same at 1000 s^{-1} whether Hill48 or Yld2000-2d is used in the simulation.

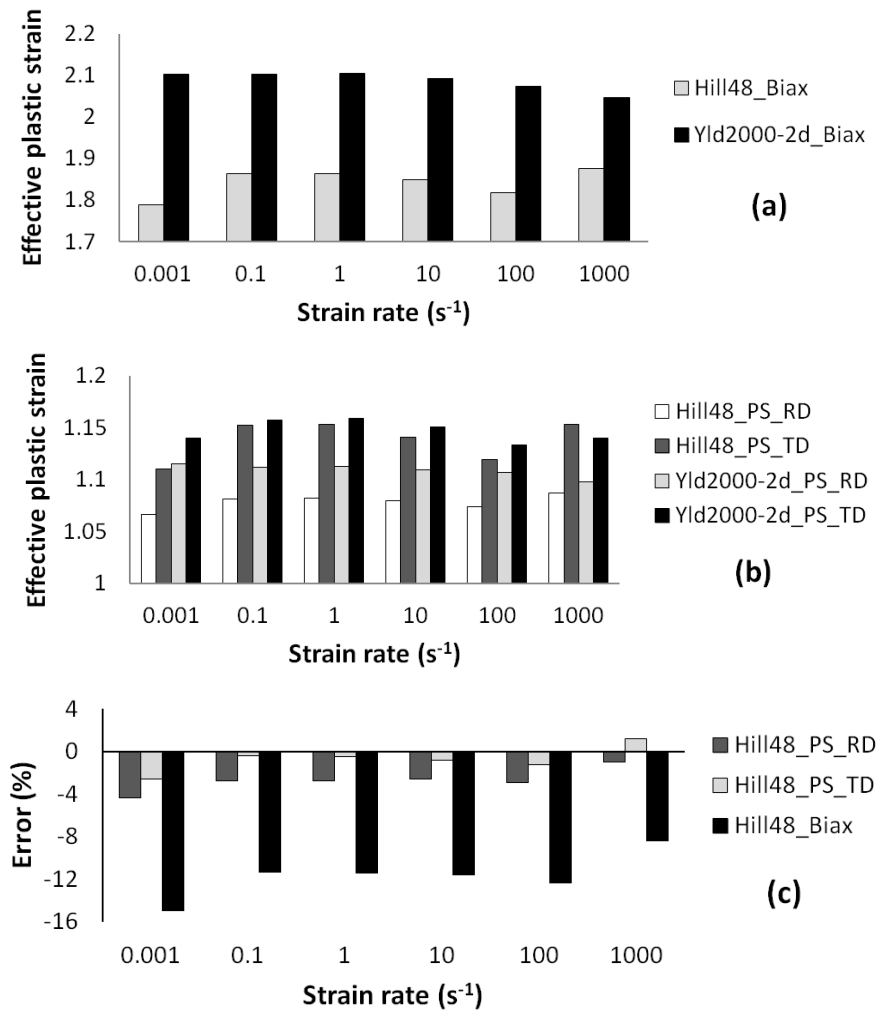


Figure 6-10. Predicted effective plastic strain for TRIP780 using Yld2000-2d and Hill48 yield functions; a) biaxial, b) plane strain and c) relative error

6.4.1.5 AA5182-O von Mises error

Figures 6-11a and 6-11b show the comparison between the effective plastic strain predicted for AA5182-O using Yld2000-2d and von Mises in biaxial and plane strain conditions, respectively. Figure 6-11c shows a maximum relative error of 7% – 10% in the plane strain condition for all strain rates, which is expected due to higher exponent in Yld2000-2d ($a = 8$) for aluminum alloy (Figure 4-35), compared to $a = 2$ in the von Mises yield function. In contrast with the plane strain condition, results show only a slight error in the balance biaxial condition due to the very small difference in the uniaxial (RD) and biaxial flow stresses of AA5182-O. The relative errors show that the effective plastic strain is almost independent of the strain rate. This is expected due to the near zero strain rate sensitivity of AA5182-O.

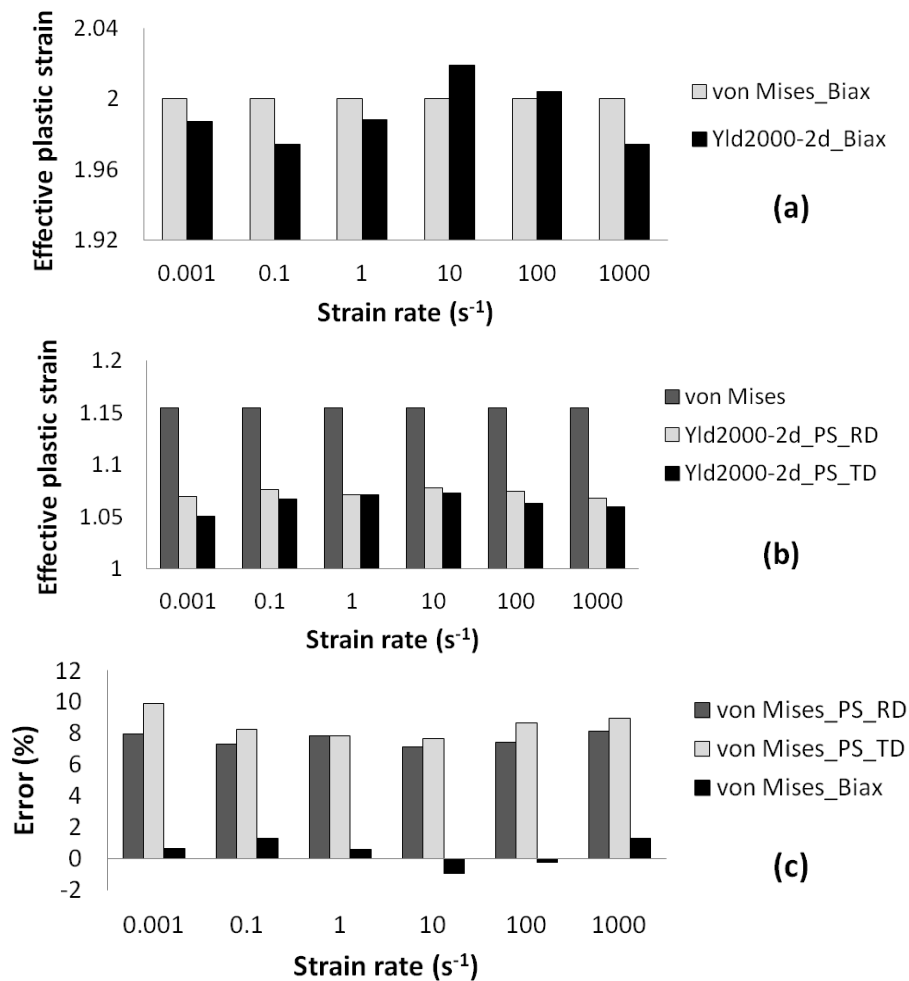


Figure 6-11. Predicted effective plastic strain for AA5182-O using Yld2000-2d and von Mises yield functions; a) biaxial, b) plane strain and c) relative error

6.4.1.6 AA5182-O Hill48 error

Figures 6-12a and 6-12b show the comparison between the effective plastic strain predicted for AA5182-O using Yld2000-2d and Hill48 in biaxial and plane strain conditions, respectively. The dependence of the Hill48 yield function on the r-values causes significant variations in the relative error as a function of strain rate for both biaxial and plane strain conditions. Hill48 introduces considerable errors in both biaxial tension (2% – 9%) and in plane strain (2% – 5%) for this AA5182-O sheet. However, it is well known that Hill48 is unable to accurately predict the behaviour of aluminum alloys.

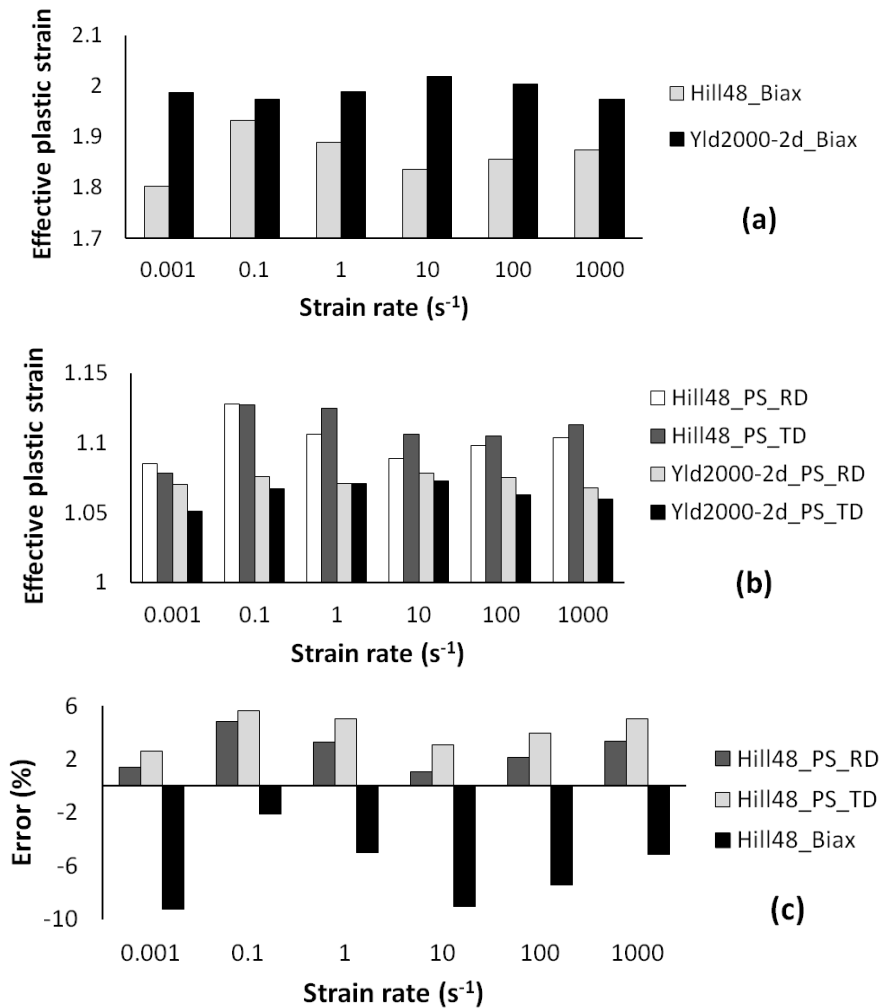


Figure 6-12. Predicted effective plastic strain for AA5182-O using Yld2000-2d and Hill48 yield functions; a) biaxial, b) plane strain and c) relative error

6.4.2 EHFF Results and discussion

The EHFF simulation results presented here provide the first quantitative assessment of the effect of material anisotropy on the strain distribution in pulsed forming. The results outlined in this section show how important material anisotropy can be, particularly at moderate and high strain rate regimes. In order to provide a more comprehensive analysis, comparisons are made for two materials (DP600 and AA5182-O) and four different specimen geometries (uniaxial, intermediate draw, plane strain and balance biaxial tension, as shown in Figures 6-2 and 6-37).

The measured major and minor strains, thickness and height of the deformed specimens are compared with the predicted results using isotropic (von Mises) and anisotropic (Yld2000-2d) yield functions. As mentioned in Section 6.2.2, EHFF specimens were prepared in such a way that the major strain in the gauge area was always parallel with the RD of the sheet. Therefore, the major strain measurements are parallel with the RD and minor strain measurements are parallel with the TD. The measured and predicted data are presented along a path at the centerline of the specimens (Figure 6.2) for all specimen geometries.

Also, for a better understanding of the deformation history of the sheet during EHFF process, an element at the centre of the specimen (where the peak strain rate occurs) was selected to investigate the effect of anisotropy on the evolution of effective plastic strain and effective strain rate. It should be noted that the EHFF simulations predict the total duration of the forming process for all specimen geometries and for both sheet materials to be between 250 to 300 μs , which is in good agreement with the results reported by Gillard et al. (2013) and Golovashchenko et al. (2013). Detailed comparisons between the measured and predicted data for the two materials and four geometries are discussed in the following.

6.4.2.1 DP600 uniaxial tension

Figure 6-13a shows that the major strain predicted with both Yld2000-2d and von Mises are in a good agreement with the measurements. The major strain distribution and in particular the peak major strain (0.36) in the gauge section are expected to be similar

for Yld2000-2d and von Mises because the simulations predicted the same maximum height (Figure 6-13d) when the same energy magnitude was applied. However, Figure 6-13d shows that the predicted profile of the DP600 uniaxial specimen is slightly different than what is observed experimentally. The main reason for this discrepancy may be the different load distribution on the sheet during the forming, which is very complex due to the interaction of the narrow gauge section of the uniaxial specimen with the water. As mentioned before, the energy magnitude of the pulse was adjusted in such a way as to achieve the same measured maximum height.

Figure 6-13b shows that the minor strains predicted using Yld2000-2d are within the range of experimental accuracy, but von Mises over-predicts the minor strains, in particular in the gauge section. The improvement in the prediction of minor strains with Yld2000-2d compared to those predicted with von Mises, also signifies that Yld2000-2d is able to more accurately predict the thickness distribution in the gauge section of the uniaxial specimen as can be seen in Figure 6-13c. Figure 6-14 shows the improved accuracy of Yld2000-2d more clearly in terms of the strain distribution in the uniaxial specimen. Results show that von Mises leads to an overestimation of the minor strain which causes the strain path to deviate from the actual strain measurements. However, when the anisotropy is taken into account, a more accurate minor strain and consequently a more accurate strain path is predicted for DP600 uniaxial specimen. Figure 6-15 shows the evolution of the predicted effective plastic strain and of the effective strain rate for an element at the centre of the gauge section (centre of the specimen). Results show approximately the same maximum effective plastic strain value (0.34 – 0.36) using Yld2000-2d and von Mises. Also, the predicted effective strain rate histories show almost the same trend with a similar peak value (2700 s^{-1}) for isotropic and anisotropic yield functions. The evolution of the plastic strain shows that almost the entire plastic deformation occurs substantially above the quasi-static strain rate regime during the EHFF process. This emphasizes the importance of considering the actual material anisotropy data at different levels of strain rate and of updating the anisotropy coefficients in this rate-dependent forming process. It should be mentioned that the results for the other EHFF specimen geometries also show that the majority of the plastic deformation occurs at intermediate and high strain rate regimes.

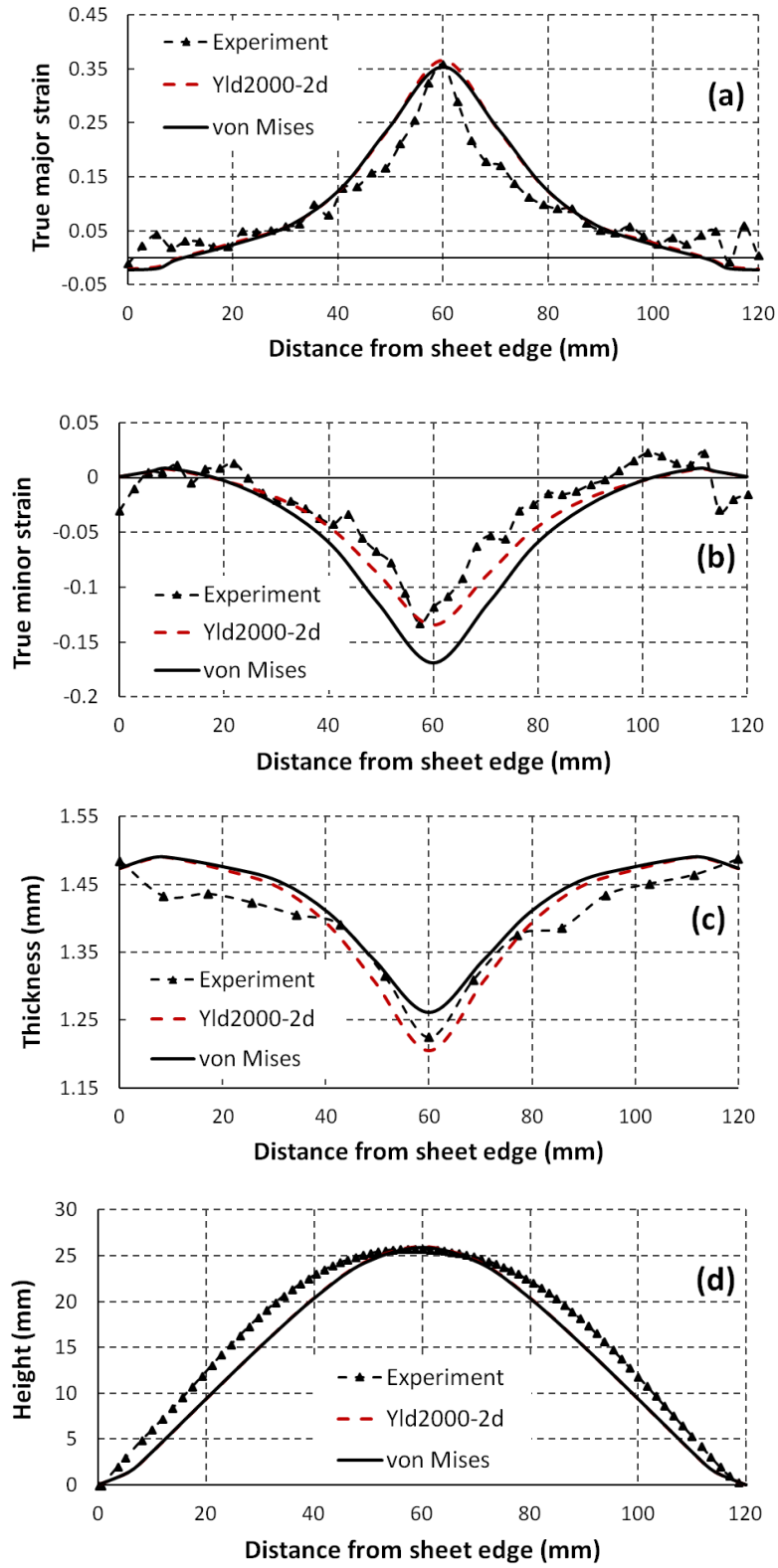


Figure 6-13. Measured and predicted data for DP600 uniaxial EHFF specimen; a) major strain, b) minor strain, c) thickness and d) height

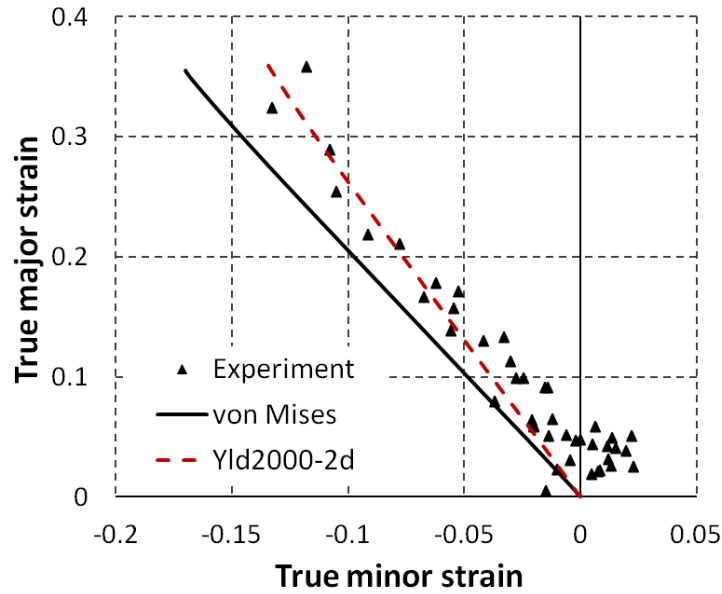


Figure 6-14 Measured strain distribution and predicted strain path for an element at the centre of the gauge section for DP600 uniaxial EHFF specimen

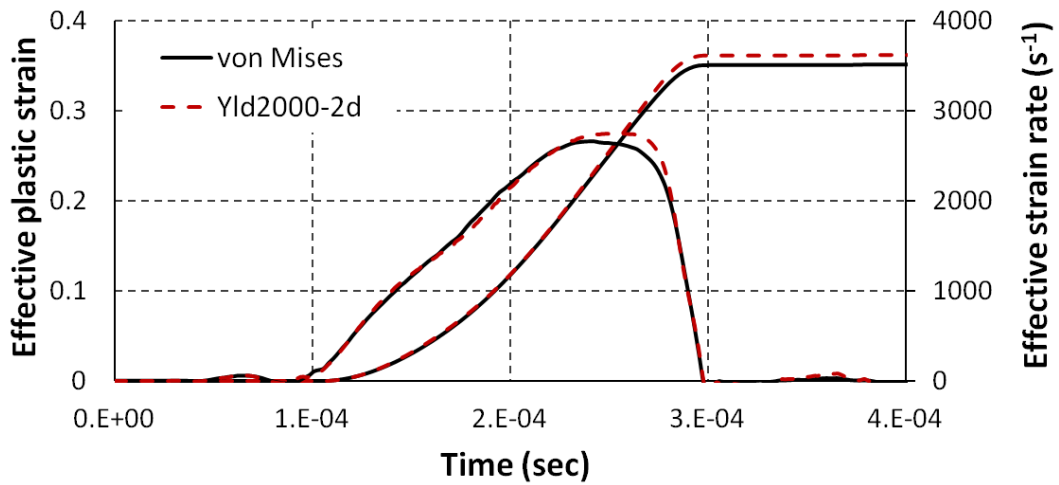


Figure 6-15. Effective plastic strain and effective strain rate histories for an element at the centre of the DP600 uniaxial EHFF specimen

6.4.2.2 AA5182-O uniaxial tension

Figure 6-16a shows that the major strain predicted with Yld2000-2d and von Mises are in good agreement with the measurements (0.31). Once again, the profile of the formed-specimens predicted with both von Mises and Yld2000-2d are somewhat different than the experimental measurements (Figure 6-16d). Figure 6-16b shows that the minor strains predicted using Yld2000-2d are in good agreement with the measurements. However, similar to the DP600 uniaxial specimen, the von Mises yield function leads to an over-prediction of the minor strains in the gauge section. Figure 6-16c shows an improvement in the predicted thickness distribution using Yld2000-2d. Compared to the results using von Mises, trends show that Yld2000-2d is able to more accurately reproduce the experimental measurements. Figure 6-17 shows that the strain path predicted using Yld2000-2d coincides well with the strain measurements on the as-formed specimen but the results predicted using von Mises show a substantial deviation from the measurements due to the over-prediction of minor strains.

Figure 6-18 shows that the effective plastic strain predicted using Yld2000-2d (0.32 – 0.33) is greater than that predicted using von Mises (0.31) for an element at the centre of the gauge section, when the same amount of energy is applied in the simulations. Also, the effective strain rate histories predicted with both criteria are almost the same, and the peak strain rate is 3000 s^{-1} .

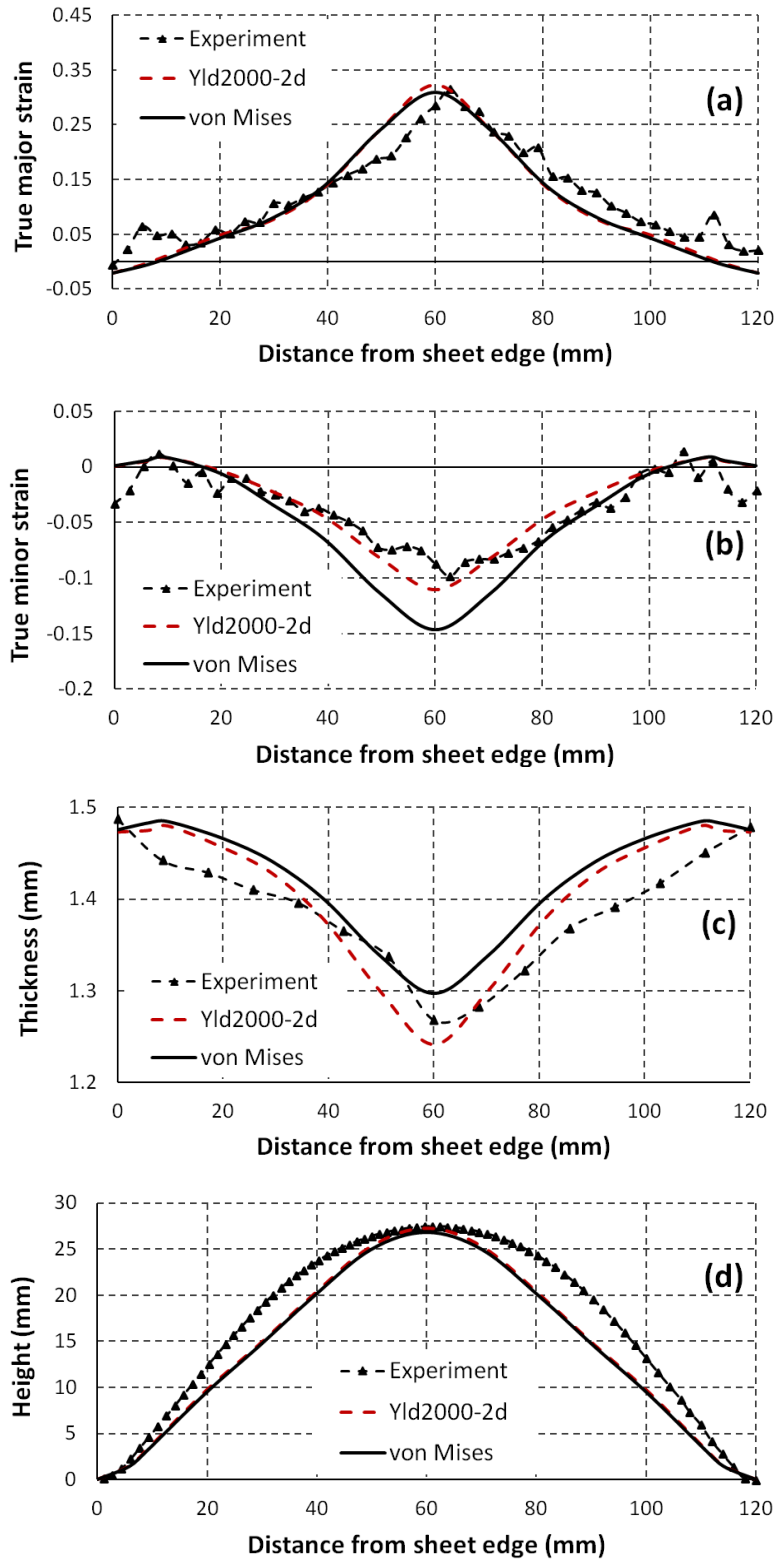


Figure 6-16. Measured and predicted data for AA5182-O uniaxial EHFF specimen; a) major strain, b) minor strain, c) thickness and d) height

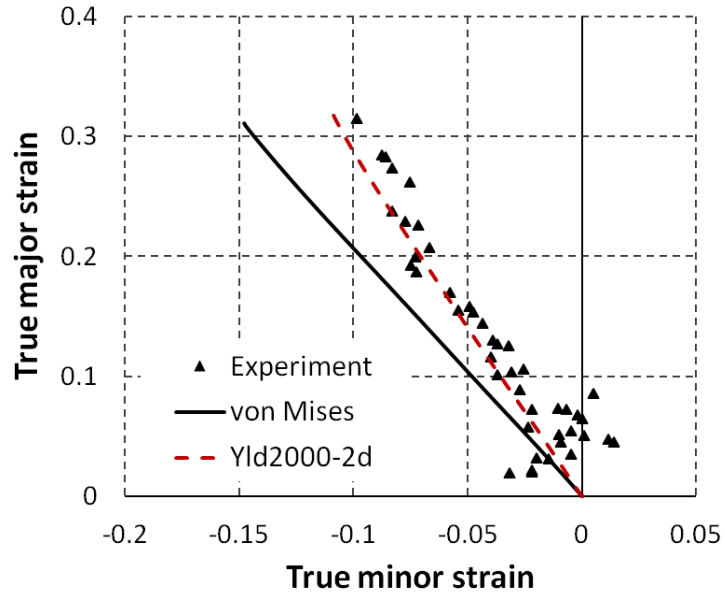


Figure 6-17. Measured strain distribution and predicted strain path for an element at the centre of the gauge section for AA5182-O uniaxial EHF specimen

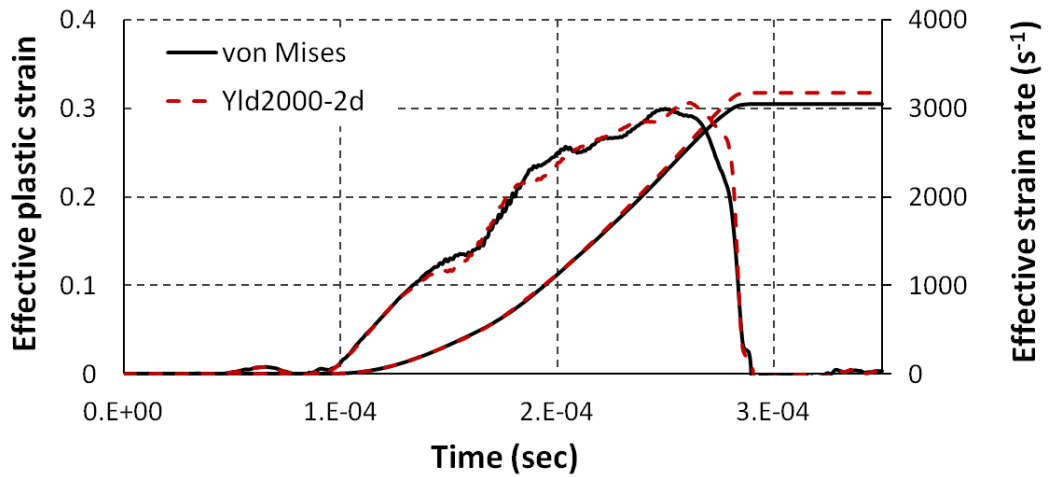


Figure 6-18. Effective plastic strain and effective strain rate histories for an element at the centre of the AA5182-O uniaxial EHF specimen

6.4.2.3 DP600 intermediate draw

Figure 6-19a shows that the major strain distributions predicted with Yld2000-2d and von Mises follow the same trend as the measured strains. Results show that Yld2000-2d (0.27) predicts a slightly greater major strain in the centre of the gauge section than von Mises. Similar to the uniaxial case, von Mises over-predicts the minor strain in the gauge section of the DP600 intermediate draw specimen, whereas results obtained with Yld2000-2d show very good agreement with the measurements both in terms of the trend and the magnitude along the entire path, as shown in Figure 6-19b. Figure 6-19c shows the ability of Yld2000-2d to accurately predict the thickness distribution and the minimum thickness (1.215 mm) in the gauge section, whereas von Mises underestimates the minimum thickness (1.275 mm), which is consistent with the over-prediction of the minor strain.

Compared to the case of uniaxial tension which showed a discrepancy between the predicted and measured height distributions, the predicted and measured profiles are very similar along the entire centreline of the DP600 intermediate draw specimen, as can be seen in Figure 6-19d. Figure 6-20 shows substantial deviation in the strain path predicted with von Mises due to the over-prediction of the minor strains in the gauge section of the intermediate draw specimen. But good agreement can be seen between the measurements (final achieved strains across the specimen) and the strain path predicted with Yld2000-2d at the centre of the specimen, which is due to the improved prediction of the minor strain with Yld2000-2d.

Figure 6-21 shows that, similar to the uniaxial case, almost the entire plastic deformation occurs at intermediate and high strain rate regimes. Results show that for almost the same maximum height of the deformed specimen, Yld2000-2d predicts a slightly greater final effective plastic strain (0.275) than the von Mises (0.255) for an element at the centre of the gauge section. And maximum effective strain rate predicted with Yld2000-2d is greater (4750 s^{-1}) than the value predicted with von Mises (3850 s^{-1}).

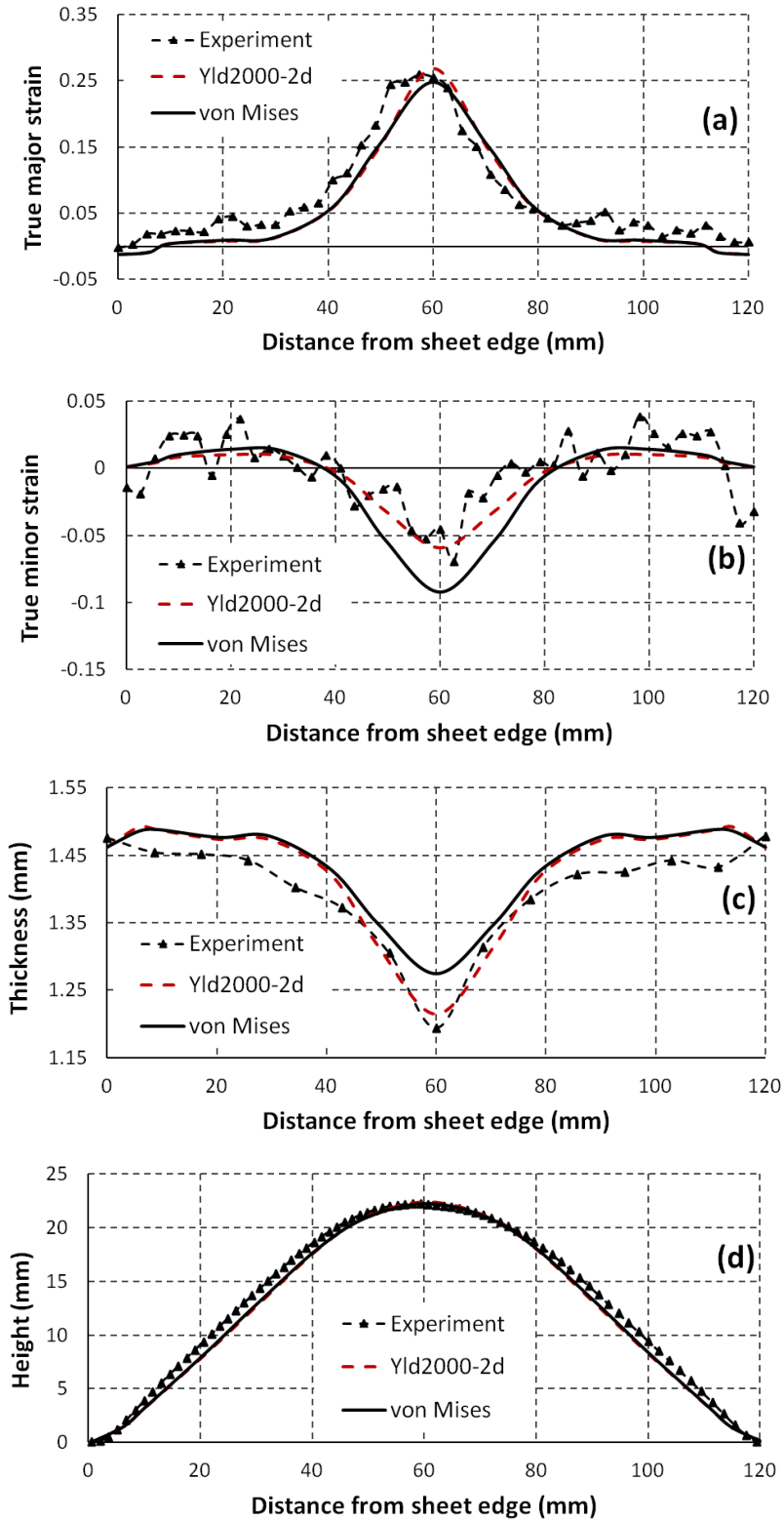


Figure 6-19. Measured and predicted data for DP600 intermediate draw EHFF specimen; a) major strain, b) minor strain, c) thickness and d) height

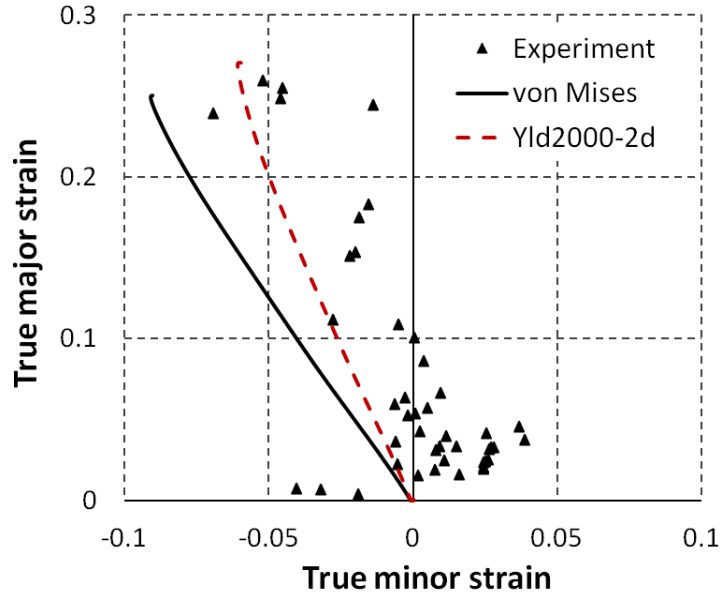


Figure 6-20. Measured strain distribution and predicted strain path for an element at the centre of the gauge section for DP600 intermediate draw EHFF specimen

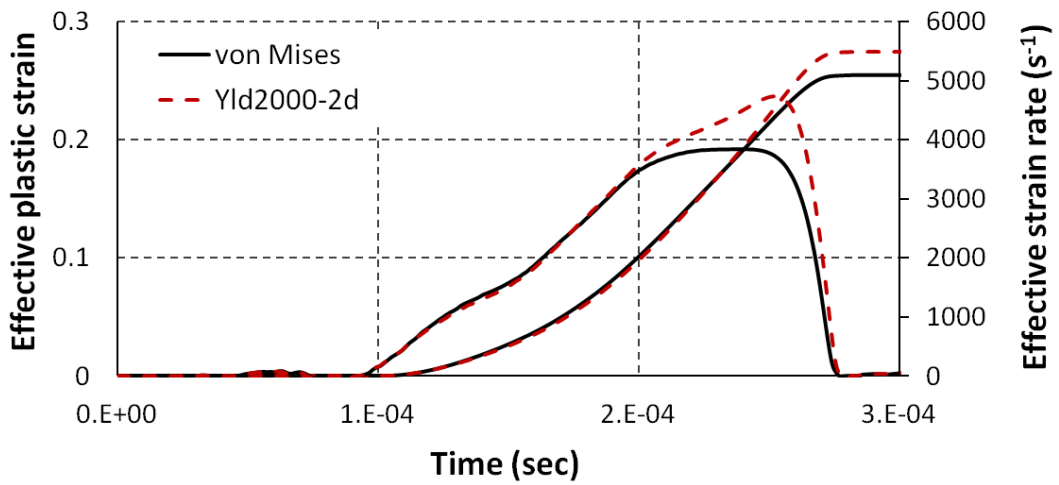


Figure 6-21. Effective plastic strain and effective strain rate histories for an element at the centre of the DP600 intermediate draw EHFF specimen

6.4.2.4 AA5182-O intermediate draw

Figure 6-22a shows that Yld2000-2d predicts a slightly greater major strain in the gauge section (0.28) than von Mises (0.265) for the AA5182-O intermediate draw specimen. Figure 6-22b shows a significant difference between the results predicted with Yld2000-2d and von Mises. Compared to the DP600 intermediate draw specimen this discrepancy is more significant due to greater value of Yld2000-2d exponent chosen for aluminum alloys ($a = 8$) compared to that for steels ($a = 6$). Von Mises results show a substantial deviation of the predicted minor strain in the gauge section compared to the measurements, but Yld2000-2d can be seen to predict the minor strains in the intermediate draw specimen much more accurately. Figure 6-22c shows that von Mises underestimates the thickness distribution, whereas thickness distributions predicted with Yld2000-2d show very good agreement with the measurements, especially in the gauge section of the AA5182-O intermediate draw.

In contrast with the DP600 intermediate draw, the height distribution predicted by both Yld2000-2d and von Mises deviates somewhat from the measurements, as shown in Figure 6-22d. Also, this figure shows that, compared to the Yld2000-2d, the von Mises underestimates the maximum height under the same applied energy magnitude. Figure 6-23 shows that when von Mises is used the predicted strain path is very different from the strain distribution that is actually measured. In contrast, the strain path predicted by Yld2000-2d is in a good agreement with the principal strains measured across the AA5182-O intermediate draw specimen. This good correlation is particularly highlighted in the gauge section which undergoes greater minor and major strains, which is the region of interest in the specimen. Figure 6-24 shows approximately the same maximum effective strain rate (3000 s^{-1}) is predicted by both Yld2000-2d and von Mises for an element in the centre of the gauge section.

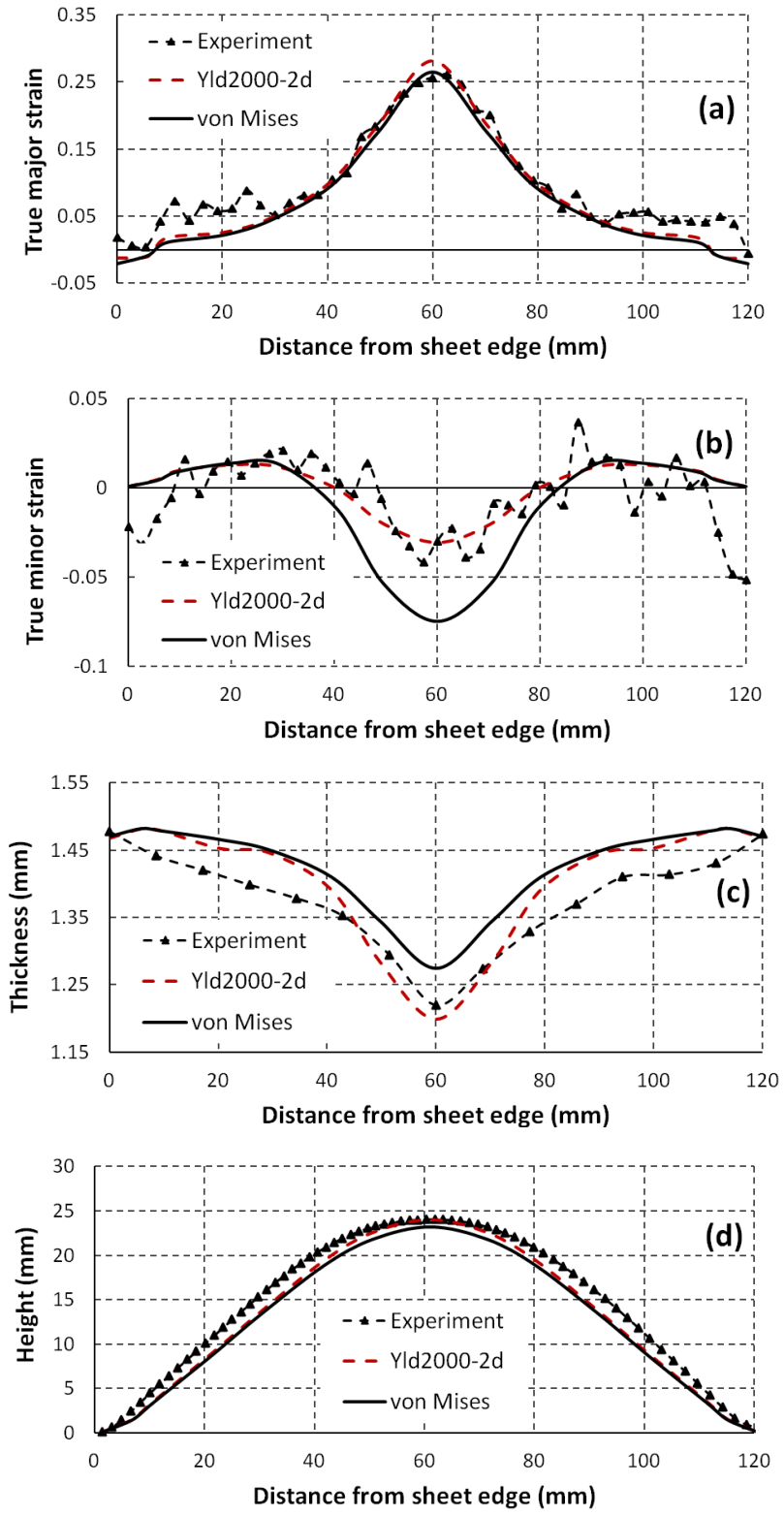


Figure 6-22. Measured and predicted data for AA5182-O intermediate draw EHFF specimen; a) major strain, b) minor strain, c) thickness and d) height

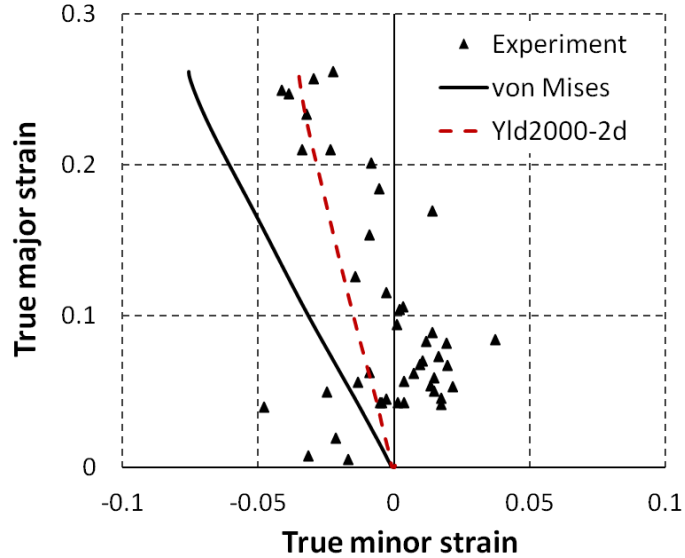


Figure 6-23. Measured strain distribution and predicted strain path for an element at the centre of the gauge section for AA5182-O intermediate draw EHFF specimen

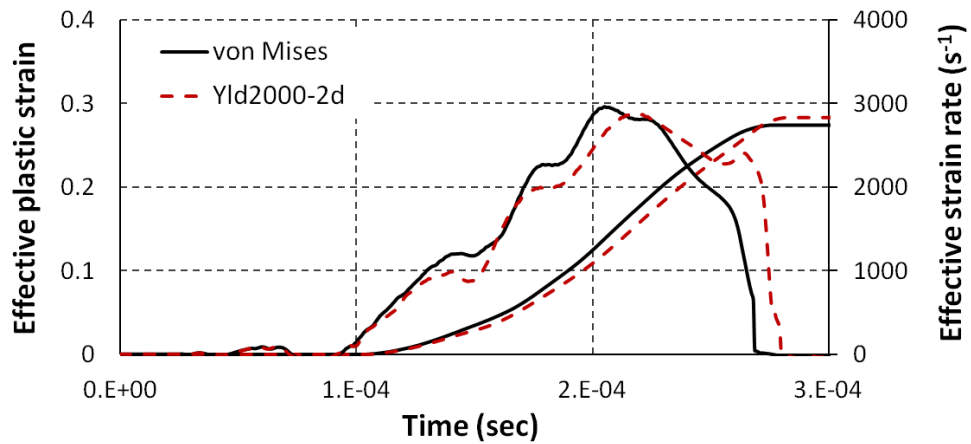


Figure 6-24. Effective plastic strain and effective strain rate histories for an element at the centre of the AA5182-O intermediate draw EHFF specimen

6.4.2.5 DP600 plane strain

Figure 6-25a shows that the predicted major strains are greater than the measured major strain (0.2) in the gauge of the DP600 plane strain EHFF specimen. This discrepancy is particularly significant for results predicted with Yld2000-2d (0.275). The main reason for this could be that the biaxial r -values (at various strain rates) were calculated based on Yld96 rather than measured experimentally. Also, another reason could be that the biaxial work hardening was assumed to remain constant for all strain

rates; however, it would be certainly be preferable to obtain the experimental biaxial flow stress at different strain rates, and in particular at high strain rates (above 1000 s^{-1}) to be able to improve the predictions. Figure 6-25b shows that both Yld2000-2d and von Mises predict minor strains that are near zero, which is in good agreement with the measurements in the gauge section of the DP600 plane strain specimen. Results show that Yld2000-2d over-predicts the absolute minor strain in the gauge section, which is no doubt related to the over-prediction of the major strain. The deviation of the minor strain from the experiment would no doubt be improved if the experimental biaxial r-value and flow stress could be obtained at high strain rates. Figure 6-25c shows that Yld2000-2d predicts a greater absolute minimum thickness than von Mises. The predicted trend for both Yld2000-2d and von Mises follows the measured thickness distribution accurately along the entire path. But, the over-prediction of the thickness by Yld2000-2d is attributed to the prediction of greater major strains in the gauge section of the DP600 plane strain specimen.

Although a greater major strain was predicted by Yld2000-2d, both Yld2000-2d and von Mises show similar height distributions both in terms of trend and peak values, which are in very good agreement with the measurements, as can be seen in Figure 6-25d. Predicting greater major and minor strains in the gauge section of the DP600 plane strain specimen with Yld2000-2d compared to the measurement with exactly the same height distribution may signify that, the biaxial r-value has a more significant effect than the biaxial flow stress in the prediction of the deformation distribution and history. Figure 6-26 shows that the strain path predicted with Yld2000-2d slightly deviates from the measurements, which is due to the over-prediction of the absolute minor strains in the gauge area. As mentioned before, obtaining the biaxial experimental r-value at high strain rate would likely help to improve the strain path prediction. Figure 6-27 shows the same trends for the effective strain rate predicted by both Yld2000-2d and von-Mises. However, Yld2000-2d over-predicts both the effective plastic strain (0.3) and the maximum effective strain rate (4850 s^{-1}) in the centre of the gauge area compared to the effective plastic strain (0.27) and the peak effective strain rate (4050 s^{-1}) predicted with von Mises.

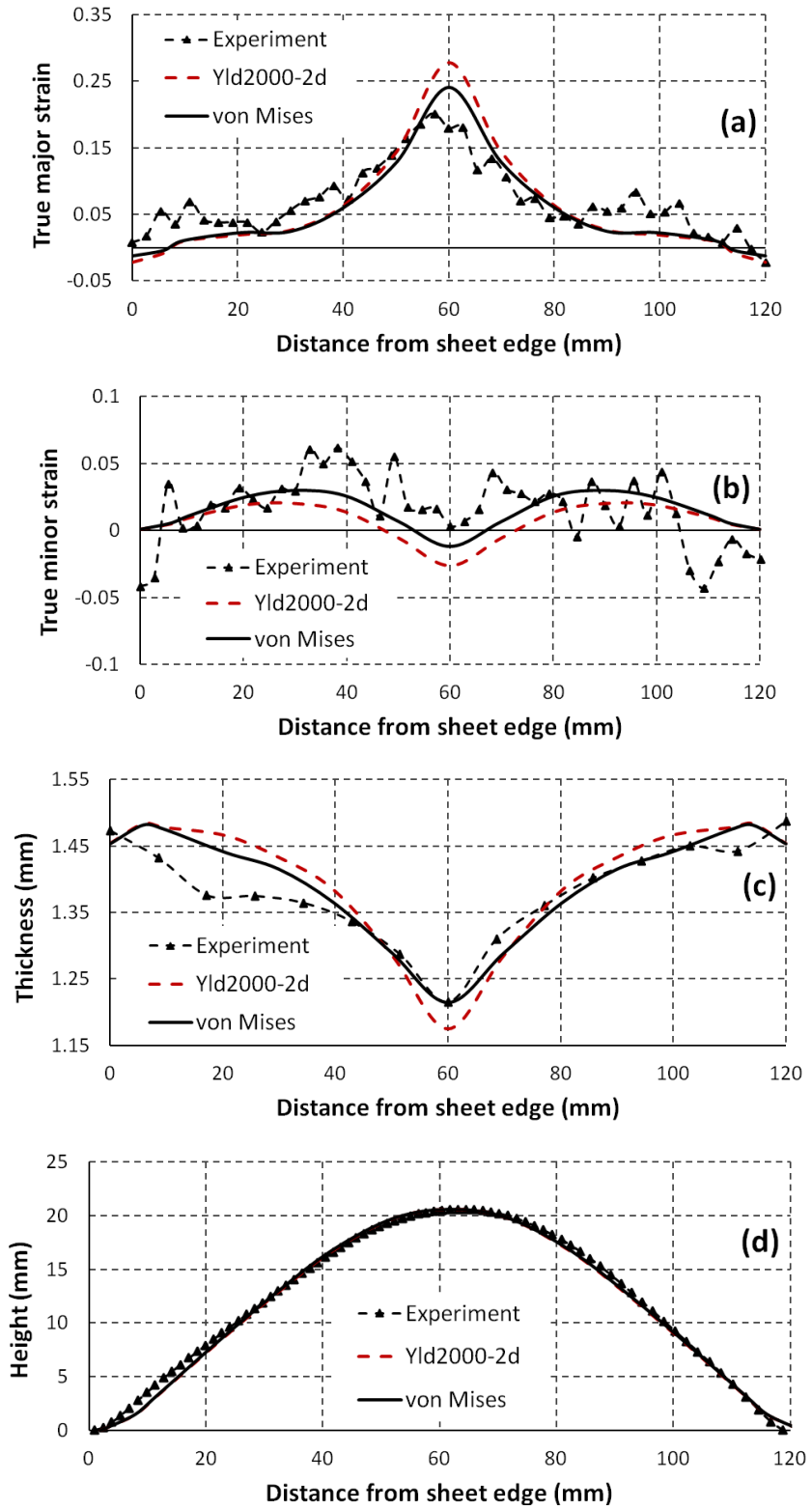


Figure 6-25. Measured and predicted data for DP600 plane strain EHFF specimen; a) major strain, b) minor strain, c) thickness and d) height

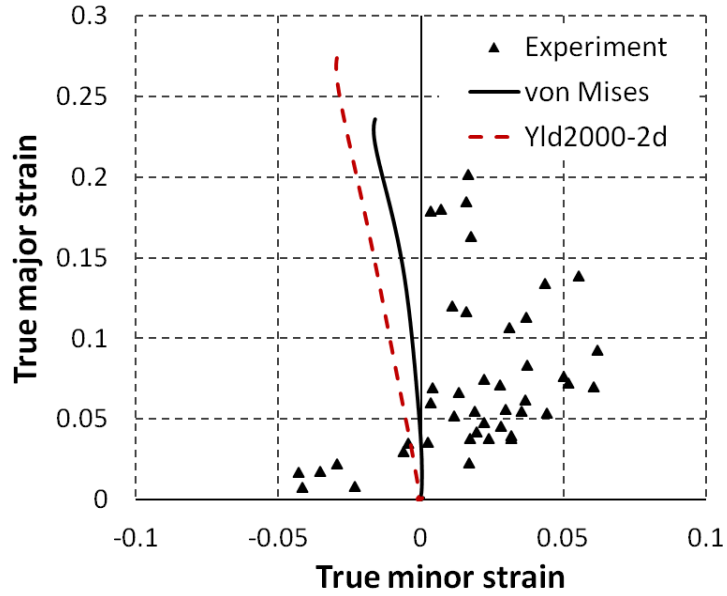


Figure 6-26. Measured strain distribution and predicted strain path for an element at the centre of the gauge section for DP600 plane strain EHF specimen

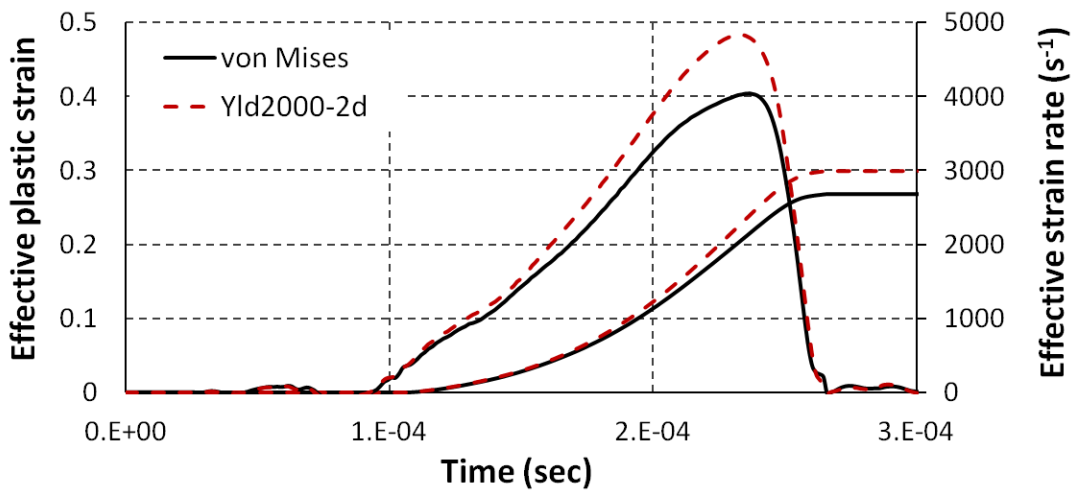


Figure 6-27. Effective plastic strain and effective strain rate histories for an element at the centre of the DP600 plane strain EHF specimen

6.4.2.6 AA5182-O plane strain

Figure 6-28a shows that both the general trend and the peak value of the major strain distribution in the AA5182-O plane strain specimen are well predicted with both Yld2000-2d and von Mises. It can be seen that a slightly greater peak major strain is predicted with Yld2000-2d compared to that predicted with von Mises. This could be due to the greater maximum height (21.8 mm) predicted with Yld2000-2d compared to von Mises (20.6 mm) with the same energy magnitude (Figure 6-28d).

Figure 6-28b shows that Yld2000-2d predicts an almost zero minor strain in the gauge area of the AA5182-O plane strain specimen, which is in very good agreement with the measured data. It should be noted that von Mises leads to a predicted minor strain distribution that is in better agreement with the measurements across the entire specimen. However, Figure 6-28c shows that the absolute minimum thickness predicted with Yld2000-2d in the centre of the gauge area is in better agreement with the measurements than that predicted with von Mises. Von Mises underestimates the absolute minimum thickness which is consistent with the prediction of a lower maximum height (Figure 6-28d) and a greater absolute minor strain value compared to those predicted with Yld2000-2d. Figure 6-28d shows that the height profile predicted with Yld2000-2d is in good agreement with the measurement, however the maximum height predicted with von Mises is lower than the measured height across the centre profile of the specimen. Figure 6-29 shows the experimentally measured strains in the AA5182-O plane strain specimen and the predicted strain paths at the centre of the gauge area: a comparison of the experimental strain data and the predicted strain paths shows the ability of Yld2000-2d to accurately describe the behaviour of AA5182-O sheet material when it is deformed in plane strain in EHFF. The strain path predicted by von Mises for an element at the centre of the gauge section shows a significant deviation from the maximum strains measured in the specimen.

Figure 6-30 shows that Yld2000-2d and von Mises predict approximately the same effective plastic strain. Also, Yld2000-2d predicts a slightly greater maximum effective strain rate (3500 s^{-1}) compared to von Mises (3250 s^{-1}).

Considering these simulation results, it appears that Yld2000-2d shows a better prediction of EHFF in the plane strain condition for AA5182-O than for DP600. There may be two reasons for this: first, an exponent of 8 is generally used for aluminum alloys compared to an exponent of 6 for steels in Yld2000-2d, which leads to a greater discrepancy between the plane strain results predicted with Yld2000-2d and those with von Mises in the case of AA5182-O than for DP600. This greater discrepancy can be seen by comparing the flow surfaces of DP600 and AA5182-O in Figure 4-33 and Figure 4-35, respectively. Another reason that the predictions for AA5182-O are in better agreement with the measurements in the plane strain condition is that, both the r-values and flow stresses of AA5182-O are almost strain rate insensitive, whereas they are rate-dependent in the DP600. It was not possible to obtain the biaxial flow stresses and r-values experimentally at different strain rates, and in particular for strain rates above 1000 s^{-1} , and the biaxial flow stresses were calculated for higher strain rates by assuming a similar work hardening behaviour for every level of strain rate). It is not surprising therefore, that the greater discrepancy was obtained for the DP600 sheet material.

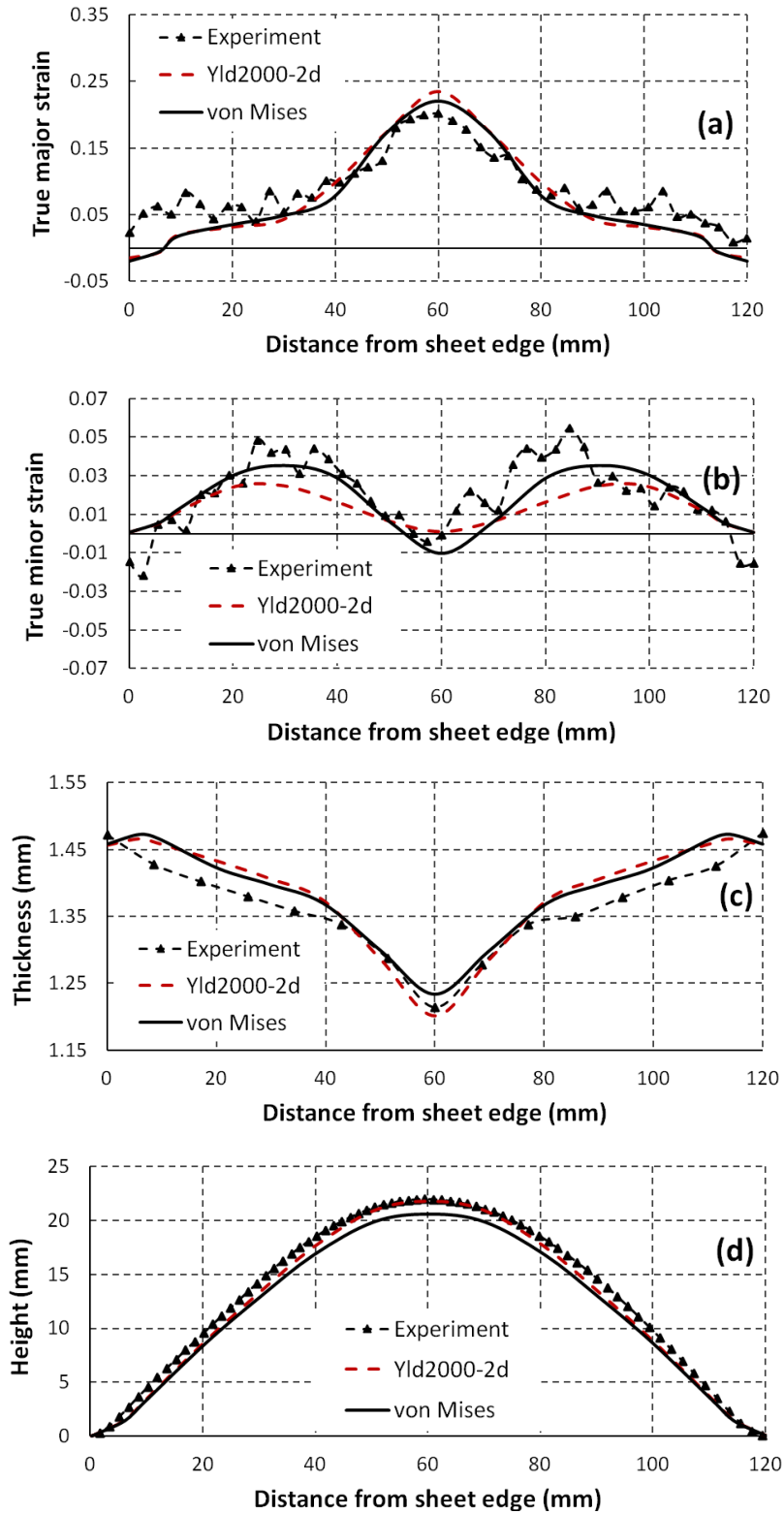


Figure 6-28. Measured and predicted data for AA5182-O plane strain EHFF specimen; a) major strain, b) minor strain, c) thickness and d) height

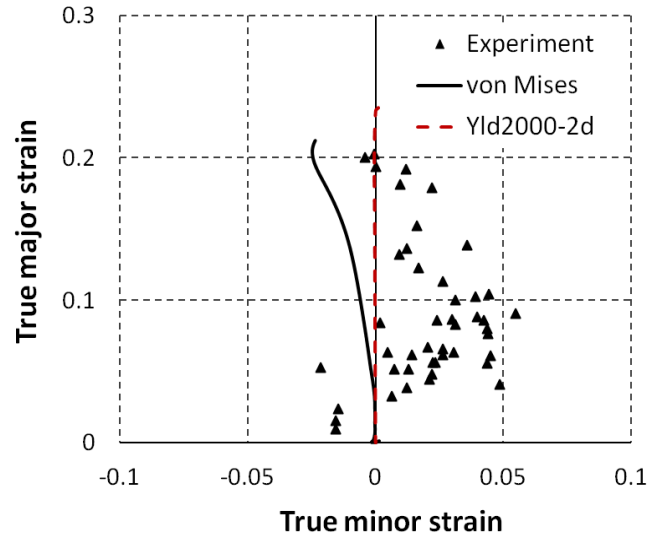


Figure 6-29. Measured strain distribution and predicted strain path for an element at the centre of the gauge section for AA5182-O plane strain EHFF specimen

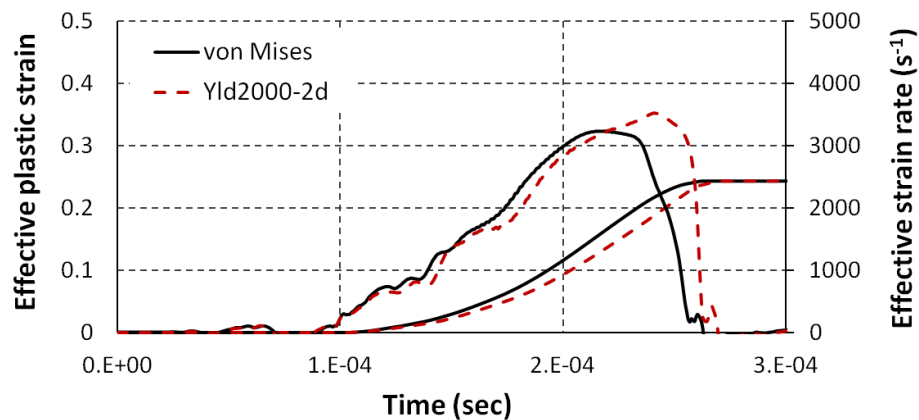


Figure 6-30. Effective plastic strain and effective strain rate histories for an element at the centre of the AA5182-O plane strain EHFF specimen

6.4.2.7 DP600 Biaxial

Figure 6-31a shows that the major strain distribution predicted with Yld2000-2d coincides very well with the measurements across the entire DP600 biaxial specimen, with a maximum major strain of 0.2 at the centre of the specimen. For the same amount of energy, von Mises over-predicts the major strain distribution with a maximum value of 0.235, which is due to the fact that von Mises predicts a lower biaxial flow stress compared to Yld2000-2d, as can be seen in Figure 4-33. Figure 6-31b shows that the measured minor strains are slightly lower than the major strains across the entire

specimen. Similar to the major strain, the minor strains predicted with Yld2000-2d are in good agreement with the measurements, whereas von Mises over-predicts the minor strains. The comparison of the measured and predicted thickness distributions shows the capability of Yld2000-2d to accurately capture both the trend and the absolute minimum value of the thickness, however von Mises over-predicts the absolute minimum thickness value near the apex of the deformed specimen, as can be seen in Figure 6-31c. The discrepancy between the thickness measurements and those predicted with von Mises is consistent with the previous observation that von Mises over-predicts both major and minor strains.

Figure 6-31d shows that von Mises over-predicts the maximum height of the DP600 biaxial specimen (29.3 mm) compared to that predicted with Yld2000-2d (27.9 mm) with the same energy magnitudes. This difference is associated with lower biaxial flow stress in von Mises compared to Yld2000-2d, which causes the material to flow faster using von Mises and results in greater major and minor strains compared to Yld2000-2d. Once again, the prediction of specimen height using Yld2000-2d correlates very well with the experimental height measurements on the DP600 biaxial EHFF specimen. As expected for the biaxial tension case, Figure 6-32 shows a proportional biaxial strain path predicted by both von Mises and Yld2000-2d for an element at the centre of the specimen. Comparison between the predicted strain paths and the maximum measured strain values (measured near the apex of the specimen) confirms the accuracy of the predicted strain path.

Figure 6-33 shows that von Mises predicts a greater effective plastic strain (0.46) than Yld2000-2d (0.415) in the centre of the DP600 biaxial EHFF specimen: this is around 11% greater. This can be expected due to the over-prediction of major and minor strains with von Mises. As a consequence of predicting a greater effective plastic strain for the same energy level, von Mises also predicts a much greater maximum effective strain rate (5650 s^{-1}) compared to Yld2000-2d (4650 s^{-1}). The greatest strain rate was reached in the centre of the DP600 biaxial specimen towards the end of the EHFF process, which is in good agreement with the dynamic mechanism of pulsed forming of circular membranes discussed by Hudson (1951) and Golovashchenko et al. (2011a).

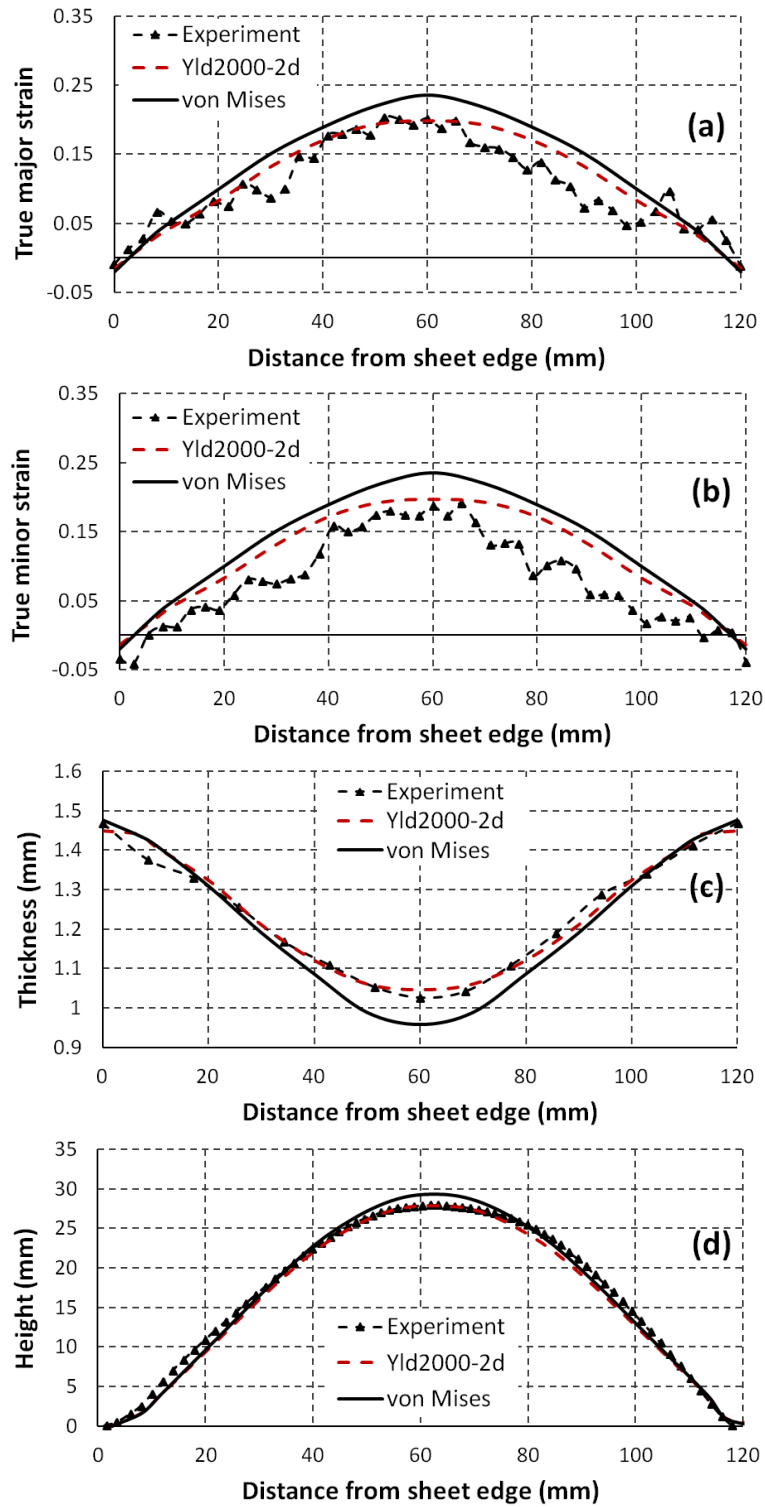


Figure 6-31. Measured and predicted data for DP600 biaxial EHFF specimen; a) major strain, b) minor strain, c) thickness and d) height

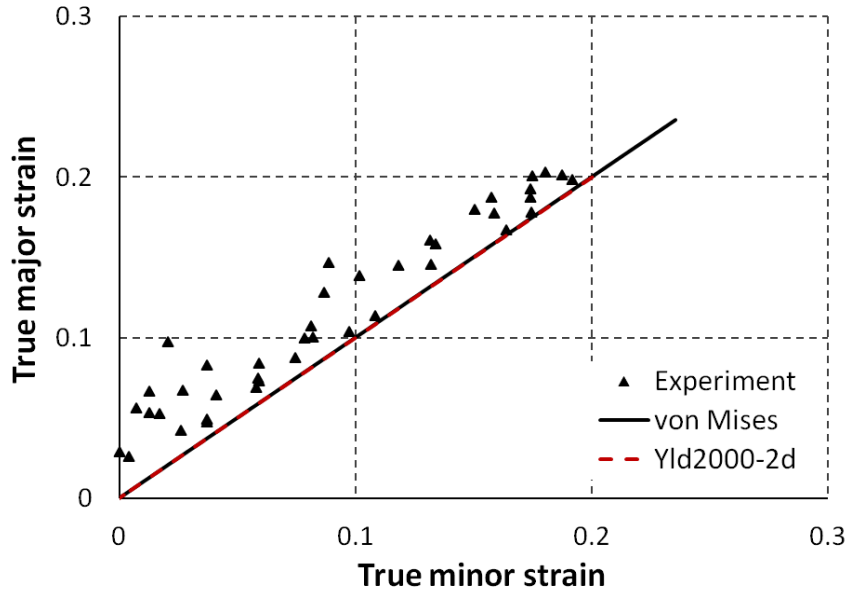


Figure 6-32. Measured strain distribution and predicted strain path for an element at the centre of the DP600 biaxial EHFF specimen

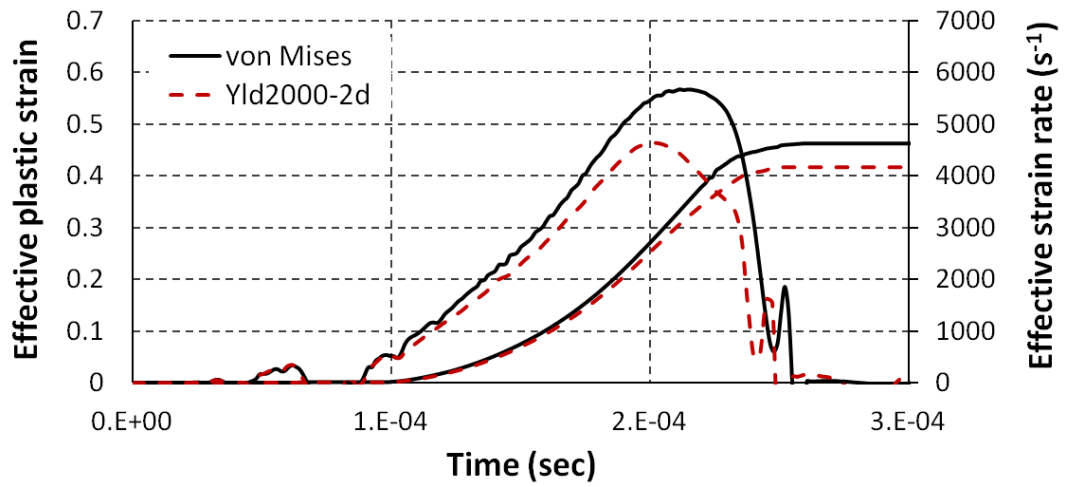


Figure 6-33. Effective plastic strain and effective strain rate histories for an element at the centre of the DP600 biaxial EHFF specimen

6.4.2.8 AA5182-O Biaxial

Figure 6-34a shows a reasonably good agreement between the measured major strain distribution and the major strains predicted with Yld2000-2d and von Mises (0.26), although the predicted peak major strains are slightly greater than the measured peak major strains in the gauge area. The difference between the major strains predicted by Yld2000-2d and von Mises is very small, due to the similar biaxial flow stress for AA5182-O at various strain rates and in particular at 1000 s^{-1} , which can be seen in Figure 4-35. Comparison of Figure 6-34a and Figure 6-34b shows that the measured minor strains are somewhat lower than the measured major strains in the centre of the specimen, whereas the predicted major and minor strains at the apex of the specimen are very similar. The difference between the measured major and minor strains in AA5182-O could be related to the unsymmetrical pressure distribution on the specimen during the EHF forming process, which results in the deviation of the strain path from the equibiaxial condition.

Figure 6-34c shows that the predicted thickness distribution coincides very closely with the measurements across the entire specimen. Results show almost the same thickness distributions are predicted by both Yld2000-2d and von Mises, because the predicted major and minor strains are similar. Figure 6-34d shows that both Yld2000-2d and von Mises predict similar height distributions that are in good agreement with the measurements. Figure 6-35 shows a proportional equibiaxial strain path predicted by both Yld2000-2d and von Mises. Comparison of the measured major/minor strains across the DP600 and AA5182 biaxial specimens, shows a greater deviation from the equibiaxial condition at the apex of the AA5182-O specimen compared to the DP600 specimen. Figure 6-36 shows that both Yld2000-2d and von Mises predict almost the same effective plastic strain (0.515) and effective strain rate (4500 s^{-1}), both in terms of the general trend and peak values for an element at the centre of the specimen. This might have been expected for AA5182-O due to the similarity of the biaxial flow curves at various strain rates.

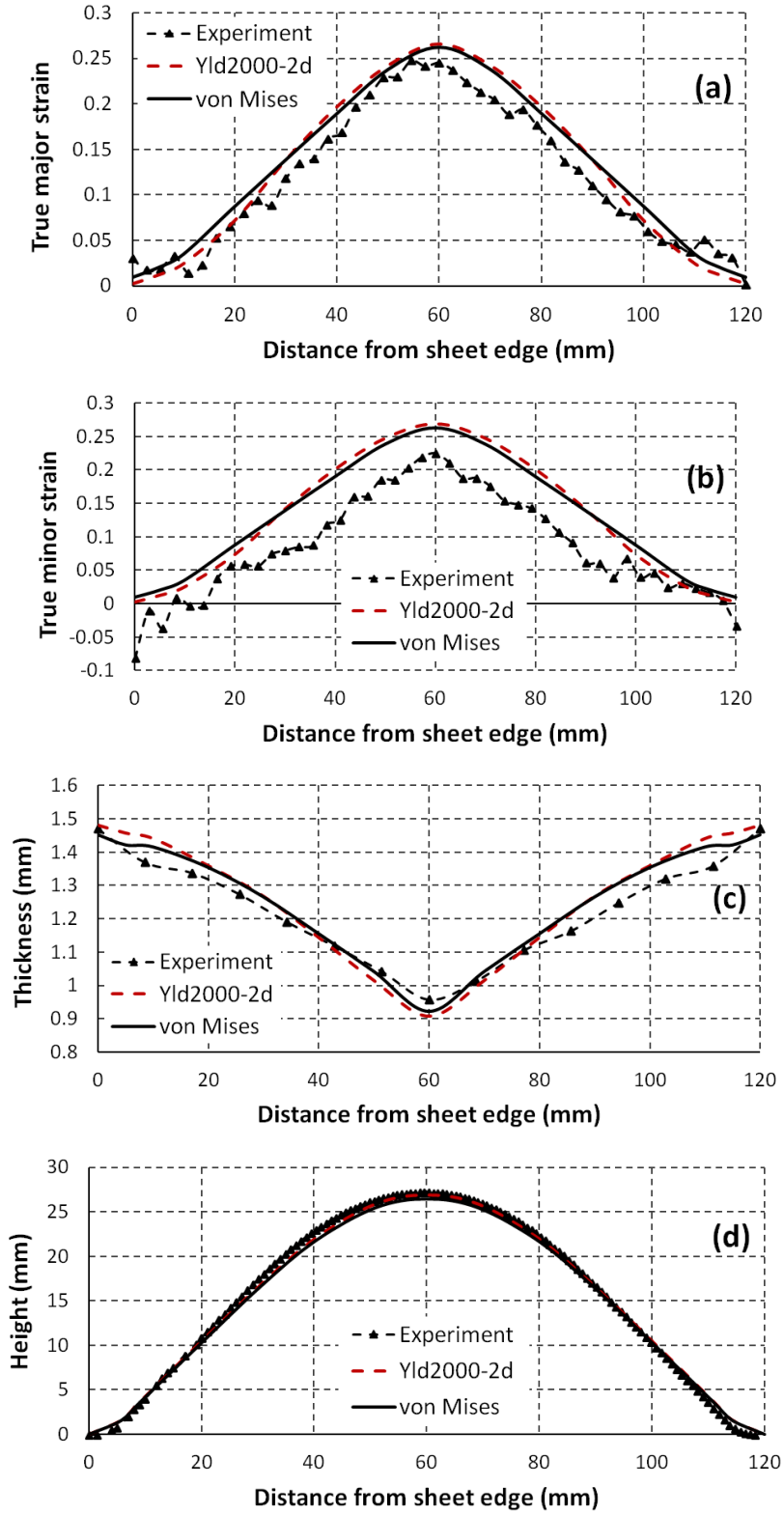


Figure 6-34. Measured and predicted data for AA5182-O biaxial EHFF specimen; a) major strain, b) minor strain, c) thickness and d) height

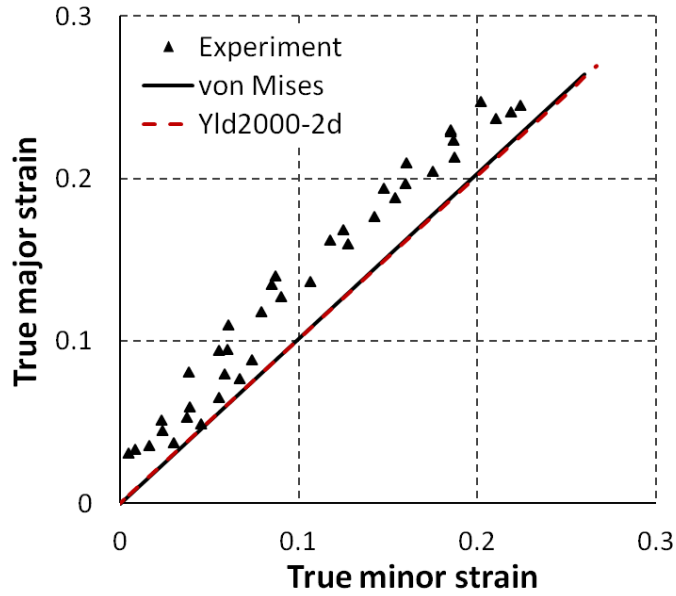


Figure 6-35. Measured strain distribution and predicted strain path for an element at the centre of the AA5182-O biaxial EHFF specimen

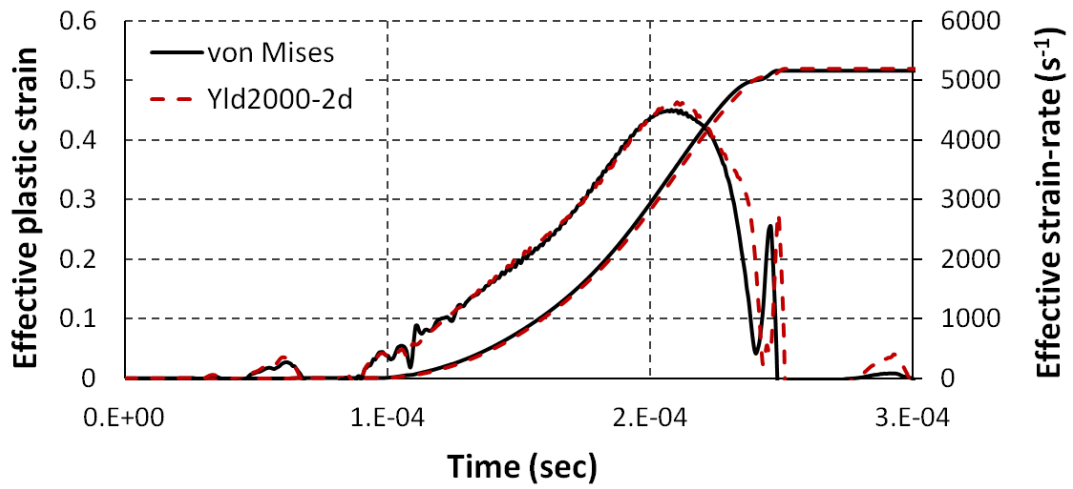


Figure 6-36. Effective plastic strain and effective strain rate histories for an element at the centre of the AA5182-O biaxial EHFF specimen

In order to visualize the final deformed part for the four EHF specimen geometries, the effective plastic strain contours of DP600 predicted by Yld2000-2d are shown in Figure 6-37. Results indicate that the strain localization occurs in the centre of the gauge section far from the free edges for all specimen geometries. This confirms that the specimen designs were effectively optimized and the experimental measurements are reliable.

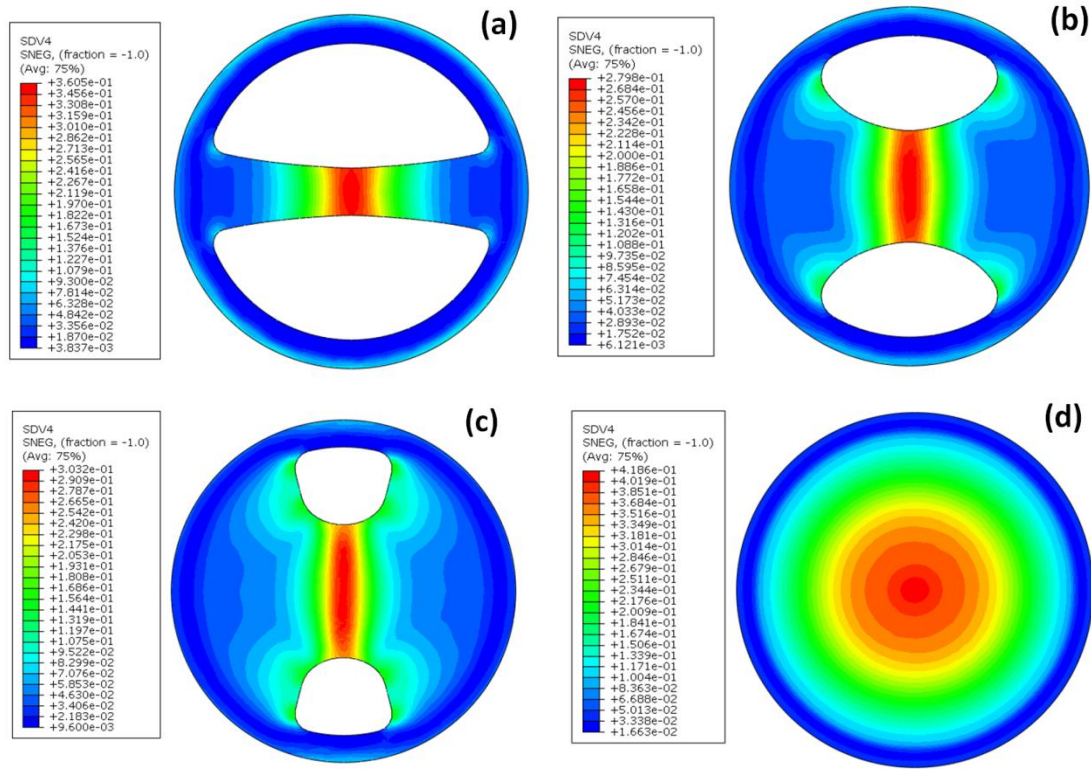


Figure 6-37. Effective plastic strain contours predicted by Yld2000-2d for DP600; a) uniaxial, b) intermediate draw, c) plane strain and d) biaxial

6.4.3 EHDF Results

In contrast with the EHFF process and with conventional sheet metal forming operations, EHDF is a rather complex forming process due to the dynamic sheet/die interaction. In order to account for the coining effect and to more accurately predict the deformation history when the sheet hits the die, it is necessary to employ solid elements in order to model the sheet in EHDF. It should also be noted that all simulations of EHDF were performed with either von Mises (3D) or Yld2004-18p (3D) yield criteria. And in

order to better understand the nature of the deformation process occurring during the EHDF and especially the role of anisotropy in die-formed specimens, the histories of major/minor strains, shear strain, effective plastic strain, effective strain rate and minimum principal stress were extracted from the FE simulations. An element on the outer surface of the sheet near the apex of the specimen and that has a direct contact with the die (5 mm from the centre of the specimen) was selected since it experiences the maximum instantaneous strain rate and all the histories were reported for this element.

Figure 6-38a shows that with the same energy magnitude, von Mises over-predicts the peak major strain (0.515) compared to Yld2004-18p (0.45). This over-prediction occurs because the von Mises biaxial flow stress is lower than that predicted with Yld2004-18p, as can be seen in Figure 4-33. A similar result was observed for the DP600 biaxial specimen in EHFF. Also, Yld2004-18p predicts a greater peak major strain (0.45) at the centre of the sheet, compared to the measured maximum major strain (0.4). This discrepancy is partly due to experimental uncertainty since the strains near the apex of the deformed specimen were very difficult to measure because the friction of the sheet against the die mostly erased the grid from the surface of the sheet. Figure 6-38b shows that the measured minor strains are lower than the measured major strains (Figure 6-38a) in the apex region. The peak minor strain predicted with Yld2004-18p (0.375) is in good agreement with the measured peak minor strain, however von Mises over-predicts the peak minor strain (0.445), which is again associated with the lower biaxial flow stress for von Mises compared to Yld2004-18p (Figure 4-33). It should be noted that the measurements show that maximum major and minor strains are concentrated rather closely to the apex area, with a rather substantial strain gradient in the radial direction.

Figure 6-38c shows predicted and measured height profiles that are very similar, with the same maximum height (37.5 mm). This is to be expected because the sheet deformation is constrained by the conical die. Simulation results also show that the predicted height distribution shows a slight rebounding somewhere between the apex and the entry radius. This could be a consequence of using rigid tools in the FE model which results in over-prediction of the contact stresses resulting from the sheet/die dynamic interaction. It should be noted that even when rigid parts are used, the computation time

is very expensive for EHDF simulations. Therefore, implementing a non-rigid die in the simulation would significantly increase the computation time and was not practical for this investigation.

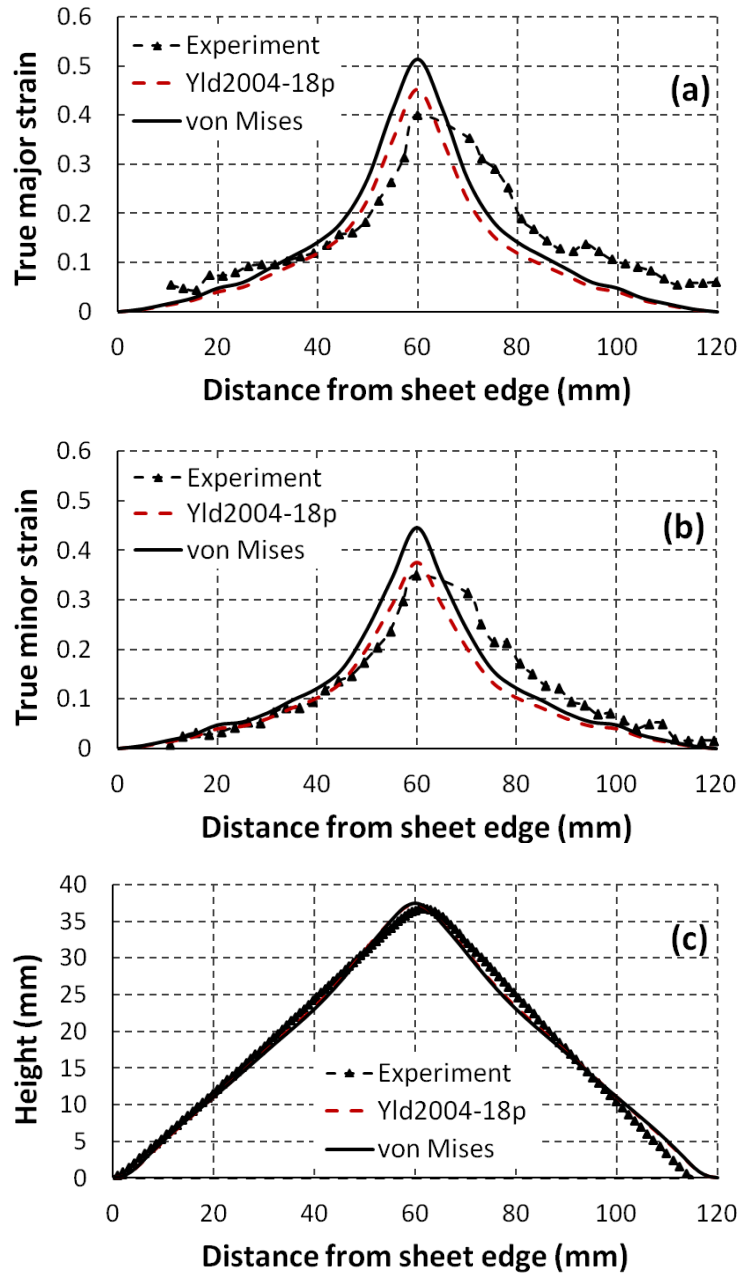


Figure 6-38. Measured and predicted data for DP600 in EHDF; a) major strain, b) minor strain and c) height

Figure 6-39 shows the strain path predicted by Yld2004-18p and von Mises for an element that initially lies 5 mm from the centre of the specimen. As mentioned before, this location was selected because this is where the maximum effective strain rate and consequently the greatest through-thickness stress were predicted. The predicted strain paths for both yield functions show a sudden increase in the major strain just after the sheet contacts the die. Yld2004-18p shows an incremental increase in major strain of 0.06 (from 0.29 to 0.35), while von Mises shows an incremental increase of 0.07 (from 0.34 to 0.41). The sudden increase in major strain while the minor strain remains almost constant, causes an abrupt change in strain path from biaxial tension to plane-strain tension when the sheet contacts the die. This effect is predicted by both Yld2004-18p and von Mises. Also, this effect can be seen in the experimental work that was reported by Balanethiram and Daehn (1992) and by Ilinich et al. (2011). This change in strain path is accompanied by a remarkable change in the stress state in the sheet at the locations that contact the die (Figure 6-41). In the analysis of the EHDF process, it is essential therefore that the effects of non-linear strain path be considered when interpreting the material formability. Results for the selected element show that around 83% (predicted by both Yld2004-18p and von Mises) of the total major strain (or 81% of the effective plastic strain as shown in Figure 6-40) occurs when the sheet material is subject to a proportional biaxial strain path before it contacts the die. Since, most of the plastic deformation in EHDF occurs under very similar condition as biaxial EHFF for.

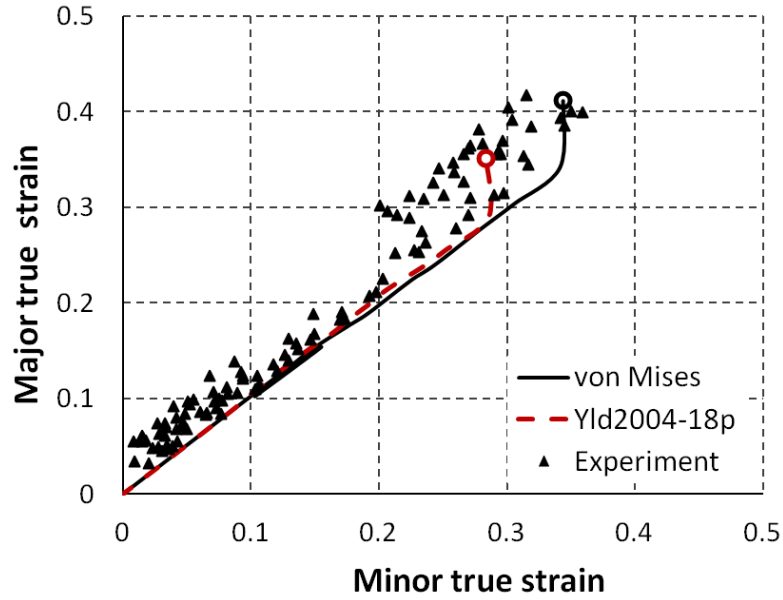


Figure 6-39. Measured strain distribution and predicted strain path for an element at 5mm distance from the centre of DP600 specimen in EHDF

Similar to DP600 biaxial EHFF, Figure 6-40 shows that von Mises predicts a greater effective plastic strain (0.88) than Yld2004-18p (0.77). This discrepancy (around 14%) is associated with the lower biaxial flow stress predicted by von Mises compared to Yld2004-18p (Figure 4-33). Both Yld2004-18p and von Mises predict that at the time of impact there is a substantial increase of effective plastic strain, which coincides with the generation of a very high strain rate and compressive through-thickness stress. The effective plastic strain history for the selected element predicted with Yld2004-18p shows an incremental increase of 0.145 (from 0.625 to 0.77), while von Mises predicts an incremental increase of 0.16 (from 0.72 to 0.88) when the sheet impacts the die. This indicates that a significant amount of plastic deformation (around 18% effective plastic strain) occurs immediately after the sheet contacts the die.

Also, Figure 6-40 shows that both Yld2004-18p and von Mises predict a remarkable increase in the effective strain rate at the moment when the selected element in the sheet impacts the die. This phenomenon is rather localized, when compared to the area of maximum strain rate in EHFF (Figure 6-33). Yld2004-18p and von Mises predict a maximum effective strain rate of approximately $16,300 \text{ s}^{-1}$ and $20,800 \text{ s}^{-1}$, respectively. The discrepancy between the Yld2004-18p and von Mises is related to the difference in

the biaxial flow stresses in these two yield functions. The lower biaxial flow stress predicted by von Mises allows the material to flow faster compared to the Yld2004-18p when subjected to the same energy magnitude. The predicted maximum instantaneous effective strain rates are in good agreement with the results reported by Golovashchenko et al. (2013) for the same sheet material and conical die, even though the chamber shape and volume were different. More details on the effect of different process parameters on the effective strain rate can be found in a paper published by the author (Hassannejadasl et al., 2014). Also, it should be noted that the total deformation time predicted by Yld2004-18p is around $270 \mu\text{s}$, which correlates quite well with the results ($315 \mu\text{s}$) reported by Gillard et al. (2013) for the same conical die but using a different chamber. The predictions indicate that the sheet material in EHDF can reach deformation rates at which the constitutive behaviour of the material is not known. i.e. results show that at least 20% of the plastic deformation can occur at strain rates that exceed $10,000 \text{ s}^{-1}$. The predicted strain rates are substantially greater than those observed in conventional metal forming or even EHFF, and are well above the rates ($1,000 \text{ s}^{-1}$) at which the split Hokinson bar tests were conducted in this work. Therefore, for more accurate prediction of the sheet deformation in EHDF, the mechanical properties and work hardening behaviour of the desired alloys should be determined at these strain rates.

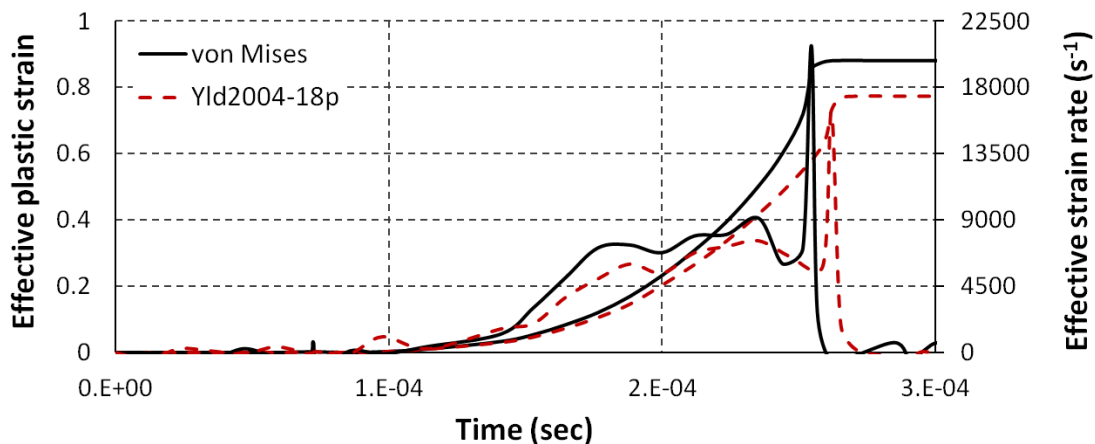


Figure 6-40. Effective plastic strain and effective strain rate histories for an element at 5mm distance from the centre of DP600 specimen in EHDF

Significant through-thickness compressive and shear stresses are generated as a result of the dynamic sheet/die interaction. These stresses induce a unique deformation mode in the sheet material and are recognized as the main mechanistic factors that are responsible for the formability improvement (Imbert et al., 2005, Golovashchenko et al. 2011a and 2011b). Figure 6-41 shows the generation of a large through-thickness compressive stress just after the sheet impacts the die. It appears that the maximum absolute through-thickness compressive stress predicted with von Mises (-810 MPa) is greater than that predicted with Yld2004-18p (-600 MPa), which is due to the greater maximum effective strain rate predicted by von Mises when the sheet hits the die (Figure 6-40). This through-thickness compressive stress causes a change in the stress triaxiality, and consequently affects the formability of the material.

Balanethiram and Daehn (1994a and 1994b) reported the first analysis of the sheet/die dynamic interaction in high speed metal forming, and showed that a significant compressive through-thickness stress can be generated, resulting in so called “inertial ironing effect”. Later on, Golovashchenko (1999) reported compressive through-thickness stresses on the order of the material yield stress from electromagnetic tube forming simulation. More recently, Imbert et al. (2005, 2011) completed numerical investigations in electromagnetic forming and suggested that the generated through-thickness compressive and shear stresses at very high strain rates produce the observed increased formability. Imbert showed that the large compressive through-thickness stress that is suddenly generated can suppress void growth and coalescence, thus increasing formability, which is also suggested in the comprehensive review of Lewandowski and Lowhaphandu (1998). Simulations of the EHDF process showed that the compressive through-thickness stress magnitude strongly depends on the constitutive material model, die geometry and the energy magnitude. A correct calculation of the trend and magnitude of the contact stress is important in order to accurately predict the damage accumulation behaviour. More details on the effect of compressive through-thickness stress on the damage accumulation in EHDF using isotropic yield function (von Mises) was reported by the author (Hassannejadasl et al., 2014).

In addition to the significant through-thickness compressive stress, large through-thickness shear stresses are also generated which result in significant through-thickness (out-of-plane) shear that contribute to the overall plastic deformation of the material. Figure 6-41 shows that the greatest through-thickness shear strain is reached at, or just after, impact. von Mises predicts a larger absolute value of the through-thickness shear strain (0.175) than Yld2004-18p (0.153), which again may be due to the prediction of a greater effective strain rate with von Mises compared to Yld2004-18p, when the sheet hits the die. The amount of through-thickness shear strain predicted with Yld2004-18p represents approximately 44% of the major strain (0.35), which indicates that the through-thickness shear stress makes a considerable contribution to the plastic deformation in EHDF.

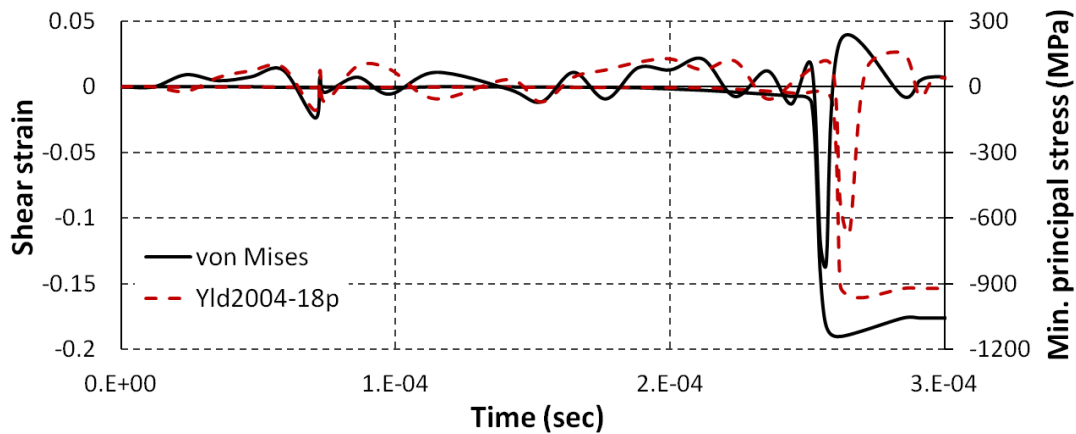


Figure 6-41. Shear strain and minimum principal stress histories for an element at 5mm distance from the centre of DP600 specimen in EHDF

Figure 6.42 shows the evolution of the pressure distribution within the chamber due to wave propagation through the water when the energy is released from a spherical volume that is equivalent to the plasma channel in the actual EHF process. Results show a spherical wave propagation shape at the very beginning of the process, before the pressure wave reaches the bottom surface of the rigid chamber. As the pressure wave evolves and reflects off the chamber wall, a very complex and discontinuous wave propagates through the water towards the sheet and drives the sheet into the die cavity by dynamic forces. The maximum predicted pressure is around 200 MPa, which is

somewhat greater than the maximum value (150 MPa) reported by Golovashchenko et al (2013). The difference could be due to the different methodologies used by the author (who used the ignition-and-growth model in ABAQUS/Explicit) and Golovashchenko et al. (who used the energy leak model in LS-DYNA) to simulate the pressure pulse in EHDF. However, regarding the maximum predicted effective strain rate and the total deformation time, the overall deformation histories predicted by the two authors are in good agreement, which confirms the reliability of the FE model created by the author.

6.4.4 Experimental and numerical energy

In order to provide a more complete comparison between the energy that was applied in EHFF and EHDF laboratory tests and that which was applied in the corresponding numerical simulations, both sets of input energy are presented in Table 6.2 and Table 6.3 for DP600 and AA5182-O, respectively. The experimental energy at the chamber was calculated by Maris (2014) based on the voltage differential measured across the electrodes using a voltage probe and also based on the current measured using a Rogowski coil that was coiled around the busbar leading in to the chamber (please see Maris, 2014, for more details). In comparison with the experimental input energy required to form a safe specimen, the energy ratios show that more energy is required in the EHF simulations to reach to the same maximum height as the experiment for both DP600 and AA5182-O. This indicates that despite the effort to model the physics of the EHF process, the equivalency of the energy is still very challenging. One main reason could be due to different techniques used to model the EHF process. However, a reasonable correlation between the experimental and numerical applied energies can be seen for each case. It should be noted that some portion of the error should be attributed to the experimental measurements, since a substantial variation and loss of energy can exist, as reported by Maris (2014).

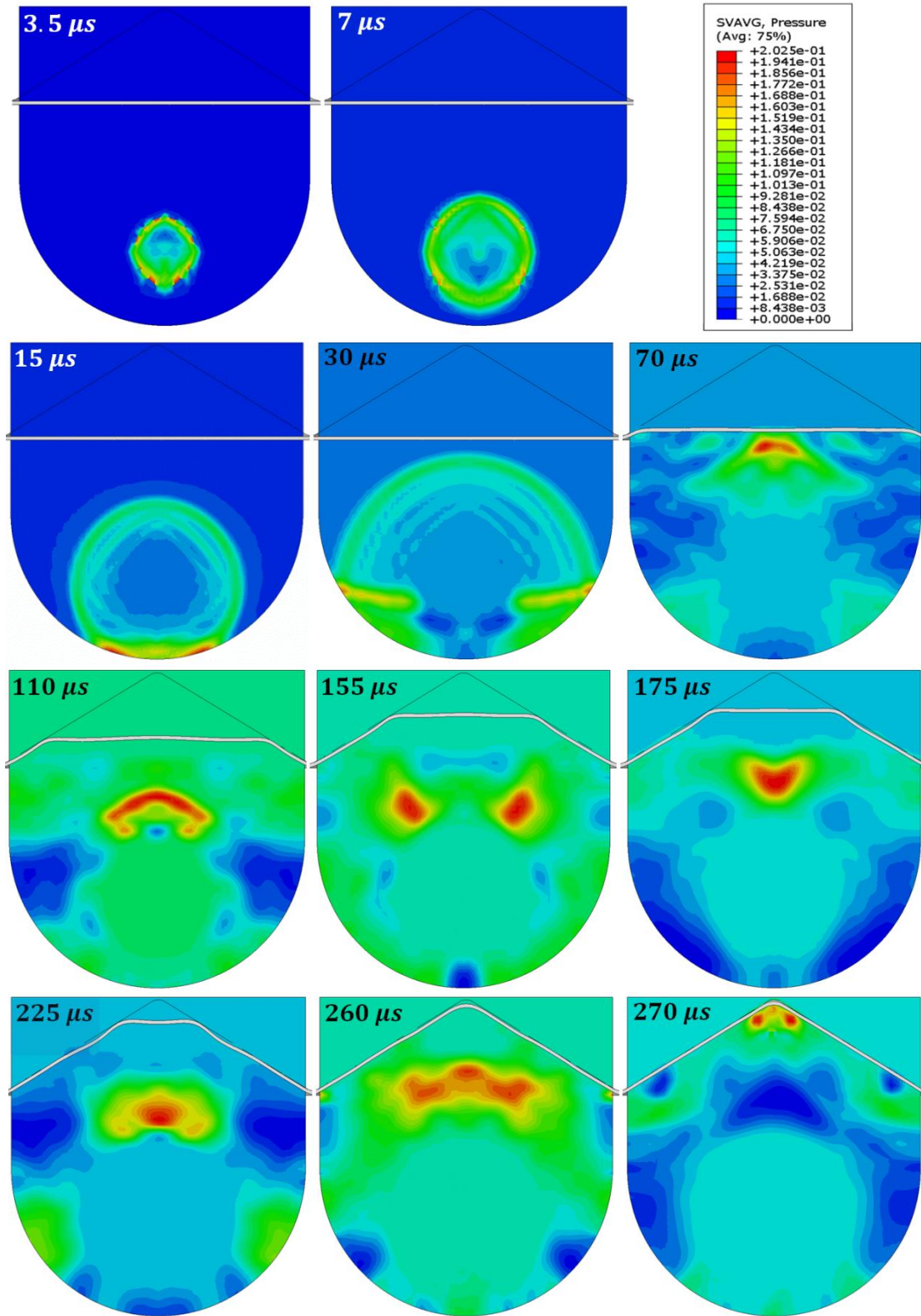


Figure 6-42. Pressure distribution history through the water during EHD (pressure unit in GPa)

Table 6.2. DP600 experimental and numerical input energy

Condition	Geometry	Experimental input energy (kj)	Numerical applied energy (kj)	Ratio of the energy
EHFF	Uniaxial	5	9.9	1.98
	Intermediate Draw	3.2	5.6	1.75
	Plane strain	2.9	4.5	1.55
	Biaxial	4.3	7.2	1.67
EHDF	Biaxial	3.5	5.7	1.63

Table 6.3. AA5182-O experimental and numerical input energy

Condition	Geometry	Experimental input energy (kj)	Numerical applied energy (kj)	Ratio of the energy
EHFF	Uniaxial	2.1	4.05	1.93
	Intermediate Draw	1.1	1.97	1.79
	Plane strain	0.95	1.43	1.51
	Biaxial	1.25	1.95	1.56

6.4.5 Computation time

One important aspect of the advanced material models that are developed for more effective simulations of sheet metal forming is the computation time. In fact, some advanced micro- and macro- constitutive models have been developed which are able to predict the elasto-plastic behaviour of sheet metals very well, but the expensive computation time is a significant disadvantage. Computation times for EHFF simulations for different geometries with von Mises and Yld2000-2d yield function in conjunction with rate-dependent KHL hardening model are shown in Figure 6-43. All simulations were performed under the same conditions (except for the geometry of the specimen) with the same computer which had 8 CPUs (2.8 GHz). For all specimen geometries in EHFF simulations the computation time using Yld2000-2d was much greater than when von Mises was used, which means that the more accurate computation comes at a cost.

The main reason is the non-quadratic nature of Yld2000-2d and the large number of first and second derivatives which need to be computed for the implicit integration scheme and that substantially increase the computation time compared to the isotropic function. It should be mentioned that using a rate-dependent hardening model and updating the anisotropy coefficients w.r.t. strain rate in every iteration is another reason the computation time increased in these EHF simulations. On average, Yld2000-2d requires more than 10 times more computation time than von Mises in order to simulate EHF.

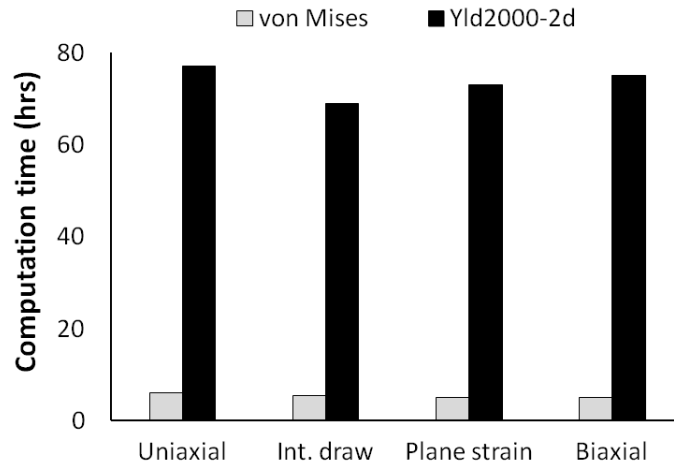


Figure 6-43. Computation times for EHF simulations

In the EHDF simulation, the computation time is further increased because solid elements are used to model the sheet. The EHDF model based on the von Mises yield function required around 19 hours to simulate the complete forming process, while it took about 283 hours (around 12 days) when using Yld2004-18p. The time and memory required to simulate an industrial scale EHDF process is almost unaffordable due to the fine mesh of solid elements (in particular out-of-plane refined elements), the very large first and second derivatives required for Yld2004-18p, the rate-dependent hardening model and the updating of anisotropy coefficients. However, since the main goal of the EHDF modeling was to understand the role of anisotropy at high strain rate regimes for only one particular material and geometry, the computation time was acceptable for this research project.

7 Overall Summary and Conclusions

7.1 Summary

In this work, the mechanical properties (including flow stresses and r-values) of three sheet materials (DP600, TRIP780, and AA5182-O) were obtained at different strain rates (0.001, 0.1, 1, 10, 100, and 1000 s^{-1}) under uniaxial tension (in the rolling, diagonal, and transverse directions) and biaxial tension conditions. Several anisotropic yield functions such as Hill48, Hill90, Barlat89, Yld96, Yld2000-2d, and Yld2004-18P were calibrated at each level of strain rate. Using the mechanical properties, a comprehensive study was then carried out to evaluate the effect of strain rate on the flow surface shape for each yield function and at each level of strain rate. Furthermore, in order to capture the hardening behaviour of the materials, three different rate-dependent hardening models (Johnson-Cook, JC; Khan-Huang-Liang, KHL; and Surajit Kumar Paul, SKP) were also calibrated.

After a thorough review of different constitutive models, several associative rate-dependent anisotropic material models (for plane and general stress conditions) were developed. The material models which feature both the updating of anisotropic yield functions, (the anisotropy coefficients are updated according to strain rate) and rate-dependent hardening model, were developed to predict both anisotropic and rate-dependent hardening characteristics as accurately as possible. The anisotropy coefficients were updated for the current instantaneous strain rate, by using 4th-order strain rate dependent polynomial functions instead of the initial constant anisotropy coefficients.

Among all the anisotropic yield functions and hardening models, Yld2000-2d (for plane stress conditions in EHFF) and Yld2004-18p (for general stress conditions in EHDF) were selected with the KHL hardening model to simulate the behaviour of the

sheet materials in these high energy forming processes. Finally, an implicit (Euler backward) integration algorithm, using the multi-step return mapping method, was used to develop the rate-dependent constitutive material models. The developed models were implemented as user-defined material subroutines (VUMATs) for ABAQUS/Explicit code to simulate EHFF and EHDF processes. EHF simulations were carried out for different forming conditions, using Eulerian elements to model the water and space between the sheet and the die, and the ignition-and-growth model as an equivalence for the generation of the pressure pulse. The EHFF process was simulated for four different specimen geometries (representing four different strain paths; uniaxial, intermediate draw, plane strain and biaxial tension), for both DP600 and AA5182-O sheet materials. Also, the EHDF process using a conical die was simulated for DP600 to investigate the role of anisotropy when the sheet undergoes substantial through-thickness compressive and shear stresses (general stress state).

7.2 Conclusions

The following conclusions can be drawn from this work:

7.2.1 Material characterization tests

- Uniaxial tensile tests for a wide range of strain rate (0.001, 0.1, 1.0, 10, 100 and 1000 s⁻¹) at room temperature show a significant strain-rate sensitivity in all three material orientations (RD, DD, and TD) for DP600 and TRIP780. In contrast, AA5182-O exhibits a near-zero or a small negative strain-rate sensitivity. A slight decrease of the work hardening rate can be seen with the increase of strain rate in some cases in certain directions.
- The flow stress ratio w.r.t. strain rate plots for DP600 and TRIP780, show a slight continuous decrease in the flow stress with increasing strain rate. i.e., the anisotropy effect associated with the flow stress decreases with increasing strain rate. The r-value shows random changes w.r.t. strain rate for the three aforementioned materials, which makes it hard to draw a general conclusion

regarding the effect of strain rate on the anisotropy behaviour associated with the r-value.

7.2.2 Yield function and hardening model calibration

- A calibration procedure was developed to determine the anisotropy parameters in various yield functions which considers the variation of flow stresses in uniaxial and biaxial tension. The anisotropy parameters were calibrated for each level of strain rate by using the uniaxial and biaxial flow stress ratios after a certain amount of strain, when they have reached stable values. Results showed that this procedure is very reasonable, since EHF simulations typically lead to large deformations across a wide range of strain rates.
- Results show that among all the hardening models considered, the KHL model is better able to capture the response of DP600 and TRIP780 in RD for the entire range of examined strain rates.

7.2.3 Effect of Updating anisotropy coefficients on the flow surface

- Results shows that Hill's family of yield functions are not able to accurately reproduce the variation of the experimental flow stresses and the r-value for any of these sheet materials. However, among all Hill's yield functions, it was shown that the flow stress and r-value directionalities are best described by Hill90-stress for the entire range of strain rates and for all three materials.
- Results for Barlat's family of yield functions shows that Yld2000-2d and Yld2004-18p are able to reproduce both the flow stress and r-value anisotropies for the entire range of strain rates and for all three materials, although Barlat89 underestimates the associated anisotropy values. The strong performance of Yld2000-2d and Yld2004-18p is associated with their formulations, which are based on two linear transformations as well as their unique calibration procedures.
- By comparing the quasistatic and updated flow surfaces predicted by Yld2000-2d, results show a considerable effect of updating anisotropy coefficients in the biaxial stress state of DP600 and TRIP780 for a strain rate of 1000 s^{-1} . For

almost all strain rates, the difference between the updated and quasistatic flow surfaces of DP600 is more significant as the value of the shear stress increases, whereas the difference remains constant for TRIP780 for almost all strain rates. In contrast with DP600 and TRIP780, almost no difference in the quasistatic and updated predicted flow surfaces of AA5182-O is seen with Yld2000-2d, due to the strain-rate insensitivity of this aluminum alloy for the examined range of strain rates.

- The comparison between the flow surfaces predicted with Hill48-r.value and the experimental data shows the inability of Hill48 to accurately capture the anisotropic data for all three materials at various strain rates. For the DP600 and TRIP780 steel sheets, results show that updating the anisotropy coefficients helps to improve the performance of the Hill48-r.value function, in-particular for biaxial stress states. This improvement is further highlighted when the shear stress term is increased.
- A significant difference can be seen between the flow surfaces predicted using the updated Yld2000-2d and those predicted with von Mises, especially in biaxial and plane-strain stress states for both DP600 and TRIP780. This difference decreases with increasing strain rate, but still remains considerable. Also, the AA5182-O flow surfaces predicted by Yld2000-2d deviate significantly from the von Mises flow surfaces at all strain rates, especially for plane strain stress states. This deviation is still considerable when significant shear stresses exist, because of the much higher exponent value ($a = 8$) in Yld2000-2d compared to that in von Mises' yield function ($a = 2$).

7.2.4 Finite element simulation

7.2.4.1 Single element (calculation of effective plastic strain)

- Results of single element simulations on DP600, in which the same amount of plastic strain was applied in RD and TD for the equibiaxial condition and either RD or TD for the plane strain conditions, show that the maximum relative error occurs in the equibiaxial condition (7%) when the effective plastic strain is

calculated using the von Mises yield function (assuming Yld2000-2d accurately predicts the effective plastic strain). Results show that the error decreases (4% at 1000 s^{-1}) as the strain rate increases. Also, comparison between the effective plastic strains predicted with Yld2000-2d and von Mises for TRIP780 show that the maximum relative error (3% – 7%) occurs in both biaxial and plane strain (RD) conditions for almost all strain rates. A maximum error of 7% – 10% exists when the effective plastic strain is predicted using von Mises for AA5182-O in the plane strain condition for the entire range of strain rates, whereas the relative error is negligible for the equibiaxial condition, as would be expected from the material flow surfaces.

7.2.4.2 EHFF

- The EHFF simulation results for both the DP600 and AA5182-O uniaxial and intermediate draw specimens show an improvement in the predicted minor strains when Yld2000-2d is used rather than von Mises. The use of Yld2000-2d also results in a better agreement of the predicted strain path with the principal strain measurements in the EHFF specimen. Furthermore, the improvement in the prediction of the minor strain with Yld2000-2d, also leads to a more accurate thickness distribution in the gauge section of the uniaxial tension specimen.

- The EHFF simulation results for the DP600 plane strain specimen show that both Yld2000-2d and von Mises over-predict the major and minor strains as well as the thickness in the gauge section when compared with the measurements. In the author's opinion, this discrepancy would be minimized if experimental biaxial r -values and biaxial flow stresses could be obtained at high strain rates (such as 1000 s^{-1}). The results predicted with von Mises for the EHFF of the AA5182-O plane strain specimen show a lower maximum height at the centre of the gauge section than that predicted with Yld2000-2d with the same amount of applied energy. Although, a greater specimen height is predicted with Yld2000-2d for the plane strain condition, almost the same peak major strain is predicted with either Yld2000-2d or von Mises; this is in spite of completely different material

behaviour of AA5182-O predicted by the two yield criteria. Results show that Yld2000-2d predicts an almost zero minor strain at the centre of the gauge section which correlates very well with the strain measurements. Also, the absolute minimum thickness predicted using Yld2000-2d is in better agreement with the measurements than that predicted with von Mises.

- The EHFF simulation results for the DP600 biaxial specimen show that von Mises predicts greater major and minor strains, thickness and height distributions compared to Yld2000-2d for the same amount of applied energy. This is because von Mises predicts a lower biaxial flow stress than Yld2000-2d. Both yield functions predict a similar proportional equi-biaxial strain path for an element at the centre of the sheet. Results for DP600 show that the von Mises effective plastic strain is around 11% greater than that predicted with Yld2000-2d for DP600, when the same amount of energy is applied. As a consequence of predicting a greater effective strain at the same energy level, von Mises also predicts a greater strain rate (5650 s^{-1}) than Yld2000-2d (4650 s^{-1}). However, Yld2000-2d and von Mises predict the same results for the AA5182-O biaxial specimen, which is not surprising considering the insensitivity of this alloy to strain rate and the similarity of the uniaxial and biaxial flow curves at various strain rates (experimental and calculated).
- The EHFF simulation results show that Yld2000-2d predicts a maximum effective strain rate in the range of $2,500 \text{ s}^{-1}$ to $5,000 \text{ s}^{-1}$, depending on the specimen geometry and the material grade. For all cases, the highest strain rate occurs in the centre of the sheet and towards the end of the EHFF process.

7.2.4.3 EHDF

- Simulation results show that a more complex deformation mechanism occurs in EHDF compared to EHFF, due to the dynamic sheet/die interaction. Results for DP600 show that, with the same applied energy magnitude, von Mises predicts greater major, minor and through-thickness shear strains and consequently a greater effective plastic strain (around 14% greater) compared to Yld2004-18p

when the sheet is formed into a conical die. Once again, this difference is due to the fact that von Mises predicts a lower biaxial flow stress than Yld2004-18p.

- The strain paths predicted with both Yld2004-18p and von Mises show a sudden increase in the major strain just after the sheet hits the die, and consequently an abrupt change in the strain path from biaxial tension to plane-strain tension. Results (predicted by both Yld2004-18p and von Mises) for an element near the apex (5 mm from the sheet centre) show that around 82% of the effective plastic strain occurs when the element has a proportional biaxial strain path before the sheet hits the die. Therefore, forming conditions in EHDF are very similar to those in biaxial EHFF, until the sheet hits the die. Therefore the results obtained in EHFF simulations using Yld2000-2d and von Mises are almost applicable to the EHDF condition, except for the through-thickness shear strain that is suddenly generated in EHDF when the sheet contacts the die.
- Results for an element 5 mm away from the centre of the sheet show that von Mises predicts a greater maximum absolute through-thickness compressive stress (−810 MPa) and a greater shear strain (0.175) compared to the values predicted by Yld2004-18p (−600 MPa and 0.153, respectively). These differences are due to the greater maximum effective strain rate predicted by von Mises (20,800 s^{−1}) compared to Yld2004-18p (16,300 s^{−1}) at the time of impact. The through-thickness shear strain predicted with Yld2004-18p is approximately 44% of the major strain, which indicates considerable contribution of the through-thickness shear stress to the plastic deformation in EHDF.

7.3 Recommendations for selecting an appropriate constitutive model for DP600, TRIP780 and AA5182-O

Yield function

- *For plane stress condition (such as EHFF);* Yld2000-2d is the best yield function for DP600, TRIP780 and AA5182-O. It should be noted that updating the

anisotropy coefficients according to strain rate is highly recommended for DP600 and TRIP780, while it is not the case for AA5182-O.

- *For general stress state (such as EHDF);* Yld2004-18p is the best choice for DP600, TRIP780 and AA5182-O. Again, similar to Yld2000-2d condition, updating anisotropy coefficients of Yld2004-18p is highly recommended for DP600 and TRIP780, while only using the initial (Quasistatic) anisotropy coefficients for AA5182-O results in a good accuracy.
- In case of shortage of experimental data to determine the anisotropy coefficients of Yld2000-2d and Yld2004-18p, it is highly recommended to use Hill90-stress (where the anisotropy coefficients are determined based on the flow stresses rather than r-values) for DP600 and TRIP780 for both plane stress and general stress state conditions.
- It should be noted that to take advantage of anisotropy yield function and describe the anisotropic behaviour of material accurately in finite element simulation of sheet metal forming processes, a substantial consideration should be done in selecting appropriate normalized flow stresses in different material orientations. It is highly recommended to look at the normalized flow stress variations versus strain and then select the normalized flow stress when it is saturated.

Hardening model

- Khan-Haung-Liang (KHL) is highly recommended for DP600 and TRIP780, which accurately describes the rate-dependency of mechanical response of these materials at various strain rates. Also, a rate-independent hardening model can easily reproduce the flow stress of AA5182-O at different strain rates, due to strain rate insensitivity. In case of using KHL for AA5182-O, the strain rate sensitivity should be set to around zero.

7.4 Future work

- The results of the simulations of EHDF indicate that the material can reach deformation rates that are beyond the range that was used to define the constitutive behaviour of the material. i.e. results show that around 20% of the plastic deformation can occur at very high strain rate regimes (above $15,000 \text{ s}^{-1}$). The predicted rates are substantially greater than in EHFF and are well above the rates ($1,000 \text{ s}^{-1}$) that were applied to characterize the tensile behaviour of the sheet materials. Therefore, for more accurate prediction of the sheet deformation in EHDF, the mechanical properties of the desired alloys should be determined at the same level of strain rate. This may also provide a better insight into the EHDF process.
- One of the main advantages of the Yld2004-18p yield function is its ability to describe the out-of-plane (through-thickness) anisotropy of sheet metals. Simulation results showed how important the effect of through-thickness compressive and shear stresses can be in EHDF, when the sheet contacts the die at high velocity. In this study, due to the unavailability of the through-thickness anisotropy of these materials at various strain rates, the out-of-plane flow stresses were set to their isotropic values. Determination of through-thickness anisotropy of the material (using measured crystallographic texture and crystal plasticity simulations) may help to further improve the predictions.
- For processes in which the sheet metal is subjected to relatively linear loading paths (such as EHFF), the simple assumption of isotropic hardening may lead to fairly accurate strain distributions. However, the results of simulations for processes in which the sheet metal undergoes reverse loading due to the successive bending and unbending that occurs when the sheet hits the die (such as in EHDF), the hardening behaviour should account for the kinematic hardening effects associated with the stress reversal. Although it is possible to develop rate-dependent advanced hardening models (such as kinematic or mixed isotropic-kinematic hardening models), it may be difficult to conduct cyclic tests at

intermediate and high strain rates, which means that it would be difficult to calibrate the advanced rate-dependent hardening models. Therefore, in this study, although it would have been beneficial to use kinematic hardening with anisotropic yielding, it was only possible to use and calibrate an isotropic hardening model. Nevertheless, the results of EHFF simulations show that the effect of anisotropy at intermediate and high strain rate regimes is accurately predicted, even though an isotropic hardening model was used.

Bibliography

- Al-Nasser, A.E., 2009. Characterization of sheet materials for stamping and finite element simulation of sheet hydroforming. The Ohio State University, M.Sc. thesis.
- Amstead, B.H., Ostwald, P.F., and Begman, M.L., 1987. Manufacturing processes, in, John Wiley and Sons, New York, 329-330.
- Andersson, A., Ohlsson, C.A., Mattiason, K., and Persson, B., 1999. Implementation and evaluation of the Karafillis-Boyce material model for anisotropic metal sheets. In: Gelin, J.C., Picart, P. (Eds.), Proceedings of NUMISHEET'99 1, Besancon, France, 115–121.
- Arminjon, M. and Imbault, D., 1994. An analytical micro-macro model for textured polycrystal at large plastic strains. *Int. J. Plasticity* 10, 825-847.
- Arminjon, M., 1991. A regular form of the Schmid law. Application to the ambiguity problem. *Textures and Microstructures* 14, 1121-1128.
- Armstrong, R.W., Ramachandran, V., and Zerilli, F.J., 1988. In: Rama Rao, P. (Ed.), *Advances in Materials and their Applications*. Wiley Eastern Ltd., New Delhip. 201.
- Baig, M., 2009. Responses of engineering materials, anisotropy and forming limit diagrams at different strain-rates and temperatures. University of Maryland Baltimore county, Ph.D. thesis.
- Balanethiram, V.S. and Daehn, G.S., 1992. Enhanced formability of interstitial free iron at high strain-rates. *Scripta Metallurgica et Materiala* 27, 1783-1788.
- Balanethiram, V.S. and Daehn, G.S., 1994. Hyperplasticity: increased forming limits at high workpiece velocity. *Scripta Metallurgica et Materiala* 30, 515–520.
- Balanethiram, V.S., Hu, X., Altynova, M., and Daehn, G.S., 1994. Hyperplasticity: Enhanced formability at high rates. *J. Materials Processing Technology* 45, 595-600.
- Banabic, D. and Cazacu, O., 2002. Anisotropy in sheet metals. In: Yang, D.Y., Oh, S.I., Huh, H., Kim, Y.H., (Eds.), *Proceedings of the Fifth International Conference and Workshop on Numerical Simulation of 3D Sheet Forming Processes*, Jeju Island, Korea, October 2001, 515–524.
- Bardelcik, A., Worswick, M.J., Winkler, S., and Wells, M.A., 2012. A strain rate sensitive constitutive model for quenched steel with tailored properties. *Int. J. Impact Eng.* 50, 49-62.
- Barlat, F. and Lian, J. 1989. Plastic behaviour and stretchability of sheet metals. Part I, A yield function for orthotropic sheet under plane stress conditions. *Int. J. Plasticity* 5, 51-66.
- Barlat, F., Aretz, H., Yoon, J.W., Karabin, M.E., Brem, J.C., and Dick, R.E., 2005. Linear transformation-based anisotropic yield functions. *Int. J. Plasticity* 21, 1009-1039.
- Barlat, F., Becker, R.C., Hayashida, Y., Maeda, Y., Yanagawa, M., Chung, K., Brem, J.C., Lege, D.J., Matsui, K., Murtha, S.J., and Hattori, S., 1997. Yielding description for solution strengthened aluminum alloys. *Int. J. Plasticity* 13, 385-401.
- Barlat, F., Brem, J.C., Yoon, J.W., Chung, K., Dick, R.E., Lege, D.J., Pourboghra, F., Choi, S.H., and Chu, E., 2003. Plane stress yield function for aluminum alloy sheet - Part I: theory. *Int. J. Plasticity* 19, 1297-1319.
- Barlat, F., Cazacu, O., Zyczkowski, M., Banabic, D., and Yoon, J.W., 2004. Yield surface plasticity and anisotropy. In: Raabe, D., Chen, L.-Q., Barlat, F., Roters, F. (Eds.), *Continuum*

scale simulation of engineering materials fundamentals microstructures process applications. WILEY-VCH Verlag, Berlin GmbH, 145-177.

Barlat, F., Lege, D.J., and Brem, J.C., 1991. A six-component yield function for anisotropic materials. *Int. J. Plasticity* 7, 693-712.

Baudoin, A.J., Dawson, P.R., Mathur, K.K., Kocks, U.F., and Korzekwa, D.A., 1994. Application of polycrystal plasticity to sheet forming. *Comput. Methods Appl. Mech. Eng.* 117, 49-70.

Becker, R.C., 1993. Simulations of earing in aluminum single crystals and polycrystals. *Mod. Sim. Mat. Sci. Eng.* 1, 203-224.

Benedict, G.F., 1987. *Non-traditional manufacturing processes*, CRC Press, New York.

Bishop, J.W.F. and Hill, R., 1951a. A theory of the plastic distortion of a polycrystalline aggregate under combined stresses. *Phil. Mag* 42, 414-427.

Bishop, J.W.F. and Hill, R., 1951b. A theoretical derivation of the plastic properties of polycrystalline face-centered. metals. *Phil. Mag.* 42, 1298-1307.

Bleck, W. and Schael, I., 2000. Determination of crash-relevant material parameters by dynamic tensile tests. *Steel research* 71, 173-178.

Boehler, J.P. and Sawczuk, A., 1970. Equilibre limite des sols anisotropes. *J. Me'canique* 9, 5-33.

Borvik, T., Hopperstad, O.S., Berstad, T., Langseth, and M.L., 2001. A computational model of viscoplasticity and ductile damage for impact and penetration. *European J. Mechanics: A/Solids* 20, 685-712.

Bruno, E.J., 1968. *High velocity forming of metals*. American society of tool and manufacturing engineers, Dearborn, Michigan.

Chachin, V.N., 1978. *Electrohydraulic treatment of structural materials*. Minsk, Nauka i Texnika, 80-87.

Cheah, L. and Heywood, J., 2011. Meeting US passenger vehicle fuel economy standards in 2016 and beyond. *Energy Policy* 39, 454-466.

Chen, J.K., H.K., Ching, and F., Allahdadi, 2007. Shock-induced detonation of high explosive by high velocity impact. *J. Mechanics of Materials and Impacts* 2, 1701-1721.

Chen, S.R., Gray III, G.T., 1995. Constitutive behavior of tungsten experiments and modeling. In: Bose, A., Dowding, R.J. (Eds.), *2nd Int. Cong. on Tungsten and Refractory Metals*, McLean, VA, Metal Powder Industries Federation, Princeton, NJ, 489-497.

Christian, J.W., 1983. Some surprising features of the plastic deformation of body-centered cubic metals and alloys. *Metall. Trans.* 14A, 1237-1256.

Chung, K. and Shah, K., 1992. Finite element simulation of sheet metal forming for planar anisotropic metals. *Int. J. Plasticity* 8, 453-476.

Chung, K., Richmond, O., 1993. A deformation theory of plasticity based on minimum work paths. *Int. J. Plasticity* 9, 907-920.

Cole, R.H., 1948. *Underwater explosions*, Princeton Univ. Press, Princeton.

Daehn, G.S., 2006. High velocity metal forming. *Metalworking: Sheet Metal Forming* 14B, ASM Handbook, 405-418.

- Dariani, B.M., Liaghat, G.H., and Gerdooei, M., 2009. Experimental investigation of sheet metal formability under various strain rates. *J. Engineering Manufacture* 223, 703–712.
- Darrieulat, M. and Piot, D., 1996. A method of generating analytical yield surfaces of crystalline materials. *Int. J. Plasticity* 12, 575-610.
- Davies, R. and Austin, E.R., 1970. Development in high speed metal forming. Industrial press Inc., New York.
- Drucker D.C. and Palgen L., 1981. On Stress-Strain Relations Suitable for Cyclic and Other Loading. *ASME J. Applied Mech.* 48, 479-485.
- Dusek, F., 1970. Plastic deformation at high strain rates. *Czechoslovak J. Physics* 20, 776-789.
- El-Magd, E., 1997. Influence of strain rate on ductility of metallic materials. *Steel Research* 68, 67-71.
- Ferreira, P.J., Sande, J.B., Fortes, M.A., and Kyrolainen, A., 2004. Microstructure development during high-velocity deformation, *Metallurgical and Materials Transactions A* 35, 3091-3101.
- Gambin, W. and Barlat, F., 1997. Modeling of deformation texture development based on rate independent crystal plasticity. *Int. J. Plasticity* 13, 75-85.
- Gambin, W., 1991. Plasticity of crystals with interacting slips systems. *Mod. Sim. Mat. Sci. Eng.* 39, 303-324.
- Gillard, A.J., Golovashchenko, S.F., and Mamutov, A.V., 2013. Effect of quasi-static prestrain on the form-ability of dual phase steels in Electrohydraulic forming. *J. Manufacturing Processes* 15, 201-218.
- Golovashchenko, S., Mamutov, V., Dmitriev, V., and Sherman, A., 2003. Formability of sheet metal with pulsed electromagnetic and electrohydraulic technologies. In: *Proceedings of TMS Symposium “Aluminum-2003”, San-Diego, 2003, 99–110.*
- Golovashchenko, S.F. and Mamutov, V.S., 2005. Electrohydraulic forming of automotive panels. In: *Proceedings of 6th Global Innovations Symposium: Trends in Materials and Manufacturing Technologies for Transportation Industries, San Francisco, USA, February 13–17, 65–70.*
- Golovashchenko, S.F., 2007. Material formability and coil design in electromagnetic forming. *J. materials Engineering and Performance* 16, 314–320.
- Golovashchenko, S.F., Bessonov, N., and Davies, R., 2011a. Analysis of sheet-die contact interaction in pulsed forming processes. *Proceeding of 10th Int. Conf. on Technology of Plasticity.*
- Golovashchenko, S.F., Bessonov, N.M., and Ilinich, A.M., 2011b. Two-step method of forming complex shapes from sheet metal. *J. Materials Processing Technology*, 875–885.
- Golovashchenko, S.F., Gillard, A.J., and Mamutov, A.V., 2013. Formability of dual phase steels in electrohydraulic forming. *J. Materials Processing Technology* 213, 1191–1212.
- Golovashchenko, S.F., Mamutov, V., and Ilinich, A.M., 2009. Electro-hydraulic forming tool having two liquid volumes separated by a membrane, U.S. Patent 7, 493,787.
- Gotoh, M., 1977. A theory of plastic anisotropy based on a yield function of fourth order (plane stress state)-I. *Int. J. Mech. Sci.* 19, 505-512.
- Gourdin, W.H. and Lassial, D.H., 1995. Multiple mechanisms in the thermally activated plastic flow of tantalum. *APS Topical Conference, Seattle, USA.*

Gray III, G.T. and Rollett, A.D., 1992. The high-strain-rate and spallation response of tantalum, Ta-10W, and T-111. In: Asfhani, R., Chen, E., Crowson, A. (Eds.), *High Strain Rate Behavior of Refractory Metals and Alloys*. TMS, Warrendale, PA, 303-315.

Grinenko, A., Sayapin, A., Efimov, S., Fedotov, A., and Krasik, Y.E., 2008. Last progress in underwater electrical wire explosion. *IEEJ Transactions on Fundamentals and Materials* 128, 31-36.

Groover, M.P., 2007. *Fundamentals of modern manufacturing, Materials, processes, and systems*, in, John Wiley and Sons, New York, 473-474.

Haowen, L., 2011. Responses and constitutive modeling of aluminum alloys, and strain-rate and temperature dependent failure criteria for F.C.C. and H.C.P. metals. University of Maryland Baltimore county, PhD thesis.

Hassannejadasl, A., Green, D.E., Golovashchenko S.F., Samei, J., Maris, C., 2014. Numerical modelling of electrohydraulic free-forming and die-forming of DP590 steel. *J. Manuf. Proc.* 16 (3), 391-404.

Hecker, S.S., 1976. Experimental studies of yield phenomena in biaxially loaded metals. *Constitutive Equations in Viscoplasticity: Computational and Engineering Aspects*. ASME, New York, 1-33.

Hershey, A.V., 1954. The plasticity of an isotropic aggregate of anisotropic face centered cubic crystals. *ASME J. Appl. Mech.* 21, 241-249.

Hill, R., 1948. A theory of the yielding and plastic flow of anisotropic metals. *Proc. R. Soc. Lond A* 193, 281-297.

Hill, R., 1950. *The Mathematical Theory of Plasticity*. Oxford University Press, Oxford.

Hill, R., 1979. Theoretical Plasticity of textured aggregates. *Proc. Camb. Phil. Soc.* 85, 179-191.

Hill, R., 1986. External paths of plastic work and deformation. *J. Mech. Phys. Solids* 34, 511-523.

Hill, R., 1990. Constitutive modelling of orthotropic plasticity in sheet metal. *J. Mech. Phys. Solids* 38, 405-417.

Hill, R., 1993. A user-friendly theory of orthotropic plasticity in sheet metals. *Int. J. Mech. Sci.* 35, 19-25.

Hosford, W.F., 1972. A generalized isotropic yield criterion. 1. *Appt. Mech. Trans. ASME* 39, 607-609.

Hosford, W.F., 1979. On yield loci of anisotropic cubic metals. *Proc. 7th North American Metalworking Conf SME, Dearborn, MI*, 191-197.

Hosford, W.F., 1985. Comments on anisotropic yield criteria. *Int. J. Mech. Sci.* 27, 423-427.

Hosford, W.F., 1992. *The Plasticity of Crystal and Polycrystals*. Oxford University Press, Oxford.

Hosford, W.F., 1996. On the crystallographic basis of yield criteria. *Textures and Microstructures* 26-27, 479-493.

Hu, X. and Daehn, G.S., 1996. Effect of velocity on flow localization in tension. *Acta Materialia* 44, 1021-1033.

- Huang, G., Yan, B., and Zhu, H., 2011. The effect of strain-rate on tensile properties and fracture strain. Presentation at great Design in Steel Seminar.
- Hughes, D.A., Kassner, M.E., Stout, M.G., and Vetrano, J.S., 1998. Metal Forming at the Center of Excellence for the Synthesis and Processing of Advanced Materials. JOM 50 (6).
- Ilinich, A.M., Golovashchenko, S.F., Smith, L.M., 2011. Material anisotropy and trimming method effects on total elongation in DP500 sheet steel, J. Materials Processing Technology 211, 441-449.
- Ilyushin A. A., 1961. On the postulate of plasticity. Prikl. Mat, Mekh. 25, 503.
- Imbert, J. and Worswick M.J., 2011. Electromagnetic reduction of a pre-formed radius on AA 5754 sheet. J. Materials Processing Technology 211, 896–908.
- Imbert, J., Winkler, S.L., Worswick, M.J., Olivera, D.A., and Golovashchenko, S.F., 2005. The effect of tool-sheet interaction on damage evolution in electromagnetic forming of aluminum alloy sheet. J. Engineering Materials and Technology 127, 145–152.
- Inal, K., Wu, P.D., and Neale, K.W., 2000. Simulation of earing in textured aluminum sheets. Int. J. Plasticity 16, 635-648.
- Johnson, G.R., Cook, W.H., 1983. A constitutive model and data for metals subjected to large strains, high strain rates and high temperatures. In: Proceedings of the 7th International Symposium on Ballistic, Hague, Netherlands, 541-547.
- Kapila, A.K., Schwendeman, D.W., Bdzil, J. B. and Henshaw, W.D., 2007. A study of detonation diffraction in the ignition-and-growth model. Combustion Theory and Modelling 11, 781-822.
- Kaps, L., Lipowsky, H.J., Meywerk, M., Werner, H., and Scholz, S.P., 1999. Auswerteverfahren zur Weiterverarbeitung von Versuchsdaten. VDEH working Group Int. Communication.
- Karafilis, A.P. and Boyce, M.C., 1993. A general anisotropic yield criterion using bounds and a transformation weighting tensor. J. Mech. Phys. Solids 41, 1859-1886.
- Khan, A.S. and Farrokh, B., 2006. Thermo-mechanical response of nylon 101 under uniaxial and multi-axial loadings: Part I, Experimental results over wide ranges of temperatures and strain rates. Int. J. Plasticity 22, 1506–1529.
- Khan, A.S. and Liang, R., 1999. Behaviors of three B.C.C. metal over a wide range of strain rates and temperatures: experiments and modeling. Int. J. Plasticity 15, 1089-1109.
- Khan, A.S. and Zhang, H., 2000. Mechanically alloyed nanocrystalline iron and copper 123 mixture: behavior and constitutive modeling over a wide range of strain rates Int. J. Plasticity 16 (12), 1477–1492.
- Khan, A.S., Kazmi, R., and Farrokh, B., 2007a. Multiaxial and non-proportional loading responses, anisotropy and modeling of Ti–6Al–4V titanium alloy over wide ranges of strain rates and temperatures. Int. J. Plasticity 23, 931-950.
- Khan, A.S., Kazmi, R., and Farrokh, B., et al., 2007b. Effect of oxygen content and microstructure on the thermo-mechanical response of three Ti–6Al–4V alloys: Experiments and modeling over a wide range of strain-rates and temperatures. Int. J. Plasticity 23, 1105–1125.
- Khan, A.S., Suh, Y.S., and Kazmi, R., 2004. Quasi-static and dynamic loading responses and constitutive modeling of titanium alloys. Int. J. Plasticity 20, 2233–2248.

- Kim, J., Kim, D., Han, H.N., Barlat, F., and Lee, M.G., 2013. Strain rate dependent tensile behavior of advanced high strength steels: Experiment and constitutive modeling, *Mat. Sci. and Eng. A* 559, 222-231.
- Kojic, M., 2002. Stress integration procedures for inelastic material models within finite element method. *Appl. Mech. Reviews* 55, 389-414.
- Lane, T., 1767. Description of an Electrometer invented by Mr. Lane; with an account of some experiments made by him with it: in a Letter to Benjamin Franklin. *Philosophical Transactions of the Royal Society* 57, 451.
- Lee, C.S., Bae, G.H., Kim, S.B., Lou, Y., Huh, H., 2010. Construction of the Hill48 and Barlat89 for Auto-body Steel Sheets considering the Strain Rate. 4th Int. Conf. on High Speed Forming, Columbus, Ohio, USA.
- Lequeu, P.h., Gilormini, P., Montheillet, F., Bacroix, B., and Jonas, J.J., 1987a. Yield surfaces for textured polycrystals-Part I: Crystallographic approach. *Acta Metall.* 35, 439-451.
- Lewandowski, J.J., Lowhaphandu, P., 1998. Effects of hydrostatic pressure on mechanical behaviour and deformation processing of materials. *Int. Materials Reviews* 43, 145–187.
- Liang, R. and Khan, A.S., 1999. A critical review of experimental results and constitutive models of BCC and FCC metals over a wide range of strain rates and temperatures. *Int. J. Plasticity* 15, 963-980.
- Lin, S.B. and Ding, J.L., 1996. A Modified form of Hill's orientation-dependent yield criterion for orthotropic sheet metals. *J. Mech. Phys. Solids* 44, 1739-1764.
- Liu, D., Yu, H., and Li, C., 2011. Experimental observations of quasi-static-dynamic formability in biaxially strained AA5052-O. *J. Materials Engineering and Performance* 20, 223–230.
- LS-DYNA Theory Manual, 2006. Livermore Software Technology Corporation.
- Maniatty, A. M., Keane, T., and Yu, J.S., 1997. Anisotropic yield criterion for polycrystalline metals using texture and crystal symmetries. *Znt. J. Solids and Strut.*, 18-26.
- Maris, C., 2014. Experimental determination of the forming limits of DP600 and AA5182 sheets in electrohydraulic free forming. University of Windsor, Windsor, CA, M.Sc. thesis.
- Mecking, H. and Kocks, U.F., 1981. Kinetics of flow and strain-hardening. *Acta Metallurgica* 29 (11), 1865–1875.
- Melander, A., Delic, A., and Bjorkblad, A., Juntunen, P., Samek, L., Vadillo, L., 2011. Modelling of electrohydraulic free and die forming of sheet steels. *Int. J. Materials Forming* 6, 223-231.
- Mellor, P.B. and Parmar, A., 1978. Plasticity of sheet metal forming. *Mechanics of Sheet Metal Forming*, Plenum Press, New York, 53-74.
- Mellor, P.B., 1981. Sheet metal forming. *Int. Metals Reversus* 26, 1-20.
- Montheillet, F., Jonas, J. J., and Benferrah, M., 1991. Development of anisotropy during the cold rolling of aluminum sheet. *Int. J. Mech. Sci.* 33, 197-209.
- Mynors, D.J. and Zhang, B., 2002. Applications and capabilities of explosive forming. *J. Materials Processing Technology* 125–126, 1–25.
- Needleman, A., 1991. The effect of material inertia on neck development, AM Press, Ann Arbour, US.

- Nemat-Nasser, S. and Yulong, L., 1998. Flow stress of F.C.C. polycrystals with application to OFHC Cu. *Acta Mat.* 46(2), 565-577.
- Nemat-Nasser, S., Guo, W.G., Nesterenko, V., Indrakanti, F., and Gu, Y., 2001. Dynamic response of conventional and hot isostatically pressed Ti-6Al-4V alloys: experiments and modeling. *Mechanics of Materials* 33 (8), 425-439.
- Oliver, S., Jones, T.B., and Fournalis, G., 2007. Dual phase versus TRIP strip steels: Microstructural changes as a consequence of quasi-static and dynamic tensile testing. *Materials Characterization* 58, 390-400.
- Olivera, D.A., Worswick, M.J., Finn, M., and Newman, D., 2005. Electromagnetic forming of aluminum alloy sheet: free form and cavity fill experiments and model. *J. Materials Processing Technology* 170, 350-362.
- Paul, S.K., 2012. Predicting the flow behavior of metals under different strain rate and temperature through phenomenological modeling. *Comput. Mat. Sci.* 65, 91-99.
- Picu, R.C., Vincze, G., Ozturk, F., Gracio, J.J., Barlat, F., and Maniatty, A.M., 2005. Strain rate sensitivity of the commercial aluminum alloy AA5182-O. *Mat. Sci. Eng. A* 390, 334-343.
- Priem, D., Marya, S., and Racineux, G., 2007. On the forming of metallic parts through Electromagnetic and Electrohydraulic processing. *Advanced Materials Research* 17, 655-660.
- Priestly, J., 1769. Experiments on the lateral force of electrical explosions. *Philosophical Transactions of the Royal Society* 59, 57.
- Psyk, V., Risch, D., Kinsey, B.L., Tekkaya, A.E., and Kleiner, M., 2011. Electromagnetic forming – a review. *Journal of Materials Processing Technology* 211, 787-829.
- Rahmaan, T., Bardelcik, A., Imbert, J., Kim, S., Worswick, M.J., 2014. Strain rate sensitivity and anisotropy of TRIP780, DP600, and AA5182-O sheet metal alloys. *Proceedings of the 4th International Conference on Impact of Lightweight Structures, Cape Town, South Africa.*
- Regazzoni, G., Kocks, U.F., and Follansbee, P.S., 1987. Dislocation kinetics at high strain rates. *Acta Metall.* 12(35), 2865-2875.
- Rohatgi, A., Stephens, E.V., Davies, R.W., Smith, M.T., Soulami, A., and Ahzi, S., 2012. Electro-hydraulic forming of sheet metals: free-forming versus conical-die-forming. *J. Materials Processing Technology* 212, 1070-1079.
- Rohatgi, A., Stephens, E.V., Soulami, A., Davies, R.W., and Smith, M.T., 2011. Experimental characterization of sheet metal deformation during electrohydraulic forming. *J. Materials Processing Technology* 211, 1824-1833.
- Sandford, J.E., 1970. Recent advances stir interest in high velocity forming. *Iron Age Metalworking International* 204, 36-38.
- Schwer, L.E., 2012. Impact and detonation of Comp-B, an example using the LS-DYNA EOS: ignition and growth of reaction in high explosives. 12th Int. LS-DYNA Users Conference.
- Seth, V.S.M., Vohnout, V.J., and Daehn, G.S., 2005. Formability of steel sheets in high velocity impact. *J. Materials Processing Technology* 45, 595-600.
- Simo, J.C., Hughes, T.J.R., 1998. *Computational Inelasticity. Volume 7 of Interdisciplinary Applied Mathematics.* Springer-Verlag, Berlin.
- Simo, J.C., Taylor, R.L., 1985. Consistent Tangent Operators for Rate Independent Elasto-Plasticity. *Comput. Meth. Appl. Mech. Eng.* 48, 101-118.

- Simo, J.C., Taylor, R.L., 1986. Return Mapping Algorithm for Plane Stress Elastoplasticity. *Int. J. Numer. Meth. Eng.* 22, 649-670.
- Sklad, M.P. and Verhaeghe, J.D., 2010. Forming limit curve based on shear under tension failure criterion. *Proceedings of the IDDRG 2010 Int. Conference. Graz, Austria*, 1-10.
- Smerd, R., Winkler, S., Salisbury, C., Worswick, M.J., Lloyd, D., and Finn, M., 2005. High strain rate tensile testing of automotive aluminum alloy sheet. *Int. J. Impact Eng.* 32 (1-4), 541-560.
- Sobotka, Z., 1969. Theorie des plastischen Fliessens von anisotropen Korpern. *Zeit. Angew. Math. Mech.* 49, 25-32.
- Spitzig, W.A, Sober, R.J., and Richmond, O., 1976. The effect of hydrostatic pressure on the deformation behavior of Maraging and HY-80 steels and its implication for plasticity theory. *Metall. Trans.* 7A, 1703-1710.
- Spitzig, W.A. and Richmond, O., 1984. The effect of pressure on the flow stress of metals. *Acta Metall.* 32, 457-463.
- Tarigopula, V., Hopperstad, O.S., Langseth, M., Clausen, A.H., and Hild, F., 2008. A study of localisation in dual phase high-strength steels under dynamic loading using digital image correlation and FE analy-sis. *Int. J. Solids and Structures* 45, 601-619.
- Taylor, G.I., 1942. The Plastic Wave in a Wire Extended by an Impact Load. British Ministry of Home Security, Civil Defense Research Committee Report RC 323.
- Toth, L.S., Van Houtte, P., and Van Bael, A., 1991. Analytical representation of polycrystal yield surface. In *Anisotropy and Localization of Plastic Deformation*. Elsevier Applied Science, London, 183-186.
- Tugcu, P. and Neale, K.W., 1999. On the implementation of anisotropic yield functions into finite strain problems of sheet metal forming. *Int. J. Plasticity* 15, 1021-1040.
- Urtiew, P.A., Vandersall, K.S., Tarver, C.M., Garcia, F., and Forbes, J.W., 2006. Shock initiation experiments and modelling of composition B and C-4. 13th International Detonation Symposium Norfolk, VA, United States.
- Van Houtte, P., 1994. Application of plastic potentials to strain rate sensitive and insensitive anisotropic materials. *Int. J. Plasticity* 10, 719-748.
- Van Slycken, J., Verleysen, P., Degrieck, J., Bouquerel, J., and De Cooman, B.C., 2007. Dynamic response of aluminium containing TRIP steel and its constituents phases. *Mat. Sci. Eng. A*, 460-461, 516-524.
- Vashchenko, A.P., Stepanov, G.V., Tokarev, V.M., Leonev, V.P., Motovilina, G.D., and Eglit, A.S., 1989. Influence of loading rate on the mechanical properties of steels of different strength levels. *Strength of Materials* 21, 1328-1335.
- Vohnout, V.J. and Daehn, G.S., 2002. Effect of quasi-static prestrain and eddy currents on limit strains in electromagnetic pulse forming of two aluminum alloys. In: *Aluminum 2002—proceedings of the TMS annual meeting*.
- von Karman, T. and Duwez, P., 1950. The propagation of plastic deformation in solids. *J. Applied Physics* 21, 987-994.
- Wakeland, P., Kincy, M., and Garde, J., 2003. Hydrodynamic loading of structural components due to electrical discharge in fluids. *Digest of Technical Papers-IEEE International Pulsed Power Conference*, 925-928.

- Weixian, Z., 1990. A new non-quadratic orthotropic yield criterion. *Int. J. Mech. Sci.* 32, 513-520.
- Wood, W.W., 1967. Experimental mechanics at velocity extremes-very high strain rates. *Experimental Mechanics* 7, 441-446.
- Worswick, M.J., and Finn, M.J., 2000. The numerical simulation of stretch flange forming. *Int. J. Plasticity* 16, 701-720.
- Yoon, J.W., Barlat, F., Chung, K., and Pourboghrat, F., Yang, D.Y., 2000. Earing predictions based on asymmetric non-quadratic yield function. *Int. J. Plasticity* 16, 1075-1104.
- Yoon, J.W., Barlat, F., Dick, R.E., Chung, K., and Kang, T.J., 2004. Plane stress yield function for aluminum alloy sheet-Part II: FE Formulation and its implementation, *Int. J. Plasticity* 20, 495-522.
- Yoon, J.W., Yang, D.Y., and Chung, K., 1999a. Elasto-plastic finite element method based on incremental deformation theory and continuum based shell elements for planar anisotropic sheet materials. *Comput. Methods Appl. Mech. Eng.* 174, 23-56.
- Yoon, J.W., Yang, D.Y., Chung, K., and Barlat, F., 1999b. A general elasto-plastic finite element formulation based on incremental deformation theory for planar anisotropy and its application to sheet metal forming. *Int. J. of Plasticity* 15, 35-68.
- Yutkin, L. A., 1950. Elektrogidravlichesky effect. U.S.S.R. State Science and Technology Press for Machine Construction, Moscow.
- Zeng, L.F., Horrigmoe, G., and Andersen, R., 1996. Numerical implementation of constitutive integration for rate-independent elastoplasticity. *Comput. Mech.* 18, 387-396.
- Zerilli, F.J. and Armstrong, R.W., 1987. *J. Applied Physics* 61 (5), 1816-1825.
- Zhao, H., 1997. *Materials Science and Engineering A* 230, 95-99.
- Zyczkowski, M., 2001. Anisotropic yield conditions. In: Lemaitre, J. (Ed.), *Handbook of Materials Behavior Models*. Academic Press, San Diego, CA, 155-165.

Appendices

A1. Anisotropy coefficients identification of Yld2004-18p

The corresponding stress tensor expressed in the embedded material frame for in-plane tension condition at degrees from the rolling direction (RD), can be written as the following

$$\boldsymbol{\sigma} = [\sigma_{\varphi} \cos^2 \varphi \quad \sigma_{\varphi} \sin^2 \varphi \quad 0 \quad 0 \quad 0 \quad \sigma_{\varphi} \sin \varphi \cos \varphi]^T \quad (\text{A1.1})$$

where σ_{φ} is the flow stress in the corresponding direction. According to the relation between the Cauchy and deviatoric stresses, the stress deviator can be expressed by

$$\mathbf{s} = \sigma_{\varphi} [(\cos^2 \varphi - 1/3) \quad (\sin^2 \varphi - 1/3) \quad -1/3 \quad 0 \quad 0 \quad \sin \varphi \cos \varphi]^T = \sigma_{\varphi} \mathbf{s}_{\varphi} \quad (\text{A1.2})$$

where σ_{φ} is given by

$$\frac{\sigma_{\varphi}}{\bar{\sigma}} = \left(\frac{4}{\Phi(\mathbf{s}_{\varphi})} \right)^{1/a} \quad (\text{A1.3})$$

The r-value for the uniaxial tension condition (r_{φ}) can be calculated as follows

$$r_{\varphi} = -1 - \frac{4a}{(\sigma_{\varphi}/\bar{\sigma}) \left(\partial \Phi / \partial s_{zz} |_{\mathbf{s}_{\varphi}} \right)} \quad (\text{A1.4})$$

For in-plane balanced biaxial tension stress state, the stress tensor can be expressed by

$$\mathbf{s} = \sigma_b [-1/3 \quad -1/3 \quad 2/3 \quad 0 \quad 0 \quad 0]^T = \sigma_b \mathbf{s}_b \quad (\text{A1.5})$$

where σ_b is given by

$$\frac{\sigma_b}{\bar{\sigma}} = \left(\frac{4}{\Phi(\mathbf{s}_b)} \right)^{1/a} \quad (\text{A1.6})$$

The r-value for the balanced biaxial tension condition (r_b) can be calculated by

$$r_b = \frac{\partial\Phi/\partial s_{yy}}{\partial\Phi/\partial s_{xx}} \quad (\text{A1.7})$$

The out-of-plane flow stresses are expressed by

$$\frac{\sigma_q}{\bar{\sigma}} = \left(\frac{4}{\Phi(\mathbf{s}_q)} \right)^{1/a} \quad (\text{A1.8})$$

where \mathbf{s}_q is obtained from the following equations, depending on the stress state

$$\mathbf{s}_q = \sigma_q [-1/3 \quad 1/6 \quad 1/6 \quad 1/2 \quad 0 \quad 0]^T \quad \text{for uniaxial tension at } 45^\circ \text{ in the (TD} \\ \text{– ND) plane,}$$

$$\mathbf{s}_q = \sigma_q [1/6 \quad -1/3 \quad 1/6 \quad 0 \quad 1/2 \quad 0]^T \quad \text{for uniaxial tension at } 45^\circ \text{ in the (ND} \\ \text{– RD) plane,} \quad (\text{A1.9})$$

$$\mathbf{s}_q = \sigma_q [0 \quad 0 \quad 0 \quad 1 \quad 0 \quad 0]^T \quad \text{for simple – shear in the (TD – ND) plane,}$$

$$\mathbf{s}_q = \sigma_q [0 \quad 0 \quad 0 \quad 0 \quad 1 \quad 0]^T \quad \text{for simple – shear in the (ND – RD) plane.}$$

A2. Implicit integration algorithm for implementation of rate-dependent hardening model (VUMAT)

Step-1. Elastic Predictor (trial stress calculation)

1.1. Calculate trial stress: $\boldsymbol{\sigma}^{Tr} = \boldsymbol{\sigma}_n + \mathbf{D}[\Delta\boldsymbol{\varepsilon}^p]$

1.2. Check for the yield condition

- If $\bar{\sigma} \leq \sigma_y$ or $\bar{\sigma} \cdot [1/\sigma_{y2}] \leq \sigma_{y1}$; then set $(\bullet)_{n+1} = (\bullet)_{n+1}^{Tr}$ and Exit.
- Else Goto step-2.

Step-2. Visco-plastic Corrector (multistep return mapping algorithm)

2.1. Initial iteration:

- $\Delta p = 0$ and $\boldsymbol{\sigma}_{n+1} = \boldsymbol{\sigma}^{Tr}$

2.2. Calculate the effective plastic strain and stress tensor ($\boldsymbol{\sigma}$):

- Use Eq. (5-2) to calculate σ_{y1} and σ_{y2}
- Use Eq. (5-13) to calculate the residuals g_1 and g_2
- If g_1 and $g_2 \leq Tolerance$ (10^{-6}); then Goto Step-1, ELSE
- Use Eq. (5.16) to calculate \mathbf{X}_i^{-1}
- Depending on the hardening model, use Eqs. (5-20a) or (5-22a) or (5-24a) to calculate $\frac{d}{d\Delta p} \left(\frac{1}{\sigma_{y2}} \right)$ and H
- Solve Eqs. (5-14) and (5-15) to find $d\Delta p$ and $\Delta\boldsymbol{\sigma}$
- Update: $\Delta p_{n+1} = \Delta p_n + d\Delta p$, $p_{n+1} = p_n + \Delta p$, $\boldsymbol{\sigma}_{n+1} = \boldsymbol{\sigma}_n + \Delta\boldsymbol{\sigma}$
- Goto 2.2.

A3. ICTP written permission



Mr. Amir Hassannejadasl,
University of Windsor,
Apt. 505 - 1177 Bloor St., Mississauga, ON,
Canada

Sep. 16, 2014

Letter of permission from the copyright owner (ICTP2014)

Dear Mr. Amir Hassannejadasl,

On behalf of the organizing committee of the 11th International Conference on Technology of Plasticity, we are pleased to give you to the permission to include the paper in your dissertation.

Paper no. : 283

Paper title: Prediction of DP600 flow surfaces at various strain-rates using Yld2004-18p yield function.

Authors: Amir Hassannejadasl, Taamjeed Rahman, Daniel E. Green, Sergey F. Golovashchenko, Michael J. Worswick

The ICTP2014 Proceedings papers will be published in Procedia Engineering.

We look forward to seeing you in Nagoya, Japan.

Sincerely,

T. Ishikawa and K. Mori
Chairmen of ICTP2014



Prof. Dr. Eng. Takashi Ishikawa
Dept. of Materials Science and Engineering, Nagoya University
Furo-cho, Chikusa-ku, Nagoya, 464-8603, Japan
Tel. +81 (0)52 789 3256, Fax +81 (0)52 789 3572
chair@ictp2014.org, www.ictp2014.org

VITA AUCTORIS

NAME Amir Hassannejadasl

PLACE OF BIRTH Shiraz, Iran

YEAR OF BIRTH 1981

EDUCATION

Isfahan University of Technology, Isfahan, Iran
B.A.Sc. in Mechanical Engineering, 2003

Sharif University of Technology, Tehran, Iran
M.A.Sc. in Mechanical Engineering, 2007

University of Windsor, Windsor, Ontario
Ph.D in Mechanical Engineering, 2014